Experimental and numerical study of sea spray generation and transport, and their consequences on the properties of the marine atmospheric boundary layer

William Bruch

Étude expérimentale et numérique de la génération et du transport des aérosols marins à l'interface air-mer pour des vents forts, et des conséquences sur les propriétés de la couche limite atmosphérique marine

THÈSE

présentée et soutenue publiquement le 10 Décembre 2021

pour l'obtention du

Doctorat de l'Université de Toulon

Mention Sciences de l'Univers –
Météorologie, Océanographie Physique et Physique de l'Environnement

par

William Bruch

Composition du jury

Président :	Alexander van Eijk	*École Centrale Nantes (Nantes)*
Rapporteurs :	Fabrice Veron	*University of Delaware (Delaware, USA)*
	Marie-Noëlle Bouin	*Centre National de Recherches Météorologiques (Toulouse)*
Examinateurs :	Peter Sutherland	*Laboratoire d'Océanographie Physique et Spatiale (Brest)*
	Pierre Tulet	*Laboratoire d'Aérologie (Toulouse)*
Invitée :	Marie Vicomte	*Direction Générale de l'Armement (Paris)*
Encadrants :	Jacques Piazzola (Directeur)	*Institut Méditerranéen d'Océanologie (Toulon)*
	Gilles Tedeschi (Co-directeur)	*Institut Méditerranéen d'Océanologie (Toulon)*
	Denis Bourras (Co-encadrant)	*Institut Méditerranéen d'Océanologie (Marseille)*

Remerciements

Tout d'abord, cette thèse n'aurait évidémment pas eu lieu sans l'écriture et la mise en oeuvre du projet par Jacques Piazzola, pour lesquels je le remercie grandement. J'en profite pour remercier Jacques pour ses bons conseils, son énergie, et sa confiance tout le long de la thèse. Je remercie également Denis Bourras et Gilles Tedeschi d'avoir acceptés de co-encadrer ce projet, et de m'avoir apporté éléments et points de vus très complémentaires pendant ma découverte des complexités la couche limite atmosphérique marine. J'ai eu la chance de profiter d'un encadrement amical et bienveillant, dont je garderai un très bon souvenir.

Je souhaite également remercier mon jury très complémentaire et dynamique d'avoir accepté d'évaluer le travail issu de ces trois années de thèse.

Après les quelques mois d'étude bibliographique typiques d'un début de thèse, le besoin de mieux comprendre l'effet des intéractions vague-vent sur la génération d'embruns devint une priorité. Ainsi, la campagne en laboratoire MATE2019 fut esquissée entre le MIO et l'équipe de recherche de la grande soufflerie de l'OSU-Pytheas (Luminy, Marseille) qui a fait preuve d'une grande énergie, ainsi qu'une impressionante expertise scientifique dans leur installation expérimentale très impressionante. Je souhaite particulièrement remercier Hubert Branger (IRPHE) et Christopher Luneau (OSU-Pytheas) avec qui nous avons enduré deux canicules dans le seul but de continuellement générer vagues, vents et spume droplets, pendant deux mois. Je suis ravi d'y avoir fait la connaissance d'Alain (deux, trois), bon carnussien et grand humoriste de la soufflerire. Je remercie également Rémi Chemin pour son aide précieuse, tel qu'à l'installation CASH de SEATECH (Toulon) où d'importantes mesures préliminaires furent effectuées avec l'aide bienvenue de Aimed Ajroud. Merci à toi Rémi, de m'avoir enseigné dans l'art du ruban adhésif et des colliers de serrage en plastique (PS: ça marche un peu moins en mer, mais sans doute parce que tu n'étais pas là). Suite à cette campagne, j'ai eu le plaisir de rencontrer et collaborer avec Lex van Eijk (ECN–TNO) dont je remercie la disponibilité, la rigueur et la capacité impressionante à trouver même les plus petites erreurs dans les plus longs articles.

C'est au SIP de l'OSU-Pytheas que je souhaite faire parvenir mes remerciements pour la disponibilité du cluster de calcul. Je remercie particulièrement Christophe Yohia (cité sur la page wikipédia du Mistral) qui m'a bien aidé dans la configuration du modèle Meso-NH pour des utilisations en Atlantique et en Méditerranée. Je remercie également Alix Limoges avec qui j'ai eu le plaisir de travailler pendant son stage de master. Je remercie également Pierre Tulet du LAERO (Toulouse) pour son apport important pour le transport d'aérosols avec Meso-NH, et son aide pour les longues périodes de débuggage, qui nous auront bien hantés pendant quelques mois. J'étends mes remerciements à Joris Pianezze pour son aide tant avec Méso-NH que sa belle collection de modèles océaniques couplés, ainsi que pendant nos trails Réunionnais aussi tendus que nos crampes.

La thèse à également compris une partie importante de mesures au large ainsi qu'en zone cotière. Je souhaite d'abord remercier l'équipe du LOPS pour leur accueil chaleureux à bord du navire de recherche océanographique l'Atalante durant la campagne SUMOS, dont Peter Sutherland, Marie-Noëlle Bouin, Louis Marié, Gwendal Maréchal aka young JB (ainsi que le reste de l'équipe scientifique et l'équipage), avec qui nous avons partagé creux, crêtes, et entrées chaudes (la mer ça creuse l'appétit et ça décoiffe). J'en profite ici pour remercier Abderrahim Bentamy du LOPS de m'avoir fait part de sa passion pour l'océanographie pendant mes années de licence, à que je dois donc beaucoup, et à qui je souhaite une formidable retraite. Je souhaite également remercier Tathy Missamou du MIO pour son aide précieuse en métrologie, jouant un rôlé clé dans le bon déploiement des capteurs d'aérosols en Méditerranée, en Loire Atlantique, et même à Brest. Je remercie également l'équipe du Air-Sea Interaction Laboratory du Scripps (USA) de nous avoir accueilli en 2019, ainsi que pour leur enthousiasme dans le contexte d'un début de collaboration, qui j'espère, se poursuivra.

Je souhaite remercier l'Agence Innovation Défense (AID-DGA) (contrat 2018-60-0038) ainsi que la Region SUD (contrat 2018-06085) pour le financement de cette thèse. Je souhaite également remercier le programme de recherche MATRAC, financé par l'ANR-ASTRID (contrat ANR-18-ASTR-0002), pour m'avoir permis de participer à divers déploiements métrologiques au site SEMREV (ECN) au Croisic, ainsi que la station d'observation de Porquerolles (MIO).

J'ai gardé les meilleurs pour la fin! Merci à mes amis de l'être, et merci à ma famille de l'avoir toujours été. J'aimerais remercier tous ces gens sympas que j'ai pu rencontrer dans la région PACA, qui fut une très belle découverte pour Camille et moi-même. Merci donc aux collègues des Burritos de la Chica, les MIOjitos, l'équipe MIOhippus, la BTP, le collectif des doctorants du MIO Marseille, et évidemment les doctorants du Bat. X avec qui nous avons arpenté mer, montagnes, arpèges, bons thés et descentes. Parce qu'ils sont trop nombreux je ne vais pas en nommer du tout, mais ils sauront se reconnaître. Je tiens également à écrire noir sur blanc, pour la descendance, que c'est bien le MIO qui a remporté la toute première victoire des Jeux du X lors de la rencontre amicale de 2021 avec le LIS ($2^{\text{ème}}$) et le MAPIEM ($3^{\text{ème}}$). Enfin, merci d'avoir été des co-doctorants et co-bureaux aussi mirifiques; Baptiste, Caroline, Kubeb.

Pour finir, merci à ma famille, douée de richesses avec ses linguistes, artistes, et écologistes, pour toutes ces années (et celles à venir) durant lesquelles vous m'avez encouragé sans relâche. Merci. Et enfin, c'est à mon tour de te remercier Camille, mon compagnon de vie et d'aventures. J'ai hâte de partager la suite avec toi, tant le passé a été rocambolesque.

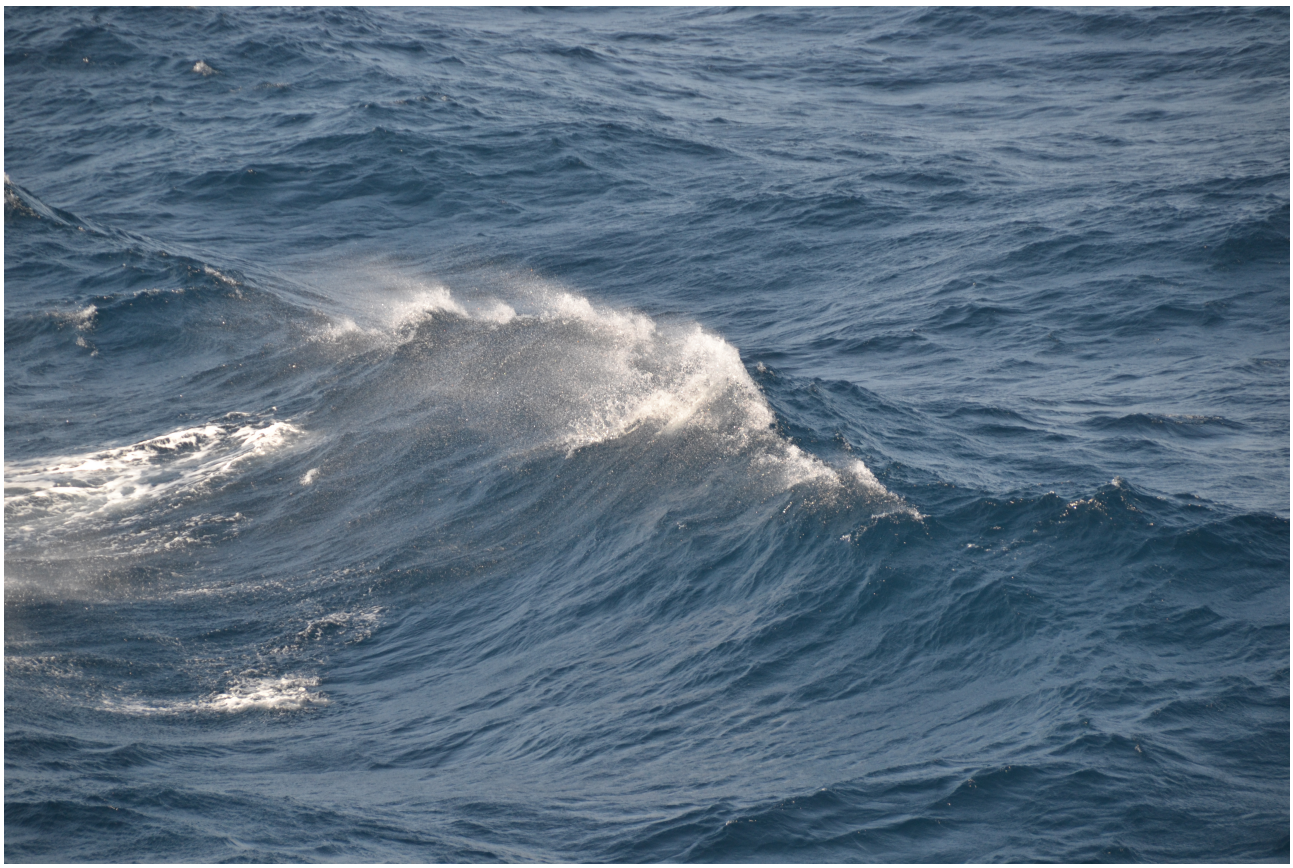

(a)

(b)

(a) Photograph of spume droplets torn from the wave crests in the Bay of Biscay during the SUMOS research Cruise, February 2021.

(b) Spume droplet generation from the wave crests in the Large Air-Sea Interface Facility (Luminy, Marseille), July 2019.

Photographs taken by William Bruch
Page layout by Matilda Bruch

Table of Contents

Extended Thesis Abstract

Sea spray are aqueous phase aerosols generated from the water surface. In the open ocean, they are generated as a result of wind-forced wave breaking and surface-tearing mechanisms. As sea spray droplets are transported in the marine atmospheric boundary layer, dynamic and thermodynamic air-droplet effects result in a complex range of feedbacks on the transfers of heat, moisture and momentum between the ocean and the atmosphere, thus affecting the weather and climate. To this day, knowledge of sea spray particles larger than 20μm radius is sparse as a result of scarce observations. Yet, these larger particles represent the majority of the sea spray volume in high wind speeds. To quantify such feedback effects, accurate knowledge of the sea spray generation flux over a wide size range is essential.

The present thesis aims to improve knowledge of the sea spray generation flux and its dependence on wind and wave interactions, with the ultimate aim of a better understanding of air-droplet dynamic and thermodynamic effects on marine atmospheric boundary layer characteristics. To this end, the effects of wind–wave interactions on the surface sea spray generation flux are investigated during the Marine Aerosol Tunnel Experiment (MATE2019), conducted at the Pytheas Institute large wave–wind facility in Luminy (Marseille, France) over the period June–July 2019. A unique range of air–sea boundary conditions was generated by configuring the laboratory with four types of wave forcing and five wind speeds spanning 8–20 m s^{-1}. Young and developed waves were included, with wave ages between 1.3 and 9.5 (defined in terms of phase speed and friction velocity). Vertical sea spray concentration profiles measured over the 0.1–47.5 μm radius range and a flux-profile method allowed estimation of the sea spray generation flux. The flux is comparable to field and laboratory fluxes reported in author studies. Scaling analysis shows that the sea spray generation is best correlated with the wave-slope variance for larger droplets (20 μm and above, assumed predominantly spume droplets generated by surface tearing). For smaller droplets (7–20 μm, presumed predominantly jet droplets generated by bubble bursting), the highest correlation is found with a non-dimensional number combining the wave-slope variance with the friction velocity cubed u_*^3. This is reflected in the formulation of two wave-state-dependent sea spray generation functions, each valid for wind speeds 12–20 m s^{-1} and droplet radii 3–35 μm, thereby covering jet and spume droplet production.

The laboratory-derived generation functions are parameterized in the MACMod (Tedeschi and Piazzola 2011) and MesoNH (Lac et al. 2018) numerical models. In the absence of forcings from a wave model, the laboratory wave-slope variance is tentatively upscaled to the field with a proposed correction to the wind-dependent Cox and Munk (1956) formulation. Meteorological and sea spray measurements made in the North-West Mediterranean (MIRAMER research cruise, 2008) and the North-East Atlantic (SUMOS research cruise, 2021) onboard the R/V Atalante are presented and serve for the validation of the numerical models. The SUMOS aerosol

measurements, collected in a 2–21 wind speed range, were performed in complement to the laboratory measurements, and are reported here for the first time. Promising modelling results are found for both laboratory generation functions, further suggesting that laboratory fluxes can be applicable in the field. Best results are found with the non-dimensional combination number P_S, where in addition to the ability of the wave slope variance to scale sea spray generation in the high wind speeds of MATE2019, the u_*^3 term allows for higher flux sensitivity to a wider range of wind speed conditions.

Keywords: Air–sea interaction - Sea spray generation - Friction velocity cubed - Wave-slope variance - Field data - Numerical modelling

Résumé en Français

Les aérosols atmosphériques sont des particules solides ou liquides en suspension dans un gaz, et se trouvent majoritairement dans les basses couches de l'atmosphère. Les origines de ces particules, naturelles et/ou anthropiques sont aussi diverses que leur taille, leur forme et leur composition. Elles peuvent être directement émises depuis les continents ainsi que l'hydrosphère, ou résulter de diverses réactions photo-chimiques dans l'atmosphère. Au cours des dernières décennies, les contributions météorologiques et climatiques des aérosols ont été mises en lumière. Les aérosols jouent un rôle majeur dans les processus physico-chimiques de l'atmosphère qui régissent le climat par diffusion ou absorption directe du rayonnement solaire, ou par des effets indirects tels que la nucléation et les précipitations des gouttelettes de nuages (Slingo 1990; Ramanathan et al. 2001; Mallet et al. 2003; Lewis et al. 2004; Mulcahy et al. 2008; Wang et al. 2014; Mallet et al. 2016; Sroka and Emanuel 2021). D'autre part, les aérosols sont importants pour la biosphère à travers le transport de minéraux dans les régions privées de nutriments, pour la santé publique avec la capacité de transporter des virus (Conticini et al. 2020; Piazzola et al. 2021), et d'autres domaines tel que le transport et la défense où ces particules peuvent affecter la profondeur optique atmosphérique, et donc la visibilité et l'éfficacité des systèmes d'assistance optroniques. De grandes incertitudes sur l'impact de ces particules persistent (Boucher et al. 2013; Zhang et al. 2016; Brooks and Thornton 2018). Une meilleure connaissance de la variabilité spatio-temporelle et des propriétés physico-chimiques de ces aérosols est donc indispensable.

Comme les océans couvrent 70% de la surface terrestre, les aérosols marins représentent une composante majeure de la masse naturelle d'aérosols (Jaenicke 1984; Yoon et al. 2007) et constituent donc un domaine de recherche dynamique, en particulier concernant leur rôle dans les événements météorologiques extrêmes tels que les précipitations provoquées par la mousson (Ramanathan et al. 2001) et les cyclones tropicaux (Wang et al. 2014; Sroka and Emanuel 2021). Ces particules varient d'échelles millimétriques à submicroniques avec des temps de résidence atmosphérique allant de quelques secondes à quelques semaines, et deviennent dominantes dans les régions océaniques et côtières à des vitesses de vent relativement élevées (Katoshevski et al. 1999; Sellegri et al. 2001). Les aérosols marins comprennent des particules nucléées à partir de précurseurs gazeux de surface (Fitzgerald 1991; Korhonen et al. 1999), des embruns en phase aqueuse (Monahan et al. 1982; Troitskaya et al. 2018) et des particules de sel marin. Des incertitudes prédictives importantes subsistent pour les embruns, généralement supermicroniques, avec de grands écarts observés entre les différents schémas d'émission couramment utilisés (de Leeuw et al. 2011; Tsyro et al. 2011; Chen et al. 2016; Neumann et al. 2016; Saliba et al. 2019). À ce jour, les conditions environnementales requises pour la génération des plus grosses gouttelettes,

dites "spume", et les conséquences sur les caractéristiques de la couche limite atmosphérique marine (CLAM) restent peu comprises (Bianco et al. 2011; Veron et al. 2012; Veron 2015; Lenain and Melville 2017a), en particulier dans les conditions extrêmes où les observations sur le terrain sont particulièrement difficiles. Comme les embruns sont transportées dans la CLAM, elles peuvent entraîner des rétroactions variées et complexes, tel que sur le transfert de quantité de mouvement entre l'atmosphère et l'océan (Fairall et al. 2009; Soloviev and Lukas 2010; Rastigejev et al. 2011), et les flux de chaleur latents et sensibles (Fairall et al. 1994; Richter and Sullivan 2014; Rastigejev and Suslov 2019). De telles rétroactions devraient influencer la météorologie à l'échelle régionale (Saruwatari and Abe 2014), en particulier dans des conditions de vent fort où les concentrations en embruns sont élevées et les gouttelettes "spume" dominent le volume total d'embruns (Andreas 1992; Andreas and Emanuel 2001). L'étude des effets de ces aérosols dépend fortement de la précision des fonctions de source d'embruns marins (Andreas 1992; Veron 2015). Dans le contexte des changements climatiques et météorologiques, des paramétrisations plus précises et universelles des flux de surface sont nécessaires. La génération et le transport des embruns marins doivent être améliorés dans les modèles numériques atmosphériques (Canepa and Builtjes 2017) ainsi que l'intégration des interactions océan, atmosphère et vagues à l'interface air-mer (Pianezze et al. 2018; Sauvage et al. 2021).

L'Institut méditerranéen d'océanographie (MIO), où s'est déroulée la présente thèse, étudie depuis plusieurs années la génération et le transport des embruns dans la CLAM à partir de mesures et de modélisation numérique. Les efforts récents incluent l'utilisation du modèle numérique MesoNH (Lac et al. 2018) développé par des équipes de recherche du Centre National de Recherches Météorologiques (CNRM) et du Laboratoire d'Aérologie (LA) pour l'étude des phénomènes atmosphériques synoptiques et à micro-échelle, y compris la génération et le transport des aérosols. Le but de ces développements est l'étude de la précision des prévisions météorologiques dans le bassin méditerranéen. Ce bassin semi-fermé, densément peuplé et relativement peu profond doit son étiquette controversée de "point chaud" du changement climatique à son taux de réchauffement plus élevé par rapport à la moyenne ainsi qu'à la diminution prévue des précipitations dans les décennies à venir (Giorgi and Lionello 2008; Planton et al. 2016; Tuel and Eltahir 2020). Abritant des vents fréquents et forts, ainsi que de fortes précipitations pendant la saison d'automne, la Méditerranée est une zone d'étude intéressante pour la compréhension de la génération, du transport et des rétroactions des embruns dans le MABL. Des conditions de vent extrêmes produites par des cyclones "quasi-tropicaux", appelés « medicanes », fait toujours l'objet de recherches actives, et l'ampleur du forçage par les flux de chaleur air-mer est actuellement sujette à débat (Miglietta and Rotunno 2019; Bouin and Lebeaupin Brossier 2020).

Étude en Laboratoire

La présente thèse vise à améliorer la connaissance du flux de génération des embruns. Pour ce faire, les effets des interactions vent-vagues sur le flux de génération d'embruns marins de surface sont étudiés lors de l'expérience nommée "Marine Aerosol Tunnel Experiment" (MATE2019), menée à l'installation vague-vent de l'Institut Pythéas à Luminy (Marseille, France) en Juin et Juillet 2019. Un ensemble unique de combinaisons vents-

vagues fut généré dans le laboratoire avec cinq types de forçage de vague et cinq vitesses de vent allant de 8 à 20 m s^{-1}. Des vagues jeunes ainsi que des vagues plus développées furent générées par l'action seule du vent, ou accompagné de vagues générées par un batteur à vagues, avec des âges de vagues compris entre 1,3 et 9,5 (définis en termes de vitesse de phase et de vitesse de frottement). Des profils verticaux de concentration d'embruns mesurés pour des rayons allant de 0.1 à 47.5 µm indiquent que la concentration évolue de manière logarithmique avec la hauteur au dessus surface, permettant ainsi d'estimer le flux de génération d'embruns à l'aide d'une méthode des profils (Monin and Obukhov 1954).

Pour les 25 combinaisons de vents et de vagues considérées, la dépendance de mécanismes physiques clés tel que le déferlement et le flux de quantité de mouvement sur les caractéristiques de vent et de vague sont comparables en laboratoire et en mer. Sur la gamme de taille des gouttelettes "spume" ($r > 20$ µm), la variance de la pente de vague $\langle S^2 \rangle$ permet de mieux décrire le flux de génération. Sur la gamme de rayons 7–35 µm, $\langle S^2 \rangle$ surpasse d'autres nombres adimensionnels pour la mise à échelle du flux de génération, dont l'âge de vague et le nombre de Reynolds R_B particulièrement adapté à la mer de vent. $\langle S^2 \rangle$ est à son tour surpassé par le nombre combiné $P_S = \langle S^2 \rangle u_*^3 / \nu_a g$, décrivant la modulation par la variance de pente de vagues du flux d'énergie entre le vent et les vagues. Cela est particulièrement vrai sur la gamme de rayon 7-20 µm où les plus petites gouttelettes "jet", issues de l'éclatement de bulles générées par le déferlement de vagues, dominent. u_*^3, couramment utilisé pour l'étude de la dissipation d'énergie des vagues et le flux de quantité de mouvement vague-vent, contribue particulièrement à ces bonnes performances. L'avantage d'utiliser $\langle S^2 \rangle$ pour la mise à l'échelle de la génération d'embruns marins réside dans le lien fort avec le déferlement des vagues(Stokes 1880; Duncan 1981; Ramberg and Griffin 1987) et les mécanismes de d'écrêtage tels que le décollement du flux d'air, en décrivant la géométrie de la surface de la mer. Contrairement aux statistiques de vagues "pic" représentées par l'âge des vagues, ou le nombre de Reynolds R_B, $\langle S^2 \rangle$ permet d'intégrer des statistiques de vagues multi-échelles dans les limites imposées par la métrologie et les contraintes de modélisation. Cette démarche de combiner différents paramètres a également été exploré par d'autres auteurs pour la mise à échelle de mesures de couverture moutonneuse et de concentrations d'aérosols marins (Brumer et al. 2017; Lenain and Melville 2017a). Les flux d'embruns déterminés en laboratoire sont comparables aux fonctions source (écrit SSGF pour "Sea Spray Generation Function") dans la littérature pour des conditions environnementales de vent et de vague similaires. Deux SSGF sont proposées pour la mise à l'échelle des flux de laboratoire obtenus sur la gamme de vents U_{10} 16–20 m s^{-1}. Les deux SSGF, mises à l'échelle avec $\langle S^2 \rangle$ (B21a) ou P_S (B21b) sont jugées valides sur la plage de rayon 7–35 µm et des vents U_{10} allant de 12 à 20 m s^{-1}.

Du Laboratoire au Terrain

La validité des SSGF de laboratoire dans des conditions réelles de terrain est étudiée. Pour ce faire, le paramètre d'échelle $\langle S^2 \rangle$ est comparé à une formulation proposée à partir

de télémesures omnidirectionnelles de vagues par Cox and Munk (1956) (noté CM), ainsi qu'un modèle spectral et omnidirectionnel de vague proposé par Elfouhaily et al. (1997) (noté ELF). La relation linéaire entre la vitesse du vent U_{10} et $\langle S^2 \rangle$ dans la formulation CM est proportionnelle à la relation moyenne observée en laboratoire entre les différents conditions testées. Un facteur de correction appliqué à la formulation CM permet une représentation satisfaisante des données en laboratoire. Cette correction suggère que le laboratoire $\langle S^2 \rangle$ est représentatif de la composante au vent (dans la direction du vent) dans un champ de vagues fortement anisotrope. Une enquête plus approfondie avec le modèle ELF suggère également que ce facteur de correction compense la contribution manquante mais mineure de la houle en laboratoire ($\approx$ 15% du $\langle S^2 \rangle$ total). La formulation CM réadaptée au laboratoire est choisie pour le forçage des SSGF, et est ainsi utilisée dans les modèles numériques utilisés durant la thèse. Dans ce dernier cas, la relation entre $\langle S^2 \rangle$ et U_{10} est supposée linéaire. Cependant, les observations en laboratoire et les simulations avec le modèle ELF suggèrent une influence d'ordre supérieur de l'âge des vagues sur $\langle S^2 \rangle$, avec une diminution observée de $\langle S^2 \rangle$ pour l'augmentation de l'âge des vagues. Comme il a été constaté que $\langle S^2 \rangle$ augmente avec le moutonnement, cela corrobore la diminution observée du moutonnement pour l'augmentation de l'âge de vagues (Schwendeman and Thomson 2015; Brumer et al. 2017). L'utilisation future d'une expression pour $\langle S^2 \rangle$ dépendante sur l'état de mer, tel que l'âge des vagues, nécessite d'avantage de recherches.

Modélisation Numérique

Les fonctions de génération d'embruns proposées à partir de mesures en laboratoire, ainsi que d'autres SSGF issues de la littérature, sont paramétrées dans les modèles numériques MACMod (Tedeschi and Piazzola 2011) et MesoNH (Lac et al. 2018). Ces deux modèles sont utilisés de manière complémentaire pour l'étude du transport d'embruns. Le flux d'embruns est fourni pour des particules ayant atteint le rayon d'équilibre r_{80} pour des conditions de 80% d'humidité relative. Cette hypothèse, compatible avec les SSGF utilisés ainsi que les conditions rencontrées lors des campagnes MATE2019, SUMOS et MIRAMER, permet de négliger les effets thermodynamiques air–particule sur le transport.

Le modèle MACMod, offre la possibilité de modéliser le transport dans des conditions idéalisées avec un champ de vent horizontalement homogène. Avec un coût de calcul relativement faible, ce modèle facilite également l'utilisation d'une variété de paramétrisations de génération d'embruns, de vent et de surface de mer. Les résultats de simulations avec MACMod, comparés aux données MIRAMER, révèlent que les SSGF B21a, B21b et OVA14 sont des choix intéressants. De plus, la comparaison des paramétrisations corrigées CM et ELF (dans le sens du vent) pour $\langle S^2 \rangle$ montre qu'à des fetchs plus courts inférieurs à 30 km et U_{10} = 10 m s $^{-1}$, le CM corrigé prédit des valeurs de $\langle S^2 \rangle$ jusqu'à 11% inférieures à celles d'ELF, mais 5% supérieures pour les fetchs plus longs. La prise en compte de l'âge des vagues peut donc aider à améliorer la précision prédictive avec B21a et B21b dans une étude future.

Le modèle MesoNH n'est pas couplé à un modèle de vague. La formulation CM ajustée au laboratoire, dépendante du vent, offre alors une solution pour l'estimation de $\langle S^2 \rangle$. Le modèle est utilisé avec les SSGF B21a, B21b et OVA14. Une modélisation réaliste à l'échelle régionale avec MesoNH révèle de forts écarts entre les vitesses de vent modélisées et mesurées lors de la campagne MIRAMER (2008) (cf. Fig. 4.7). De tels écarts vont impacter le transport des aérosols marins. Il est donc actuellement difficile d'évaluer les performances des différentes SSGF et du modèle dans le contexte de la campagne MIRAMER. Ces résultats sont attribués à la proximité de la zone d'étude avec la côte, ainsi qu'aux faibles vitesses du vent et aux faibles durées d'échantillonnage qui auraient entravé la mesure d'embruns pendant MIRAMER. Ces hypothèses sont compatibles avec les meilleurs résultats obtenus pour des petits rayons proches de 1.5µm.

Dans le cas de la campagne SUMOS effectuée en Atlantique Nord-Est (2021), la correspondance entre les vitesses de vents modélisées et mesurées est bien meilleure ($R^2 = 0.93$). Des meilleurs résultats sont également obtenus pour les concentrations d'embruns marins lors de la comparaison entre concentrations mesurées et modélisées. La fonction de génération OVA14 semble fortement surestimer et sous-estimer les concentrations pour les particules inférieures et supérieures à la gamme de taille 1–5 µm, respectivement. B21a et B21b produisent des résultats d'avantage en accord avec les mesures. B21b s'avère la plus performante avec une sensibilité plus grande aux variations de concentrations observées pendant SUMOS, principalement en raison du terme additionnel u_*^3. B21a fonctionne tout aussi bien pour les particules plus grosses typiques de la gamme des gouttelettes "spume", rappelant les bonnes performances de mise à l'échelle de la génération de gouttelettes spume par $\langle S^2 \rangle$ observées pendant MATE2019. Dans l'ensemble, les résultats indiquent que les SSGF de laboratoire mis à l'échelle fonctionnent raisonnablement bien dans des conditions de terrain.

Conclusion

Alors que les flux de chaleur, d'humidité et de quantité de mouvement induits par les embruns deviennent importants et pourtant restent peu quantifiés en conditions de vents extrêmes, il devient essentiel de développer des fonctions de génération d'embruns précises et adaptables à une grande variété de conditions. Nous avons développé, mis à l'échelle et testé sur le terrain des fonctions de génération d'embruns dépendantes du vent et des vagues. Ces travaux de thèse indiquent que l'utilisation de paramètres liés au vent et aux vagues permettent de mieux décrire les processus de génération d'embruns. Les deux fonctions proposées dépendent de la variance de pente de vagues, permettant donc l'intégration d'informations multi-échelles. Combiné avec la vitesse de frottement au cube u_*^3, le nombre adimentionnel P_S permet de représenter le flux de manière précise sur la gamme de taille 3–35 µm étudiée.

Validé à l'aide de mesures de terrain acquises lors des campagnes MIRAMER et SUMOS, le modèle régional MesoNH, utilisant les fonctions de génération de laboratoire, permet une prédiction précise de la concentration d'embruns pour les gouttelettes

"jet" et "spume", pour une diversité de conditions environnementales. Nous soulignons l'importance de continuer à développer des SSGF de plus en plus précises, avec l'inclusion d'aérosols atmosphériques provenant de sources diverses, telles que les aérosols biogéniques, les poussières et la pollution. En effet, la compréhension des différents effets des aérosols tel que sur la météorologie et le climat nécessite une vue d'ensemble sur le large spectre de taille que représentent les aérosols atmosphériques.

General Introduction

As far as carved, written, painted and paleoclimatic records go, the climate as well as the weather, have rhythmed the lives of all living creatures on Earth. The importance of variations in weather and climate on society is evidenced by the depiction of such phenomena as deities in polytheistic religions. Spanning seasonal, interanual, decadal and centenial timescales, the climate has oscillated between conditions hostile or favourable to population thriving, sometimes even driving global extinction events. A well known example is the Permian–Triassic event where high atmospheric concentrations in greenhouse gases are believed to have resulted in increased temperature and ocean water acidity. At shorter timescales, transient weather events have shown to be potentially challenging for populations and structural integrity, as in the case of storms, cylones and floods. As illustrated by the current climate change debait, the ability for Human populations to adapt resides in the intricate relationship between science and the cultural acceptance of paradigms and scenarios such as *nature cornucopia*, the unfolding of nature's resources in response to human innovation, *nature evolving*, the co-evolution of humans and nature, and *nature resilient*, whereby nature is malleable, predictable but ultimately indestructable (Holling et al. 1995; O'Riordan 2014). Since the late fifties, understanding of the climate system has significantly evolved. Scientists continue to evince and investigate impacts of climate change on atmospheric and oceanic chemical, biological and physical processes. Anthropogenic "footprints" such as emissions and land use are under scrutiny such as at the Mauna Loa observatory, boasting a 63-year (and increasing) record of atmospheric CO_2 concentrations. Knowledge of weather-making processes and therefore weather prediction has also much improved with time, especially since the beginning of the 80s with the availability of satellite-based observations.

Atmospheric aerosols are solid or liquid particles suspended in a gas, and are often located in the lower atmosphere. The origins of these particles, natural and/or anthropogenic, are as diverse as their size, shape and composition. They can be directly emitted into the atmosphere from Earth's landmass and hydrosphere, or result from chemical reactions. Over the past few decades, the effect of aerosols on weather and climate has come to light. Aerosols play a major role in the physicochemical processes of the atmosphere that govern the climate through direct scattering or absorbing of solar radiation, or through indirect effects such as cloud droplet nucleation and precipitation (Slingo 1990; Ramanathan et al. 2001; Mallet et al. 2003; Lewis et al. 2004; Mulcahy et al. 2008; Wang

et al. 2014; Mallet et al. 2016; Sroka and Emanuel 2021). Aerosols are also important for Earth's life cycle by transporting minerals in nutrient-deprived areas, for public health with the capacity to transport viruses (Conticini et al. 2020; Piazzola et al. 2021), and can significantly affect visibility by significantly increasing atmospheric optical depth. Large uncertainties on the impact of these particles such as on radiative forcing remain (Boucher et al. 2013; Zhang et al. 2016; Brooks and Thornton 2018). Better knowledge of the spatio-temporal variability and physicochemical properties of these aerosols is essential.

As Earth's oceans cover 70% of Earth's surface, marine aerosols consitute a major component of the natural aerosol mass (Jaenicke 1984; Yoon et al. 2007) and an active field of research, particularly for their impact in extreme weather events such as monsoon driven rainfall (Ramanathan et al. 2001) and tropical cyclones (Wang et al. 2014; Sroka and Emanuel 2021). These particles range from millimetric to sub-micronic scales with atmospheric residence times ranging from seconds to weeks, and become dominant in the open ocean and coastal regions at relatively high wind speeds (Katoshevski et al. 1999; Sellegri et al. 2001). Marine aerosols include particles nucleated from surface-sourced gaseous precursors (Fitzgerald 1991; Korhonen et al. 1999), aqueous-phase sea spray droplets (Monahan et al. 1982; Troitskaya et al. 2018), and sea salt particles. Significant predictive uncertainties remain for sea spray, with large deviations observed between commonly used emission schemes (de Leeuw et al. 2011; Tsyro et al. 2011; Chen et al. 2016; Neumann et al. 2016; Saliba et al. 2019). To this day, the environmental conditions required for the generation of the larger spume droplets and the resulting consequences on the characteristics of the marine atmospheric boundary layer (MABL) remain poorly understood (Bianco et al. 2011; Veron et al. 2012; Veron 2015; Lenain and Melville 2017a), especially in extreme wind conditions where field observations are particularly difficult. As sea spray droplets are transported in the MABL, they can result in a complex range of feedbacks on the momentum transfer between the atmosphere and the ocean (Fairall et al. 2009; Soloviev and Lukas 2010; Rastigejev et al. 2011), as well as latent and sensible heat fluxes (Fairall et al. 1994; Richter and Sullivan 2014; Rastigejev and Suslov 2019). Such sea spray feedbacks are expected to influence regional-scale meteorology (Saruwatari and Abe 2014), especially in strong wind conditions in which their concentrations are high and spume droplets dominate the total volume of sea spray (Andreas 1992; Andreas and Emanuel 2001). The study of such sea spray effects is highly reliant on the accuracy of sea spray generation functions (Andreas 1992; Veron 2015). In the context of changing climate and weather patterns, more accurate and universal surface flux parameterizations are required. Sea spray generation and transport must be improved in atmospheric numerical models (Canepa and Builtjes 2017) as well as the integration of ocean, atmosphere and wave interactions at the air-sea interface (Pianezze et al. 2018; Sauvage et al. 2021).

The Mediterranean Institute of Oceanography (MIO), where the present PhD was conducted, has been studying sea spray generation and transport in the MABL from measurements and numerical modellings for several years. Recent efforts include the

use of the MesoNH numerical model (Lac et al. 2018) developed by research teams at the Centre National de Recherches Météorologiques (CNRM) and the Laboratoire d'Aérologie (LA) for the study of atmospheric synoptic and microscale phenomena, including aerosol generation and transport. The aim of such developments is the study of weather prediction accuracy in the Mediterranean basin. The densely populated semi-enclosed and relatively shallow Mediterranean Basin owes its debated label of climate change "hot-spot" to its higher rate of warming relative to the global ocean, and predicted decrease in precipitation in the decades to come (Giorgi and Lionello 2008; Planton et al. 2016; Tuel and Eltahir 2020). Home to frequent and strong wind events, as well heavy rainfall during the autumn season, the Mediterranean is an interesting study area for the understanding of sea spray generation, transport and feedbacks in the MABL. The additional occurence of extreme wind conditions produced by tropical-like cyclones, named "medicanes" is still the focus of active research, and the scale of forcing by air-sea heat fluxes is currently subject to debate (Miglietta and Rotunno 2019; Bouin and Lebeaupin Brossier 2020).

This thesis is dedicated to the better understanding of sea spray generation dependence on wind and wave characteristics in the open ocean, sea spray transport in the atmosphere and the resulting impacts on the MABL. The first chapter of this thesis details the extent of current knowledge on sea spray aerosol generation and transport, as well as a theoretical basis for the wind and wave processes that occur at the air-sea interface. Chapter 2 presents two sea spray field measurement campaigns conducted in the North-West Mediterranean Basin and the the North-East of the Atlantic Ocean, as well as the experimental configuration of the MATE2019 laboratory study. Chapter 3 presents two new wave-wind-dependent sea spray generation functions obtained from laboratory measurements, and investigates prospects for upscaling to the field and use in full-scale numerical simulations, presented in Chapter 4. Chapter 4 uses the complementary MAC-Mod and MesoNH numerical models for the study of the transport of sea spray aerosols. Results are compared with available field observations. Finally, Chapter 5 summarizes and discusses results presented in the thesis. The importance of accurate and complete sea spray generation functions for the study of air-sea heat, momentum and moisture fluxes is discussed in detail.

Chapter 1

Atmospheric Aerosols

Contents

In this first chapter we present general definitions of aerosol atmospheric processes, flux estimates and mathematical aspects (cf. Sect 1.1). Ensues a literature review of sea spray generation and transport (cf. Sect 1.2), at the heart of the present thesis. The good understanding of wind and wave processes is essential for the study of the marine atmospheric boundary layer and inherent sea spray processes. The theoretical and experimental basis of wind, waves and wave-wind interaction is also presented (cf. Sect. 1.3–1.4).

1.1 Generalities

1.1.1 Definitions

Aerosols are by definition suspended particles in a gas. In the atmosphere, aerosols present a variety of different compositions and morphologies, generated from a wide variety of different sources. As well as the proximity to a source and particle residence times, the predominance of a particle type will depend on the unit. Indeed, arerosols can be described according to their number, surface area, volume or mass in the atmosphere.

In the present thesis, aerosols are mostly described by their number N per unit volume of air (cm^{-3}) per droplet radius r increment dr (μm^{-1}), unless specified otherwise. In most cases particle concentrations are measured over different particle size bins of different widths. Concentrations are commonly normalized by the bin width. If dN denotes the number of particles in the size range r to $r+dr$, the size-dependent distribution (assumed continuous) of aerosols can be written as follows,

$$n(r) = \frac{dN}{dr}, \qquad (\mathrm{cm}^{-3}\ \mu\mathrm{m}^{-1}) \tag{1.1}$$

As detailed in Seinfeld and Pandis (1997), the surface $n_S(r)$, volume $n_V(r)$ and mass $n_M(r)$ concentrations can be calculated from $n(r)$

$$n_S(r) = 4\pi r^2 n(r), \qquad (\mathrm{cm}^{-3}\ \mu\mathrm{m}) \tag{1.2}$$

$$n_V(r) = \frac{4}{3}\pi r^3 n(r), \qquad (\mathrm{cm}^{-3}\ \mu\mathrm{m}^2) \tag{1.3}$$

$$n_M(r) = \frac{\rho_p}{10^6} n_V(r), \qquad (\mu\mathrm{g\ m}^{-3}\ \mu\mathrm{m}^{-1}) \tag{1.4}$$

where ρ_p is the particle density in g cm^{-3} converted to μg cm^{-3} with a 10^6 conversion factor. The concentration distributions can also be represented as a function of the natural logarithm $ln(r)$

$$n^e ln(r) = \frac{dN}{dln(r)}, \tag{1.5}$$

or of the base 10 logarithm $log(r)$

$$n^\circ log(r) = \frac{dN}{dlog(r)}. \tag{1.6}$$

It can also be useful to know the total number (or mass or volume) of aerosols N_T over a given size range and volume of air. The total number concentration can be written

$$N_T = \int_0^\infty n(r)dr, \qquad (\mathrm{cm}^{-3}). \qquad (1.7)$$

The total concentration describes a number of particles per cm^3. The accuracy of the N_T estimate depends on the increment radius dr as well as the choice of integral radius bounds.

The generation flux $\frac{dF}{dr}$ is represented here as the number of particles emitted from the source per unit area per radius increment per second ($\mathrm{m}^{-2}\ \mathrm{s}^{-1}\ \mu\mathrm{m}^{-1}$). The flux is generally derived from aerosol concentration measurements and scaled against physical parameters for the formulation of aerosol size-dependent generation functions.

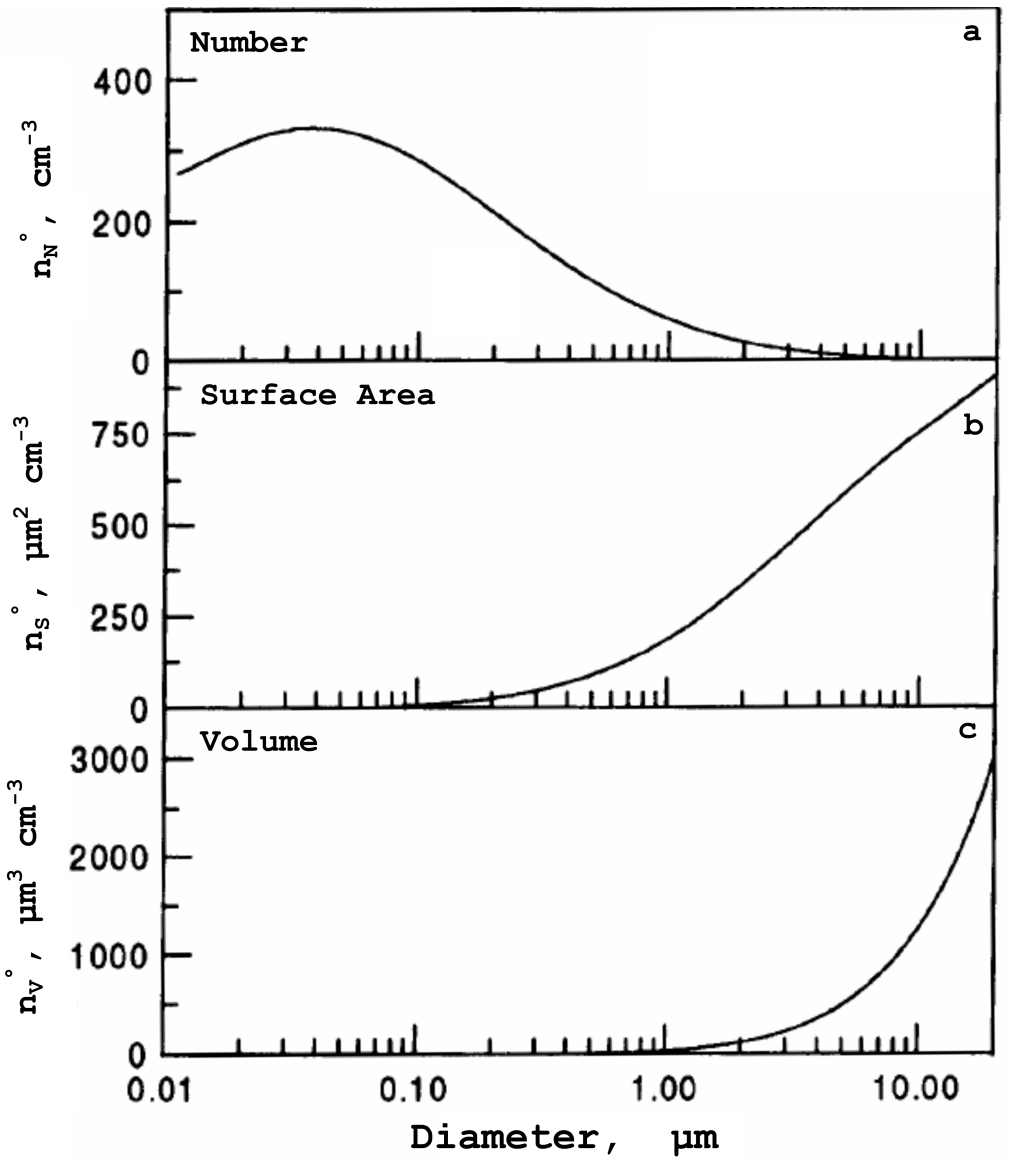

Figure 1.1: Different representations of the aerosol concentration spectrum according to number (a), surface (b) and volume (c). This example is taken for desert dust aerosols (figure adapted from Seinfeld and Pandis (1997)).

Figure 1.1 shows an example of number, surface area and volume concentrations of

desert dusts as a function of the base 10 logarithm, with the radius increment dr equal to 1. Higher number concentrations are found for the smaller radii ($\lesssim$ 1 µm radius) whilst surface and volume concentrations increase with increasing radius. The surface and volume concentrations are calculated assuming spherical particles. The integral of the area under the curves is equal to the total concentration N_T. The distributions are represented as a function of the base 10 logarithm $log(r)$ which is sometimes used to compensate for the distortion induced by graphical log-scale projections.

1.1.2 Overview of Aerosol Sources and Composition

Aerosols of different morphology and composition result from different sources and atmospheric transformations. Aerosols can be primary or secondary according to their origin. Figure 1.2 illustrates the main primary produced aerosols (black text), and the gaseous precursors (orange text) or secondary aerosols (blue text). Aerosols can be generated from Earth's continents (to which we include the cyrosphere), liquid-phase water-covered regions, and the atmosphere.

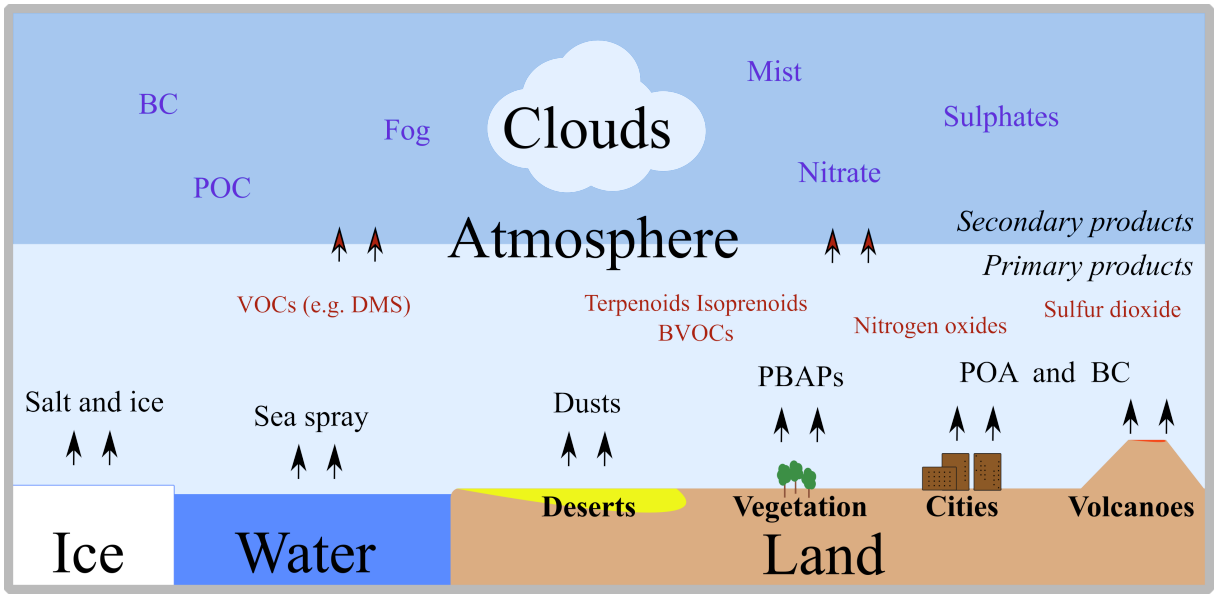

Figure 1.2: Schematic of primary (black text) and secondary (purple text) aerosol generation, gaseous precursors (orange). The sources of primary aerosols are indicated in bold. The vertical atmospheric distribution of primary and secondary aerosols is not always representative of reality, and serves for clarity.

Primary sources include mineral dust, sea spray, sea salt, suspended in the air through the mechanical effects of wind erosion on dust, sea water and ice covered regions. Other primary sources count fossil fuel and biomass burning events (primary organic aerosols denoted POA that include PBAPs, black carbon denoted BC) as well as terrestrial (for example bacteria, viruses, spores, pollen, plant fibres) and marine primary biological aerosol particles (PBAPs). An example are submicron marine aerosols (Leck and Keith Bigg 2008; Russell et al. 2010) generated by surfactants (Sellegri et al. 2006). In most cases, each

aerosol type has its own source. For example, mineral dusts are dominant in often equatorial desert areas and generated by the suspension of dust particles through the surface friction of the wind. Sea salt and sea spray on the other hand are marine aerosols that can dominate in coastal and offshore study sites and are mainly generated from processes in relation to the wave-modulated ocean surface shape and bubble-bursting induced by the breaking of wind-forced waves. Black carbon is the major anthropogenic light-absorbing constituent in aeorosols and is mainly sourced from the combusion of fossil fuels and biomass (Myhre et al. 2013). Recent studies have also investigated the generation of sea salt aerosols through the sublimation of blowing snow and wind-blown frost flower crystals, with dependence on wind speed and snow cover salinity (Huang et al. 2018).

Secondary aerosol generation relies on the presence of gaseous precursors (orange text in Fig. 1.2) and primary aerosols in the atmosphere. Sufficient knowledge of gas-phase chemical mechanisms is required for secondary aerosol prediction as the gas-gas and gas-particle reactions are vast and complex. Precursor gases include fossil fuel combustion products such as nitrogen oxides, and biogenic emissions of volatile organic compounds (VOCs) (Myhre et al. 2013) (e.g. isoprenoids and terpenoids) and biogenic VOCs (BVOCs) (Vivaldo et al. 2017). These precursors play an important role in the nucleation process often resulting from photo-chemical reactions (cf. Fig. 1.3). A well known yet debaited example of gas-phase nucleation is the oxidation of the ocean-sourced *dimethyl sulphide* (DMS) (Katoshevski et al. 1999; Vogt et al. 2010; Korhonen et al. 2008). DMS, the largest natural source of sulphur in the atmosphere, is produced by marine phytoplankton and is transferred from ocean water to the atmosphere due to wind-induced mixing of surface water. Examples of secondary atmospheric aerosols are particulate organic carbon (POC) resulting from the aggregation of compounds (Daisey et al. 1986; Saxena and Hildemann 1996), sulfate aerosols associated with volcanic activity (Boulon et al. 2011) and coal combustion (Meagher et al. 1967), nitrate salts resulting from the interaction between sea spray and dusts and nitrogen oxides (Gibson et al. 2006), organic carbon essentially generated the oxidation of forest and oceanic emissions of VOCs (Spracklen et al. 2008), and from cloud processes such as condensation (Ervens et al. 2011) such as fog and mist. Secondary aerosol generation strongly depends on the mass and size distribution of primary aerosols that allow condensation of the secondary species (Pandis et al. 1993). These aerosols are generally small (< 1 micrometer) and have liefetimes of days to weeks. Sulphate dominate atmospheric aerosol composition in large parts of the densely populated and highly polluted northern hemisphere (Zhang et al. 2007).

Table 1.1, adapted from the IPCC report on clouds and aerosols (Boucher et al. 2013), indicates the minimum and maximum natural yearly emissions of aerosols and aerosol precursors. Among these natural sources, primary aerosols generated from wind erosion such as marine aerosols (sea spray and marine POA), mineral dusts and terrestrial PBAPs represent the most significant sources, representing a total of 7×10^3 Tg yr^{-1} on average. For comparison, estimates of anthropogenic aerosol and aerosol precursor emissions for

all major sources total year 2000 range between approximately 214.9 and 392 Tg yr^{-1} (including the mass of anthropogenic sulphur dioxide in sulfates) (Boucher et al. 2013).

Table 1.1: Estimates of global natural emissions of aerosols and aerosol precursors. Units are Tg yr^{-1} except for BVOCs (monoterpenes and isoprene), in TgC yr^{-1}, and dimethysulphide (DMS), in TgS yr^{-1}. Figure taken from Boucher et al. (2013).

Source	Natural Global	
	Min	Max
Sea spray	1400	6800
including marine POA	2	20
Mineral dust	1000	4000
Terrestrial PBAPs	50	1000
including spores		28
Dimethylsulphide (DMS)	10	40
Monoterpenes	30	120
Isoprene	410	600
SOA production from all BVOCs	20	380

1.1.3 Aerosol Dynamics

During their transport in the atmosphere, aerosols and precursors are eventually transformed or deposited to the surface. Modes, identified from aerosols measurements, consist in concentration bell-shaped peaks that are commonly mathematically represented by probability density functions (cf. Figs 1.1 & 1.3) and that are thought to result from the different aerosol source and transformation mechanisms that operate in the atmosphere. Figure 1.3 schematically illustrates normalized aerosol number concentrations (vertical axis) as a function of particle diameter (horizontal axis). The lognormal distributions represent a total of nine modes, each representing atmospheric aerosol processes. The width (standard deviation) and amplitudes of these modes allow to describe the radii at which certain processes become dominant.

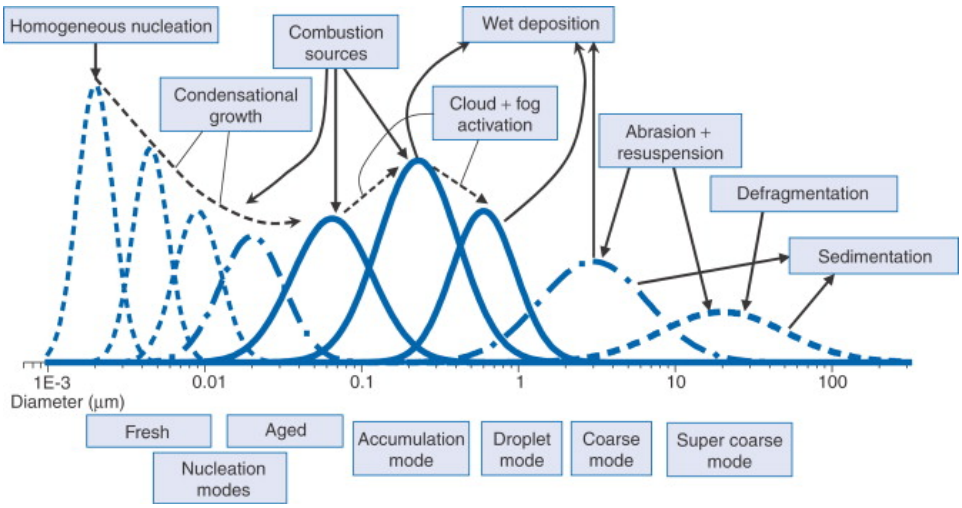

Figure 1.3: Size spectrum of atmospheric aerosol particles represented by idealized modes. Concentrations (vertical axis) are normalized. Figure taken from Birmili and Hoffmann (2006).

Wind erosion (abrasion) and combustion sources represented in Fig. 1.3 are examples of aerosols and precursors that are highly important for processes such as aerosol nucleation and condensation (nucleation modes or the Aitken mode) (Pandis et al. 1993) that lead to the formation of relatively small aerosols. The accumulation mode represents the aggregation and coagulation mechanisms of aerosols and precursors that collide, thus forming new particles such as POCs. The droplet mode is essentially a result of cloud processing, in which ambient humidity (or ambient saturation ratio) can bring the size of cloud droplets to an equilibrium size. Aerosols and precursors can be removed from the atmosphere by deposition. In the case of smaller particles and precursors, deposition at the surface essentially results from diffusive sedimentation, or from wet deposition as large droplets such as rain wash them out of the atmosphere. The generally larger coarse mode particles can also be subject to wet deposition, but are especially dominated by gravitational settling as a result of their significant mass.

Conservation Equations

The general dynamical equation (Friedlander 1977; Seinfeld and Pandis 1997) writes,

$$\frac{\partial n(r)}{\partial t} = (f_{convection} + f_{diffusion} + f_{coagulation} + f_{growth} + f_{sources/sinks} + f_{external})(n(r)), \quad (1.8)$$

and allows to model the evolution of the aerosol size distribution as a function of different sources, sinks, and atmospheric aerosol transformation mechanisms. As coarse aerosols are often generated from the surface and subject to gravitional settling, aerosol concentrations vary with height above the surface (z), radius (r), time (t) and position along the 2-D horizontal plane (denoted X). The latter is only relevant in the case

of spatially non-homogeneous external conditions and source terms, which is typically observed in the field. Considering these definitions, the aerosol concentration conservation equation becomes

$$\frac{\partial n(r(t),X,t,z)}{\partial t} = -\overrightarrow{U}.\overrightarrow{\nabla} n(r(t),X,t,z) - \overrightarrow{\nabla}.\overrightarrow{F}(r(t),X,t,z) + S(r(t),X,t,z) \quad (1.9)$$

where $\overrightarrow{U}$ represents the mean wind components u, v and w (corresponding to x, y and z directions). $(\overrightarrow{U}.\overrightarrow{\nabla})n(r(t),X,t,z)$ is the convective flux representative of the mean droplet velocity, and $S(r(t),X,t,z)$ represents the size-dependent sources and sinks for the transport equation. $-div\overrightarrow{F}(r(t),X,t,z)$ represents the aerosol flux components (other than by convection or in the source and sink terms) in the vertical and 2-D horizontal planes. Assuming horizontal homogeneity (and omitting temporal and spatial notations in the following), and negligible horizontal turbulent diffusion, we can write:

$$\frac{\partial n(r)}{\partial t} = -\overrightarrow{U}.\overrightarrow{\nabla} n(r) - F_z(n(r)) + S(n(r)). \quad (1.10)$$

The remaining F_z is the vertical aerosol flux which can be decomposed into three terms (Fairall and Davidson 1986):

$$F_z = \overline{w'n(r)'} - V_g n(r) - \Gamma_n \frac{\partial n(r)}{\partial z} \quad (1.11)$$

$$I \qquad II \qquad III$$

where I represents vertical transport by turbulent diffusion, and II dry particle deposition under the form of a gravitational particle settling velocity. III describes droplet molecular diffusivity, where the diffusive flux depends on the concentration gradient. Particle collison, coalescence and breakup can be considered (Pruppacher and Klett 1978) but can be neglected in the case of the larger coarse aerosols as a result of their lower concentrations in the atmosphere (Veron 2015). V_g is the steady gravitational settling velocity of the particles, to which slip velocity effects can be added for coarse aerosols. We add that the generation flux of aerosols from the surface is considered constant with height, assuming a constant flux layer (cf. Sect. 1.3.1).

Deposition Velocity

The aerosol generation flux and the aerosol deposition velocity require parameterizations. The lifetime of a particle is heavily dependent on its size as smaller particles are deposited at slower velocities than larger particles (Slinn et al. 1978; Carruthers and Choularton 1986; Seinfeld and Pandis 1997). Residence times range from seconds to mintes for the largest particles, to days and weeks for the smaller particles (de Leeuw et al. 2011). The size-dependent dry deposition has also been shown to depend on the predominance of

laminar or turbulent regimes in and around a surface boundary layer (Slinn et al. 1978; Slinn and Slinn 1980; Carruthers and Choularton 1986; Fairall and Davidson 1986). In a surface boundary layer, these regimes are height-dependent. A classical dry deposition parameterization separates three layers: a diffusive quasi-laminar sublayer, a turbulent transport surface layer, and a mixed layer. In turbulent flow, typical of conditions necessary for coarse mode aerosol generation by wind erosion, particles particles are exposed to turbulent eddies and the gravitational settling velocity V_g is thought to differ from the mean deposition velocity V_d (Wang and Maxey 1993). V_g can be formulated as

$$V_g = \Big(\frac{2g}{9\nu}\Big(\frac{\rho_p}{\rho_{air}}\Big)r^2\Big)C_c \tag{1.12}$$

where ρ_p and ρ_{air} are the aerosol and ambient air densities, respectively. Dry deposition and sedimentation is also described by brownian diffusivity D_p (cf. term III, Eq. 1.11) calculated using

$$D_p = \Big(\frac{kT}{6\pi\nu\rho_{air}r}\Big)C_c. \tag{1.13}$$

k is the Boltzmann constant, T is the ambient temperature, and ν is the air kinematic viscosity. In Equ. 1.12–1.13, C_c is the Cunningham correction factor, allowing to account for slip effects of a particle in a flow.

1.1.4 Aerosol Sampling and Flux Methods

Count Statistics and Stationarity

In the field, conditions are spatially and temporally transient. The classical approach for the understanding of aerosol processes is to simultaneously measure concentrations and environmental variables of interest. For an unmoving observer and at relatively short timescales, steady conditions can be assumed and verified from observations. Sample durations must also be long or frequent enough to accurately capture the phenomenon of interest. In the case of aerosol measurements, a certain number of particles of a given size must be measured to ensure sufficient particle count statistics. Sample durations must be increased for larger and therefore relatively scarce coarse mode particles. Observations closer to the source, where particle concentrations are higher, can be a solution to reduce sample times. It is not uncommon for authors to warn of possible underestimates for the largest particles such as the case of coarse mode sea spray aerosols (Smith et al. 1993; Fairall et al. 2009), and some reprocessings of existing datasets aim to retrospectively compensate for such metrological constraints (Andreas 1998). Stationarity of observations is typically investigated by verifying Gaussian or Rayleigh probability distributions, or the convergence of the cumulative average of the scalars over the sample duration.

Different methods exist for the estimation of the aerosol flux $\frac{dF}{dr}$ in the field. Three

methods for the estimation of the flux from concentration measurements are presented in the following, namely the equilibrium, eddy covariance, and log-profile methods.

The Equilibrium Flux Method

As a result of metrological and environmental constraints, aerosol measurements are often limited to a couple of aerosol probes in the field, typically placed on observation towers, ship masts, or airplanes. When the source is well identified, such as Earth's surface in the case of coarse mode sea spray and dust aerosols, it is possible to estimate the aerosol flux using the equilibrium method. The equilibrium method consists in assuming that the aerosol flux $\frac{dF}{dr}$ is equal to the product of the gravitational settling velocity V_g and the aerosol concentration $\frac{dN}{dr}$ (Smith et al. 1993; Hoppel et al. 2002) (cf. Fig. 1.7). This technique has a limited validity range of 10–20 µm particles typical of course mode aerosols, as a result of other non-negligible aerosol dynamics and metrological challenges. Indeed, in the case of smaller particles, the long timelengths ($\approx$ 1 day) necessary for small particles to reach equilibrium is sometimes greater than the particle lifetime due to the the contribution of other transport terms such as wet deposition. Authors also note that poor counting statistics typical of particles greater than 20 µm may explain some of the significant discrepancies in $\frac{dF}{dr}$ observed with this method. The equilibrium method may be applicable for particles larger than 20µm in conditions of high and extreme aerosol generation conditions, in which equilibrium is theoretically reached in a matter of hours (Hoppel et al. 2002).

The Eddy-Covariance Flux Method

The eddy-covariance method consists in the study of the covariance between the numerous eddies of different sizes present in turbulent flow, and a scalar such as aerosol concentration. With the assumption of locally and horizontally homogenous flows ($d/dx = d/dy = 0$), only the vertical flux is significant. The vertical net aerosol flux ($\overline{w'n(r)'}$) is obtained by substracting the deposition flux ($\overline{n(r)'V_d}$). The eddy-covariance method has been used in a number of recent studies for the estimation of vertical dust and sea spray fluxes, and has the advantage of requiring a single sample point in contrast with the log-profile method. In the case of sea spray, this flux method was first successfully applied to aerosol fluxes at sea by Nilsson et al. (2001) and has since been used in a range of conditions (Yang et al. 2019; Nilsson et al. 2021). However, studies have for the most part focused on relatively small submicronic particles, as the rarer supermicronic particles complicate covariance statistics. The efficiency of this sampling technique may be limited to particles of approximately 1 µm and below which respond to turbulence (Richter and Sullivan 2013), in contrast to larger particles that are relatively insensitive to turbulent structures as a result of their significant inertia (Veron 2015). A useful tool to estimate the behaviour of a particle in a flow is the Stokes number. Instrumentation constraints include

the requirement of high-frequency wind and aerosol samplers to resolve the diversity of turbulent structures, and the necessary proximity of wind and aerosol sampling systems whilst avoiding possible interference between sensors.

The Log-Profile Flux Method

The log-profile method is among the most commonly used methods for the estimation of scalar fluxes. Assuming streamwise homogeneity, this method is valid for wall-bound flow where the flow speed increases as a logarithmic function of the orthogonal distance from the wall (cf. Sect 1.3). Taking the example of sea spray and dust coarse mode aerosols, the log-profile method requires the measurement of vertical concentration profiles above the surface. The concentration measurements must be made within the surface log-layer (cf. Fig. 1.9) where the aerosol flux is assumed constant with height. Knowledge of the concentration profile slope allows to estimate N_*, the concentration at the closest point to the surface. The considered coarse mode aerosols are often generated by the surface wind friction. The N_* is therefore scaled with the friction velocity u_*, which can also be obtained from vertical wind speed profiles. The flux is therefore a mean flux, equal to the product u_*N_*. This flux method has the advantage of requiring mean wind and concentration values along the profile, and is potentially valid for a very wide range aerosol sizes as long as good enough aerosol count statistics are attained. Limitations of this method are the difficulty to measure wind and aerosol profiles in the field all whilst assuming that all concentration measurements are made in stationary conditions with a horizontally homogenous aerosol source.

1.2 Sea Spray Properties

1.2.1 Overview

As presented in previous sections, marine aerosols include a large range of sources such as sea salt, sea spray and marine primary organic matter. As efficient condensation nuclei, generated in significant quantities (cf. Table 1.1), marine aerosols play an important role in cloud formation and cloud brightness (Latham and Smith 1990), which governs processes that are key for the determination of weather, as shown in the case of tropical cyclones (Hoarau et al. 2018). Marine aerosols can be dominant in often densely inhabited coastal regions (Gong 2003; Piazzola et al. 2013). They include sea spray droplets which have the particularity of being acqueous-phase aerosols that carry significant quantities of sodium chloride, calcium and potassium (Sellegri et al. 2001; Yoon et al. 2007; Piazzola et al. 2012). These droplets may transport other substances from the surface or the atmosphere (through wet deposition), which can include contaminants (for example inorganic carbon, organic pollutants, sun lotion) that are potentially harmful to populations and ecosystems (Piazzola et al. 2016; Johansson et al. 2019) by affecting air quality through

the physical and chemical interactions with other types of aerosols and gases, thus altering atmospheric composition (Knipping and Dabdub 2003; Angle et al. 2021). More relevant to the present thesis, sea spray include both directly and indirectly generated droplets injected in the air from the sea surface, that can significantly impact momentum, heat, moisture and mass transfer at the air-sea interface, especially in high wind conditions (Andreas 1992; Fairall et al. 1994; Perrie et al. 2005).

1.2.2 Primary and Secondary Generation Mechanisms

Indirect sea spray generation is associated with the relatively small bubble-mediated jet and film droplets produced by wave breaking (cf. Figs. 1.4a and 1.4c), effective for wind speeds around 4 m s^{-1} and above (Blanchard 1963; Spiel 1994). The transition from film to jet droplet dominance is thought to occur at radii 2–4 μm (Cipriano and Blanchard 1981; Woolf 1997) with jet droplets dominating over the 2–20 μm range and sometimes reaching 50 μm or more (Newitt 1954; Andreas 1998; Berny et al. 2021). The direct sea spray generation mechanisms dominant at wind speeds higher than 10–12 m s^{-1} (Monahan et al. 1986; Andreas et al. 2010) consist in the surface-tearing of larger (radius $r > 20$ μm) spume droplets that are directly ejected into the airflow. Spume droplet generation has been associated with Kelvin-Helmoltz instabilities and air-flow separation in strong wind conditions (Phillips 1969; Mueller and Veron 2009; Soloviev and Lukas 2010). Monahan et al. (1986) noted that bubble-bursting droplet and spume droplet generation were equivalent at approximately 9 m s^{-1} wind speed. Overall, sea spray can be found in micrometric to millimetric scales, resulting in second to day-long residence times.

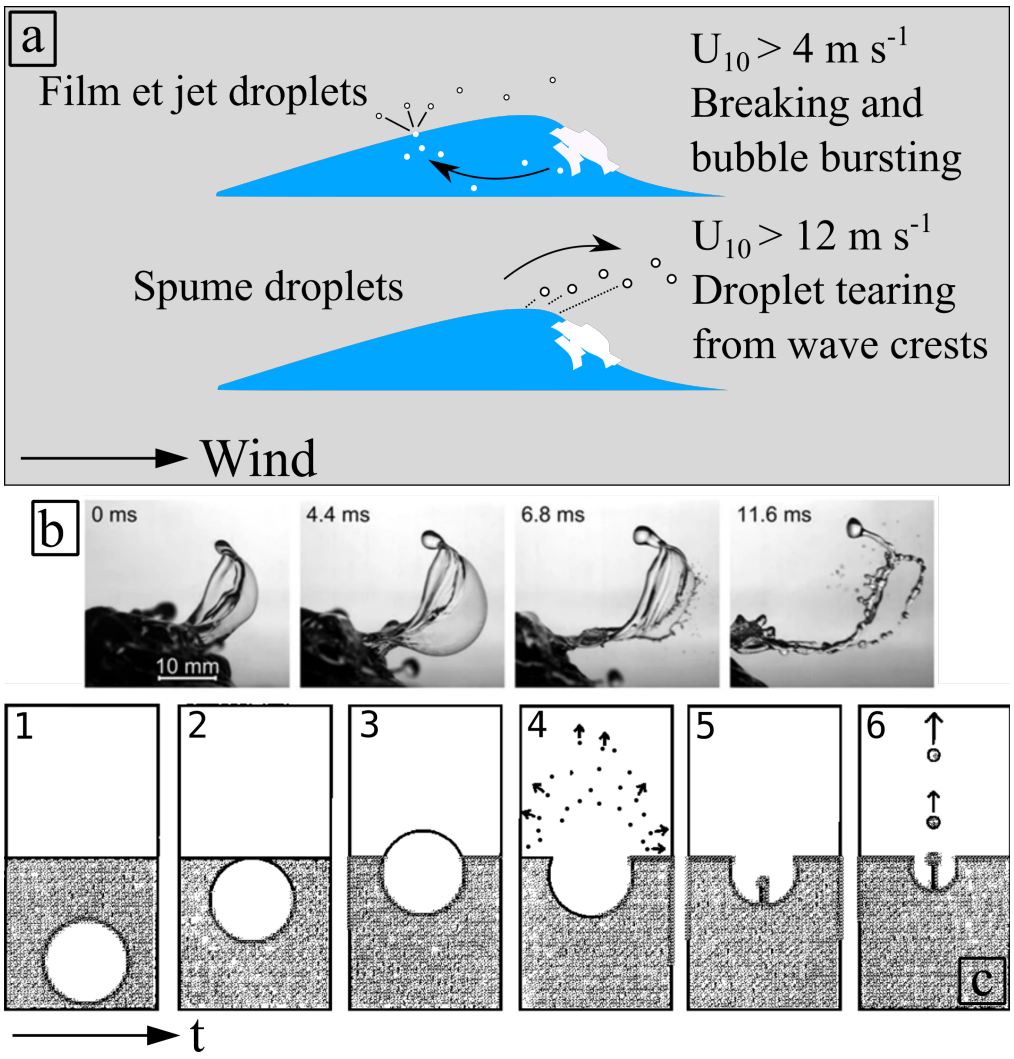

Figure 1.4: (a) Overview of wind and wave-driven film, jet and spume droplet generation mechanisms with approximate activation thresholds at 4 m s^{-1} (whitecapping and resulting bubble-bursting) and 12 m s^{-1} (spume droplet ejection from wave crests). (b) High frequency images (elapsed time indicated in milliseconds) of formation and break-up of bag into droplets; the dominant mechanism of sea spray generation at high wind speeds (Taken from Troitskaya et al. (2017)). (c) Schematic of film (panel 4) and jet droplet (6) generation as the result of a rising (panels 1 to 3) and bursting (panels 4 to 6) air bubble typically entrained by wave breaking. Chronology of events goes from left to right. Adapted from Lewis et al. (2004).

Anguelova et al. (1999) noted the tearing of spume drops at the wave crests by the wind, and found spume droplet generation to be strongly related to the whitecap coverage. At the microphysical scale, studies have shown that waves modulate the airflow, and processes such as airflow separation, i.e. the detachment of the boundary layer (cf. Sect. 1.3.2), can occur as the wind flows over a wave crest (Grare et al. 2013; Buckley and Veron 2019). At the wave crests, the bag breakup of small canopies (cf. Fig. 1.4b) of water produced by wind surface friction is a potential mechanism for spume droplet generation (Veron et al. 2012; Troitskaya et al. 2018). The generation of spume droplets by ligaments formed from breaking and wind-forced waves has also been investigated (Marmottant and Villermaux 2004; Mueller and Veron 2009). Environmental factors influencing spume

droplet generation are numerous. All in all, little is known about the conditions and mechanisms behind the generation of particles of radii greater than 20 µm (Veron et al. 2012; Veron 2015; Lenain and Melville 2017a). In some cases, large droplets were observed 30 meters above the mean water surface (Fairall et al. 2009; Lenain and Melville 2017a), which further raises questions about how such large particles are transported. A better parameterization of the droplet generation flux and transport over this range is needed since a major portion of the total volume of sea spray droplets is thought to be within the 10–200 µm radius range (Andreas 1992).

1.2.3 Existing Generation Source Functions

Relatively few sea spray generation functions (SSGFs) can be found in the literature. Though recent improvements in measurement techniques have reduced uncertainties for $r <$ 10-20 µm (Norris et al. 2013a; Veron 2015), significant scatter persists for the larger spume droplets. This is evident in Figure 1.5 where most of the existing SSGFs are represented as a function of the particle radius at formation r_0, or the radius of particles having reached equilibrium in 80% ambient relative humidity (see Sect. 1.2.6 for additional information). Sea spray can also be described using the dry particle radius r_D. r_D and r_{80} are often considered equivalent (Ovadnevaite et al. 2014) for small particle sizes. The formulation of more accurate SSGFs applicable to a wide range of conditions is essential for the better understanding of the role of sea spray on extreme weather events (Sroka and Emanuel 2021).

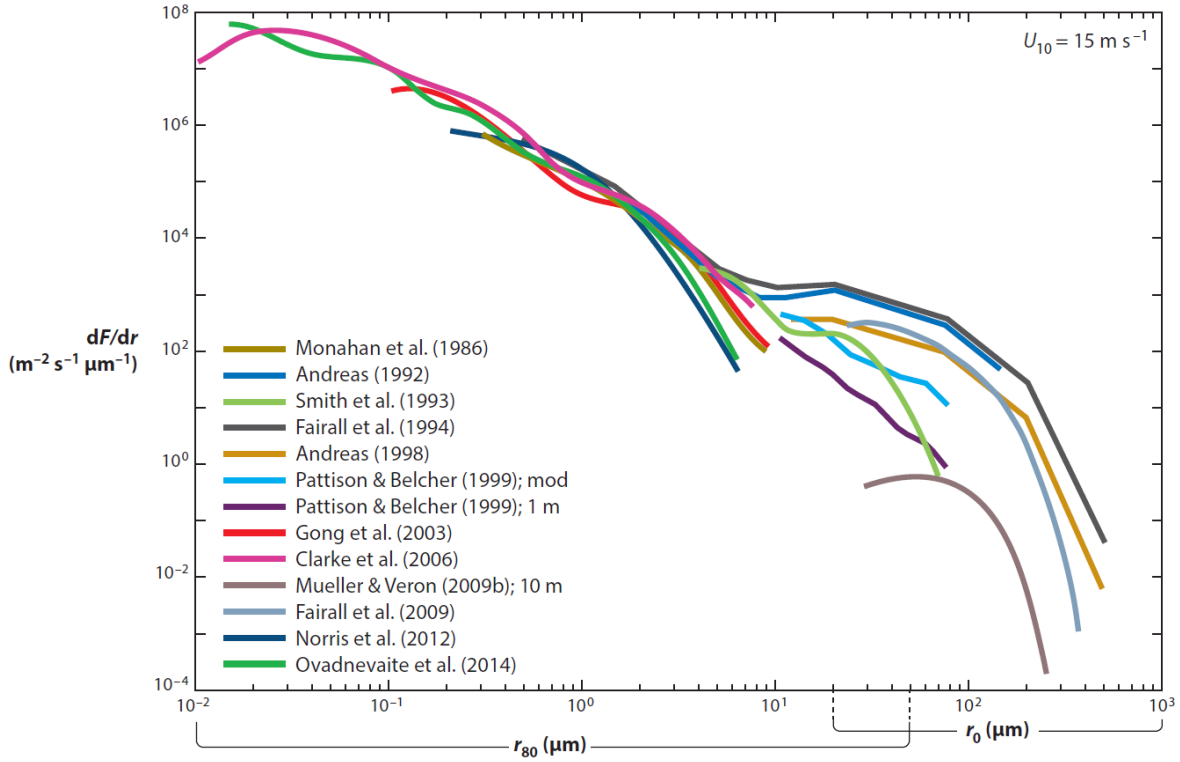

Figure 1.5: Selection of SSGFs proposed before 2015. Taken from Veron (2015).

The sea spray flux or SSGF is known to depend on numerous environmental parameters such as the wind and wave fields (de Leeuw 1986; Iida et al. 1992; Smith et al. 1993), the sea surface temperature (Mårtensson et al. 2003), and the composition and salinity of the seawater (Sellegri et al. 2006; Mehta et al. 2019; Vanderplow et al. 2020). Although wind speed alone was traditionally used to parameterize whitecapping and aerosol generation – cf. the SSGFs of Monahan et al. (1986); Smith et al. (1993); Andreas (1998); Gong (2003); Schulz et al. (2004) – there is increasing evidence that this is not sufficiently accurate, and additional environmental conditions have to be taken into account, wave parameters especially. Various authors have considered scaling droplet generation with non-dimensional numbers such as the wave age (Lafon et al. 2007; Demoisson et al. 2013; Laussac et al. 2018), the wind–sea Reynolds number R_B (Iida et al. 1992; Zhao et al. 2006; Troitskaya et al. 2018). The Reynolds number R_B was first introduced by Toba and Koga (1986) as $u_*^2/(\nu_a \omega_p)$ with the air kinematic viscosity ν_a and the wind–sea spectrum peak angular frequency ω_p, thus describing turbulence at the wind–wave boundary, and is sometimes written as a function of the significant wave heigth H_s (Norris et al. 2013b; Ovadnevaite et al. 2014; Yang et al. 2019). The wave age is defined as the ratio between the wave phase velocity c_p and a wind parameter (for example the wind friction velocity u_*), and is generally used to describe wave-field developement and wave–wind equilibrium.

Other authors have used whitecap coverage for the scaling of film, jet (Laussac et al. 2018) and spume droplet generation (Anguelova et al. 1999). In a similar fashion, wave energy dissipation – considered proportional to u_*^3 (the third power of the friction velocity u_*) by several authors – has also been considered for the study of droplet, bubble and whitecap generation (Wu 1988; Newell and Zakharov 1992; Andreas 1998, 2002; Zhao and Toba 2001; Zhao et al. 2006; Fairall et al. 2009). Of the different wave parameters used to scale sea spray generation, the wave slope (analogous to the wave steepness) has not yet been considered. Nevertheless, it is an interesting candidate because of its strong relation to wave breaking (Stokes 1880; Duncan 1981; Ramberg and Griffin 1987), whitecap production (Banner et al. 2002; Brumer et al. 2017), and therefore sea spray bubble-bursting and surface-tearing generation mechanisms. The wave slope is also thought to modulate the airflow at the wave crest (Veron 2015; Richter et al. 2019; Husain et al. 2019), which is of crucial importance for air–sea momentum transfer and surface-tearing mechanisms. The wave slope variance, unlike the wave slope, can integrate multiscale wave slope information. The relationship between the wave-slope variance and the wind speed at the wind–wave boundary is relatively well documented (Cox and Munk 1956; Plant 1982; Vandemark et al. 2004; Bringer et al. 2013; Lenain et al. 2019). In a context of relatively sparse measurements of small-scale waves (Munk 2009), authors have stressed the importance of multiscale surface wave shapes and wave breaking parameters in mass, momentum and energy transfers at the air-sea interface (Grare et al. 2013; Sutherland and Melville 2013; Veron 2015; Lenain and Melville 2017a). Bock et al. (1999) reports that air-sea gas fluxes are strongly driven by the short wind waves, in turn well represented by the wave slope variance.

Table 1.2 presents the size ranges, scaling parameters, and parameter validy ranges validity ranges of the SSGFs proposed by Monahan et al. (1986) (herein M86), Smith et al. (1993) (S93), Andreas (1998) (A98), Gong (2003) (G03), Ovadnevaite et al. (2014) (OVA14), and Laussac et al. (2018)(L18).

Table 1.2: Selection of SSGF parameterizations. The OVA14 scaling parameter is a wave height-dependent Reynolds number, where ν_w is the kinematic visocity of water, and the SSGF is proposed for dry particle radii r_D. We add that in M86, G03 and L18 the whitecap coverage is also an important parameter, most often calculated from the wind speed.

Parameterization	Size Range (μm)	Scaling Parameter	Study Range U_{10} (m s $^{-1}$)
M86	0.3–20 (r_{80})	U_{10}	6–13
S93	1–25 (r_{80})	U_{10}	0–30
A98	2–500 (r_{80})	U_{10}	0–32.5
G03	0.07–20 (r_{80})	U_{10}	6–17
OVA14	0.015–3 (r_D)	$u_* H_s/\nu_w$	3–18
L18	0.5–20 (r_{80})	c_p/u_*	8–16

1.2.4 Sea Spray Spectral Representations

As seen previously (cf. Sect 1.1.3), peaks in concentration spectra observed in a number of studies are associated with different size-dependent generation and transport mechanisms, and are commonly identified as modes. These modes are most often mathematically represented using normal or lognormal distributions, that need to be correctly centered over the radius range of the aerosol process of interest. Also, the shape of the mathematical relationship between concentrations and radius must be realistic. Some researchers have studied such shapes, with the identification of d^{-3} and d^{-5} power laws relating concentrations to particle diameter d for diameters smaller and larger than 10 μm, respectively (Lenain and Melville 2017a). The lognormal probability density function has often been used for its generally good fit to common aerosol distributions (Seinfeld and Pandis 1997). The modal median radii as well as the modal standard deviation are used to parameterize these distribution. The lognormal distribution can be written for a number of modes m

$$n^e ln(r) = \sum_{i=1}^{m} \frac{N_i}{\sqrt{2\pi} ln\sigma_i} exp(-\frac{1}{2} \frac{ln^2 \frac{r}{r_i}}{ln^2(\sigma_i)}) \tag{1.14}$$

where r_g, σ_g and N_i are the median radius, standard deviation and the total number concentration of the lognormal distribution for a given mode i. r is the radius increment.

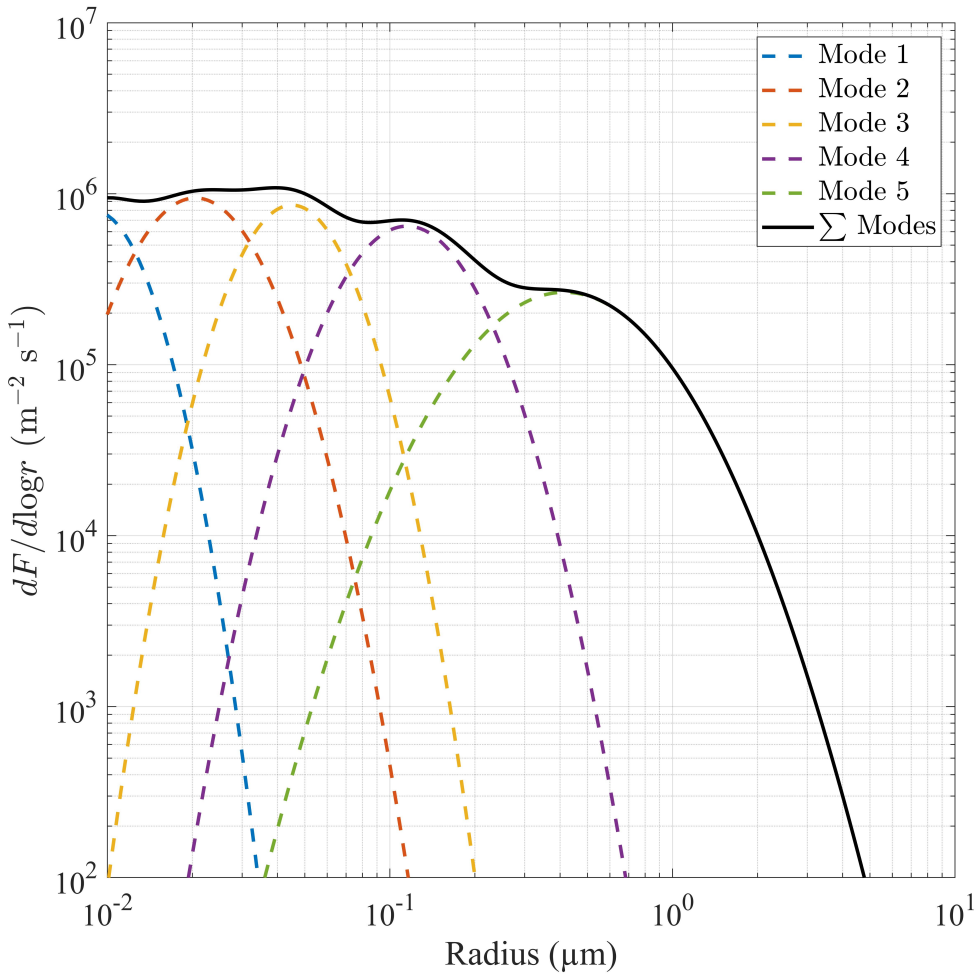

Figure 1.6: Lognormal modes (colored lines) and sum (black line) of the Ovadnevaite et al. (2014) sea spray generation function for wind speed U_{10} = 18 m s^{-1} and a Re_{HW} wave height-dependent Reynolds value of 6.3 × 10^6.

Some authors such as Ovadnevaite et al. (2014) represent SSGFs as the sum of lognormal distributions. Figure 1.6 is an example of the OVA14 SSGF and the five underlying modes calculated for a 18 m s^{-1} wind speed case, and a significant height estimated using the JONSWAP model (Hasselmann et al. 1973) (cf. Sect. 3.3.1). Normal (gaussian) distributions have also proved to be an adequate choice for the mathematical representation of generation and concentration spectra, namely for the larger coarse sea spray (Demoisson et al. 2013; Laussac et al. 2018). In most cases, the modal median and the standard deviation are kept constant, whilst the amplitude of the generation flux is modulated by the scaling parameter(s).

Though this is, to our knowledge, rarely described in publications, direct observations of sea spray concentration distributions and flux measurements show that the median and standard deviation of the modes also vary as a function of the forcing parameters. Also, some modes are only activated when a certain set of environmental conditions are met. Figure 1.7 illustrates this with concentration distributions for a range of wind speeds reported by Smith et al. (1993). In this figure, we can see that in the vicinity of 10 µm radius, no sea spray is observed at 0 m s^{-1} wind speed, but becomes increasingly present as wind speeds reach 10 m s^{-1} and above. It is even possible to note a light shift of the modal radii to smaller concentrations as the wind speed increase. This is in accordance with the spume droplet activation threshold.

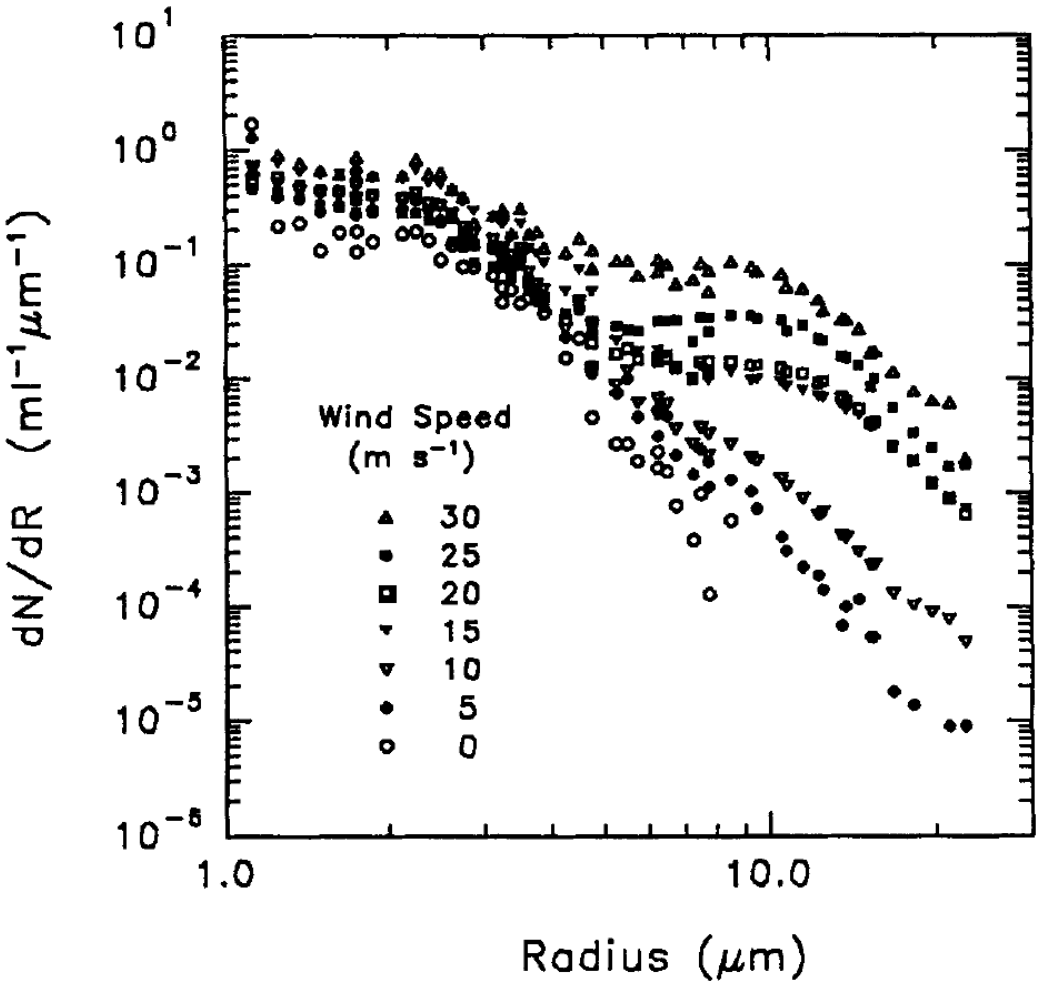

Figure 1.7: Concentration distributions measured for a range of wind speeds reported by Smith et al. (1993).

Following the different sources and sinks presented in Eq. 1.8, some numerical models (MesoNH model - Lac et al. (2018) - cf. Sect 4.3) transport lognormally represented modes rather than concentrations at individual radii (MACMod - Tedeschi and Piazzola (2011) - cf. Sect. 4.2). In such models, sources and sinks will act differently over the range of particles sizes found in a given mode, thus affecting the modal median and standard

deviation of each mode over time and space. Such encouraging developments allows to better resolve the complex atmospheric aerosol dynamics.

1.2.5 Air-Droplet Thermodynamics

As discussed in the previous sections, spray droplets are ejected into the atmosphere following a number of physical processes. Aside from classical aerosol dynamics (cf. Sect 1.1.3), sea spray droplets have the peculiarity of evaporating and exchanging heat when ejected into the highly turbulent near-surface spray evaporation layer (cf. Fig. 1.9, Sect 1.3.1). Lagrangian models have been developed to model these air-droplet thermodynamic processes (Andreas 1989, 1992; Edson and Fairall 1994; Andreas et al. 2008; Mueller and Veron 2014a,b). Current understanding of droplet microphysical processes indicates that once in the evaporation layer the droplets exchange sensible heat (denoted H) with the atmosphere and cool to an equilibrium temperature within a couple of seconds, thus warming the ambient air. Once this is achieved, the droplets begin to evaporate and therefore extract latent energy (denoted E) from the atmosphere, which can in turn cool the air. These droplet-modulated heat fluxes cumulate with the interfacial heat fluxes H_{int} and E_{int} to determine the total heat fluxes H_{tot} and E_{tot} that represent the net flux emitted out of the evaporation layer into the higher levels of the atmosphere (cf. illustration in Fig. 1.9, Sect. 1.3.1). The equilibrium vapor pressure, indicating the evaporation rate of a solution droplet considering an ambient relative humidity, is given by the Kelvin equation (Pruppacher and Klett 1978). Following developments (Andreas 1989) allowed to formulate the temporal evolution of a saline or freshwater droplet radius in the turbulent marine atmospheric boundary layer (MABL)

$$\frac{dr}{dt} = \frac{f_w D'_w M_w e_s(T_a)}{\rho_p r R T_a} \times [Q_{RH} - \frac{1}{1+\delta} exp(\frac{L_\nu M_w}{R T_a} \frac{\delta}{1+\delta} + \frac{2 M_w \Gamma_p}{R T_a \rho_w r (1+\delta)} - \frac{I \Phi_s m_s (M_w/M_s)}{(4\pi r^3 \rho_p/3) - m_s})]. \tag{1.15}$$

The terms in brackets describe the mechanisms that drive the droplet moisture content. From left to right, the first of four terms in brackets describes the modulation of the water vapor diffusion between the air and droplet by the relative humidity Q_{RH}. The three remaining terms predict the humidity at the droplet surface as a function of (from left to right) the air-droplet temperature gradient (with $\delta = (T_p/T_a) - 1$ and L_ν the latent heat of vaporization), the droplet surface tension and curvature (with Γ_p the flat surface surface tension), and the effect of dissolved salts on the surface vapor pressure (with Φ_s the osmotic coefficient and I the number of salt dissociates). f_w is a ventilation coefficient, M_w and M_s are the molecular weights of water and salt, respectively. D'_w is the modified thermal conductibity of air. $e_s(T_a)$ is the saturation vapor pressure at the air temperature T_a. ρ_p is the droplet density, r is radius. R is the universal gas constant.

In the saltwater case, droplet salinity increases over time as the pure water is lost

to evaporation. Increasing salinity slows evaporation, and the droplets tend towards an equilibrium radius. As a result of this, it has become customary to work with sea spray at a radius r_{80}, the hypothetical equilibrium radius reached by the droplet after sufficient lengths of time in an ambient relative humidity of 80%. Very large sea spray particles reaching up to millimetric radii (Anguelova et al. 1999; Veron et al. 2012) will only reside in the atmosphere for short lengths of time, and the initial radius r_0 is then adapted. (Andreas 1989) proposes the expression $r_{80} = 0.518 r_0^{0.976}$ for the conversion between the initial and equilibrium radii. Figure 1.8 presents examples of the sea spray droplet radius evolution as a function of the initial droplet temperature (T_w), the air temperature (T_a), the intial droplet salinity S (in PSU), and the ambient relative humidity (RH). The initial droplet radius in all tests is 10 µm. Reducing the ambient humidity from 90% to 82% for freshwater droplets leads to the almost total evaporation of the droplet after two seconds in the atmosphere (black dashed line). As the salinity and ambient humidity is increased and the initial air-droplet temperature gradient is reduced, droplet evaporation effects are reduced.

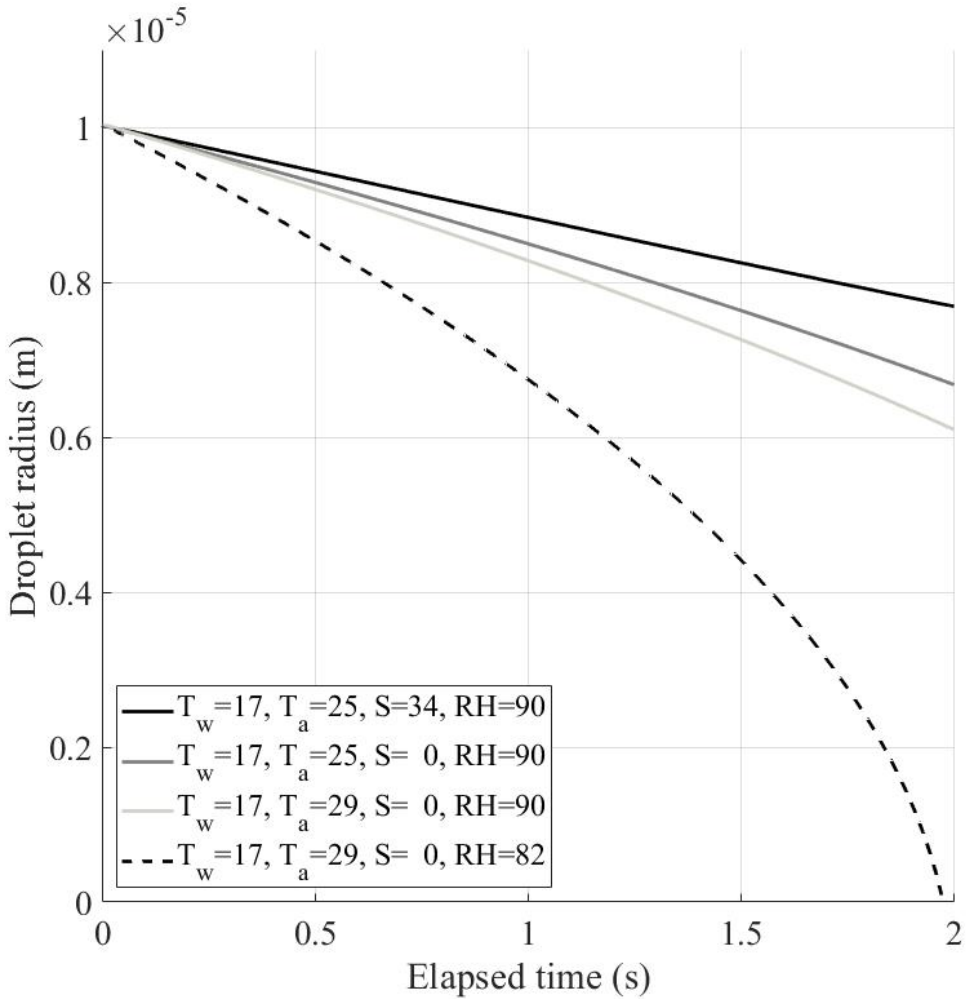

Figure 1.8: Microphysical simulations results illustrating the effects of salinity, water-air temperature gradients and air relative humidity on the rate of droplet radius change dr/dt for a 10µm initial radius, using Equ. 1.15.

The understanding of air-droplet thermodynamics also requires knowledge of air-droplet dynamics, such as the droplet velocity relative the surrounding flow (slip velocity), and the droplet height. Generally, the relative humidity tends to decrease with increasing distance from the water surface (cf. Appendix 7). Likewise, the height of the droplet will have an influence on the air-droplet temperature gradients. The rate of change in droplet temperature and water content therefore also depends on its position along the vertical humidity and temperature profile. The study of droplet turbulent transport remains mainly theoretical. Microphysical models currently transport droplets in random turbulent motions (Brownian or Gaussian Markov processes), allowing to better understand the physical mechanisms that drive sea spray generation. Such methods offer precious insight on mechanisms such as spume droplet generation, thought to be highly dependent on airflow separation and gustiness (Mueller and Veron 2014a; Wu et al. 2017). The significant numerical costs of lagrangian models make them inoperable for routine meteorological applications. Alternatively, Eulerian regional transport models have proven useful for regional sea spray transport, and are employed in Chap. 4. Also, the suspension and change in sea spray droplet properties have feedbacks on the MABL, and is breifly discussed in Chap. 5. The accuracy of sea spray mediated fluxes is highly dependent on the accuracy of the sea spray generation functions, which are in turn dependent on the robustness of the scaling relationship between the generation flux and the environmental characteristics such as winds and waves. In the following section we present general theory describing waves and the structure of the MABL.

1.2.6 The Effective Generation Flux

In many studies, the radius-dependent generation flux $\frac{dF}{dr}$ is actually the effective flux of particles $\frac{dF_e}{dr}$. The effective flux represents the spray droplets that are ejected out of the emission layer, and into the evaporation layer, several meters above the sea surface (Lewis et al. 2004; de Leeuw et al. 2011). Here we consider that the emission layer has the same vertical extent as the wave boundary layer, i.e. from the sea average surface height to the height of the highest waves (Iida et al. 1992), herein referred to as the effective emission height z_e (cf. Fig. 1.9, Sect. 1.3.1). The total flux $\frac{dF_T}{dr}$ of droplets generated from the sea surface is always greater than $\frac{dF_e}{dr}$ as a result of the portion of droplets that fall back into the sea almost instantly (though diffusive or gravitational sedimentation) without exiting the emission layer. The effective flux of droplets $F_e(r)$ represents the droplets that will significantly affect the MABL momentum, heat and moisture fluxes, among other atmospheric interactions. The contribution of droplets within the emission layer is, to our knowledge, not well known, but may contribute to the formation of a viscous two-phased layer (Lighthill 1999) and is later discussed in Chap. 5 (Sect. 5.2.3).

1.3 The Marine Atmospheric Boundary Layer

1.3.1 Wall-Bound Turbulent Fluxes

In the atmospheric boundary layer, the interaction between the airflow and a surface induces turbulence due to very high Reynolds numbers. In the marine atmospheric boundary layer (MABL) the airflow interacts with the sea surface. The highly turbulent MABL makes the connection between the Earth's oceans and the atmosphere, and momentum, mass, heat and moisture fluxes that occur have significant impacts on weather and climate. Figure 1.9 presents the wind profile in the sea surface-bound MABL (black lines and text), as well as the typical sea spray distribution (blue lines and text) in conditions of wind-forced breaking waves. The MABL is highly turbulent and extends several hundred meters above the water surface to reach the bottom of the free troposphere, where the wind is geostrophic and coarse mode aerosols are rare as a result of limited turbulent advection at such heights. The height of the MABL can also be estimated from the vertical aerosol concentration profile (Garratt 1994).

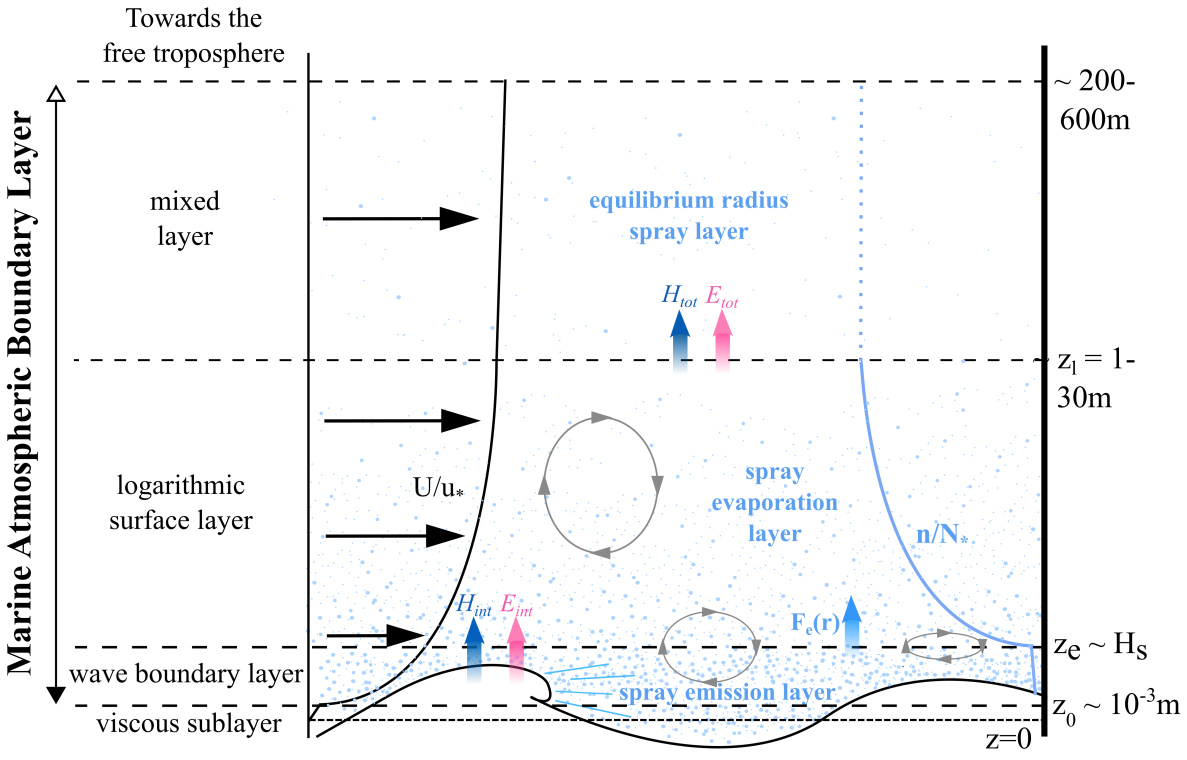

Figure 1.9: Schematic of wind (black text and lines) and aerosol (light blue text and lines) distributions in the MABL, in an example case of wind-forced breaking waves. Values for the MABL layer heights, such as for the roughness length z_0 and the effective height z_e, were compilated from the literature (Iida et al. 1992; Chalikov and Rainchik 2011; Cathelain 2017). Are also represented the interfacial and total sensible (dark blue arrows) and latent (pink arrows) heat fluxes (inspired from Veron (2015)).

Figure 1.9 illustrates the strong links between the vertical wind profile, the underlying waves, and the emission and transport of aerosols. As illustrated, the MABL counts four

distinct regions, the heights of which vary according to wind, wave and atmospheric stability characteristics. The first region closest to the surface is the viscous sublayer, where molecular effects dominate. The height of this layer is often referred to as the roughness length z_0, of approximately 0.1–1 millimeters. In this layer, the vertical profiles of meteorological parameters such as wind speed are commonly assumed linear with height. The wave boundary layer lies above the diffusive layer, and extends to the bottom of the logarithmic layer at height z_e. z_e is a couple of meters high relative to the mean sea level, roughly corresponding with the significant wave height H_s (Iida et al. 1992; Chalikov and Rainchik 2011). The second region is the logarithmic layer where turbulent fluxes dominate and are assumed independent of height. This so-called constant flux layer extends from the top of the wave boundary layer to z_l, i.e. 1–30 meters above the sea level. The accepted definition for the surface layer height z_l is the smallest height at which fluxes vary by more than 10% relative to the sea surface flux value (Tennekes and Lumley 1992). The mixed layer owes its name to its vertically homogenous aerosol distribution of marine and continental primary and secondary aerosols (Fairall and Davidson 1986).

The turbulence born from the interaction between the wind and the water surface takes the form of vertically directed flow updrafts and downdrafts induced by eddies (grey ellipses). Turbulent eddies create fluctuations in velocity, and the turbulent motions associated with the eddies are random. If we consider this surface as a flat and smooth surface, then the Reynolds decomposition of a steady flow observed at a fixed location can be expressed as

$$u = \overline{u} + u', \tag{1.16}$$

where u is the sum of the ageostrophic streamwise wind flow components in the x direction, $\overline{u}$ is the mean flow, and u' the fluctuations in the wind around the mean flow associated with turbulence. The time-average of such fluctuations is generally considered equal to zero. At these spatial scales, we can consider the Boussinesq approximation (limited density gradients) and negligible Corolis effects (constant direction of the mean wind). Assuming horizontal homogeneity and neglecting pressure gradients, the Reynolds-averaged momentum balance reads

$$\frac{\partial U}{\partial t} = -\frac{\partial \overline{u'w'}}{\partial z} - \nu \frac{\partial^2 U}{\partial z^2} \tag{1.17}$$

where the first term describes the time variation of the ageostrophic wind U. The second term represents the vertical gradient of the along-wind component of the Reynolds stress tensor $\overline{u'w'}$, associated with the dominance and multiscale distribution of vertical eddy-driven motions Townsend (1972). The momentum flux $\overline{u'w'}$ is the correlation between perturbations in the u and w components. Except in the case of DNS simulations where all the scales are resolved, models require a so-called sub-grid parameterization for $\overline{u'w'}$. The last term represents the viscous stress with the viscosity ν, increasingly

negligible for increasing distance from the viscous sublayer. Neglecting the last term, and considering a stationary MABL ($\partial U/\partial t = 0$), then we have the momentum balance, describing constant turbulent vertical movements according to height

$$\frac{d\overline{u'w'}}{dz} = 0. \tag{1.18}$$

A common quantity for the description of boundary layer turbulence is the friction velocity u_* , equal to the square root of the momentum flux $\sqrt{-\overline{u'w'}}$. The water surface considered here as a wall, $U = 0$ for $z = 0$. According to Townsend (1972), the vertical profile of horizontal wind speed follows a logarithmic profile

$$U(z) = \frac{u_*}{\kappa} log \frac{z}{z_0} \tag{1.19}$$

where $\kappa \approx 0.4$ is the universal Von Kármán constant. The roughness length z_0 is equal to $0.14\nu/u_*$ on a flat surface. z_0 depends on the roughness of the surface (Stull, 1988). The logarithmic layer is considered as an equilibrium layer between turbulent kinetic energy dissipation (denoted ϵ) and mechanical production Townsend (1972), which gives

$$-\overline{u'w'}\frac{dU}{dz} = \epsilon. \tag{1.20}$$

The dissipation is then written $\epsilon = \frac{u_*^3}{kz}$. Equation 1.20 describes the increasing spatial extent of eddies as a function of the distance z above the water surface. In the highly turbulent atmosphere, turbulent theories need to be adjusted as a result of buoyancy, affecting atmospheric stability. Considering this, Equ. 1.20 can be rewritten as a function of the momentum turbulent diffusion coefficient

$$K_T = \frac{\kappa u_* z}{\phi(z/L)} \tag{1.21}$$

where $\phi(z/L)$ is the Monin-Obhukhov Similarity (herein MOS) theory for momentum. L is the Monin-Obhukhov length (Stull 1988), which can be formulated as

$$L = -\frac{u_*^3 \overline{\theta_\nu}}{\kappa g \overline{w'\theta'_\nu}} \tag{1.22}$$

where θ_ν and θ'_ν are a reference potential temperature and its turbulent component, respectively. g is gravity acceleration, and u_* the friction velocity. Generally, atmospheric stability in the MABL will depend on the air temperature T_a and the sea surface temperature T_w. When $T_w < T_a$, L becomes positive and K_T is reduced due to atmospheric stability. When $T_w > T_a$, L is negative and K_T increases, indicating atmospheric instability, resulting in local convection. In the MABL, convective events will most often be associated with a net flux of heat from the ocean surface to the atmosphere. When

$T_w = T_a$, the atmosphere is neutral. For the measurement of vertical fluxes such as sea spray, knowledge of the state of atmospheric stability is important. In the following thesis, neutral conditions generally assumed.

Evaporation at the ocean surface results in the turbulent surface flux of moisture from the ocean to the atmosphere under the form of vapour. This latent heat flux intensity depends on the gradients between water surface and ambient air humidity, and can later lead to cloud formation upon the condensation of the emitted water vapour. As a general rule, the relative humidity Q_{RH} in the diffusive sublayer is assumed close to 98%. Profiles in the MABL have shown that Q_{RH} decreases with increasing distance from the water surface. As a result of evaporation (Stull 1988), the air-sea temperature gradient results in the turbulent sensible heat flux, which decribes the transfer of heat through the air-sea interface. Similar to the sea spray flux, the air-sea interface is a source of moisture and heat. Equation 1.22 implies that temperature gradients affect momentum. This has been evinced by a number of experimental campaigns for latent and sensible heat. Indeed, vertical temperature gradients were shown to influence the vertical wind profile, and consequently the vertical turbulent momentum flux (Pollard 1978; Bourras et al. 2004).

Energy budget closure in the MABL is the focus of a collossal amount of research, and remains an open question (Bourras et al. 2019). Today's phenomenological understanding of processes, as well as the validity of existing theoretical models and parameterizations, is largely limited by the complexity of field and laboratory measurements.

Empirical Formulations

The friction velocity can be measured from wind profiles, or by directly measuring the u and w components. In numerical models, empirical formulations offer a relatively simple estimation of quantities such as u_*. Assuming neutral conditions in the MABL, the MOS theory can be summarized as

$$C_D U^2 = u_*^2 \tag{1.23}$$

where U is the mean wind speed, and C_D is the drag coefficient. As the sea surface is never truly flat, empirical formulations derived from field and laboratory observations have been proposed. The most simple formulations generally depend on the wind speed at the 10 meter reference U_{10}, generally considered simple to measure. In the Large and Pond (1981) empirical formulation, C_D can be determined from U_{10} with

$$C_D = (0.49 + 0.065U_{10})10^{-3} \qquad U_{10} \geq 11\text{m s}^{-1} \tag{1.24}$$

$$C_D = 0.0012U_{10} \qquad U_{10} < 11\text{m s}^{-1} \tag{1.25}$$

The roughness length z_0 can be calculated according to the Charnock formula, with a threshold at 2 m s^{-1} added by Smith (1988), below which z_0 is constant:

$$z_0 = 0.11\frac{\nu}{u_*} + a_c\frac{u_*^2}{g} \qquad U_{10} \geq 2\text{m s}^{-1} \tag{1.26}$$

$$z_0 = 3.10^{-5} \qquad U_{10} < 2\text{m s}^{-1} \tag{1.27}$$

where $a_c = 0.016$. Such formulations are valid for a certain range of conditions as a result of their empirical or semi-empirical nature. They are useful as they require few input variables. However, in the search for increasingly universal and accurate formulations, the estimation of quantities in the MABL must include other parameters, such as surface wave characteristics. With or without local winds in the MABL, waves are often present at the surface, and deform the air-sea interface. The presence of waves can therefore affect friction velocity u_* and drag. This is detailed in the following section.

1.3.2 Wave Boundary Processes and Parameterizations

Relatively recent field campaigns and modelling efforts indicate that the drag coefficient C_D is larger than those proposed by Large and Pond (1981) and Smith (1988) among others, and are not necessarily a linear function of wind speed. Surface waves, often present as a result of local and distant wind events, increase the surface area of the air-sea interface. Bulk parameterizations such as the widely known COARE 3.0 (Fairall et al. 2003) and more recent COARE 3.5 (Edson et al. 2013), largely based on experimental campaigns, integrate the effects of surface gravity waves on momentum, heat and moisture fluxes. Common variables used to describe the wave field are the wave height H, the wave-slope S, and the wave age defined as the ratio between the wave phase speed and the wind speed, or the wind friction velocity u_*.

So far, the parameterization of the Charnock coefficients with wind or wave characteristics show almost indistinguishable results, either suggesting that the wind speed is sufficient, or that the effect of waves is so far over-simplified (Bourras et al. 2019). Such air-sea turbulent flux parameterizations are currently valid up to wind speeds of about 25 m s^{-1} (Fairall et al. 2003; Drennan et al. 2007; Edson et al. 2013) but not necessarily in extreme weather events. Other than in cases of wind-driven seas, waves waves can transmit energy into the MABL. This is in accordance with the heuristic idea that waves will absorb energy from the airflow when the wind speed is greater than the phase speed, but will transfer energy to the airflow in the opposite case in which the waves travel faster than the overlying airflow. This has also questionned the validity of MOS theory for cases of swells outrunning weak winds.

In the first few meters above the mean water surface, the atmospheric layer is most strongly influenced by the presence of waves (Bourras et al. 2019). This layer is the wave boundary layer (cf. Fig. 1.9), the height of which depends on the extent of the wave-induced perturbations on the flow (Chalikov and Rainchik 2011). Authors such as Kudryavtsev et al. (2014) and Hara and Sullivan (2015) add a third term to the Reynolds

decomposition of the flow in the wave boundary layer, and describe the momentum flux as a function into horizontal mean, turbulent fluctuations, and wave fluctuations

$$u = \overline{u} + u' + u_w. \tag{1.28}$$

$\overline{u}$ is the mean wind component, u' is the turbulent component, and u_w the wave-mediated turbulent component.

An example of wave-induced turbulent processes in the wave boundary layer is airflow separation, consisting in the detachment of the boundary layer into a wake. The importance of both wave geometry and wind speed for the occurence of airflow separation has especially been evidence through laboratory studies (Buckles et al. 1984) more recently with the help of particle image velocimetry systems (Buckley and Veron 2017, 2019; Vollestad and Jensen 2021) and large eddy simulations numerical modelling (Sullivan et al. 2018; Husain et al. 2019). Airflow separation events are intermittent, wave-phase-locked, and result in and increase in turbulent kinetic energy downwind of the wave crests (Buckley et al. 2020; Yousefi et al. 2021). Studies indicate that the C_D threshold reached at very strong winds is related to airflow separation (Soloviev et al. 2014) and the sea spray-driven formation of an increasingly viscous two-phase layer (cf. Chap. 5, Sect. 5.2.3).

1.4 Gravity Wave Breaking and Wave-Wind Equilibrium

1.4.1 Theoretical Basis

We have discussed wave-wind interactions and outlined the mechanisms that drive sea spray generation as well transport in the airflow. Waves, however, are not horizontally homoegenously distributed, and present non-linear relationships with the wind. Understanding temporal and spatial wave characteristics is essential for the understanding of sea spray processes. The ocean surface is a complex overlap of a wide range of wave types, each with different source, sink and propagation mechanisms. The different wave components can be classified according to distinctive characteristics such as the period or the wavelength. Among the waves directly generated by the wind are the capillary waves (generally below 10 Hz frequency) dominated by surface tension effects, and the gravity waves (with frequencies generally between 1 Hz and 0.04 Hz) mainly dependent on gravitational forces. It is admitted that gravity and surface tension effects are equivalent for $\lambda = 1.7$cm, and the surface tension is dominant for $\lambda \leq 5$ mm. Gravity waves are the main drivers of turbulent mixing at the air-sea interface, to which we limit our research in the present thesis. These waves can be separated into two categories; the equilibrium frequency range where wave components have reaches equilibrium such as swell-like components and some wind wave components, and the saturation range in which wave components have not reached equilibrium, such as wind waves down to the capillary wave

range. Gravity wave dispersion evolves as a function of depth, and wave-bottom interactions occur when the wavelength λ becomes comparable to the water depth. The present thesis only considers sea spray generation in deep water conditions in which λ is small compared to the height of the water column h ($h > \frac{\lambda}{2}$).

The Wave Spectrum

The wave height can be described in different ways, and is used in some SSGFs with the example of that proposed by Ovadnevaite et al. (2014). The significant wave height H_s (in meters) is thought to correspond with the visual impression an observer can have of the wave height. H_s is the most common wave elevation parameter. When considering a timeseries of wave heights measured by a wave gauge, H_s represents the third of highest waves. It can also be calculated from the surface elevation variance E with

$$H_s = 4\sqrt{E} \tag{1.29}$$

where $\sqrt{E}$ is a length scale associated with the wave amplitude, and indirectly the wave energy. The wave energy in the wave spectrum is generally represented as a function of frequency f, or the wavenumber k. Considering that waves observed in the field are always directionally spread, the omnidirectional wavenumber spectrum $S_e(k)$ obtained from the azimuthal integration of the directional spectrum $S_e(k, \phi)$ writes

$$S_e(k) = \int_0^{2\pi} S_e(k, \phi) k \; d\phi, \tag{1.30}$$

which allows to reformulate H_s as

$$H_s^2 = 16 \int_0^{\infty} dk \; S_e(k). \tag{1.31}$$

A number of wave spectral models provide the elevation spectrum, allowing to calculate E. Existing parameterizations also allow to calculate H_s from other variables such as the wind speed, and the fetch length. Such parameterizations are often valid in a limited number of cases. Here the JONSWAP (JOint North Sea WAve Project) formulation (Hasselmann et al. 1973) is presented and adapted to the North-West Mediterranean using observations made during the EMMA campaign (Lafon et al. 2004; Laussac et al. 2018):

$$H_s = \alpha \Big(\frac{U_{10}^2}{g} \Big) \Big(\frac{gX}{U_{10}^2} \Big)^{\beta} \tag{1.32}$$

X is the fetch length in meters, U_{10} is the wind speed at 10 meters height, and g is the acceleration due to gravity. Here, $\alpha = 7 \times 10^{-5}$ and $\beta = 0.89$.

The wave spectrum, generally obtained from the Fourier transform of sufficiently high frequency surface elevation measurements, allows to estimate key gravity wave variables such as the peak frequency f_p used alongside H_s (Zhao and Toba 2001; Ovadnevaite et al. 2014) for the expression of turbulence over waves through the wave height-dependent Reynolds number

$$Re_{HW} = \frac{u_* H_s}{\nu_w} \tag{1.33}$$

where ν_w is the kinematic viscosity of water.

Wave Growth

For actively wind generated waves, the effects of spectral flux divergence (directional spread), wind input, and dissipation balance among themselves. As waves receive energy from the wind though induced surface-pressure fluctuations (Phillips 1985), the wave field gains in amplitude and steepness. When a critical steepness value is reached, wave energy is dissipated through turbulent breaking (Stokes 1880; Ramberg and Griffin 1987; Duncan 1981). Non-linear interactions between wave components can result in a shift of energy towards lower frequencies within the gravity wave spectrum, eventually leading to the generation of lower frequency and high wavelength wave components, the wave age will progressively increase. The characteristics of the wave energy spectrum will depend on the stage of development, and the fetch (Hasselmann et al. 1973; Babanin and Soloviev 1998), which describes the duration, intensity and spatial extent of the forcing of waves by the wind. In limited fetch conditions, the wave field has not yet reached equilibrium with the wind, and therefore the wave field remains wind-forced and dissipative. Heuristically, as the wave phase speed c_p becomes equal or greater than the surface friction velocity u_*, wind-driven wave growth is reduced. Conditions in which the wave field has reached equilibrium describe unlimited fetch conditions. The ratio between wind and wave speed is called the wave age c_p/u_*. The phase speed of a wave is written

$$c_p = \frac{g}{2\pi f_p} = 2c_g, \tag{1.34}$$

where g is the gravitational acceleration, and T is the wave period (in seconds).

Figure 1.10 describes the relationship between u_*/c (c the wave speed) and the wave growth rate $2\pi\beta$. Miles' theory (black line) as well as field (open symbols) and laboratory (crosses and filled symbols) further illustrate this, with the higher growth rate values observed for conditions in which the friction velocity is higher than the wave speed. The state of equilibrium can also be estimated by identifying the portions of the wave probability density function where the wave shape follows a f^{-4} (typical of equilibrium range) and f^{-5} (typical of saturation range) slope (Phillips 1985; Thomson et al. 2013) (cf. Appendix 2).

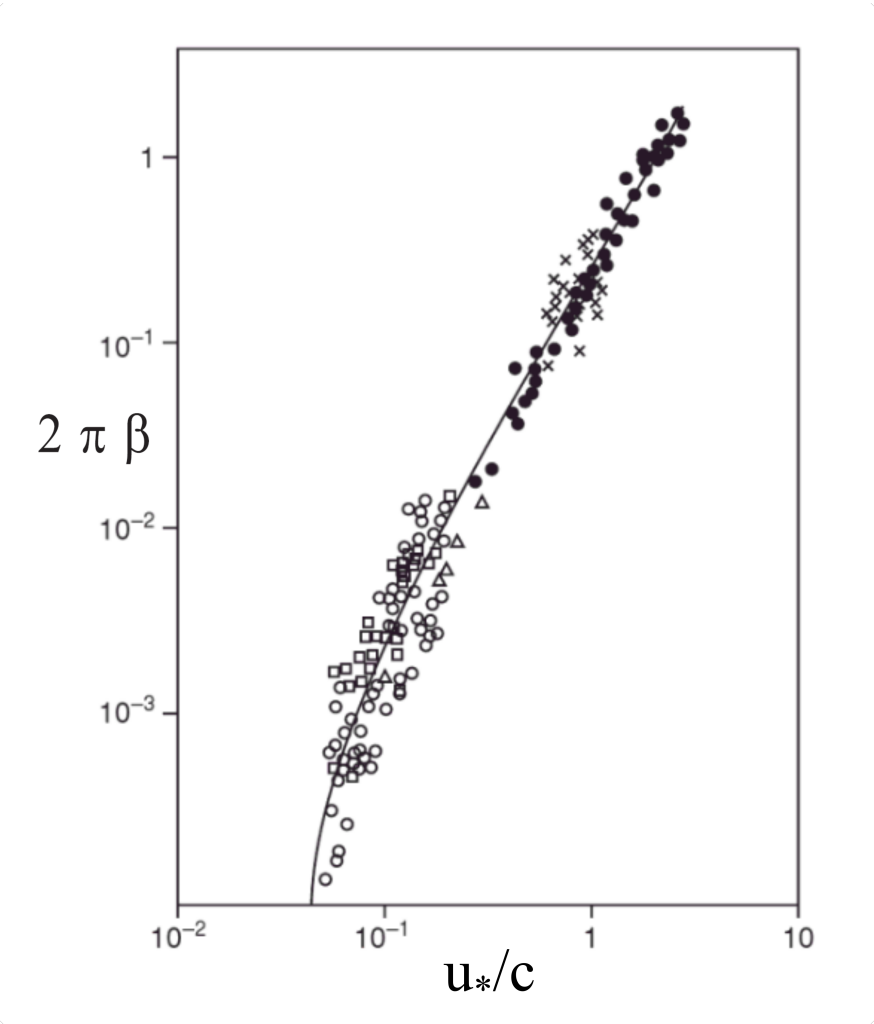

Figure 1.10: The wave growth rate as a function of the dimensionless phase speed u_*/c from measurements compiled by Plant (1982) (open symbols) and laboratory data (filled symbols and ×'s). The solid line represents Miles' theory. Figure adapted from Janssen and Janssen (2004).

1.4.2 A Wave Age Dependent Model

As shown in Fig. 1.10, wave growth scales rather well with wave age. Elfouhaily et al. (1997) continue this work by proposing a wave age-dependent omnidirectional spectral model, based on field and laboratory measurements, and used and validated in a wide range of studies (Hauser et al. 2008; Bringer et al. 2013). The spectral model combines different pre-existing spectral wave formulations to cover a wide wavenumber range, and the wave age serves to unify the spectrum. The model requires an input wave age, as well as a wavenumber range.

The model does not directly provide the wave-slope variance, but needs to be calculated from the wavenumber spectrum. The omnidirectional wavenumber spectrum $S_e(k)$ can be converted to the frequency spectrum $S_e(f)$ with

$$S_e(f) = S_e(k)\Big[\frac{1}{4\pi}\frac{g + 3\gamma_0 k^2}{gk + (\gamma_0 k^3)^{0.5}}\Big]^{-1} \tag{1.35}$$

where $\gamma_0 = 7.44 \times 10^{-5}$ (m^3/s^2), g is the acceleration due to gravity, and k the wavenumber (Boisot et al. 2015). The gamma coefficient becomes especially important when the surface tension becomes significant relative to the effect of gravity on the considered waves. We also note that the wavenumber bins corresponding to the S(k) spectrum need to be converted to frequency bins. This is done using the dispersion relationship:

$$gk + \gamma_0 k^3 - (2\pi f)^2 = 0 \tag{1.36}$$

The second moment of the wave spectrum spectrum describes contributions of short and long waves, and is equal to the wave-slope variance.

1.4.3 Wave-Slope Variance

The wave-slope variance $\langle S^2 \rangle$ is inherently related to wave breaking (cf. Sect 1.4.1), whilst also being associated with the sea surface roughness by describing the sea surface shape. The wave-slope variance is most often written as $\langle S^2 \rangle$ in the present thesis, with S a wave-slope timeseries. The wave-slope variance is also often referred to as the mean square slope, denoted MSS.

Studies have shown that much of the $\langle S^2 \rangle$ is found in the saturation range of the wave spectrum, where wind waves are typically found, as well as in the capillary range (Elfouhaily et al. 1997; Lenain and Melville 2017b). $\langle S^2 \rangle$ can be obtained from field measurements through the collection of wave-slope time series, from often optical remote sensing techniques due to the long-studied relationship between $\langle S^2 \rangle$ and backscatter (Donelan and Pierson Jr 1987; Apel 1994; Liu et al. 2000), or can be calculated from the wave energy spectrum. A well known example of the remote estimation of $\langle S^2 \rangle$ are the sunglitter measurements made from aerial photographs by Cox and Munk (1956) (cf. Equ. 3.1, Sect. 3.1.2).

Here we write $\langle S^2 \rangle$ as a function of the second moment of the wavenumber spectrum.

$$\langle S^2 \rangle = \int_0^\infty dk \; k^2 \; S_e(k), \tag{1.37}$$

The wave-slope variance can therefore be calculated from wave spectral models such as that proposed by Elfouhaily et al. (1997) presented in Sect. 1.4.2 above. $\langle S^2 \rangle$ is considered linear with wind speed by authors (Cox and Munk 1956), but is expected to fluctuate with wave age in the Elfouhaily et al. (1997) spectral model.

The $\langle S^2 \rangle$ allow to integrate information contained in both the higher and lower frequency components of the wave field, and can therefore be considered as a multiscale variable compared to variables that often describe the fundamental spectral peak information, such as f_p and H_s. It is important to add that the direct measurement of $\langle S^2 \rangle$ over a large λ range is often complicated by the cutt-off λ values imposed by the instru-

mental dispositions. The shorter wavelengths are often omitted for this reason, despite the fact that they contain the majority of the total $\langle S^2 \rangle$.

1.4.4 Wave Breaking Measurements and Parameterizations

Whitecapping has been associated with various fluxes at the air-sea interface, such as sea spray generation. Resulting from wave breaking, the whitecap coverage $W(\%)$ is the percentage of the water surface covered by primary whitecaps that represent the active breaking, and secondary whitecaps that represent the residual bubble bursting processes that continue for a certain duration after the wave has broken. As shown previously (cf. Sect 1.2.3) the whitecap coverage plays an important role in existing sea spray generation functions. The whitecap coverage has most often been represented as a function of wind speed, as shown by the following expression proposed by Monahan and O'Muircheartaigh (1986):

$$W(\%) = 3.84 \times 10^{-6} U_{10}^{3.41}. \tag{1.38}$$

A range of techniques and methods exist to estimate $W(\%)$ in the scientific community. The most common method for $W(\%)$ estimates is the calculation of the percentage of white patches at the sea surface from photographs, and resulting values are highly sensitive to the threshold used to identify whitecaps, as well as the estimate of the surface area in the photograph. Also, the capacity of U_{10} to scale $W(\%)$ in a range of wind and wave conditions is sometimes questionned. Figure 1.11 taken from work published by de Leeuw et al. (2011) illustrates the significant deviations between authors in the relationship between $W(\%)$ and the wind speed U_{10}. Across all shown authors, deviations in $W(\%)$ values range between one and four orders of magnitude for a given wind speed. Deviations are reduced when considering the more recent studies (open squares) but still reach up to two orders of magnitude.

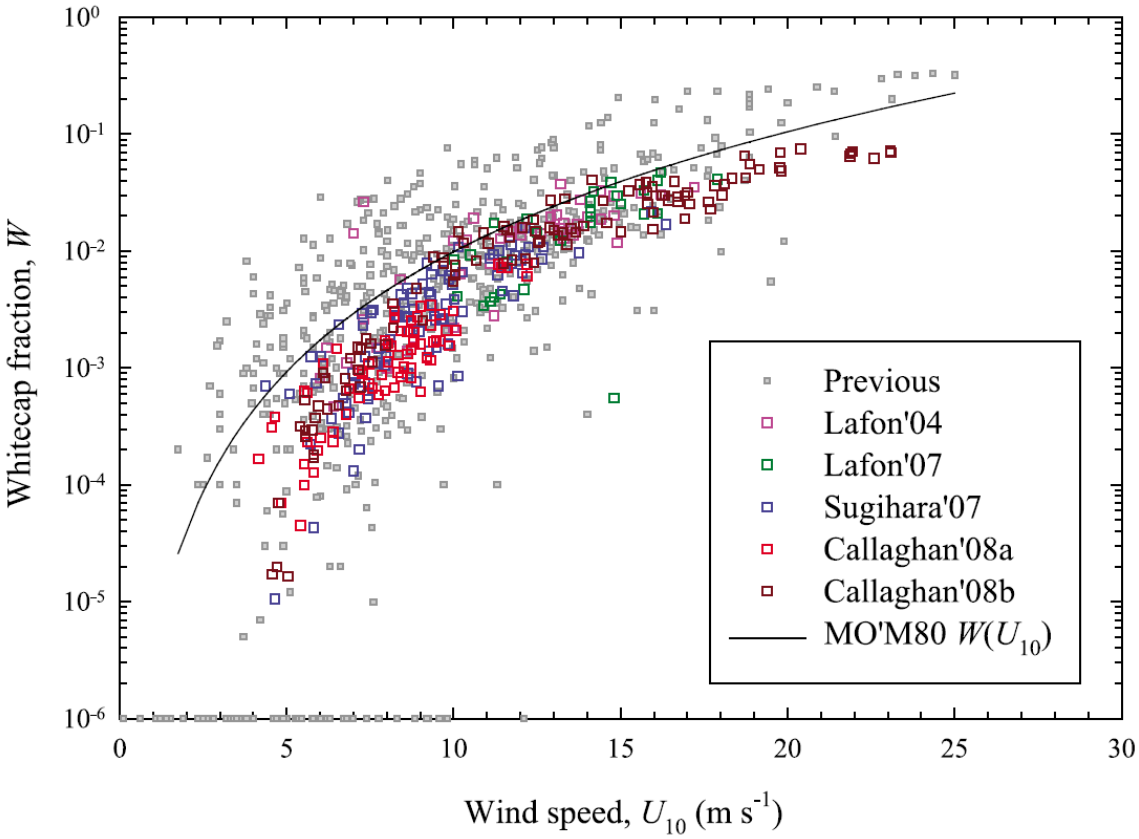

Figure 1.11: The whitecap fraction W represented as a function of the wind speed U_{10} using data from a range of studies. Figure taken from de Leeuw et al. (2011).

Whitecap coverage has been scaled using the friction velocity u_*^3 by authors such as Wu (1988), also used to scale momentum transfer to waves and wind-forced wave energy dissipation (Newell and Zakharov 1992; Fairall et al. 2009). More recently, attemps have been made to scale whitecap coverage with wave field statistics (Lafon et al. 2007; Brumer et al. 2017). Laussac et al. (2018) propose new coefficients for the formulation scaling whitecap with the wave age (here written as c_p/U_{10} initially proposed by Lafon et al. (2007):

$$W(\%) = 20(c_p/U_{10})^{2.5} \qquad c_p/U_{10} \leq 0.35, \tag{1.39}$$

$$W(\%) = 0.6(c_p/U_{10})^{-0.41} \qquad c_p/U_{10} > 0.35. \tag{1.40}$$

The separation between primary and secondary whitecaps, important for the understanding of fluxes at the air-sea interface, is difficult with such classical image techniques. An alternative to this technique is the wave breaking length distribution $\Lambda(c_{br})$ (Phillips 1985; Kleiss and Melville 2011; Sutherland and Melville 2013; Romero 2019) with c_{br} the speed of the breaking. The different moments of $\Lambda(c_{br})$ allow to describe wave breaking kinematics and dynamics, including the wave energy dissipation, the momentum flux, and the rate of air entrainement. Though the breaking length distribution is not used in the

present thesis, we acknowledge its potential for the future study of air sea fluxes. In the study by Lenain and Melville (2017a), the breaking length distribution is used to scale sea spray concentrations.

Chapter 2

Experimental Strategy: Study Sites and Instrumentation

Contents

2.1 Introduction

Uncertainty in the source (cf. Fig. 1.5, Sect. 1.2.3) of sea spray translates into significant uncertainties on aerosol number concentration in the marine atmosphere, and can only be constrained by *in situ* observations (Heintzenberg et al. 2000; Jaeglé et al. 2011; Boucher et al. 2013). Sea spray field measurements are as scarce as they are challenging. We aim to make up for the relatively scarce sea spray observations with an extended database gathering field data from the Mediterranean and the Atlantic Ocean. In the following section

we detail field (SUMOS, North-East Atlantic, early 2021) and laboratory (MATE2019) sea spray, wind and wave measurements carried out in the context of the present thesis. Field data were collected in the North-West of the Mediterranean basin during the MIRAMER (2008) campaign. Both presented Mediterranean and Atlantic campaigns took place onboard the R/V Atalante.

2.2 The North-West Mediterranean MIRAMER campaign

2.2.1 General Presentation

The MIRAMER campaign took place aboard the R/V Atalante between the 15th and 28th May 2008 in the Toulon-Hyères bay in the North-West Mediterranean. This area is known for its frequent winds, often dominated by Westerly and North-Westerly winds such as the Mistral and the Tramontane, and Easterly winds originating from the Ligurian Sea. A variety of wind directions and vessel locations during the MIRAMER campaign allowed for infinite fetch conditions reaching up to 270 km, as well as limited fetch conditions when the vessel was near the coast with an offshore wind direction. Since the work by Laussac et al. (2018), the data has been partially reanalyzed for the purpose of this study, allowing for an increased total of 17 stations. These stations correspond to locations at which the stationned vessel and instruments onboard were facing incident winds. Meteorological and aerosol concentrations were measured at each station. Further details on the campaign are available in previous work by Demoisson et al. (2013) and Laussac et al. (2018).

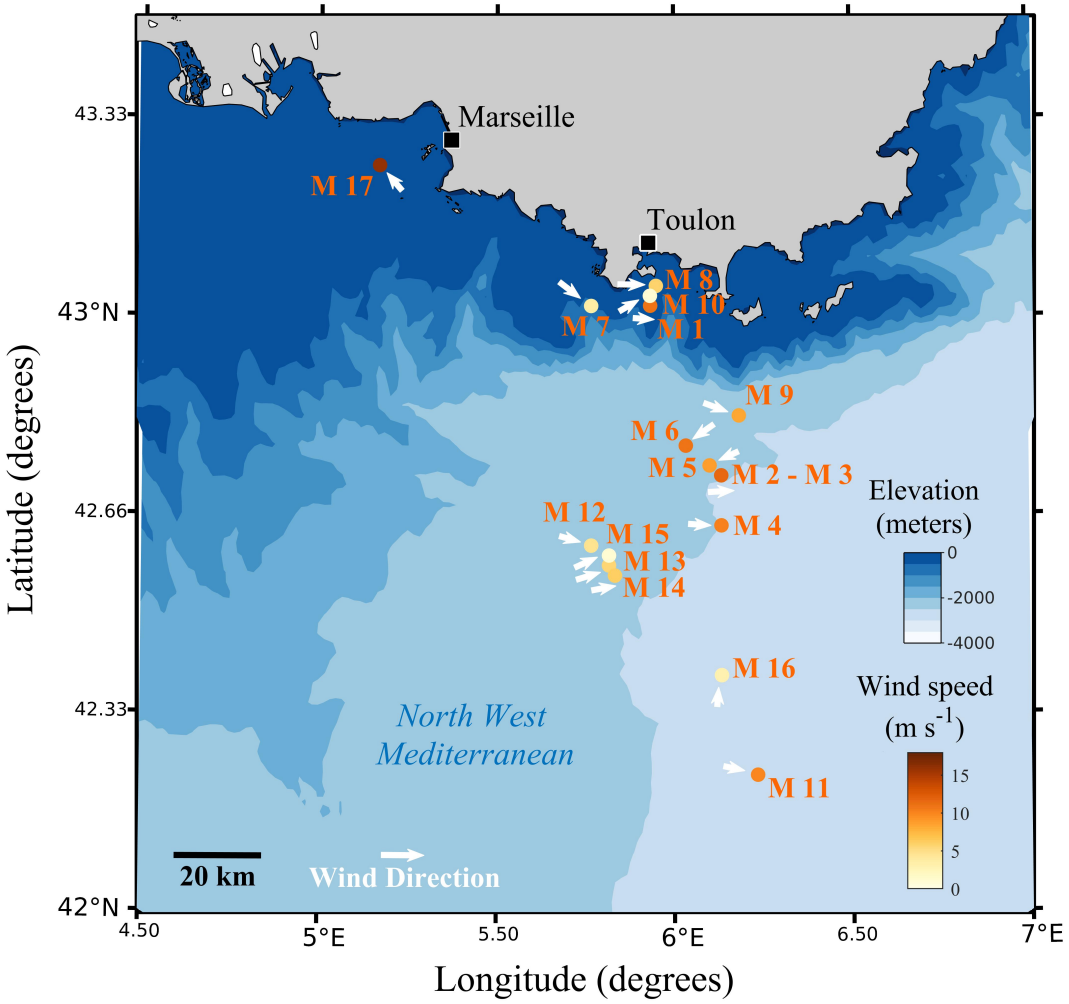

Figure 2.1: MIRAMER research cruise stations and corresponding true wind speed measurements collected at the foremast. The white arrows show the mean wind direction measured during the ship stations. The bathymetry represented in the background is the ETOPO1 (Amante and Eakins 2009) product, showing deep water conditions.

During MIRAMER, Recorded wind speed spanned the U_{10} 1–16 m s^{-1} range. Eight stations recorded winds between 8 and 12 m s^{-1}, and another eight recorded winds below 8 m s^{-1}. Figure 3.1 displays station locations (coloured dots) as well as associated true wind directions (white arrows). The dot symbol color scheme indicates the wind speed at each station. Table 3.1 lists the wind speed (and corresponding standard deviation), wind direction (direction of provenance), sample duration (for meteorological and aerosol measurements) and station references. When possible, fetch lengths were estimated at the study locations from airmass backward trajectories (Demoisson et al. 2013; ?).

Table 2.1: Overview of the MIRAMER stations represented in Fig. 3.1, with corresponding wind speed and wind direction measured onboard the R/V Atalante. The sample durations of the meteorology and aerosol concentrations are indicated in minutes. When possible, the fetch lengths at the vessel location are provided in km.

Date	Hour	Fetch length (km)	Wind speed (m s^{-1})	Wind direction (degrees)	Speed standard deviation	Sample duration (minutes)	Station reference
18/05/2008	12:30	12	10.8	273	0.43	20	M 1
	16:00	N/A	12.0	274	0.27	29	M 2
	17:00	N/A	11.48	274	0.26	21	M 3
	19:45	180	10.2	272	0.53	32	M 4
19/05/2008	07:15	35	8.75	77	1.03	30	M 5
	10:00	60	10.81	64	0.72	32	M 6
	17:30	N/A	3.61	314	0.56	25	M 7
20/05/2008	14:30	N/A	5.77	274	0.31	32	M 8
	18:30	50	8.22	310	1.04	29	M 9
21/05/2008	09:50	N/A	1.03	202	0.46	17	M 10
	16:00	270	9.86	279	0.6	29	M 11
22/05/2008	07:25	N/A	4.62	290	0.29	24	M 12
	13:30	N/A	5.63	257	0.17	33	M 13
	18:00	N/A	6.17	265	0.27	28	M 14
23/05/2008	09:00	N/A	1.0	231	0.2	29	M 15
24/05/2008	14:00	N/A	3.1	179	1.94	28	M 16
26/05/2008	14:30	150	15.96	127	2.32	29	M 17

The air and water temperature, as well as the relative humidity (RH) were measured during the campaign at the top of the main mast, approximately 28 meters above the mean water level (MWL). The average station relative humidity measured during the campaign was 73%. On the air and water temperature gradients were small, with mean temperatures of 18.2°C and 17.6°C respectively. As presented in Chapter 1, these conditions typically describe neutral conditions. The temperature (panel a) and relative humidity (panel b) timeseries using data collected at each of the 17 stations are shown in Fig. 3.2. Considering the height of the main mast and the typically increasing RH with proximity to the water surface in the MABL, we estimate the RH to be close to 80% at the sea spray sampling location at the top of the 15-meter-high foremast.

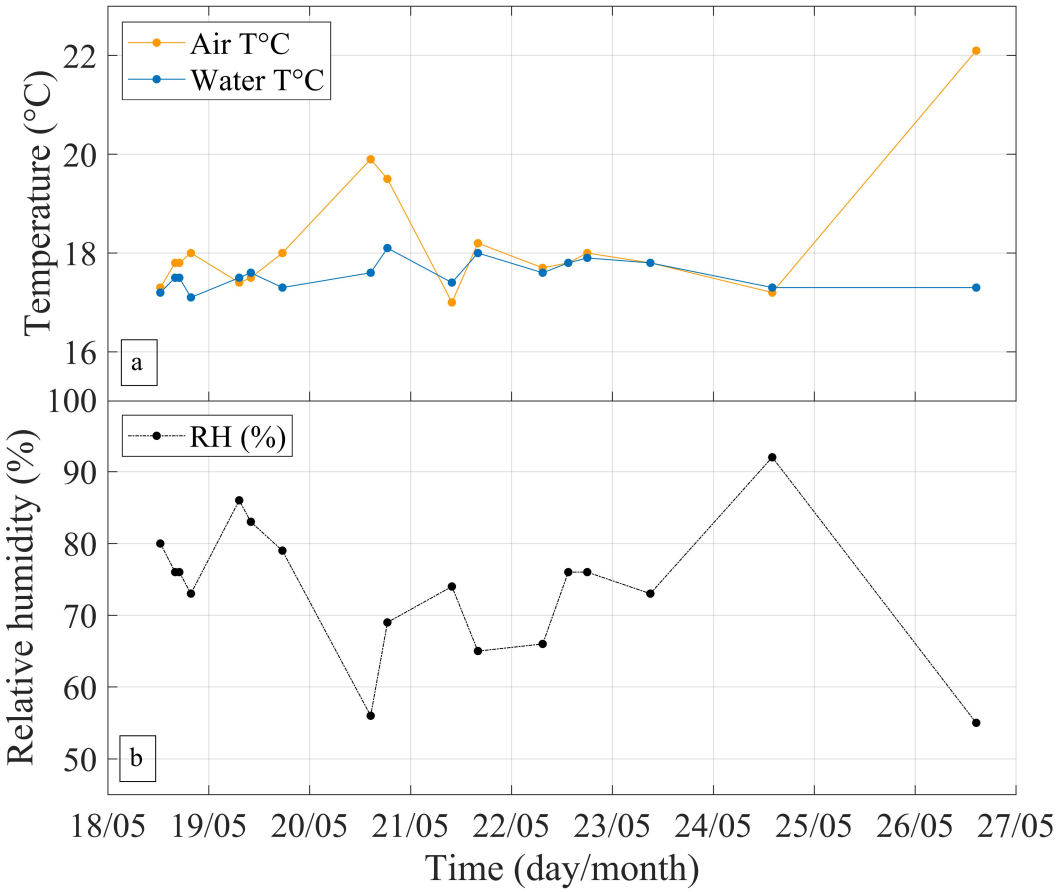

Figure 2.2: Timeseries of (a) air and water temperature, and (b) relative humidity measured at each of the 17 presentation stations. Measurements were made onboard the R/V Atalante at approximately 28 meters above the MWL.

2.2.2 Experimental Configuration

During the MIRAMER campaign, two probes (Particle Measurement Systems, Boulder, Colorado, USA) were placed at the top of the foremast for the sampling of aerosol concentrations. A CSASP-100-HV-ER probe, sampling over the 0.1–47.5 µm radius range, was placed on top of a CSASP-200 sampling probe, sampling over the 0.1–10 radius range.

Figure 2.3: CSASP sensors and wind sensors mounted at the top of the R/V Atalante foremast during the MIRAMER campaign. A CSASP-100-HV-ER probe is placed above a CSASP-200 probe.

2.2.3 Key results

Results presented in Demoisson et al. (2013) and Laussac et al. (2018) are briefly reiterated here. Sea spray concentrations and generation fluxes have traditionnally been scaled using wind speed. Figure 2.4 presents examples of measured concentrations on a log-scale as a function of wind speed for particles of radius 1.5µm (cf. Fig. 2.4a) and 10µm (cf. Fig. 2.4b). The relationships are expressed by linear fitting functions (solid black line) and corresponding R^2 values. For radii of 1.5µm and 10µm, wind speed proves to be a poor choice for the scaling of concentrations, with R^2=0.34 and R^2=0.06 respectively. As explained in Chapter 1, sea spray generation and transport has been shown to depend on wave breaking and near-surface wind dynamics, which in turn depend on a variety of environmental characteristics; meteorological and gravity wave parameters in particular.

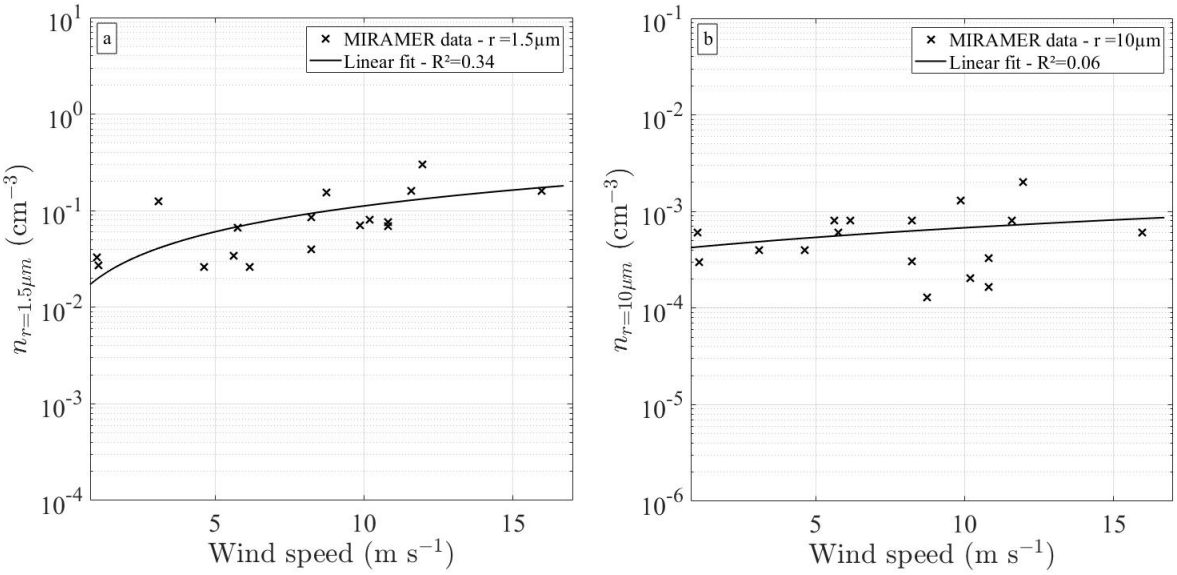

Figure 2.4: Concentrations at the 17 MIRAMER stations for (a) $r = 1.5\mu$m and (b) $r = 10\mu$m, as a function of U_{10} wind speed. Black solid lines show linear fits to the data, with corresponding coefficents of determination R^2.

Laussac et al. (2018) proposed to use the wave age for the scaling of sea spray concentrations, as well as the formulation of the sea spray generation flux. Figure 2.5 uses data taken from (Laussac et al. 2018) to exhibit that the wave age (here written c_p/U_{10}) seems to better scale sea spray concentration than wind alone. For the same radii as presented in Fig. 2.4, R^2 values increase twofold to 0.68 for r =1.5μm, and significantly to 0.32 for r =10μm. For r =1.5μm, measured concentrations increase with wave age for $c_p/U_{10} < 1$, describing conditions favourable to wind-induced wave breaking. Conditions with c_p/U_{10} > 1, which typically indicates that the waves have reached a certain equilibrium translating in reduced breaking, concurs with an observed sea spray concentration decrease. Over the presented range wave age range, concentrations for particles of 10μm radius seem to increase with wave age, and to tend towards a constant value. However, no decrease is observed for increasing wave age.

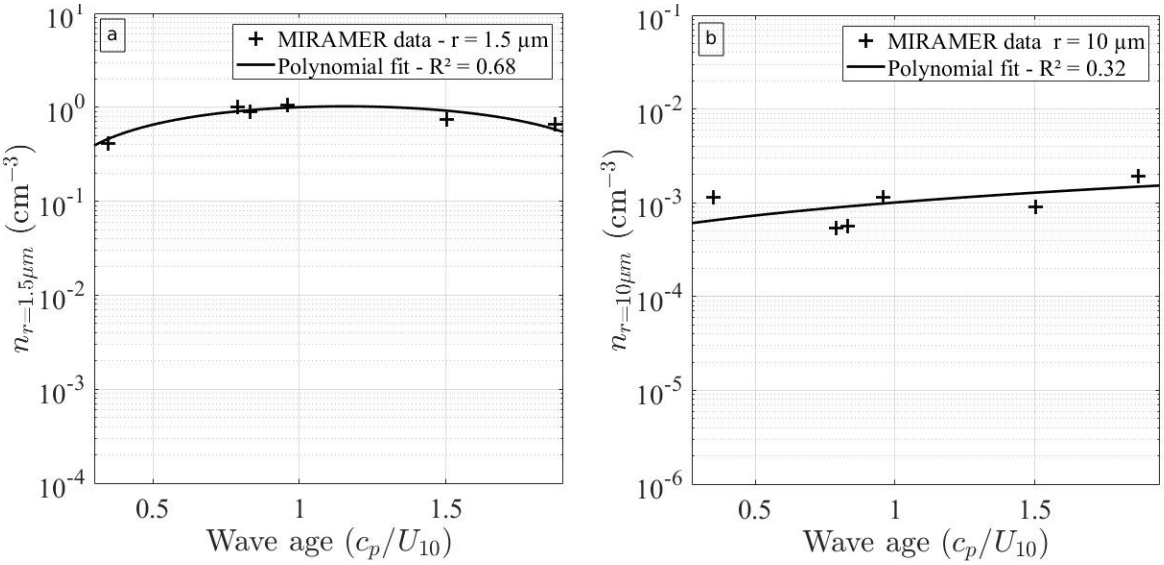

Figure 2.5: Concentrations at the 17 MIRAMER stations for (a) $r = 1.5\mu$m and (b) $r = 10\mu$m, as a function of wave age c_p/U_{10}. Black solid lines show linear fits to the data, with corresponding coefficents of determination R^2.

Generally, the MIRAMER campaign was hampered by low wind speed conditions and short sample durations ranging from 17 to 33 minutes (cf. Table 2.1). In addition, measurements of larger particles by the CSASP-200 probe may have been affected by the proximity of a ship navigation light. Amidst such uncertainties, additional field measurements are required.

2.3 The North Atlantic SUMOS campaign

The SUMOS research cruise, funded by the Centre National d'Etudes Spatiales (CNES), took place in the Bay of Biscay onboard the R/V Atalante over 25 days between February and March 2021. The campaign was led by the Laboratoire d'Océanographie Physique et Spatiale (LOPS). The aim of the deployment was to further investigate air-sea interface processes using modern scientific methods and equipement, and more specifically to participate in the calibration of CFOSAT SWIM and SCAT instruments dedicated to the measurement of surface wave and wind fields, respectively. Among the variety of campaign objectives, we present aerosol (carried out by the Mediterranean Institute of Oceanography) and meteorological measurements, and interpretations. This section presents field data later used for numerical model validation in Chapter 4.

2.3.1 General Presentation

The expedition set out from the port of Brest (France) on the 11th February with low atmospheric temperatures nearing zero degrees Celsius (cf. Fig 2.8), and strong North-Easterly winds exceeding 20 m s^{-1}. Within 24 hours, the vessel reached the study area with

warmer atmospheric conditions. A persistant anticyclone positioned over the European continent prevented Westerly depressions originating off the North-American coast from reaching the study area during most of the campaign duration. As later shown in Fig. 2.8, this mostly led to Southerly and North-Easterly winds in the study area, sometimes accompanied by South-Westerly swell. This configuration resulted in often fetch-limited conditions, limited by surrounding Spanish and French coastlines.

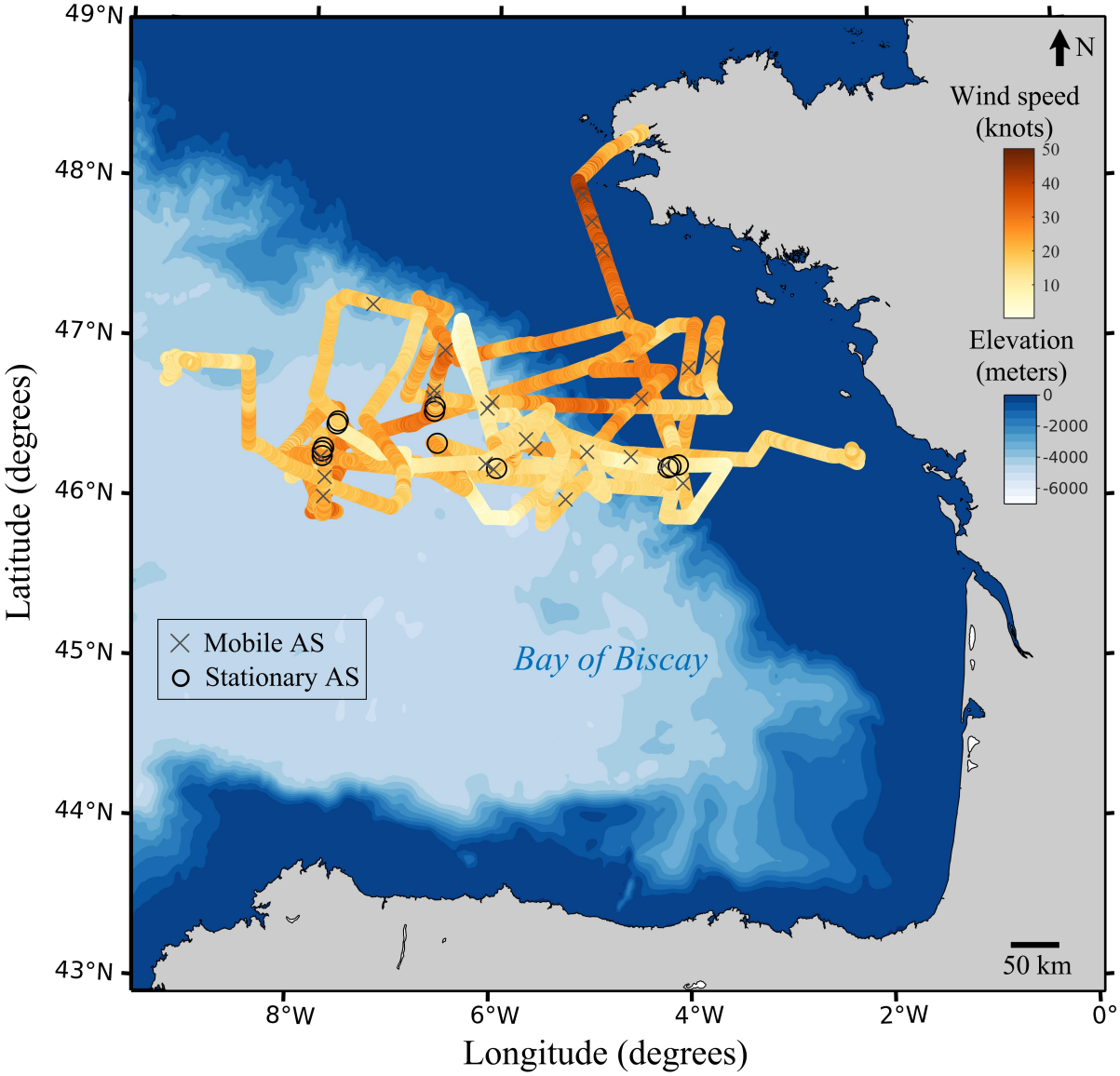

Figure 2.6: R/V Atalante course during SUMOS research cruise. The coloured closed circles indicate the vessel location every minute, and the color scheme allows to represent the corresponding true wind speeds measured at the top of the foremast. The grey "×" symbol shows the average position of the different mobile aerosol stataions (MASs), and the black "○" symbol indicates the average position of the stationary aerosol stations (SASs). The bathymetry represented in the background uses the ETOPO1 (Amante and Eakins 2009) product to show the extent of the relatively shallow continental plateau at ≈ 200m depth and less.

Marine aerosol and meteorological measurements were continuous, except for occasional maintenance. The present study includes a total of 38 aerosol stations (AS). Stations were determined after the campaign by selecting data segments meeting a number of requirements. For example, the angle between the CSASP inlet direction (aligned with the ship bow) and the true wind direction must be lower than 45° for optimal aerosol sampling conditions and possibly limited flow distortions around the bow (Dupuis et al. 2003; Bourras et al. 2009). Other conditions include stationary processes over the duration of each station, as well as the sufficient duration of the segment to allow for good enough particle count statistics for all measured particle sizes (0.1–47.5µm range). In the following, the minimum station duration is approximately 50 minutes. Further analysis could possibly double the number of eligible stations, especially at high winds where suitable count statistics can be obtained faster. The ASs are separated into two categories. A first type is the stationary aerosol station (SAS) corresponding to measurements made when the ship was stationary (black "∘" symbol in Fig. 3.4), with a speed under 3 knots. The second type – the mobile aerosol station (MAS) – includes segments during which measurements were acquired whilst the ship was on the move (dark grey "×" symbol in Fig. 3.4) at a speed above 3 knots, reaching up to 11 knots. This distinction is a precautionary measure relative to the marine aerosol measurements. Indeed, elevated ship speeds would sometimes lead to strong impacts of waves against the bow, ejecting large quantities of sea water into the air. Furthermore, the apparent wind speed resulting from the combined wind and the ship motion sometimes reached high values that could possibly alter the air flow rate in the CSASP probes, despite the isokinetic (flow regulating) nature of the probe inlets. The isokinetic nature of the probes is under investigation (cf. Appendix 5).

Instrumentation

The vessel is equiped with its own weather station which transmits meteorological data to Météo France. The two-dimensional wind field (u and v components) are measured at the foremast, and the main mast. In addition, the main mast boasts relative humidity and temperature measurements (cf. Fig. 2.7e) located approximately 28 meters above the mean water level. Four CSASP probes were positioned at the front of the ship (cf. Fig 2.7a). At the top of the foremast, both a CSASP-100-HV and a CSASP-200 probe were placed (cf. Fig 2.7c). This is our preferred location as the distortion of the ship on the air flow and possibly on sea spray are expected to be limited. This location is herein referred to as L1, and is the main focus of the following study. Another couple of probes made up of a CSASP-100-HV-ER and a CSASP-200 are positioned at the foot of the foremast, and is referred to as L2. Though the L2 probes are positioned above the bow, it is likely that the airflow is more perturbed there. The CSASP-100-HV, measuring particles up to radii 22.75 µm, is placed at the top of the mast where larger particles are scarce. The CSASP-100-HV-ER, extending to 47.5 µm particles, is placed in L2 where larger particles are expected to be more frequent. The L1 probes were raised approximately

50cm above the foremast platform to further reduce possible perturbations caused by a ship navigation light. Considering waterline measurements made at the beginning and the end of the campaign, the mean height above the foremast platform above the MWL during the campaign is estimated at 15.38 meters. Positioned above one another, L1 CSASP-100-HV and CSASP-200 inlets were therefore respectively 16 and 16.2 meters above the MWL. The L2 CSASP-100-HV-ER and CSASP-200 inlets were respectively positioned 8.95 and 9.15 meters above the MWL.

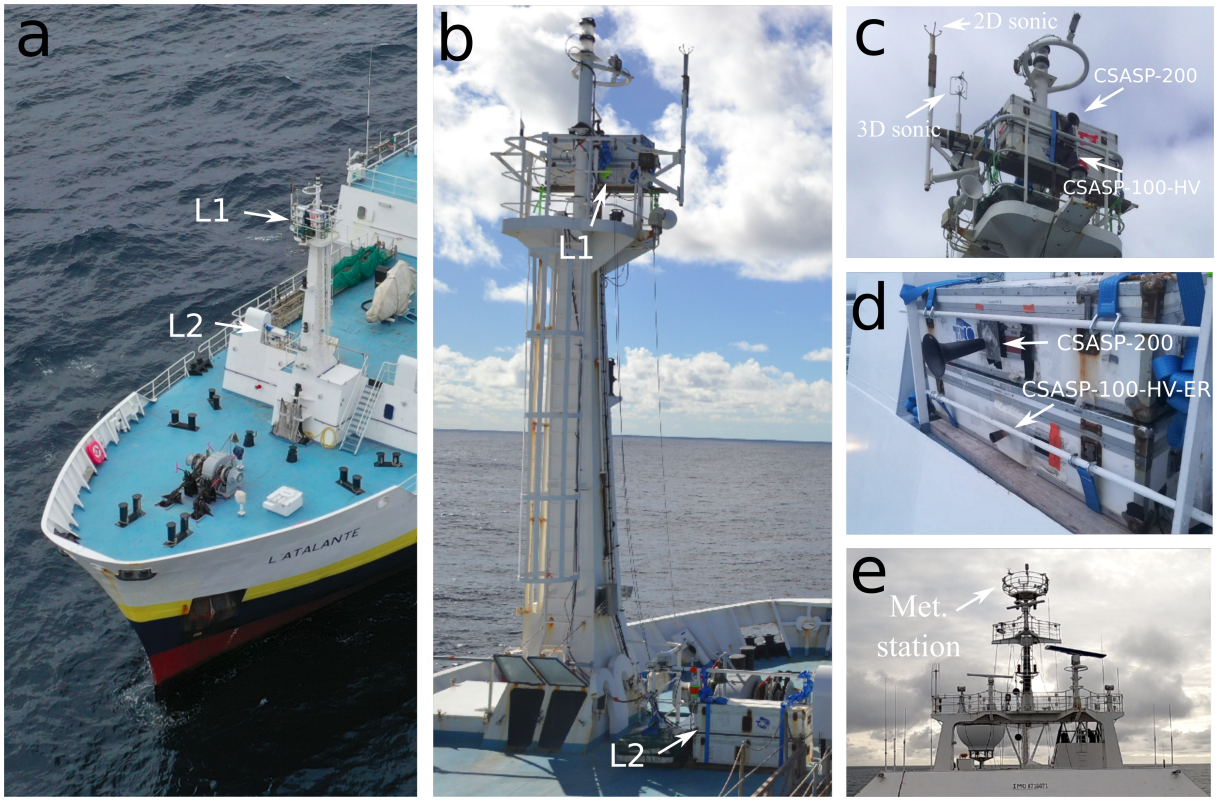

Figure 2.7: An aerial drone view of the (a) front (courtesy of Peter Sutherland – LOPS), and (b) back of R/V Atalante's foremast. Front-views are shown of two CSASP sensor couples in their protective cases at sample locations L1 (c) (courtesy of Emma Bent – LOPS) and L2 (d). (e) Photograph of the main mast surmounted by its meteorological station.

Environmental conditions

The true wind speed and direction at the main mast and foremast, calculated from the vessel course, apparent wind speed and direction, are shown in Fig. 2.8b. The air (solid yellow curve) and the water (blue solid curve) temperature are represented in Fig. 2.8c. Other than during the cold spell observed during the first two days of the campaign, air and water temperatures are similar with respective overall average temperatures of 11.53°C and 12.0°C. As a result of the small average air-sea temperature gradients observed during the SUMOS campaign, the air-sea heat fluxes are expected to be small, and

the atmosphere neutral. The relative humidity was measured continuously, though issues with the sensor resulted in missing data towards the end of the campaign. After removal of the bad data, the average RH over the entire campaign is 73% 28 meters above the MWL, and can be expected to be closer to 80% at L1 and L2. Another humidity sensor placed at the foot of the foremast near L2 was saturated very early and throughout the campaign. This is a reminder of how challenging humidity measurements can be at sea where air is humid and loaded with sea spray.

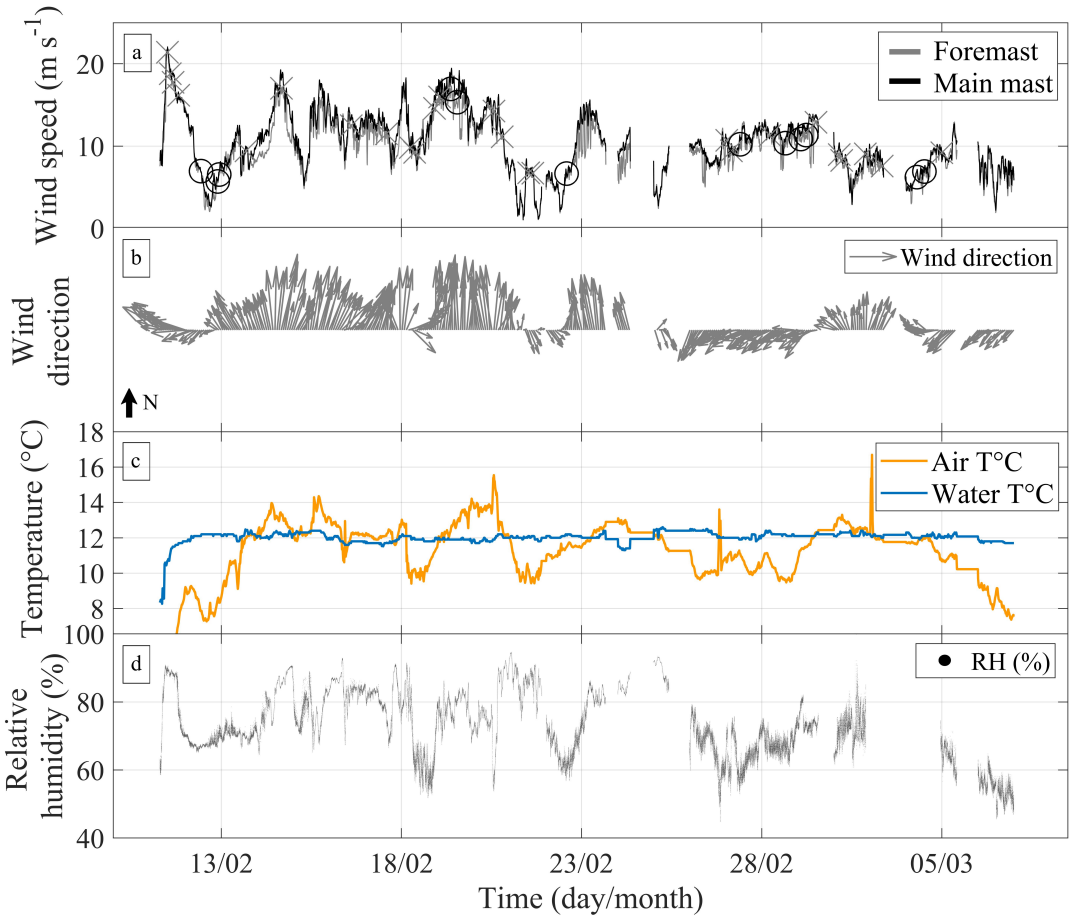

Figure 2.8: Data collected by the meteorological station onboard R/V Atalante. (a) the time-series of the true wind speed (m s^{-1}) measured at the main mast (black solid line) and the foremast (grey solid line). The average date of the MASs ("×" symbol) and SASs ("○" symbol) are also shown. (b) the true wind direction represented by grey arrows (up is North), the lengths of which are proportional to the wind speed. (a) and (b) represent wind data when the aerosol sampling sytems were operational. (c) shows the air (orange solid line) and water temperature (blue solid line), in degrees Celsius. (d) shows the relative humidity (%).

Winds were frequent during the campaign, with more than 9 days with winds greater than 10 m s^{-1} recorded at the foremast. These conditions accompanied with wave breaking were favourable for sea spray generation. Photographs taken in $U_{10} \approx 12$ m s^{-1} winds on 1st March 2021 show spume droplet ejection events from the breaking wave crests (cf. Fig. 2.9a) as well as haze (cf. Fig. 2.9b) most likely as a result of air-sea processes such

as sea spray generation in the MABL. This is in agreement with the 12 m s^{-1} threshold for significant spume droplet generation (Monahan et al. 1986; Andreas et al. 2010).

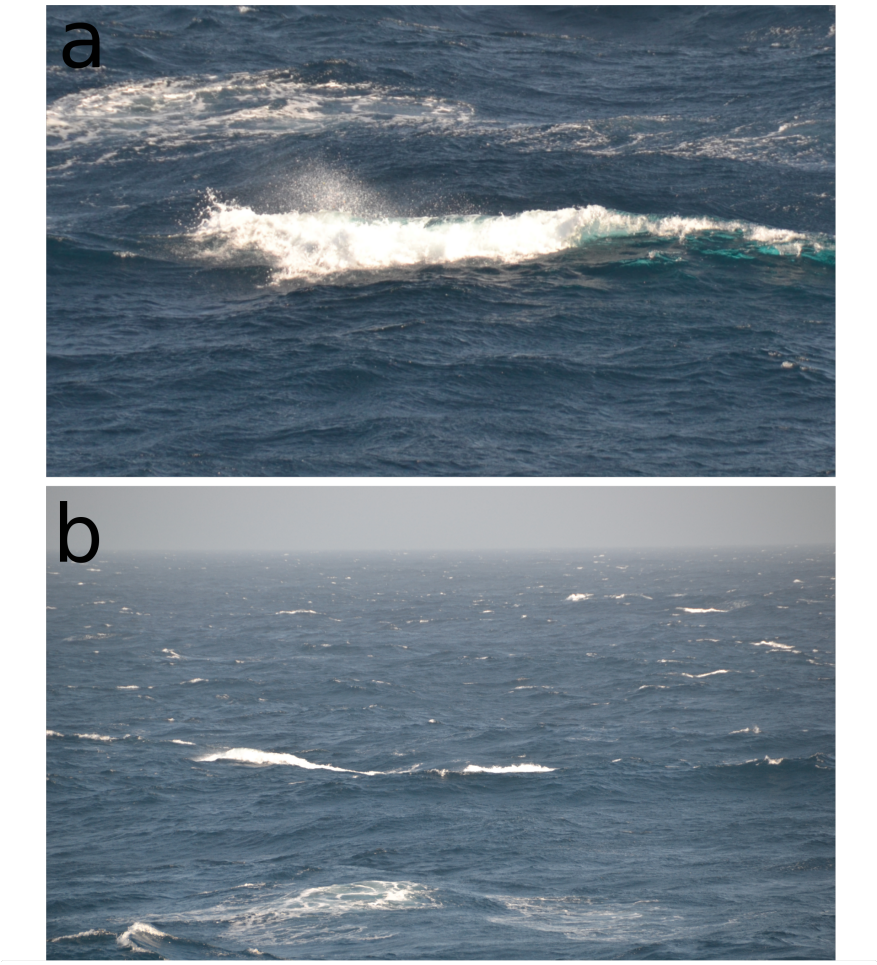

Figure 2.9: Photographs of sea surface taken aboard R/V Atalante on 1st March 2021 (at approximately 1330 UTC) in $U_{10} \approx 12$ m s^{-1} winds. (a) Close-up of a sea spray generation event as droplets are ejected from a breaking wave and (b) whitecaps and haze.

2.3.2 Marine Aerosols

Probe Intercalibration

The four CSASP probes were tested in the laboratory without wind prior to the field campaign. All probes were set to measure the same background noise, and were corrected using a coefficient to match concentrations of the L1 probes calibrated with latex particles of known sizes. Figure 2.10 shows the background noise measured by all probes after correction. Separate fitting functions show that, after correction, the probe couples in L1 and L2 perform well against each other with $R^2 = 0.99$ and $R^2 = 0.96$ respectively.

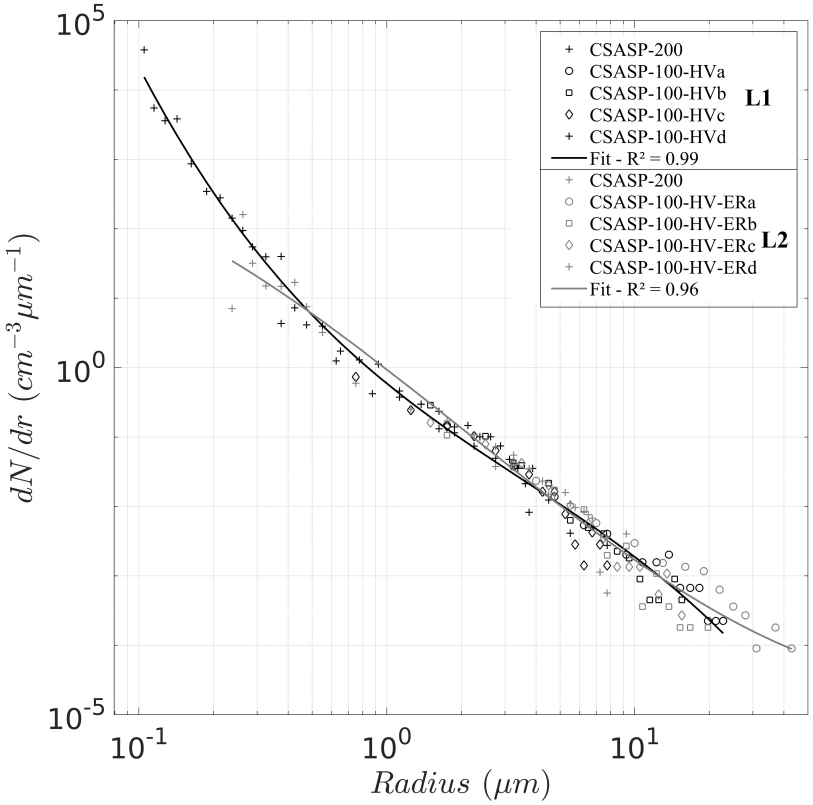

Figure 2.10: CSASP sensor intercalibration ahead of SUMOS field campaign. The black solid line is a functional fit to the L1 sensor distribution spectra. The grey solid line is a functional fit to the L2 sensor distribution spectra. The different symbols represent the single sample range of the CSASP-200 (+), and the four sample ranges of the CSASP-100-HV-ER and CSASP-100-HV probes.

First Results

Referring to the foremast wind speed timeseries presented in Fig. 2.8a, aerosol concentrations (cf. Fig 2.11) are found to evolve with wind speed. The highest concentrations are found at the highest wind speeds. Figure 2.11 shows this with the example of radii 1.87, 10.75 and 21.25 µm. This is an expected result found in a number of studies as wind is the main driver behind wave breaking and surface tearing processes in the open ocean (Smith et al. 1993; Monahan et al. 1986; Gong 2003). Figure 2.11a indicates that this relationship is not as clear for smaller droplets. This may result in the greater difference between aerosol concentration and generation for small particles with higher lifetimes. Figure 2.11 also presents the standard deviation (a moving standard deviation over a five-hour moving window) associated with the concentration measurements. This highlights a common problem with aerosol measurements, as the ratio between the mean and the standard deviation can sometimes be smaller than 1. The ratio between the mean concentration and the standard deviation is smallest for the larger droplets (cf. Fig. 2.11b and Fig. 2.11c), which is understandable as these droplets are relatively scarce and their presence is highly intermittent.

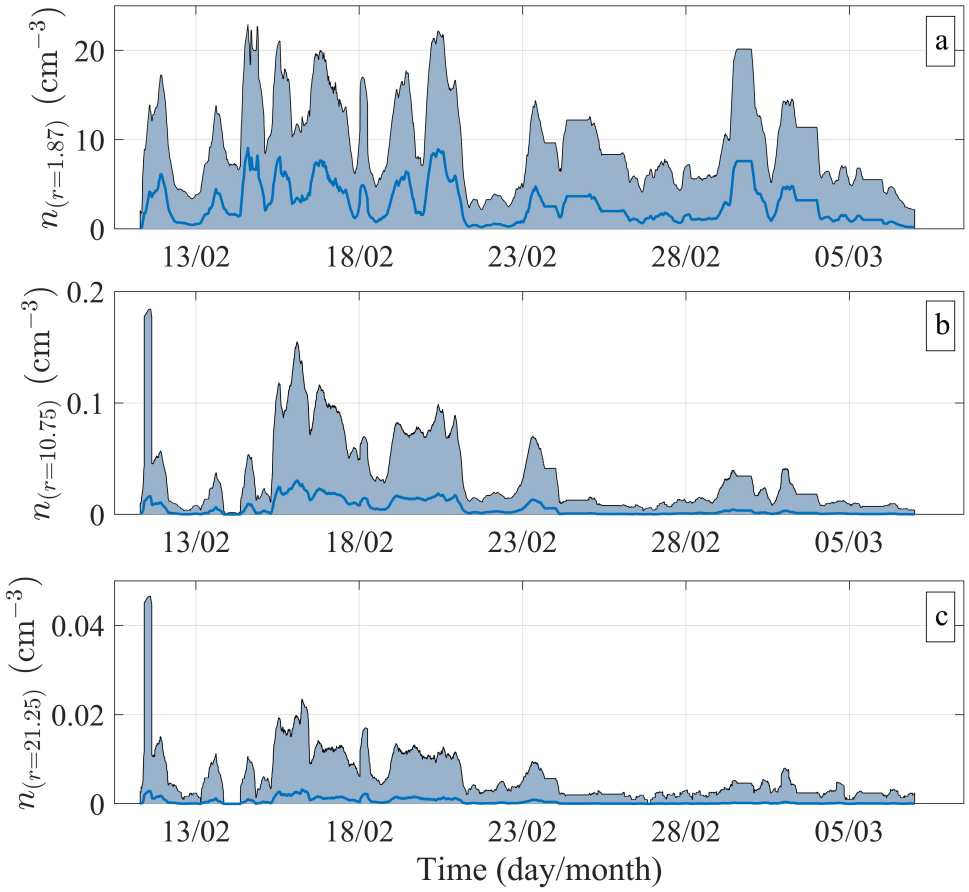

Figure 2.11: Moving averages (blue solid lines) and moving standard deviations (blue shading) of aerosol concentration measurements at radii 1.87 (a), 10.75 (b) and 21.25 (c) µm, computed over five-hour windows.

The importance of wind on sea spray generation is also highlighted in Fig. 2.12, where the averaged aerosol concentration spectra at two different stations are shown. As a general rule, concentrations increase over the study radius for increasing wind speed. We find that at U_{10}=6 m s^{-1}, concentrations rapidly decrease in the jet and spume droplet predominance range ($r \gtrsim 5\mu$m). At U_{10}=18 m s^{-1} however, concentrations are found to be higher over the entire size range, especially above 10µm radius, with the addition of a possible spume droplet mode extending the distribution to the maximum measurable droplet radius of 22.75 µm.

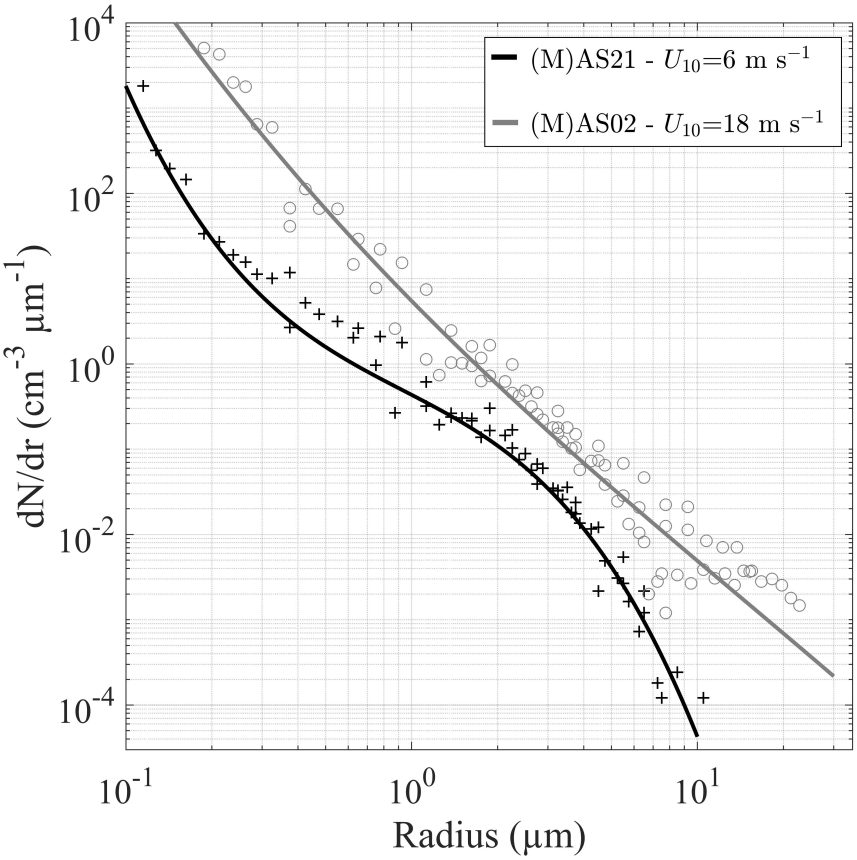

Figure 2.12: Aerosol distribution spectra showing number concentrations as a function of particle radius. Stations 2 (grey solid line and circles) and 22 (MASs, black solid line and plus signs) are represented, with respective U_{10} wind speeds of 6 and 18 m s^{-1}.

Figure 2.13 shows aerosol concentrations as a function of wind speed. The relationship is represented by a power law. This power law is found to be a better choice for particles equal or larger than 5µm (R^2 =0.57, cf. Fig. 2.13c). Below this radius, the relationship between wind speed and concentrations seems to become linear, but with generally poor fitting statistics resulting from high scatter in the relationship. This is expected as smaller particles travelling further than large particles are less correlated to the local generation conditions, such as the local wind speed and wave breaking conditions. Comparing the concentration measurements in Figs 2.13a and 2.13b we find that for a similar radii, the CSASP-200 system overestimates concentrations relative to the CSASP-100-HV system. Whilst the average deviation is of approximately a factor 2 for particles below 10 m s^{-1} wind speed, it increases to reach a factor 4 around 20 m s^{-1}. An interesting clue here are the averaged SAS and MAS values in both panels. Whilst SAS and MAS show similar trends from CSASP-100-HV data (cf. Fig. 2.13a), the MAS concentrations are significantly higher in the case of the CSASP-200 system (cf. Fig. 2.13b). The current hypothesis is that the significant apparent wind speed caused by the motion of the vessel and the incident wind speed is capable of affecting the flow rate in the CSASP-200 probes,

but not that of the CSASP-100-HV, as a result of different inlet shapes (cf. Appendix 5). The current approach to amend this is to correct the probe inflow as a function of the incident wind speed (and possible the wind orientation relative the probes). This has been investigated over the 0–15 m s^{-1} range available at the LASIF tunnel (Luminy, Marseille), but is currently difficult to investigate at higher winds. As a precautionary measure, the data collected by the CSASP-100-HV is used in priority for the remainder of the study.

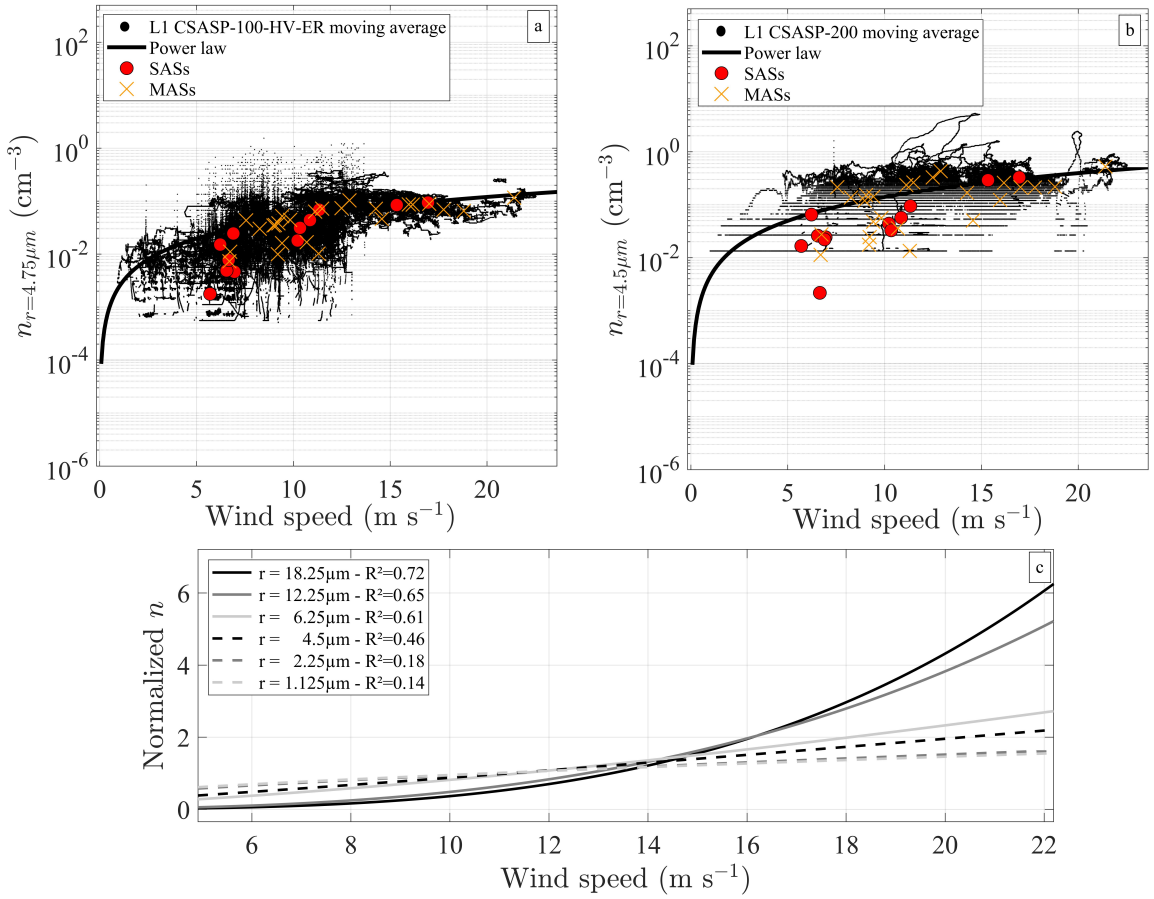

Figure 2.13: Moving average of the aerosol concentrations represented in log-scale measured by (a) the L1 CSASP-100-HV at 4.75µm radius and (b) the L1 CSASP-200 at 4.5µm radius, as a function of the foremast wind speed. The aerosol concentrations (1 Hz) and wind speed (1 Hz) moving averages are calculated with 360 second windows. Power laws are fitted to the data. Are also plotted the stationary aerosol stations (SASs) (red dots) and the mobile aerosol stations (MASs) (orange crosses). (c) shows power laws of the normalized number concentration n as a function of wind speed for the 38 campaign stations. The individual station values are not shown for clarity, but the R^2 values provide information on the strength of the power law fits. Normalizing n by the mean concentration per radius allows to compare the trends for the selected range of different radii.

2.4 The MATE2019 Laboratory Experiment

2.4.1 Introduction

In the field, sea spray generation measurements are very challenging (cf. Sect. 1.1.4). Also, a wide range of wind and wave combinations can be encountered. In an attempt to circumvent this problem, sea spray aerosol size concentrations were measured for a total of 20 wind and wave combinations as part of the Marine Aerosol Tunnel Experiment (MATE2019) from June to July 2019. To reproduce a similar range in environmental conditions, the laboratory experiments also included a unique range of wind and wave conditions, which, to the knowledge of the authors, is the most extensive range ever used for studying sea spray generation in a laboratory configuration. The aim is to develop a universal wind and sea state-dependent SSGF applicable for radii typical of jet and spume droplets.

2.4.2 Experimental Configuration

With the advantage of easier instrumentation and control over important environmental parameters compared to the complexity of the field, the laboratory has proven to be a valuable alternative to the field (open ocean) for the study of wave–wind boundary processes and sea spray generation (Toba and Koga 1986; Fairall et al. 2009; Ortiz-Suslow et al. 2016; Troitskaya et al. 2018). Therefore, we conducted a series of experiments in the wave–wind tunnel at the Observatoire Sciences de l'Univers (OSU) Pytheas Institute ocean–atmosphere laboratory in Luminy, France. The Pytheas Institute ocean–atmosphere interactions facility in Luminy (Marseille, France), schematically represented in Fig. 2.14, consists of a water tank associated with a recirculating wind tunnel on top of it. The facility currently allows the use of fresh water only. The water tank is 40 m long, 2.6 m wide, and has a wave-dissipating beach at the downwind end to avoid wave reflection. On the upwind end, the facility is equipped with a programmable submerged piston-like wave maker located at the bottom of a cavity below the air tunnel and controlled by an electrohydraulic motor. Wave properties such as amplitude, frequency, and slope can therefore be selected. Waves can attain amplitudes reaching approximately 15 cm. The air-channel ceiling is slightly inclined to the fetch to avoid airflow acceleration and the related longitudinal pressure gradient generated by the thickening of the wall and water surface boundary layers (Coantic et al. 1981). To reduce turbulence as the airflow encounters the water surface, a thin buoyant sheet is placed at the surface of the water at the entrance of the tunnel. The wind speed in the facility is adjustable, reaching approximately 15 m s^{-1}. Glass walls on either side of the laboratory make it possible to monitor the experiment at the location of the instruments (Fig. 2.14).

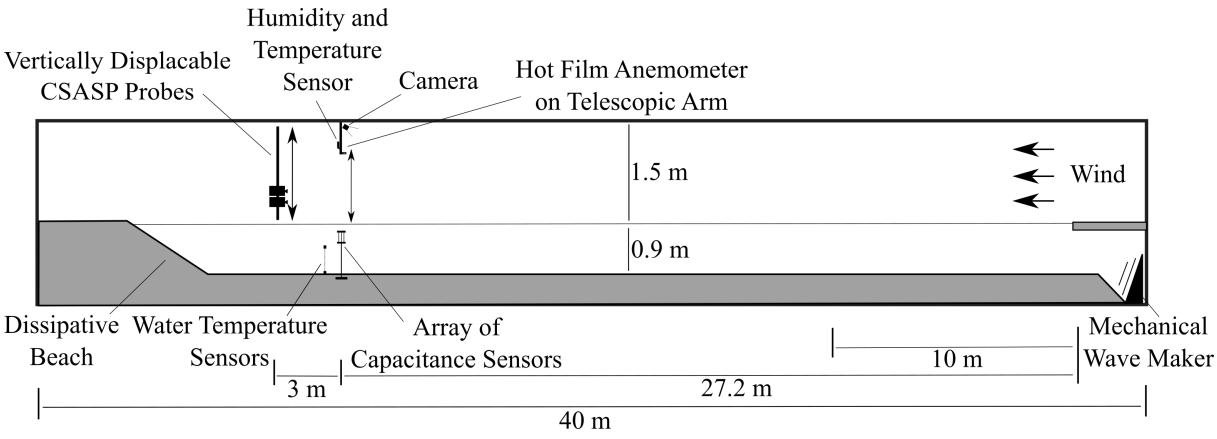

Figure 2.14: Side view of the experimental configuration in the laboratory

For the experiments in June–July 2019, the water depth was set to 90 cm, leaving 150 cm between the water surface and the ceiling of the wind tunnel. As schematically represented in Fig. 1, instruments used for the measurements of air, water, wind, and wave characteristics were placed at the 27.2 m fetch mark. A sensor positioned 81 cm above the mean water level (MWL) was used to measure air relative humidity (RH) and temperature (T_a). Vertical profiles of wind speed and air temperature between 15 and 66 cm above the MWL were obtained using sensors mounted on a telescopic arm. The water temperature was measured at both 20 and 60 cm depths beneath the MWL. A camera with 60 Hz sampling frequency placed on the tunnel ceiling allowed estimation of the whitecap coverage during the experiments from colour images. Though not schematically represented in Fig. 1, a higher-frequency 128 Hz camera was used to film through the glass wall of the tunnel for monitoring purposes only. Finally, at the 30 m fetch mark, vertical profiles of the sea spray number concentration were measured using two particle probes mounted onto a vertically displaceable frame.

2.4.3 Wave Generation and Characterization

The water surface elevation was measured by an array of two calibrated capacitance wave gauges placed at the 27.2 m fetch mark. The sample frequency for the wave gauges was 256 Hz allowing a wide range of wave surface elevation and slope frequency spectra to be sampled. The sensors were aligned orthogonally to the general wave direction, and were placed 1 cm from each other to ensure accurate wave-slope measurements.

Four types of waves were generated. Five different wind speeds in the range 8–20 m s^{-1} were applied over each wave type, for a total of 20 laboratory wind–wave configurations. The first type of wave was generated solely by the wind, resulting in pure wind waves. The other three types of waves were generated using the piston wave maker and are referred to as short wave forcing (peak frequency f_p = 1.3 Hz and wavelength λ = 0.92 m), intermediate wave forcing (f_p = 1.1 Hz and λ = 1.29 m), and long wave forcing (f_p = 0.8 Hz and λ = 2.4 m). These conditions were selected to ensure that near-equilibrium

with the overlying wind field was either never met, or met at different wind speeds. Deep water conditions are theoretically confirmed for all types of forcing except the long wave case. This is also the wave type that is least forced by the wind and can be considered representative of the wind over swell conditions that can be found in the field. Together, the 20 tunnel wind and wave combinations span a range of wave ages c_p/u_* between 1.3 and 9.6. Wind and wave characteristics are summarised in Table 3.1 (cf. Sect. 3.1.1).

The wave sensor array provides several parameters that are useful to relate the wave properties measured at the 27.2 m fetch mark to the sea spray concentrations measured at the 30 m fetch mark. The significant wave height H_S is determined using $H_s = 4\sigma_\eta$, where σ_η is the standard deviation of the surface elevation (η) time series measured by the wave sensor array.

The wave-slope variance $\langle S^2 \rangle$ is considered equal to the wave mean square slope. It is calculated from the time series of the wave-slope S, for wavelengths $\lambda > 2$ cm (strong majority of waves dominated by gravity). The use of classical Fourier analysis allows determination of the peak frequency f_p from the wave elevation energy spectra. Finally, the wave phase speed c_p is determined from the phase shift between the wave gauges as the waves propagated along the wave sensor array.

2.4.4 Whitecap Measurements

To quantify the wave breaking, the whitecap coverage $W(\%)$ is estimated from video colour images taken by a camera mounted at the tunnel ceiling (cf. Fig. 1). The system takes images at 60 Hz frequency with dimensions 2704 × 2028. These images are spatially referenced to allow estimating the approximate surface area of each pixel. To identify the whitecaps, a separation method is used that applies a greyscale conversion and a subsequent intensity threshold to the image. The surface areas of the pixels above threshold are then added and divided by the total image surface area for an estimate of the whitecap surface coverage $W(\%)$. Using a time series of images, it was found that $W(\%)$ estimates converge to an average value within approximately 120 frames. This method for whitecap estimation is commonly used (Lafon et al. 2007; Lenain and Melville 2017a; Brumer et al. 2017), and although the selection of the intensity threshold may be subjective, we expect that our whitecap coverage estimates capture the relative amount of wave breaking induced by various wind and wave conditions.

2.4.5 Wind Measurements

A hot film wind sensor (E+E Elektronik, Langwiesen, Austria) mounted onto a telescopic arm was used to measure vertical profiles of wind speed U at the 27.2 m fetch mark (cf. Fig. 2.14). This sensor was calibrated against a reference sonic anemometer on several occasions during the experiments. To ensure representative wind statistics, convergence of the wind speed time averages was achieved for each height z along the $U(z)$ profiles,

with averages spanning over 20 to 80 min in accordance with the sea spray aerosol sample durations (cf. Sect. 2.4.6). Some subsets of wind data obtained at 15 cm of the MWL were eliminated from the dataset to avoid erroneous measurements caused by large droplet impacts on the hot film sensor.

The wind speed reference used in this study is U_{10}, i.e. the wind speed at 10 m above MWL. Assuming a logarithmic wind profile and neutral conditions, Monin and Obukhov (1954) scaling allows evaluation of U_{10} and the friction velocity u_* from the measured $U(z)$ profile values with

$$U(z) = \frac{u_*}{k}\ln(\frac{z}{z_0}), \tag{2.1}$$

where $k = 0.4$ the von Kármán constant, z is the measurement height above MWL, and z_0 the roughness length. The latter is retrieved by extending the wind profile with data from the more elevated part of the wind profile that is not significantly affected by the wave field. During the experiments, z_0 estimates varied between 0.2 and 2.5 mm.

Figure 2.15 presents the experimental wind profiles for all 20 laboratory configurations (data points with horizontal error bars) as well as the corresponding theoretical profiles obtained with Eq. 2.1. For clarity and indicative purposes only, the average friction velocities $\bar{u_*}$ calculated over the four different wave types for each individual tested wind speed are also presented. The experimental profiles exhibit near-logarithmic behaviour, and the gradient increases for increasing reference wind speed U_{10}, in accordance with a fully developed turbulent layer near the water surface as encountered in the field. This is further evidenced by the wind–sea Reynolds number (R_B, first presented in Sect. 1.2.3) that was greater than 10^3 in the laboratory for reference wind speeds U_{10} of 12 m s^{-1} or more, thereby signifying that the airflow in the boundary layer is in a fully turbulent regime and wind–sea breaking occurs (Toba et al. 2006).

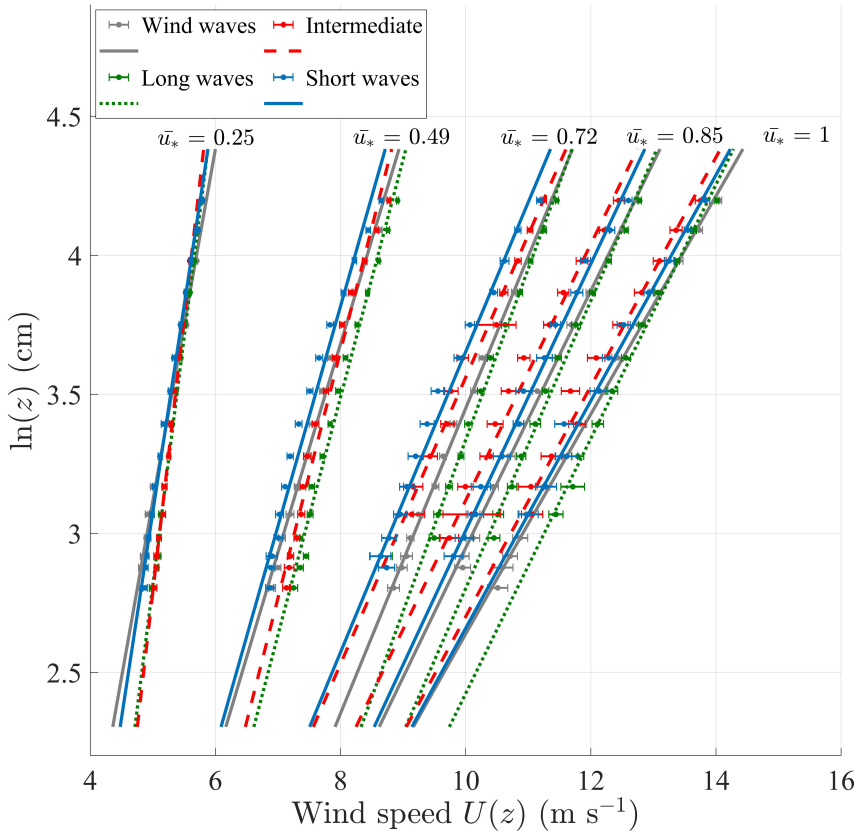

Figure 2.15: Measured $U(z)$ profiles for all 20 laboratory configurations (horizontal bars) with associated theoretical profiles (lines) calculated with Eq. 2.1. Average friction velocities $\bar{u}_*$ pertain to the five wind speeds set in the laboratory

2.4.6 Sea Spray Aerosol Measurements

The measurement of sea spray in the tunnel was carried out using two CSASP (Classical Scattering Aerosol Spectrometer) probes (Particle Measurement Systems, Boulder, Colorado, USA). This type of probe has been proven reliable in numerous experiments by the authors and others (Frick and Hoppel 2000; Savelyev et al. 2014; Petelski et al. 2014). Our two probes have overlapping particle radius ranges allowing for a combined range of 0.1 to 47.5 µm. Prior to the experiments, both probes were calibrated with latex particles of known sizes. The CSASP-100-HV-ER probe samples by rotating over four sets of 15 size bins, in total spanning from 0.5 to 47.5 µm radius. The CSASP-200 samples over a single set of 31 size bins ranging from 0.1 to 10 µm radius. The probes send data to the controller every second, and aerosol number concentrations for each bin size are obtained by averaging over a chosen sample (integration) time. Since number concentrations were expected to decrease with increasing height above the water surface, sample times varied from a minimum of 20 min at $z = 35$ cm to a maximum of 80 min at $z = 82$ cm in order to improve droplet count statistics. Nevertheless, particle concentrations for radii greater than 35 µm were statistically unreliable and had to be discarded. It was veri-

fied that droplet concentrations were stationary over the duration of the experiment once equilibrium for a particular laboratory configuration was established.

During the experiments, the probes were placed on top of each other. Droplet number concentrations were measured at five different heights for each of the 20 laboratory configurations. For the CSASP-100-HV-ER, samples were made at heights z = 35, 41, 51, 65, and 82 cm above the MWL. These heights are used as reference, and the CSASP-200 concentrations are interpolated to these heights. The airflow inside a long wind tunnel is not completely homogenous, and very slight transverse counter-rotating streamwise vortices or cells may appear (Holmes et al. 1996; Pope 2000), with a very weak divergence or convergence zone along the middle of the width of the tunnel. As it is usually done at the wind–wave facility, the probes were slightly shifted away from the centreline of the facility. For all laboratory configurations, both aerosol probes were temporarily positioned at the tunnel entrance to verify that no background aerosols entered or recirculated in the tunnel. The absence of background aerosols at the tunnel entrance for radii greater than 3 µm implies that all particles detected at the 30 m fetch mark are solely produced over the upwind 30 m fetch length. As a precautionary measure to ensure stationary laboratory conditions and to minimize any possible aerosol background from previous experiments, a waiting period of approximately 30 min was applied at the initialization stage of each tested laboratory condition.

After generation at the water surface, the hygroscopic aerosols adjust their size to the ambient humidity and temperature of the airflow. This process is different for salt water than for the fresh water used in the tunnel, as fresh water droplets can evaporate more quickly and completely than salt water droplets that reach an equilibrium size (Pruppacher and Klett 1978; Andreas 1989; Edson and Fairall 1994; van Eijk et al. 2001; Mueller and Veron 2014a; Mehta et al. 2019). During the experiments, the relative humidity (RH) in the laboratory varied between 79 and 82%, with an average water temperature at 0.2 m depth of 18°C, and an average air temperature T_a at 85 cm height of 25°C. We therefore assume that sea spray number concentrations correspond (roughly) to RH = 80%. Since the rate of fresh water droplet evaporation at RH = 80% is relatively small, we assume that our measured droplets are representative for salt water droplets at their RH = 80% equilibrium radii. However, this assuption fails if the fresh water droplets are relatively small or have long residence times before reaching the aerosol probes as evaporation can then become substantial (Veron 2015). To avoid such evaporation effects over the length of the wave–wind facility, only radii greater than 7 µm are considered for the proposed source functions (see Sect. 3.3) in accordance with Fairall et al. (2009). Thus, we may consider that the fresh water droplet distributions measured in the tunnel are analogous to salt water droplets at RH = 80%. Since the processes that generate the fresh water droplets in the tunnel are the same as for sea spray in the field, we denote the droplets in the tunnel as sea spray below.

Aerosol concentrations are often expressed as number concentrations dN/dr (cm^{-3}

μm^{-1}; the number of particles N of a given radius r measured per unit volume of air) or volume concentrations dV/dr (the volume for a given radius measured per unit air). We use mostly number concentrations, with a single exception (Sect. 3.2.1, Fig. 3.4). The conversion from number to volume concentrations (cm^{-3} cm^{-3} μm^{-1}) is made by assuming that the droplets are spherical:

$$\frac{dV}{dr} = \frac{dN}{dr}\frac{4}{3}\pi r^3. \tag{2.2}$$

2.5 Discussion and Conclusion

The measurement of aerosols is a challenge. CSASP-type sensors have proven reliable in numerous experiments (Frick and Hoppel 2000; Savelyev et al. 2014; Petelski et al. 2014), but are difficult to deploy in high winds due to their weight and size. At lower wind speeds, the near-absence of large spume droplets is a limiting factor for suitable count statistics. Furthermore, aerosol probe accuracy remains an issue, such as with the sometimes questionable assumption of constant flow at high to very high wind speeds, despite the use of isokinetic inlets. Most existing sensors rely on Mie scattering, theoretically applicable in the case of a homogenous sphere, which is not always true. Progress has been made over recent years for the measurement of micrometric to millimetric particles, such as with cloud imaging probes (Fairall et al. 2009; Lenain and Melville 2017a) adapted for deployment on airplanes, but such solutions remain costly. We consider that further metrological progress is urgent for a better representation of sea spray fluxes and concentrations in the field and in the laboratory.

We have presented the experimental configurations and preliminary results of the MIRAMER, SUMOS and MATE2019 campaigns. During each experiment, air-sea fluxes were expected to be low as a result of the low air-sea temperature gradients that are typical of these regions, resulting in stable or neutral atmospheric conditions. This signifies that measured concentrations and fluxes during all three campaigns result from generation and transport dynamics with negligible buoyancy-driven convection, and limited air-droplet thermodynamics. The ambient relative humidity at sensor height was close to 80% in almost all cases, which allows us to work with the assumption of an r_{80} radius in the following thesis. This database therefore offers a strong basis for the study of sea spray generation and transport processes without the complexity of additional thermodynamic processes. Good understanding of generation and transport in these conditions should help understand the role of sea spray in conditions of extreme wind speed and unstable atmospheric conditions, such as in tropical cyclones.

In the present thesis, focus is made on open conditions, with no assumed impacts of topography on wind, wave and resulting sea spray generation and transport. Over a decade of sea spray observations collected by the MIO from a land-based observatory on the island of Porquerolles, has served for previous studies (Piazzola et al. 2009; Laussac et al.

2018). Though not considered here, this database is promising for the study of coastal sea spray emissions which directly impact the atmosphere in often densely populated areas.

Chapter 3

Towards a Complete Sea Spray Function: Reconciliating Laboratory and Field Observations

Contents

Following the description of the laboratory experimental configuration (cf. Sect. 2.4), Chapter 3 presents MATE2019 results. The collection of wind, wave and sea spray

concentration measurements allows to distinguish two wind and wave-dependent non-dimensional numbers for the scaling of jet and spume droplet generation (cf. Sect. 3.2.2–3.2.5). Two sea spray generation functions are proposed, and comparison is made with existing laboratory and field-derived SSGFs. With the aim of completing the present study with smaller marine aerosols, we propose to combine laboratory SSGFs with a field-based wind and wave dependent SSGF (cf. Sect. 3.3). With the aim of parameterizing existing numerical models with laboratory SSGFs (cf. Chap. 4), methods to reconcile laboratory wind, wave and sea spray observations with the field are investigated (cf. Sect 3.4).

3.1 Laboratory Wave and Wind Results

3.1.1 Wave Measurements

Table 3.2 characterizes all 20 laboratory configurations in terms of the significant wave height H_s, the wave-slope variance $\langle S^2 \rangle$, the friction velocity u_*, and the whitecap coverage $W(\%)$. The table shows that the wind field forces the wave field, resulting in increased wave height, wave-slope variance, and breaking, as evidenced by H_s, $\langle S^2 \rangle$ and $W(\%)$. In some cases, however, the significant wave height and wave-slope decrease for high wind speeds as wave energy dissipation by wind-induced breaking becomes temporarily greater than the energy input from the wind to the waves (cf. Table 3.1). This is especially the case for the intermediate wave forcings for wind speeds increasing from 16 to 18 m s^{-1} where wave breaking was especially high. Further evidence of the forcing of the wave field by the wind is the decrease in f_p for increasing wind speed observed at the 27.2 m fetch mark, with the exception of the long wave forcing which conserves the 0.8 Hz frequency prescribed by the wave maker throughout the experiments. The momentum transfer from the wind to the waves is therefore relatively low for the long wave forcing in comparison to the other wave forcings, resulting in relatively low $U(z)$ gradients (Fig. 2.15) and whitecap coverages $W(\%)$ (Table 3.1).

This nonlinear behaviour of the parameters listed in Table 3.1 highlights the importance of correctly understanding the boundary processes, such as the state of wind–wave equilibrium. Though not shown here, f^{-5} and f^{-4} spectral shapes were identified for the individual wave spectra, but it proved difficult to quantify the wave–wind equilibrium this way. We therefore abide by the heuristic idea that when the phase speed c_p is greater than the overlying wind speed (e.g., the friction velocity u_*) then the underlying waves are no longer forced by the wind field. Thus we use the wave age defined as c_p/u_* to quantify the wind–wave equilibrium.

Our laboratory configurations yield wave age c_p/u_* values ranging from 1.3 to 9.6 where the higher values correspond to the long wave forcing combined with the lowest wind speed (8 m s^{-1}). These values are generally lower than those recorded in the field because of the comparatively much shorter fetch length in the laboratory.

Table 3.1: Wave–wind boundary characteristics for the different laboratory configurations: significant wave height H_s (cm), wave-slope variance $\langle S^2 \rangle$, friction velocity u_*, wave phase speed c_p, and whitecap coverage $W(\%)$

Forcing	$U_{10} = 8$ m s^{-1}					$U_{10} = 12$ m s^{-1}				
	H_s	$\langle S^2 \rangle$	u_*	c_p	$W(\%)$	H_s	$\langle S^2 \rangle$	u_*	c_p	$W(\%)$
Wind	3.2	0.026	0.32	0.78	0.13	5.5	0.039	0.54	0.99	0.29
Short	9.7	0.037	0.28	1.19	0.28	12.4	0.053	0.52	1.29	0.62
Intermediate	13.2	0.033	0.21	1.42	0.32	16.7	0.047	0.46	1.49	0.53
Long	12.0	0.024	0.23	2.2	0.16	13.8	0.03	0.48	1.7	0.25
	$U_{10} = 16$ m s^{-1}					$U_{10} = 18$ m s^{-1}				
Wind	8.3	0.056	0.75	1.1	0.8	9.63	0.062	0.89	1.25	1.25
Short	13.7	0.063	0.76	1.33	1.17	15.4	0.066	0.85	1.54	1.45
Intermediate	20.1	0.087	0.8	1.50	2.55	18.4	0.08	0.89	1.59	4.65
Long	16.5	0.046	0.66	2.1	0.73	19.6	0.055	0.79	2.14	0.84
	$U_{10} = 20$ m s^{-1}									
Wind	11.3	0.073	1.05	1.32	2.0					
Short	15.2	0.072	1.01	1.63	2.25					
Intermediate	17.6	0.078	1.0	1.57	3.19					
Long	21.6	0.065	0.9	2.15	1.19					

3.1.2 Whitecap Measurements

As previously noted, several studies have related whitecapping to the generation of film, jet, and spume droplets. For comparison, it is therefore important to ascertain whether the whitecap production in the laboratory differs from the field. To this end, we use data collected during the EMMA (Etat de Mer et Modélisation d'Aérosols) campaign which took place in Toulon-Hyeres bay, yielding wave, wind, and whitecap coverage data for wind speeds in the 10–18 m s^{-1} range and wave ages c_p/u_* in the 14–28 range (Lafon et al. 2007). We compare our laboratory whitecap coverage to that measured in fetch-limited field conditions during the EMMA campaign using a similar image-processing technique with intensity threshold separation. Laboratory data obtained at 8 m s^{-1} wind speed are not included in this comparison because the relatively small amount of wave breaking may reduce the accuracy of the whitecap coverage estimates.

Multiple independent scaling studies have proven R_B to be a successful scaling tool for $W(\%)$ (Zhao and Toba 2001). However, the evaluation of R_B requires the wave peak frequency ω_p, which differs significantly between the laboratory and the field. The relatively short fetch in the laboratory and the wave maker settings lead to shorter wavelengths and a relatively greater number of wave crests per unit area (Mueller and Veron 2009). To allow for better comparison between the laboratory and the field, the $W(\%)$ values are therefore normalized by the wave peak frequency. Figure 3.1a shows the relationship between the normalized $W(\%)$ and R_B. The data trends from both the laboratory (+) and the field (▼) seem similar by yielding nearly identical slopes when fitted by a power law, though be acknowlegde that R^2 values are relatively low. In absolute magnitude there is a factor 1.5 difference between the laboratory and the field with the lower $W(\%)$

values for the laboratory. A possible explanation is the absence of surfactants and salt in the laboratory, which in the field contribute to whitecap formation and increase whitecap lifetime (Callaghan et al. 2012). Consequently, the lower rate of whitecap formation and lifetime in the laboratory may signify that our whitecap coverage is more representative for the process of active wave breaking, which we refer to as the wave breaking coverage.

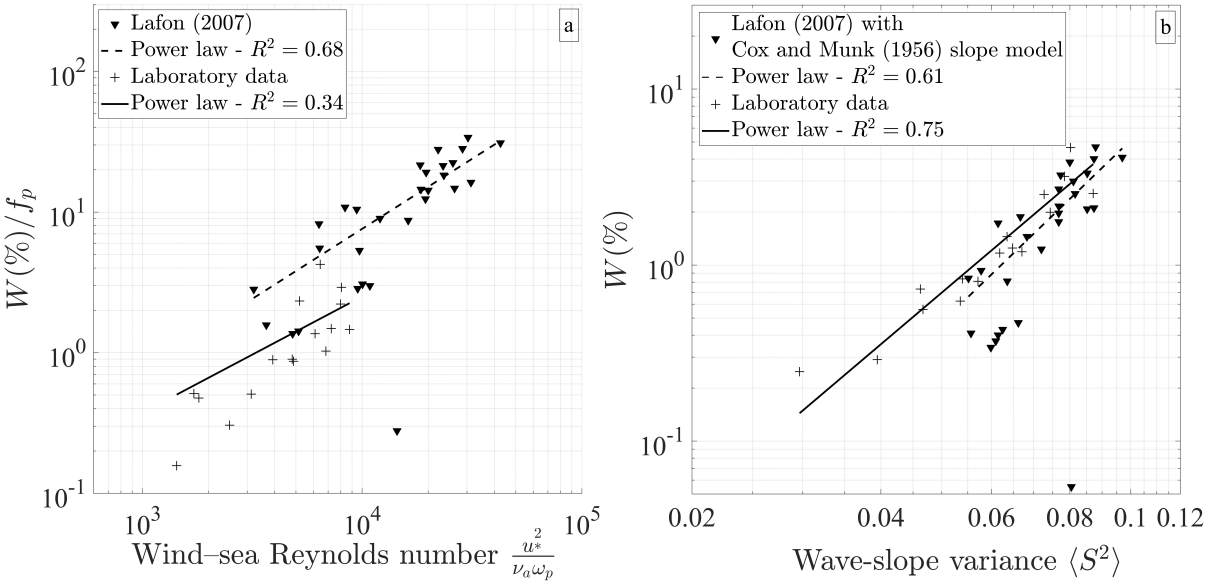

Figure 3.1: Comparison between laboratory and field data (Lafon et al. 2007) (a) f_p-normalized whitecap coverage $W(\%)$ estimates as function of the wind–sea Reynolds number R_B, and (b) $W(\%)$ as a function of the wave-slope variance $\langle S^2 \rangle$. Lines and corresponding R^2 statistics represent power laws fitted to the data

A further comparison between the laboratory and the field is obtained by scaling $W(\%)$ to the wave-slope variance $\langle S^2 \rangle$. In this case, $W(\%)$ does not need to be normalized by the peak frequency as the wave-slope variance $\langle S^2 \rangle$ integrates a very large part of the wave frequency spectrum and corresponding wave-slopes, unlike the peak wave characteristics required for wind–sea Reynolds number R_B. For the EMMA campaign data (Lafon et al. 2007), $\langle S^2 \rangle$ is estimated from the measured wind speed data (Cox and Munk 1956) as

$$\langle S^2 \rangle = 0.003 + 5.12 \times 10^{-3} U_{12.5} \pm 0.004, \tag{3.1}$$

where the wind speed $U_{12.5}$ is calculated from the EMMA campaign U_{10} measurements using classical Monin and Obukhov (1954) theory. It is worth noting that Eq. 3.1 (Cox and Munk 1956) was determined from airborne observations of sun glitter resulting in the contribution of a wide range of wave scales including non-breaking waves, which is to some extent comparable to the wide range of wavelengths included in the laboratory wave-slope variance.

Figure 3.1b presents the $W(\%)$ scaling by $\langle S^2 \rangle$, demonstrating that laboratory (+) and field (▼) data almost overlap. The laboratory data is well fitted ($R^2 = 0.75$) by the

power law

$$W(\%) = 6.02 \times 10^3 \langle S^2 \rangle^{3.025}. \tag{3.2}$$

The good fit of this power law to field data (Fig. 3.1b) suggests that Eq. 3.2 may have a validity range extending to both the laboratory and the field. The strong correlation between $\langle S^2 \rangle$ and $W(\%)$ suggests that the wide range of the wave-slope spectrum inherent to $\langle S^2 \rangle$ allows separation of breakers and non-breakers. This corroborates conclusions from a north-Pacific field campaign (Schwendeman and Thomson 2015), where the wave-slope variance amongst the different existing slope parametrizations is found to scale best with $W(\%)$ by considering the slopes of the shorter waves, thought to be important for whitecap production. In contrast, the scaling of whitecap coverage with wave steepness (often written as $H/(2\lambda)$) has proven difficult (Schwendeman and Thomson 2015) or even unsuccessful (Holthuijsen and Herbers 1986).

3.2 Laboratory Sea Spray Results

3.2.1 Spray Aerosol Size Distribution Spectra

Figure 3.2 presents two typical size distributions as measured in the laboratory, and the figure shows the sea spray distributions for wind speeds $U_{10} = 16$ m s^{-1} and $U_{10} = 20$ m s^{-1}, measured 55 cm above MWL and during the intermediate wave forcing. For convenience, polynomial functions (solid and dashed lines for 16 and 20 m s^{-1}, respectively) have been fitted to the distributions. The polynomial functions show that the number concentration of all but the smallest particles increases with increasing wind speed. This behaviour is observable at any height above MWL and for all four types of wave forcing. The concentration increase is consistent with the increased $W(\%)$ for increasing wind speeds (cf. Table 3.1) and hence the enhanced droplet generation. Furthermore, the size distribution shows a relative abundance of particles with sizes around 1 and 10 µm. This corroborates the established size ranges of film and jet droplets, respectively. The droplet spectra for larger radii change markedly at wind speeds lower than 12 m s^{-1}, where number concentrations for $r > 15$ µm are negligible. This corroborates the assumption that these larger droplets are predominantly spume droplets, and that their generation mechanism activates at wind speeds around 12 m s^{-1}. This was confirmed by our high-speed video footage, which revealed surface tearing and bag break-up only for wind speeds higher than 12 m s^{-1}. In conclusion, the above observations suggest that similar droplet generation mechanisms are active in the laboratory and in the field.

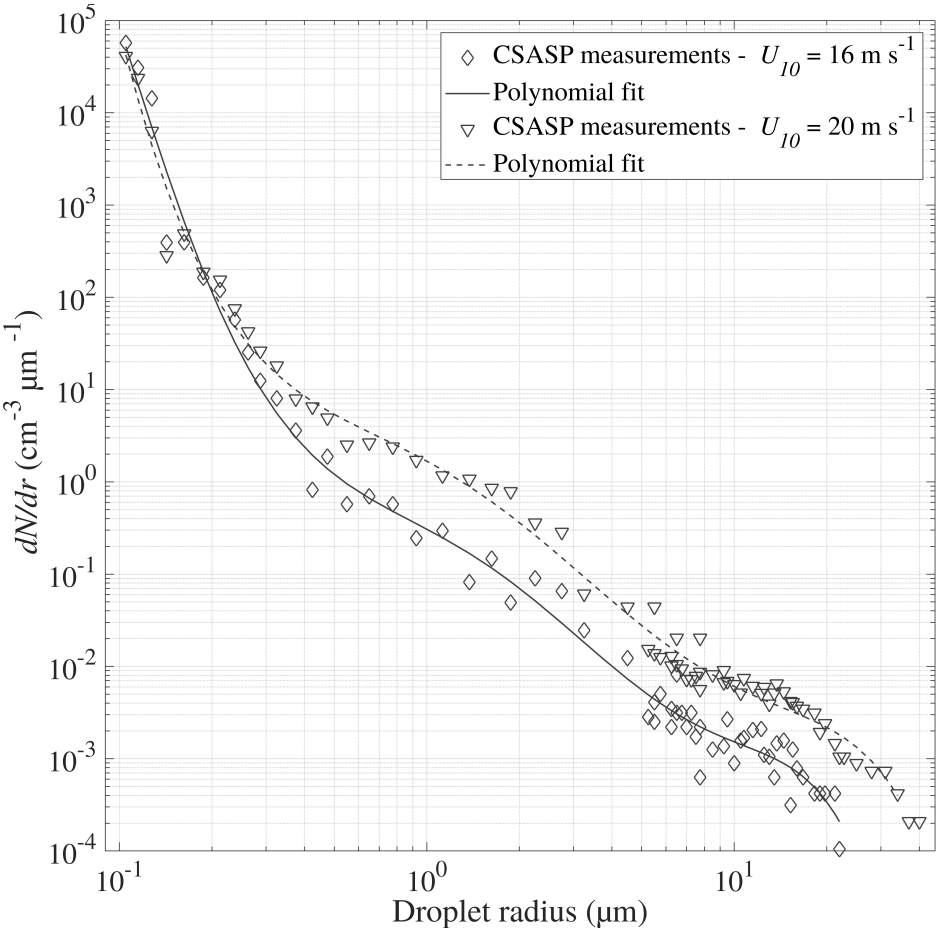

Figure 3.2: Sea spray number concentration size distribution at 55 cm above the MWL for the intermediate wave forcing

Let us now consider the vertical distribution of the freshly generated particles. Figure 3.3 shows number concentration profiles obtained at U_{10} = 20 m s^{-1} as a linear function of the natural logarithm of height $\ln(z)$. Two sets of profiles are shown, for droplets of 10 and 20 µm radius, and each set contains data for the four different types of wave forcing. The symbols of individual data points refer to the type of wave forcing. The lines denote linear functions fitted to the experimental data. Figure 3.3 suggests that the vertical number concentration profiles of sea spray are near-logarithmic with height above MWL. This behaviour is general for all radii in the 7–35 µm range. Though not shown here, R^2 values of the individual fits all exceed 0.95 for the three highest tested wind speeds. Though not presented in Fig. 3.3 for clarity, the standard deviation in number concentrations is highest closest to the water surface, especially for intermediate and short wave forcing, but remains very small with a maximum value approaching 10^{-5} cm^{-3} µm^{-1} at z = 0.35 m. As the environmental conditions were stationary during the measurements for each individual laboratory configuration, this greater variability (standard deviation) in near-surface concentrations could be associated with wave-induced and phase-locked modulation of the airflow, which can lead to flow separation. These mechanisms have recently been observed in microphysical laboratory experiments (Buckley and

Veron 2019; Richter et al. 2019; Husain et al. 2019). Whether this modulation effect also caused stronger fluctuations in the near-surface sea spray concentrations in the laboratory remains hypothetical as the maximum sample frequency of the particle probes does not allow resolution of these fluctuations assumed to occur at frequencies approaching f_p or higher.

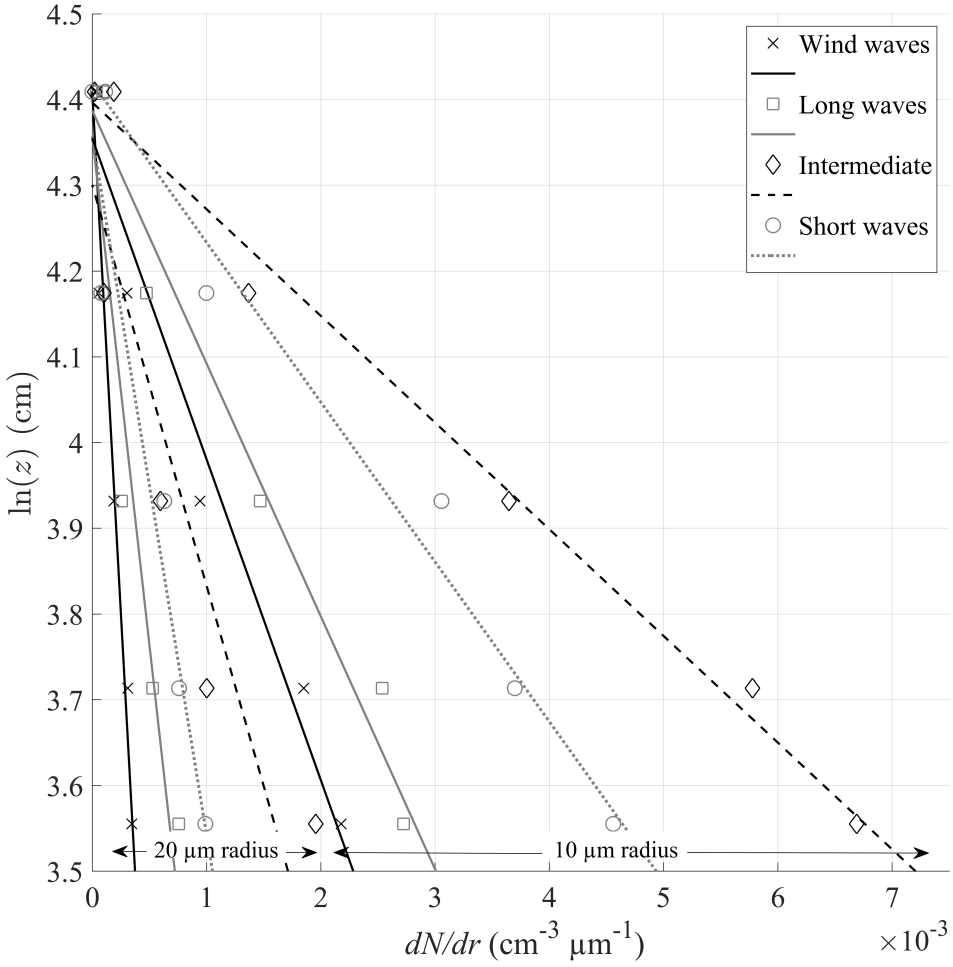

Figure 3.3: Sea spray number concentration profiles at 20 m s^{-1} wind speeds as a function of height, represented as $\ln(z)$. Symbols denote experimental data, lines linear fits to the data

Figure 3.3 also demonstrates that the type of forcing affects the vertical concentration gradients. The stronger gradients are observed for intermediate and short wave forcings, whereas the forcing by wind alone results in a less pronounced concentration decrease with height. To further investigate the effect of sea state, Fig. 3.4 focuses on the aerosol size distributions over the 6–47.5 µm radius range obtained at $z = 35$ cm, and for wind speed $U_{10} = 20$ m s^{-1}. Individual datapoints represent an average over several particle bin sizes (spanning $\pm$ 4 µm) for clarity, and horizontal and vertical error bars illustrate the standard deviations in average size and concentration, respectively. The data is presented on a log-log scale, and individual datapoints are connected by lines to provide an indication of the volume spectrum. As identified by the legend in Fig. 3.4, we present data for the four types of wave forcings using in the laboratory.

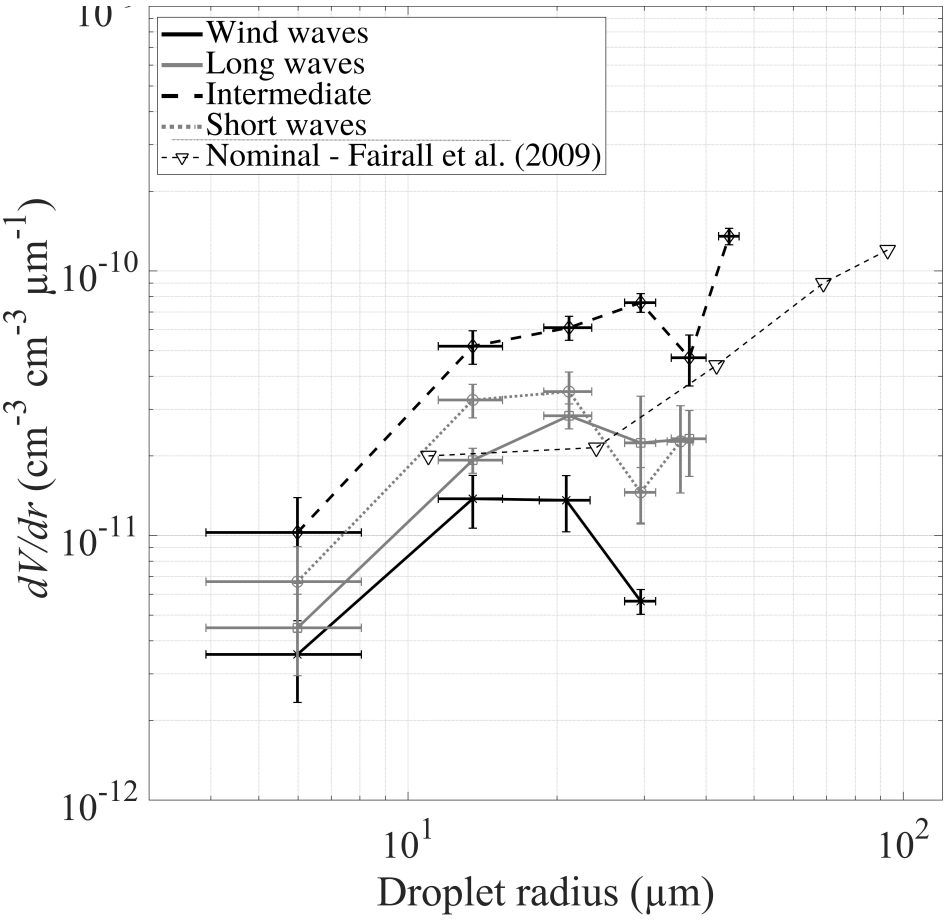

Figure 3.4: Sea spray volume concentrations for $U_{10} = 20$ m s^{-1} at 35 cm above the MWL, for the four forcings used in the laboratory. The Fairall et al. (2009) SPANDEX data measured at 31.5 cm above MWL corresponding to their nominal condition is presented for comparison

Figure 3.4 depicts volume rather than number concentrations. Comparison with Fig. 3.2 reveals that while large droplets are less numerous, they represent the larger part of the volume (or mass). Presenting the data as volume concentrations allows us to better detail the differences between the four types of wave forcing. Visual comparison of the four curves reveals that wind forcing alone results in the lowest concentrations (solid black line) and a distribution that strongly decreases for $r > 20$ µm. The three wave maker forcings all result in higher volume concentrations than with the wind forcing: the increasingly high concentrations found for the long, the short, and the intermediate condition correspond well with the increase in whitecap $W(\%)$ and wave-slope variance $\langle S^2 \rangle$ for these three types of forcing (cf. Table 3.1), and hence, the production of droplets.

A literature survey for comparable laboratory data identified the Fairall et al. (2009) SPANDEX (Spray Production and Dynamics Experiment) dataset as the most suitable. These authors also used a wind–wave interaction tunnel with fresh water and a mechanical wave paddle for the wave forcings. The triangles in Fig. 3.4 (connected by the thin dashed line) represent the volume concentrations reported by Fairall et al. (2009), obtained at 31.5 cm height for 16.7 m s^{-1} wind speed (corresponding to their nominal forcing) measured at

40 cm above MWL (roughly equivalent to 28 m s^{-1} at U_{10}), a 1.36 Hz peak wave frequency (same as our short wave forcing), and friction velocity $u_* = 1.44$ m s^{-1}. Though the wind speed and friction velocity were 50% greater than for the present study, the SPANDEX volume concentrations are of the same order of magnitude as our wave-forced data (cf. Fig. 3.4). This unexpected overlap may be explained by experimental differences such as tunnel dimensions (more than three times the height between the water surface and the tunnel ceiling compared with SPANDEX) leading to possibly different boundary effects. Another explanation may also be related to the different wave amplitudes between both experiments ($\approx$ five times greater in the present study) resulting in shorter distances between the probes and the wave crests in the case of MATE2019 despite comparable sample heights in the present comparison.

3.2.2 Scaling Parameters for Surface Sea Spray Generation

In the previous section we have demonstrated that the sea spray concentration depends on properties of both the airflow and the sea state. To bridge these two domains, we scale the sea spray surface generation using non-dimensional numbers representing the physical processes on the wind and wave side of the wave–wind boundary. The non-dimensional numbers are determined from the set of parameters (u_*, ω_p, c_p, H, λ, X, g, ρ_a, ρ_w, ν_a, ν_w, Γ), where X is the fetch length, g the acceleration due to gravity, ρ_a and ρ_w are air and water densities, respectively, ν_w is the water kinematic viscosity, and Γ is the water surface tension. Here, the air kinematic viscosity ν_a is constant and equal to 1.55×10^{-5} m^2 s^{-1}, approximately equal to the air viscosity at the mean laboratory air temperature during MATE2019, which was 25°C.

As a first step, we focus our attention on the air kinematic viscosity. Several studies have indicated that water droplets and water vapor can alter the air viscosity, but the effect on the momentum flux is thought to be small at less than 3% (Fairall et al. 2009). We therefore consider the non-dimensional groups ν_a/ν_w and ρ_a/ρ_w to be constants. We also expect the surface tension Γ to be constant and remain negligible due to the relatively long wavelengths considered here (strong majority of gravity waves). Then, we can express the sea spray aerosol generation flux as a function of the non-dimensional numbers that are the inverse wave age ($= u_*/c_p$), the wind–sea Reynolds number R_B (determined from both wind (u_*^2) and peak wave (ω_p) characteristics), and the wave steepness. In line with the discussion following Eq. 3.2, the wave-slope variance $\langle S^2 \rangle$ is used instead of the wave steepness ($H/2\lambda$). The inverse wave age is preferred to the wave age for physical coherence, as the former is expected to increase for increasing R_B and $\langle S^2 \rangle$. We create a fourth scaling parameter by combining the inverse wave age, the wind–sea Reynolds number and the wave-slope variance by

$$P_S = R_B \langle S^2 \rangle (\tfrac{c_p}{u_*})^{-1},$$

which, considering the deep water dispersion relation $c_p = gT/2\pi$ (T the wave period),

reduces to

$$P_S = \frac{u_*^3}{\nu_a g}\langle S^2 \rangle, \tag{3.3}$$

where P_S describes the wave-slope variance-modulated wind energy input to the waves. This number combines two experimental quantities, $\langle S^2 \rangle$ provided by the wave sensor array, and u_*^3 provided by the wind speed vertical profiles, providing information on the wind-dependent sea state and wind-induced dissipation, respectively. Here, P_S is a modification to the P threshold for the activation of droplet and bubble formation at the water surface (Newell and Zakharov 1992; Fairall et al. 2009). This allows the investigation of air–sea interaction processes from a multiscale point-of-view, assuming that the smaller and larger scale wind and wave components significantly contribute to boundary-layer mechanisms responsible for sea spray generation.

3.2.3 Scaling of the Sea Spray Generation

This section discusses the scaling of the sea spray by the four scaling parameters introduced above. For this, we use the concentrations measured 35 cm above the MWL (i.e., the lowest height of our aerosol samplers) since concentrations can be assumed representative of the generation flux if measured near the water surface (Wu 1993; Andreas 1998). The scaling relationships are presented for droplet radii of 7.5 µm (Fig. 3.5) and 25 µm (Fig. 3.6), which are considered representative of the behaviour of the droplets in the 7–20 µm and the 20–35 µm size range, respectively. In this manner, we provide separate scaling for the sea spray predominantly produced by bubble bursting (7–20 µm) and surface-tearing (20–35 µm) mechanisms.

Figures 3.5a and 3.6a report the scaling with wave age. The presented data correspond to the wind–wave (blue dots), long wave (pink dots), intermediate wave (red dots) and short wave (green dots) forcing at 16, 18, and 20 m s^{-1} U_{10} wind speeds. Data of the same type of forcing are fitted to a linear function, denoted by a dashed line of the same colour. The black solid line represents a linear fit to all 12 datapoints, and the R^2 value of the fit is given in the graphs ($R^2 = 0.13$ for scaling with wave age for particles of 7.5 µm). Although the wave age seems to correctly scale concentrations for individual wave forcings, no clear relationship is found between the measured concentrations and wave age when all data is included. Therefore, we conclude that wave age is not well suited for the scaling of sea spray generation for both young wind-forced waves, and older swell-type waves.

Nevertheless, it is interesting to further discuss Figs. 3.5a and 3.6a. The overall decrease in near-surface concentrations for increasing wave age for each individual color corresponding to individual wave types (Figs. 3.5a and 3.6a) corroborates observations made in the field, as less whitecap is produced by older swell-type waves or wind waves modulated by older waves in contrast to wind waves alone (Schwendeman and Thomson

2015; Brumer et al. 2017). Both figures show that relatively high sea spray concentrations are found for the intermediate and short forcings, with corresponding wave age values of approximately 1.7. This can be expected considering the high values of $W(\%)$ and $\langle S^2 \rangle$ for these types of forcing (cf. Table 3.1). High droplet concentrations associated with young, steep, and strongly breaking waves are typical of fetch-limited wave fields (Lafon et al. 2007). Specifically, for the larger 25 µm particles (cf. Fig. 3.6a) such a peak can be related to droplet ejection microphysics as younger steeper waves induce airflow separation (Reul et al. 2008), which is thought to play an important role in droplet ejection from the wave crests (Mueller and Veron 2009; Veron et al. 2012; Richter et al. 2019).

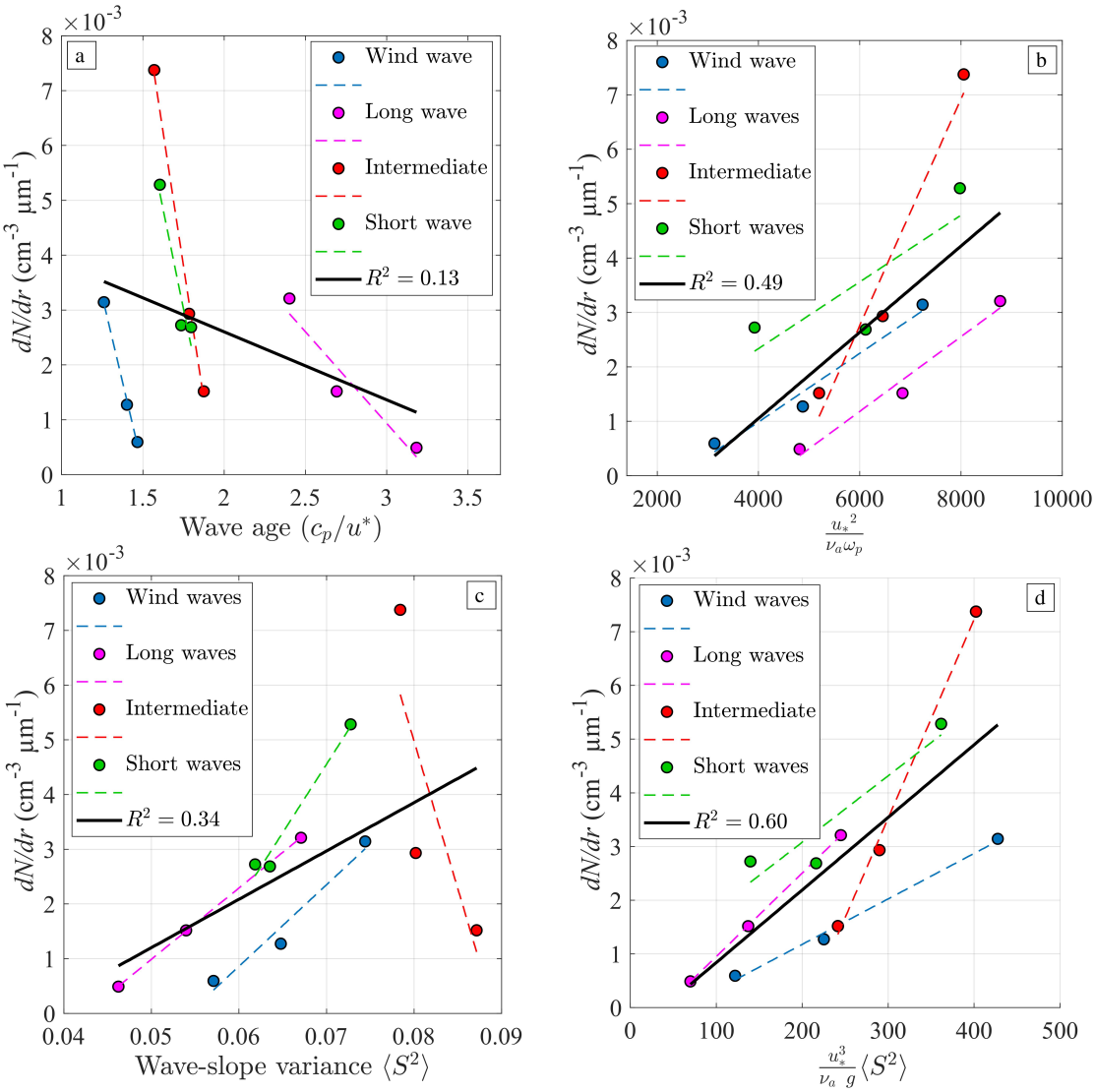

Figure 3.5: Scaling of dN/dr with (a) wave age, (b) R_B, (c) $\langle S^2 \rangle$ and (d) $P_S = \langle S^2 \rangle u_*^3 / \nu_a g$ for particles of radius 7.5 µm, 35 cm above MWL. Individual types of wave forcing are represented in colour, with U_{10} wind speeds ranging from 16 to 20 m s^{-1}. Solid black lines in all panels represent linear fits to all 12 datapoints

We now turn our attention to Figs. 3.5b and 3.6b, which present the wind–sea Reynolds number R_B as a scaling parameter for the sea spray concentration. The Reynolds

number has proven to be strongly related to whitecap coverage and wave breaking (cf. Sect. 3.1.2) as well as sea spray concentrations for wind waves especially (Iida et al. 1992; Toba et al. 2006; Troitskaya et al. 2018). This seems confirmed by the overall (solid black line) trend line in Figs. 3.5b and 3.6b, which is relatively close to the data corresponding to wind waves. The data show less spread than for scaling with wave age, and most types of forcing follow the overall trend, despite systematic differences in droplet concentrations. The overall fit quality for the 7.5 µm particles amounts to $R^2 = 0.49$ and similar values were noted for other radii in the 7–20 µm range. The wind–sea Reynolds number R_B does not perform as well over the 20–35 µm radius range, as demonstrated by $R^2 = 0.31$ for the 25 µm particles (Fig. 3.6b). The better performance for smaller radii can be explained by the information on turbulence intensity at the wind–wave boundary layer contained in R_B. We expect this to be key for the smaller droplets that are more subject to turbulent diffusion and less affected by gravitational settling than the larger spume droplets (Andreas et al. 2010).

The scaling of spray concentrations by the wave-slope variance $\langle S^2 \rangle$ is presented in Figs. 3.5c and 3.6c. The most striking feature of these figures is the behaviour for the intermediate wave forcing, which yields decreasing aerosol concentrations with $\langle S^2 \rangle$, whereas the other types of forcing all yield increasing concentrations. This behaviour can be traced back to the earlier observation (Sect. 3.1.1) that the intermediate forcing yields a decrease in significant wave height with increasing $\langle S^2 \rangle$ (and a less clear increase of $W(\%)$, which was attributed to (exceptionally) efficient wave energy dissipation compared with the other three types of forcing. This contrasting behaviour for the intermediate forcing causes the overall fit quality for smaller particles to be less than when scaling with R_B (R^2 of 0.34 versus 0.49). Over the 20–35 µm range however, the wave-slope variance offers the best scaling performance for all four scaling parameters ($R^2 = 0.55$). The wave-slope variance thus appears well adapted for the scaling of near-surface spume droplet concentrations (Fig. 3.6c).

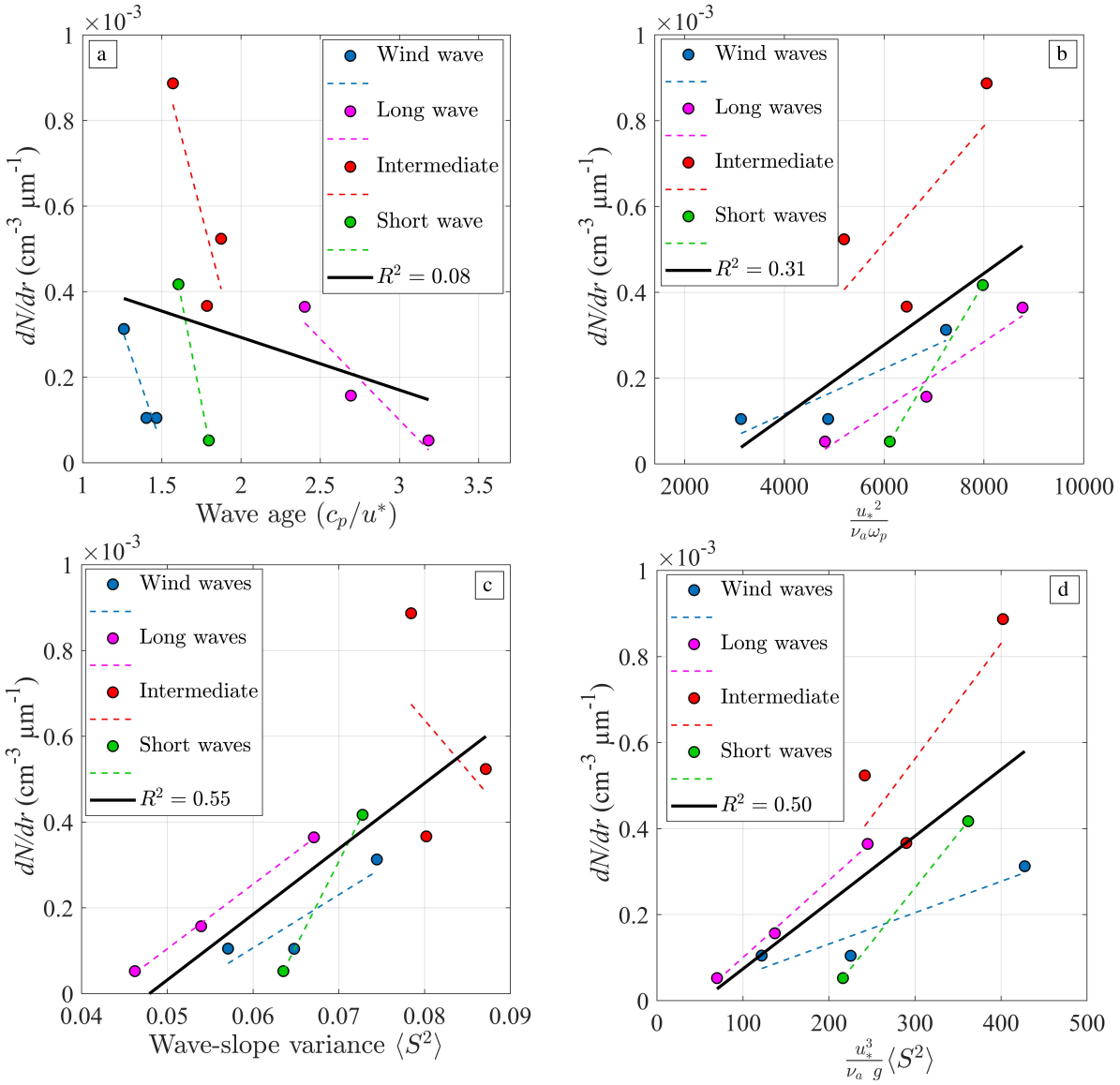

Figure 3.6: Scaling of dN/dr with (a) wave age, (b) R_B, (c) $\langle S^2 \rangle$ and (d) $P_S = \langle S^2 \rangle u_*^3/\nu_a g$ for particles of radius 25 µm, 35 cm above MWL. Individual wave forcings are denoted by colours, for U_{10} wind speeds ranging from 16 to 20 m s^{-1}. Solid black lines in all panels represent linear fits to all 12 datapoints

Finally, we scale near-surface concentrations as a function of the combination of non-dimensional numbers $P_S = \langle S^2 \rangle u_*^3/\nu_a g$. Results show that the combined number P_S scales the particle concentrations better than either the wave age or the wind–sea Reynolds number. In comparison with the wave-slope variance the combined number performance is improved over the 7–20 µm range ($R^2 = 0.60$ versus $R^2 = 0.34$ for $r = 7.5$ µm), but about equal for particles greater than 20 µm ($R^2 = 0.5$ versus $R^2 = 0.55$ for $r = 25$ µm). However, the combined number results in similar trends for all four types of wave forcing, including the intermediate forcing (compare panels c and d). This suggests that the combined number is capable of scaling sea spray generation for a wider range of environmental conditions than $\langle S^2 \rangle$ alone. We therefore conclude that the combined

number is well suited for the simultaneous scaling of breaking wave (bubble bursting) and surface tearing mechanisms.

3.2.4 Combined Scaling Parameters

Our fourth scaling parameter is similar to the non-dimensional numbers suggested by Brumer et al. (2017) and Lenain and Melville (2017a). The latter authors combine the wave steepness, the wave age, and a Reynolds number depending on the significant wave height H_s ($R_H = H_s u_*/\nu$). A similar number was also used by Brumer et al. (2017) for the scaling of whitecap coverage. Preliminary laboratory studies on the scaling of sea spray concentrations in the 7–35 μm radius range by the number proposed by Lenain and Melville (2017a) suggest that the scaling does not significantly change when substituting R_H with R_B. However, significantly better scaling is achieved when the wave steepness ($H/2\lambda$) is replaced with $\langle S^2 \rangle$.

As mentioned in the introduction, the parameter u_*^3 has proven to be a worthy candidate to scale wave energy dissipation and input from the wind field necessary for bubble and droplet production (Newell and Zakharov 1992; Andreas 1998, 2002; Zhao and Toba 2001; Zhao et al. 2006; Fairall et al. 2009). Though not detailed in the present scaling analysis, a preliminary study allowed the evaluation of the scaling performance of u_*^3 for near-surface concentrations. Results reveal a similar performance to the combined number with good scaling results over the 7–20 μm range ($R^2 = 0.56$ for $r = 7.5$ μm) with less satisfactory performance for larger droplets ($R^2 = 0.23$ for $r = 25$ μm). Associating scaling performances of u_*^3 (best for $r < 20$ μm) with $\langle S^2 \rangle$ (best for $r > 20$ μm) in the combined number (Eq. 3.3) allows good scaling of sea spray aerosol generation over the 7–35 μm range, suggesting that the combination of both allows to the scaling of production in a wider range of conditions than $\langle S^2 \rangle$ alone.

3.2.5 The Laboratory Generation Flux

In this section, we consider a suitable scaling parameter for the spray generation flux (dF/dr), and we derive this flux from the sea spray concentration profiles measured in the laboratory (cf. Fig. 3.3), at each resolved particle size. We only use the data obtained for the higher wind speeds (16, 18, and 20 m s^{-1}), but we include all four types of wave forcing. As a first step we approach the vertical concentration profiles with a function depending on the natural logarithm of measurement height (cf. Fig. 3.3),

$$N^r(z) = N_*^r \ln(z) + C^r, \tag{3.4}$$

where r denotes the dependence on the droplet radius, and the aerosol concentration at the surface N_*^r (m^{-3}) is determined by extrapolating the measured aerosol concentration profiles to the MWL. The sea spray flux dF/dr (m^{-2} s^{-1}) is subsequently obtained by

multiplication with the friction velocity u_*,

$$\frac{dF}{dr} = N_*^r u_*. \tag{3.5}$$

We evaluate N_*^r for each radius (bin) greater than 7 µm measured by our aerosol probes. This method is commonly used for the estimation of the sea spray flux in the field (Petelski et al. 2014), as well as for the results of large-eddy simulations (Richter et al. 2019). However, the use of a logarithmic function to describe the concentration gradient is debated, and other authors have prefered a power law (Fairall et al. 2009; Ortiz-Suslow et al. 2016). Rather than entering this debate, we abide by the adequate fit of logarithmic functions to our data (cf. Fig. 3.3). We note that concentrations profiles were measured in the log-layer, and the flux describes that of r_{80} particles.

As discussed in the previous section, both the wave-slope variance and the combined number are good candidates to scale droplet generation. The combined number is found suitable over the entire study radius range, and the wave-slope variance for spume droplets. Thus, Fig. 3.7 shows the size-dependent sea spray generation flux dF/dr (evaluated using Eq. 3.5) as a function of both the combined number (panel a) and the wave-slope variance (panel b), for various representative droplet radii between 8.5 and 30 µm. Individual data for a specific radius were fitted to a power law presented as lines in Fig. 3.7. As expected, the figure demonstrates that the combined number and the wave-slope variance are also good scaling parameters for the generation flux. In accordance with the positive slopes in Figs. 3.5 and 3.6 (panels c and d), increasing values of combined number or wave-slope variance lead to a stronger flux. Although it is difficult to conclude visually from Fig. 3.7, a comparison of panels a and b reveals the better scaling performance of the combined number for smaller radii, as reflected in the quality of the fit for the particles of 8.5 µm. Finally, an interesting feature in Fig. 3.7a–b is the sea spray size dependence of the relationship between the scaling flux and the scaling parameter. The flux rate of increase with increasing scaling parameter values is lowest for the larger droplets, and seems to converge towards a maximum in the jet droplet range as the curves become almost parallel for $r < 15$ µm. This suggests uneven radius-dependent flux strength variations over the sea spray spectrum according to the forcing.

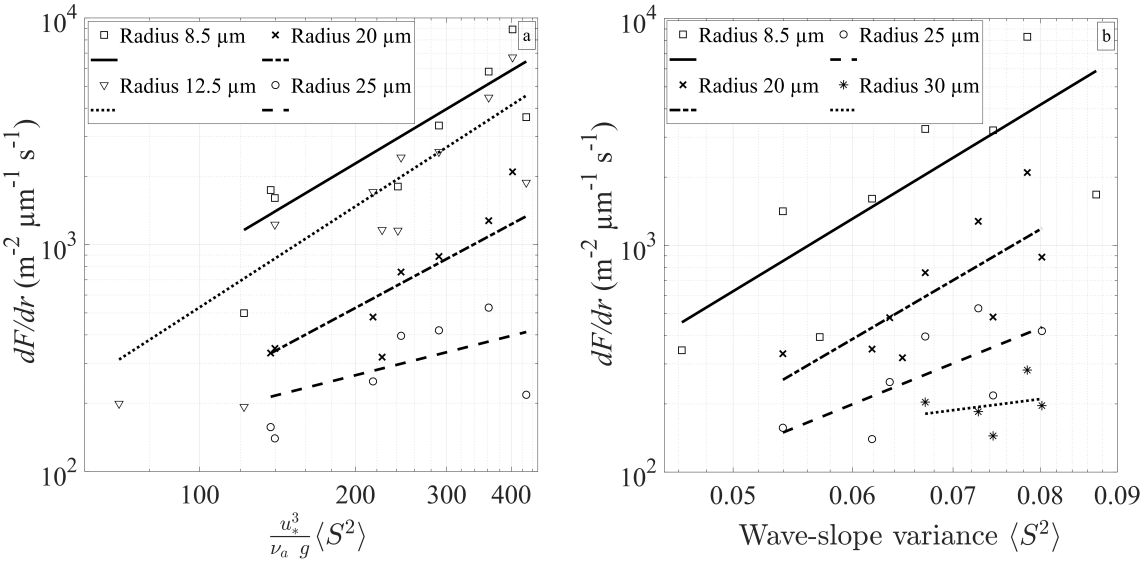

Figure 3.7: The laboratory dF/dr sea spray flux as a function of (a) the combined number $P_S = \langle S^2\rangle u_*^3/\nu_a g$ and (b) the wave-slope variance $\langle S^2\rangle$. Lines denote power law fits to data for individual radii

3.2.6 Cross-Study Comparison

This section presents a comparison of our generation flux to others reported in the literature. Since most existing fluxes rely on data acquired in the field, we must ascertain that our laboratory data can be compared to the field data. Comparing air–sea interaction processes and resulting sea spray generation in laboratory conditions to the field data is not a straightforward task due to the greater complexity of the natural environment. It is important that physical mechanisms at play in the laboratory, as well as the resulting sea spray generation fluxes, be similar to those observed in the field. The former question has already been discussed regarding the wind flow (Sect. 2.4.5), the wave field (Sect. 3.1.1), and the whitecap coverage (Sect. 3.1.2), which are all found to follow the same physics as in the field. As for the sea spray concentrations, Sect. 3.2.1 demonstrates the expected behaviour with increasing concentrations for increasing wind speed, a dependence on wave-state, as well as a near-logarithmic concentration profile later used to calculate the laboratory generation fluxes (Eqs. 3.4 and 3.5).

The above reasoning leads us to compare our laboratory sea spray generation flux to four (field and laboratory) flux formulations published in the literature. For this comparison, we have evaluated our generation flux for the laboratory pure wind forcing for 18 probe size bins over the 5–30 µm radius range, with friction velocity $u_* = 1.05$ m s^{-1} and wind speed $U_{10} = 20$ m s^{-1} (cf. Table 3.1). The flux is depicted in Fig. 3.8 as the black solid line. The triangles denote the radii for which the dF/dr was evaluated, to which a polynomial function is fitted to facilitate comparison with the other generation spectra. Figure 3.8 also represents fluxes from the literature: Smith et al. (1993) denoted by S93

and the grey solid line, Andreas (1998) denoted by A98 and the dotted line, Laussac et al. (2018) denoted by L18 and the dashed line, and Fairall et al. (2009) denoted by F09 and the grey dashed line. The latter flux was obtained from laboratory data, the other three from field data. The Andreas (1998) and Smith et al. (1993) flux models solely depend on wind speed U_{10} and are evaluated here for $U_{10} = 20$ m s^{-1}. The F09 flux is estimated for $u_* = 1.35$ m s^{-1}, and is only valid for $r \geq 24$ µm. Finally, L18 flux strength depends on the whitecap coverage, in turn defined in terms of the wave age, and has a 0.5–20 µm radius validity range. For comparison between L18 and the laboratory generation flux (wave age equal to 1.25), we select data corresponding to the Infrared Sea Surface Radiation Measurements (MIRAMER) campaign sample location at 12-km fetch (Demoisson et al. 2013; Laussac et al. 2018) used for the configuration of the L18 SSGF (Laussac et al. 2018). At this sample location, the wave age ($c_p/u_* = 3.9$) is estimated with a fetch-dependent formulation (Hasselmann et al. 1973; Donelan et al. 1985) well-adapted to the north-west Mediterranean (Lafon et al. 2004). The L18 generation flux is calculated using a wave-age-dependent whitecap formulation (Lafon et al. 2007; Laussac et al. 2018).

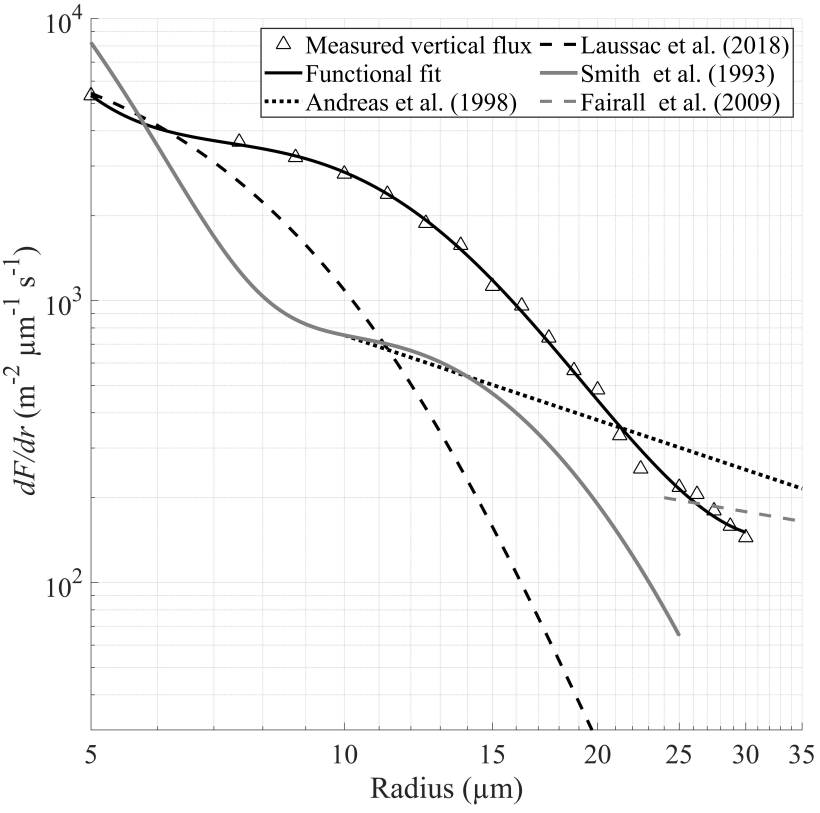

Figure 3.8: Vertical sea spray production fluxes at $U_{10} = 20$ m s^{-1}

Figure 3.8 shows that the various flux estimates have a spread of an order of magnitude. While this may seem significant, the spread is quite typical (Andreas 1998; Lewis et al. 2004; Veron 2015). Our flux function has the same strength as S93, A98, and L18

for particles of 5 μm, but suggests a stronger flux than these other functions as radius increases. Specifically, our flux curve includes a shoulder (or peak) around 10–15 μm, also seen in S93, which we attribute to a peak in jet droplet production. A similar shoulder is observed in the aerosol size distributions measured at 55 cm height above the surface (cf. Fig. 3.2). Moving forward to radii in excess of 15 μm, the typical domain of spume droplets, the strength of L18 and S93 generation functions decrease rapidly. In both cases, larger droplet concentrations are thought to have been underestimated as a result of the notable sample heights above the mean water level, resulting in low particle diffusion to sample locations and poor count statistics for spume droplets. In the case of L18, the experiment was hampered by the near-absence of high wind speed events, relatively short sample durations, and the suspected partial obstruction by a nearby ship navigation light of a probe dedicated to larger droplet sampling. Poor count statistics in the larger size bins often lead to the exclusion of these droplets from the analysis as was done here for droplets with $r > 35$ μm. The reformulation of S93 in A98 by Andreas (1998) represents an attempt to correct the generation flux for these larger spume droplets, and Fig. 3.8 shows the A98 droplet fluxes for this size range are more comparable to our measurements. For the larger radii ($r > 25$ μm), our flux function yields an equal strength to F09. Because the sizes of these larger particles are close to the maximum operating range of our probes, it is difficult to conclude, but both our flux curve and F09 seem to indicate that the decrease in strength reduces with radius. This may point to the presence of another shoulder around 30 μm, suggesting a possible peak in spume droplet generation.

3.3 Formulation of the New Sea Spray Generation Functions

The previous sections demonstrate that the laboratory generation flux depends on both wind and wave characteristics, with different responses for individual radii. The dependence on radius is traditionally accounted for by parametrizing the SSGF with one or more modes centred around modal radii (Monahan et al. 1986; Demoisson et al. 2013; Ovadnevaite et al. 2014; Laussac et al. 2018). These modes can be represented with normal, log-normal, or other distributions that are commonly used to reproduce measured aerosol distribution characteristics. Modes are often associated with specific aerosol processes, such as the generation of jet or spume droplets. We adopt this methodology by introducing two modes at 7 and 25 μm radius, which we consider representative for jet and spume droplets, respectively. The choice of these centre radii was inspired by the shapes of the flux and concentration curves shown in Figs. 3.2 and 3.8, respectively. Since Fig. 3.2 clearly shows that droplets smaller than 7 μm are abundant in the tunnel, we postulate a third mode centred around 2.5 μm on the basis of the shape of the aerosol distributions. To obtain a flux strength for droplets smaller than 7 μm (that were excluded from our analysis), we suggest L18. At this time, we limit the use of L18 to the 3–7 μm range. A smooth transition between the field-determined L18 and the laboratory data is attained by seeking a best fit between L18 flux distributions over the 3–7 μm range, and the labo-

ratory flux distributions. The 7 µm radius marks the transition between both fluxes (cf. Fig. 3.9). To achieve this combination of flux functions, the whitecap coverage used in L18 (originally calculated from the wave age) (Laussac et al. 2018) is recalculated here as a function of the scaling parameters (cf. Sect. 3.2.2). In the following, the L18 $W(\%)$ is estimated from $\langle S^2 \rangle$ using Eq. 3.2.

Section 3.2.3 reveals that the flux can be successfully scaled by a combined number P_S, but that the wave-slope $\langle S^2 \rangle$ also yields acceptable results, especially for larger particles. Therefore, we formulate two SSGFs in terms of three normally distributed modes, valid for droplets between 3–35 µm radius and wind speeds U_{10} ranging from 12–20 m s^{-1} as

$$\frac{dF_X}{dr_{80}} = \sum_{i=1}^{n} \frac{F_i(X)\tau^{-1}}{\sigma_i\sqrt{2\pi}} \exp(-\frac{1}{2}(\frac{r_{80}-\mu_i}{\sigma_i})^2), \tag{3.6}$$

where X is the scaling parameter (P_S or $\langle S^2 \rangle$), r_{80} is the particle radius at $RH = 80\%$, dF_X/dr_{80} is the size-dependent SSGF determined from environmental parameters contained in $F_i(X)$, and τ is the whitecap decay rate; μ_i and σ_i are the mean radius and standard deviation of each of the three modes, respectively. The SSGFs can be given in terms of r_{80}, because the underlying laboratory data were obtained for 80% humidity (cf. the discussion in Sect. 2.4.6). In formulating the SSGFs, we find the best results are obtained using normal modes, whereas other authors have preferred log-normal modes (Ovadnevaite et al. 2014). Possibly, this signals that normal modes are more suitable for the larger droplets studied here. Numerical values for Eq. 3.6 are specified in Table 3.2, which shows that flux amplitudes are expressed as power laws of $\langle S^2 \rangle$ and P_S, as suggested with the apparent power-law behaviour between scaling parameters and fluxes presented in Fig. 3.7. In addition, the whitecap decay rate is given a value of 3.53 s (Monahan et al. 1986). Though not discussed at length here, we add that research on the whitecap decay is scarce and further study for the consideration of this decay rate as a tuning parameter for sea spray generation would be interesting. With our focus on the 16–20 m s^{-1} range in our analysis, we are confident that both SSGFs are valid over the 12–20 m s^{-1} range as a result of the strong relationship between the parameters $\langle S^2 \rangle$ and P_S and the physical mechanisms known to drive production (Sects. 2.4.5 and 3.1.2) at these wind speeds.

Table 3.2: Parameters for the two SSGFs

i	σ_i	μ_i	$F_i(\frac{u*^3}{\nu_a g}\langle S^2 \rangle)$	$F_i(\langle S^2 \rangle)$
1	2.1	2.5	$4.37 \times 10^2(\frac{u*^3}{\nu_a g}\langle S^2 \rangle)^{0.92}$	$4.94 \times 10^7(\langle S^2 \rangle)^{2.45}$
2	7	7	$6.84 \times 10^1(\frac{u*^3}{\nu_a g}\langle S^2 \rangle)^{1.41}$	$7.88 \times 10^7(\langle S^2 \rangle)^{2.3}$
3	12	25	$4.75 \times 10^1(\frac{u*^3}{\nu_a g}\langle S^2 \rangle)^{1.11}$	$1.3 \times 10^7(\langle S^2 \rangle)^{2.39}$

The two new SSGFs are presented in Fig. 3.9 as two series of solid lines, where panels a and b denote results for the SSGF in terms of the combined number P_S and

$\langle S^2 \rangle$ respectively. These lines are in greyscale according to the values of the scaling parameters; the greyscale is indicated on the right of the individual panels. The range of values was chosen to correspond with the laboratory configurations for all types of wind speeds between 16 and 20 m s^{-1}. The experimental flux data obtained in these configurations are visualized by the greyscale plus signs in Fig. 3.9. Finally, Fig. 3.9 also presents the flux spectra prescribed by the L18 SSGF (Laussac et al. 2018) over the 3–7 µm range, which, as mentioned above, was modified so that the whitecap coverage $W(\%)$ scaling parameter (originally calculated from the wave age), was recalculated to depend on either P_S or $\langle S^2 \rangle$. The recalculated L18 flux spectra are represented by the greyscale dashed lines.

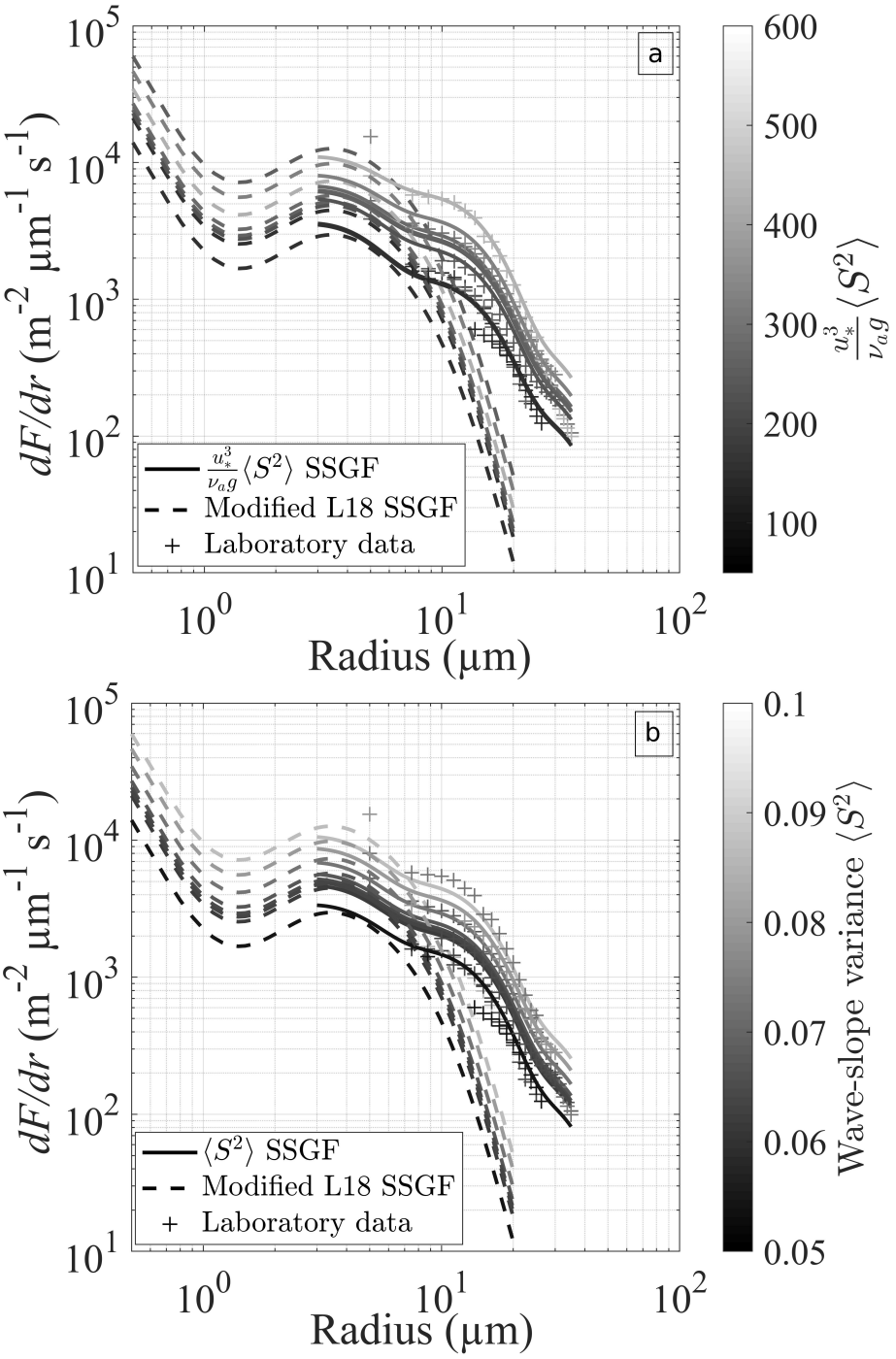

Figure 3.9: The altered L18 SSGF (dashed lines) and the (a) combined number P_S and (b) wave-slope variance $\langle S^2\rangle$ SSGFs. Line scales of grey depend on respective non-dimensional (a) P_S and (b) $\langle S^2\rangle$ values.

Figure 3.9 demonstrates that the two SSGFs reproduce the experimental flux data obtained in the tunnel quite well, although differences of up to a factor of two remain. In view of the already noted significant spread in individual flux functions reported in the literature (Tsyro et al. 2011; Chen et al. 2016; Neumann et al. 2016), we consider this performance adequate. Figure 3.9 also demonstrates that the two modes at 7 and 25 μm adequately reproduce the shape of the tunnel spectra, in contrast with the systematic flux

underestimations observed for SSGFs composed of modes centred around smaller droplet radius ranges (e.g., S93 and L18). Finally, Fig. 3.9 also shows that both SSGFs connect reasonably well to L18. While this was expected with a 2.5 µm mode inspired by L18 flux strengths, this result offers a perpective for a future coupling between the new SSGFs and L18, thereby extending a universal function to the 0.1–35 µm range. These results also offer a perspective for future improvements on the combination of laboratory and field sea spray measurements.

3.3.1 Completing the Laboratory Source Functions

In the following, we refer to B21a as the wave-slope variance-dependent SSGF, and B21b the combination number-dependent (P_S) SSGF. The proposed SSGFs are initially based on laboratory aerosol flux measurements over the 7–35 µm range, predominated by jet and spume droplets. The SSGFs are extended down to 3 µm particles using the L18 SSGF proposed from field observations. The study of smaller particles in the laboratory further exposes measurements to the effects of evaporation, as well as the absence of salts, surfactants, biogenic aerosols and secondary whitecaps compared to the field. The smaller particles, which represent the highest number concentrations in the MABL (cf. Figs 1.5 and 1.6, Sect. 1.2.3) are not yet accounted for. A possible way to amend this is to combine the laboratory SSGFs with a field-based SSGF scaled by both wind and wave parameters. The Ovadnevaite et al. (2014) source function depends on the wave height-dependent Reynolds number Re_{HW}. With no apparent difference in the scaling performance of Re_{HW} and Re_B, these air-sea Reynolds numbers are found to perform reasonably well for the scaling of sea spray generation over the jet droplet range (cf. Fig. 3.5), as also reported by other authors (Toba et al. 2006; Lenain and Melville 2017a). We propose to complete the laboratory SSGFs with that proposed by Ovadnevaite et al. (2014).

The OVA14 SSGF uses the sum of lognormal distributions (cf. Equ. 1.14, Sect. 1.2.4). For clarity, we adapt the normal distribution parameters presented above for the laboratory SSGFs (cf. Table 3.2) to lognormal distributions, detailed in Table 3.3. This additional formulation facilitates the use of both laboratory SSGFs in numerical models that only use lognormal distributions.

Table 3.3: Lognormal parameters for the two laboratory SSGFs. g is the acceleration due to gravity, and ν_a is the air kinetic viscosity.

i	σ_i	μ_i	$F_i(\frac{u*^3}{\nu_a g}\langle S^2\rangle)$	$F_i(\langle S^2\rangle)$
1	1.55	2.5	$47.61(\frac{u*^3}{\nu_a g}\langle S^2\rangle)^{0.92}$	$5.38\times10^6(\langle S^2\rangle)^{2.45}$
2	1.8	7	$1.69(\frac{u*^3}{\nu_a g}\langle S^2\rangle)^{1.41}$	$1.94\times10^6(\langle S^2\rangle)^{2.3}$
3	2.1	25	$0.448(\frac{u*^3}{\nu_a g}\langle S^2\rangle)^{1.11}$	$1.31\times10^5(\langle S^2\rangle)^{2.39}$

For the purpose of the following comparison between OVA14 and B21 SSGFs, and for simplicity, the wave significant wave height H_s required for the calculation of Re_{HW} is calculated using the JONSWAP model (Hasselmann et al. 1973; Lafon et al. 2007) with a 50 km fetch, typical of wind-sea conditions. The laboratory H_s values are not used, as possible wave height upscaling factors have not been investigated in the present study. Combining the OVA14 and laboratory SSGFs does not necessarily entail the summing of all eight modes together. Figure 3.10 shows that summing OVA14 (blue solid lines with individual modes as dashed lines) with the B21A and B21B source functions (solid and dotted grey lines) leads to a complete spectrum (red solid line) over the 0.015–35 µm radius range. A transition area between the OVA14 and B21 SSGFs can be seen in the whereabouts of 3–4 µm, which coincidently corresponds with their upper and lower validity ranges, respectively. The OVA14 and B21 SSGFs therefore seem compatible and show promise for the modelling of marine aerosols over a large size range.

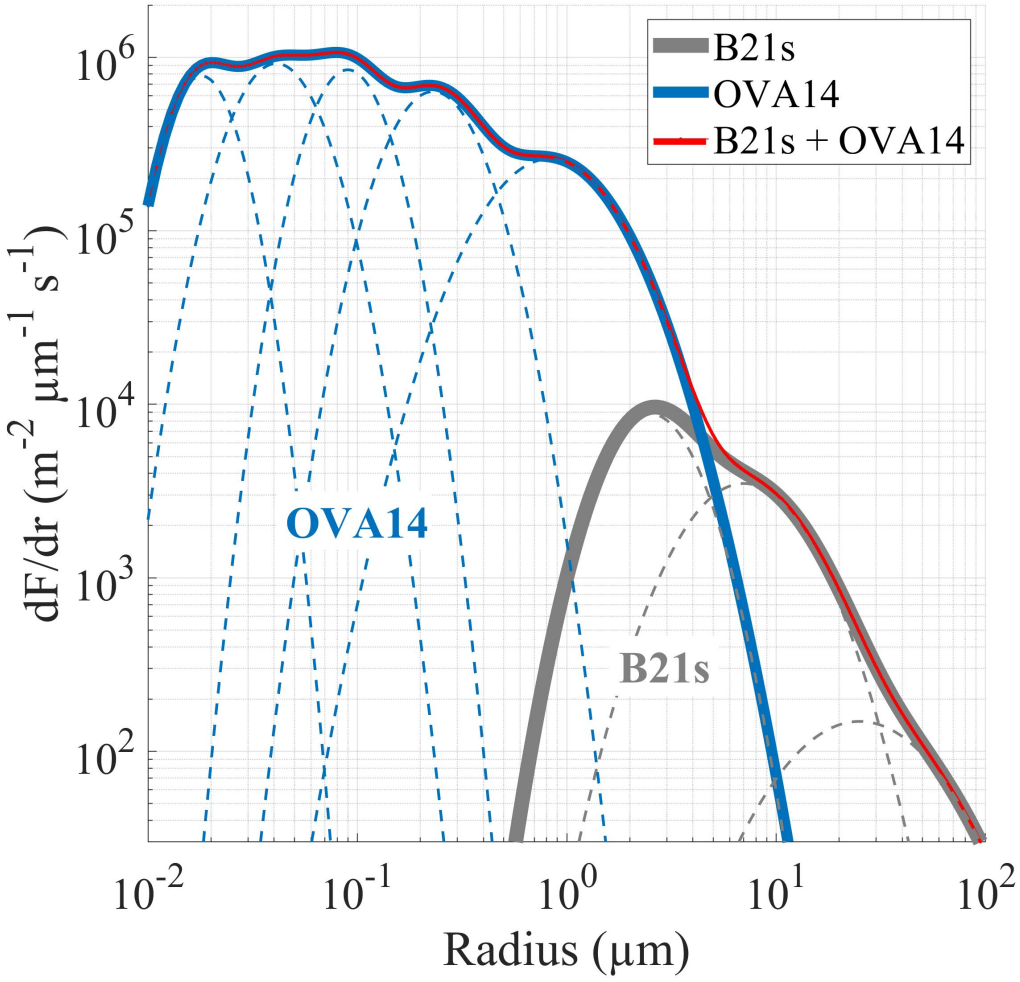

Figure 3.10: Example of OVA14, B21A and B21B source functions and underlying modes for the U_{10}=18 m s^{-1} and intermediate wave condition tested in the laboratory. Using the JONSWAP model, H_s = 3.5m. The sum of both B21 SSGFs with the OVA14 SSGF is represented by the red solid line.

3.4 Upscaling From the Laboratory to the Field

In this section, we further investigate the plausability of using MATE2019 SSGFs use in "full-scale" numerical atmospheric models (cf. Chapter 4). Though not presented in previous sections, a JONSWAP spectrum (Hasselmann et al. 1973) was generated by the wavemaker (f_p=0.9 Hz for U_{10}=0 m s^{-1}) during the MATE2019 laboratory campaign. The JONSWAP spectral input in the laboratory required longer wave, wind and aerosol sampling durations to verify stationarity, and the number of vertical points in each concentration profile was limited to three, instead of five in all other conditions. So far, the JONSWAP wave condition and the associated concentration profiles are deemed insufficient for accurate flux estimates. In the following, the JONSWAP measurements are systematically included. No significant differences from the other wave conditions tested in the laboratory are observed.

3.4.1 On Wave-Slope Variance in the Laboratory and the Field

Both SSGFs formulated in this study depend on $\langle S^2 \rangle$ calculated from multiple gravity wave components and associated wave scales. However, for use in regional models, accurate estimates of $\langle S^2 \rangle$ are essential for the accurate respresentation of sea spray generation. As previously explained, historical studies and following works (Cox and Munk 1956; Lenain and Melville 2017a) often consider the wave-slope variance $\langle S^2 \rangle$ as a linear function of the U_{10} wind speed, or the wind friction velocity u_*.

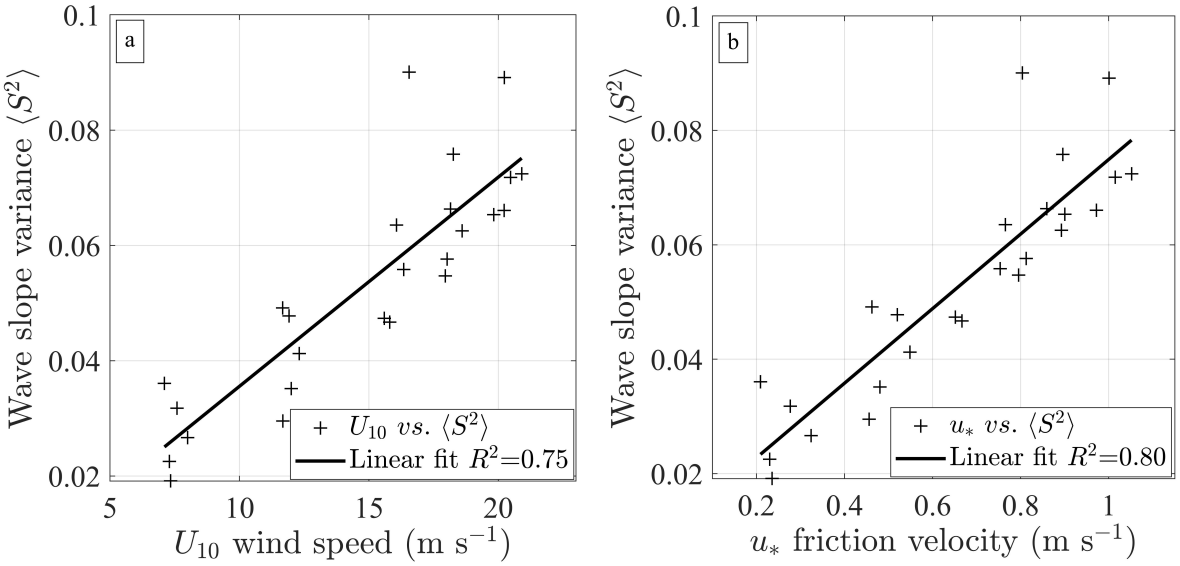

Figure 3.11: Wave-slope variance as a function of (a) wind speed U_{10} and (b) friction velocity u_* during MATE2019. Laboratory data is represented by crosses. R^2 values correspond to the linear fitting functions represented by black solid lines.

Figure 3.11 shows that a linear relationship is also applicable in laboratory conditions.

$\langle S^2 \rangle$ values are represented as a function of U_{10} (left panel) and u_* (right panel). The relationships are quite strong, with R^2=0.75 when using U_{10}, and R^2=0.80 with u_*, thus confirming the linear relationship between wind and wave-slope variance reported by other authors. This leads us to compare the relationship between wind speed and $\langle S^2 \rangle$ obtained in the laboratory, to that described by the Cox and Munk (1956) formulation (denoted CM herein). Obtained using airborne sun glitter observations, the CM formulation (cf. Eq. 3.1) represents the omnidirectional $\langle S^2 \rangle$ (the sum of upwind and crosswind components) as a function of wind speed. In the laboratory, the $\langle S^2 \rangle$ is only measured in the upwind direction as a result of the alignement of the wave gauges with the general wind and wave direction (cf. Sect. 2.4.2 & 2.4.3), and the crosswind components are omitted.

Figure 3.12 shows that the $\langle S^2 \rangle$ values obtained from the CM formulation (blue solid line) are systematically greater than the values measured in the laboratory (black crosses and corresponding fitting function). The deviation between both curves is actually linear. A factor 0.66 correction to the CM distribution (red solid line) results in a very good match to our experimental data. Interestingly, this factor can be associated with anisotropy observed in field conditions with comparable 0.8 and 0.71 crosswind to upwind ratios obtained from airborne observations by Cox and Munk (1956) and Lenain et al. (2019) respectively. It is also a good match with the 0.66 ratio found from spaceborne observations (Bréon and Henriot 2006) and the 0.6–0.7 range predicted in the Elfouhaily et al. (1997) omnidirectional wave model, as shown in the present study and elsewhere (Hauser et al. 2008). This leads to think that present study laboratory measurements provide an upwind $\langle S^2 \rangle$ comparable to the field for a same given U_{10} wind speed. Though the wavelengths tested in the laboratory were shorter than in the field, the shorter waves can represent the largest part of the overall $\langle S^2 \rangle$. This is further investigated in the following.

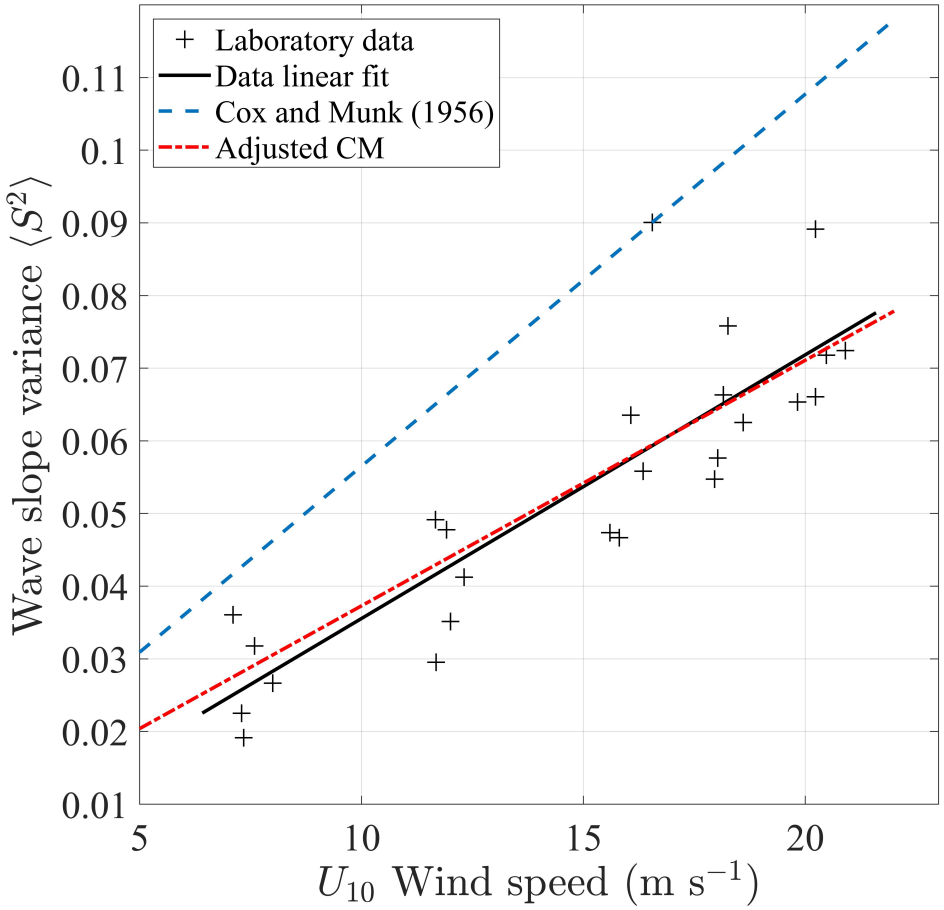

Figure 3.12: Wave-slope variance as a function of U_{10} wind speed for laboratory data (black crosses and black solid line), the CM formulation (blue dashed line), and the adjusted CM (red dashed-dotted line).

We can also note from Fig. 3.11 and Fig. 3.12 that for a given wind speed, a range of different $\langle S^2 \rangle$ values are found for each different wave condition tested in the laboratory, suggesting that $\langle S^2 \rangle$ does not scale with U_{10} alone. Figure 3.13 illustrates U_{10} as a function of $\langle S^2 \rangle$ for all individual five wave conditions and associated wind conditions. It appears that the linear relationship between the wave-slope variance and the wind speed is stronger for all individual wave conditions ($R^2 > 0.98$) compared with all wind and wave combination together, but with increased deviations for the intermediate wave case ($R^2 > 0.82$). These results suggest that the increase in $\langle S^2 \rangle$ for increasing U_{10} and inherent wave growth is approximately linear within small wave age ranges. However, the deviation between the different incident wave types suggests a higher order dependence of $\langle S^2 \rangle$ on other factors. We assume that this results from seastate contributions to $\langle S^2 \rangle$.

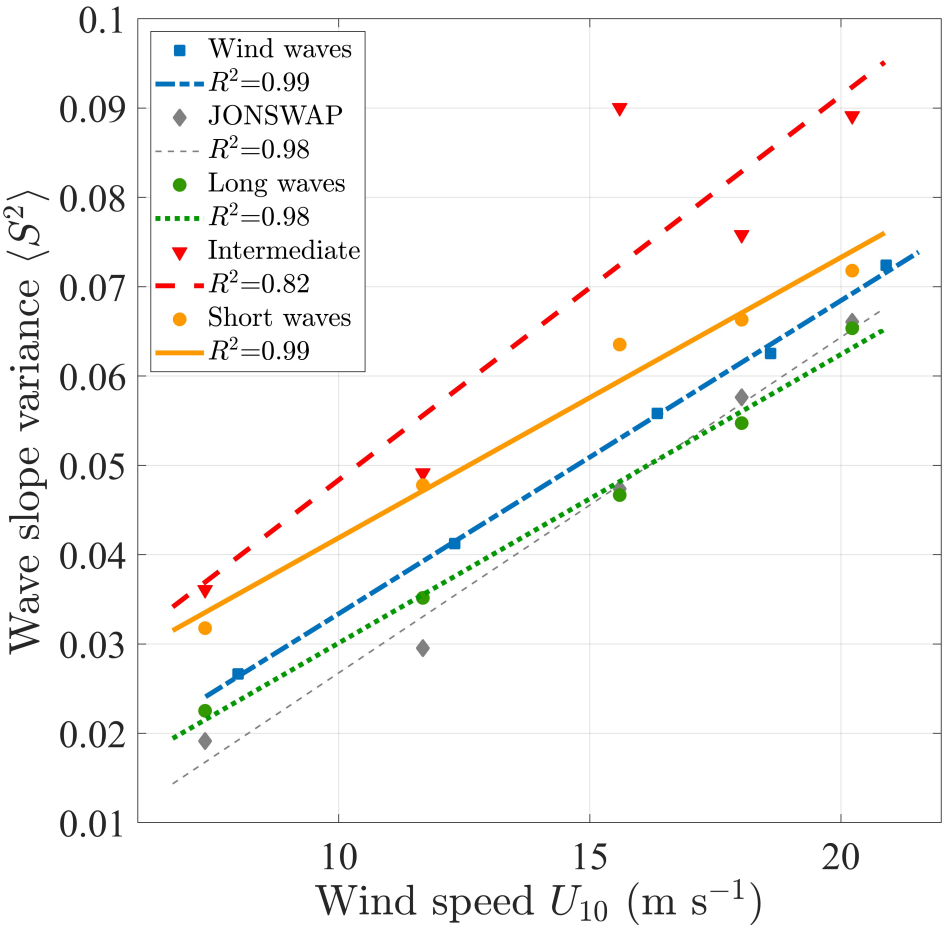

Figure 3.13: Wave-slope variance as a function of U_{10} wind speed for wind wave (blue dashed-dotted line and squares), JONSWAP (grey thin dashed line and diamonds), long wave (dark green dotted line and circles), intermediate (red dashed line and triangles) and short wave (orange solid line and circles) conditions. Curved are fitted to the experimental data, and corresponding R^2 values are shown.

The influence of sea state characteristics on $\langle S^2 \rangle$ is investigated using a wave spectral model. The Elfouhaily et al. (1997) spectral wave model (herein referred to as ELF) depends on the inverse of the wave age $\Omega = (\frac{c_p}{U_{10}})^{-1}$ and was proposed using field and laboratory observations, thus allowing validity over a large range of conditions. Figure 3.14 shows two examples of laboratory short wave (cf. Sect. 3.1) energy spectra (black solid line) for $U_{10} = 8$ m s^{-1} (Fig. 3.14a) and $U_{10} = 20$ m s^{-1} (Fig. 3.14b) obtained from the wave gauge data. The theoretical phase speed c_p of laboratory waves is used for the calculation of $\Omega = (\frac{c_p}{U_{10}})^{-1}$ (the inverse of the wave age), required for the calculation of the Elfouhaily et al. (1997) spectrum (cf. Appendix 1 for comparison with c_p derived from measured phase shift). The ELF model spectra are obtained considering a 2cm $< \lambda <$ 3 m wavelength range, in agreement with the range observed in the laboratory. The resulting ELF model omnidirectional (dark grey) and upwind (light grey) spectra are represented for comparison.

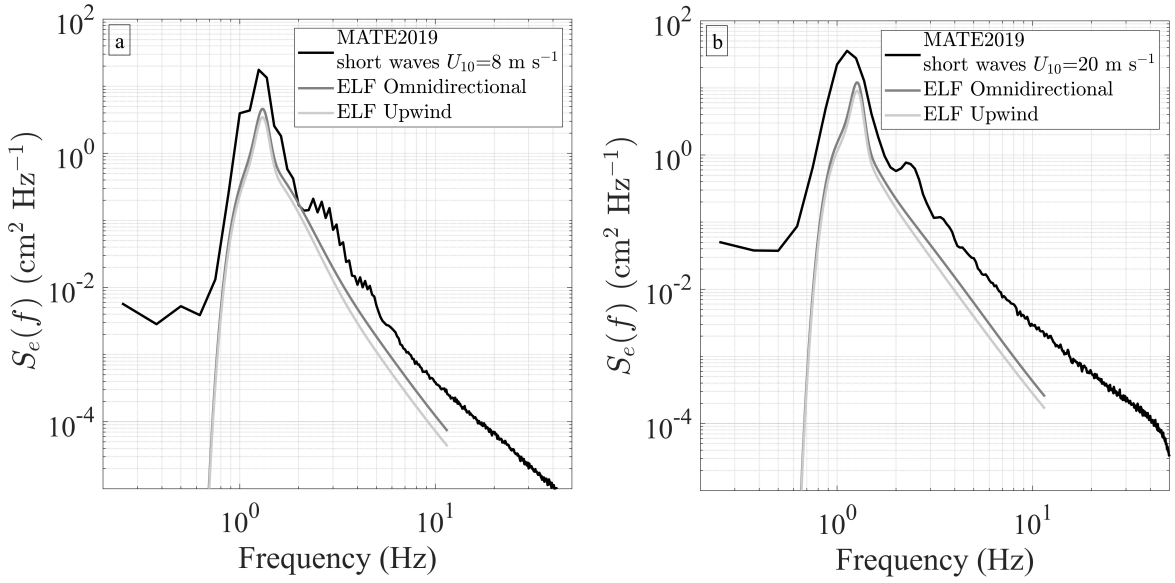

Figure 3.14: Wave energy-frequency spectra derived from MATE2019 laboratory measurements (black solid lines) and the omnidirectional (dark grey solid line) and upwind (light grey solid line) components of the ELF spectral model. These wave characteristics are presented for (a) U_{10} = 8 m s^{-1} and (b) U_{10} = 20 m s^{-1} wind speeds.

As shown in Fig. 3.14, the ELF model is able to correctly represent the peak frequency in the low wind speed case (cf. Fig. 3.14a), but a slight shift to higher frequencies is noticeable at higher wind speeds (cf. Fig. 3.14b), suggesting a possible underestimation of the wind-induced wave growth by the ELF model relative to the laboratory. Both panels show that the model predicts lower wave energy than measured in the laboratory, including in the case of the upwind model components ideally thought to match the essentially upwind laboratory measurements. The deviation between laboratory and ELF spectra is greater in the high wind speed case and especially at the higher frequencies where wind-forcing significant contributes to the energy of the wave components. This further suggests that at these relatively small wave scales, the ELF model may perform better in longer swell-like conditions, rather than developing waves.

As seen in Chapter 1, $\langle S^2 \rangle$ can be calculated from the second moment of the wave energy spectrum. We therefore calculate $\langle S^2 \rangle$ from the ELF wave spectrum. The ELF model requires an input wave age. For this purpose we force the model with wind and wave data collected during the EMMA field campaign (Lafon et al. 2007), as well as during the MATE2019 laboratory campaign. In the case of the laboratory data-forced ELF model (herein MATE2019-ELF), the wavelength range is 2cm $< \lambda <$ 3 m, corresponding with the MATE2019 minimum λ measurable by the wave gauge range, and the absence of waves for $\lambda >$ 3 m in the laboratory. In the case of EMMA-forced ELF calculations (herein EMMA-ELF) the 2cm $< \lambda <$ 90 m range is used to capture the majority of the gravity wave spectrum for the field conditions selected for this study. This was verified with $\lambda = 2\pi c_p^2/g$ (where g is the gravitational acceleration). The EMMA-ELF calculations are also made

over the laboratory 2cm $< \lambda <$ 3 m range, to compare the laboratory wave conditions with the higher frequency components observed in the field. Results of the comparison between MATE2019-ELF and EMMA-ELF calculations are shown in Fig 3.15. The three orange dashed curves and overlapping symbolds represent the crosswind (circles), upwind (triangles) and total (diamonds) EMMA-ELF $\langle S^2 \rangle$ values, with restriction 2cm $< \lambda <$ 3 m range. The three blue solid curves and overlapping symbolds represent the crosswind (circles), upwind (triangles) and total (diamonds) EMMA-ELF $\langle S^2 \rangle$ values, with a 2cm $< \lambda <$ 90m range. The blue dashed-dotted line represents the total MATE2019-ELF $\langle S^2 \rangle$ values computed over the 2cm $< \lambda <$ 3 m range. Finally, for comparison with these model results, the black solid line represents the fit to the $\langle S^2 \rangle$ values measured in the laboratory (cf. black solid line in Fig. 3.12). We highlight the fact that with the ELF model, the lower wavelength limit is a very sensitive setting, extending the limit to include λ=1cm waves drastically increases the total omnidirectional $\langle S^2 \rangle$.

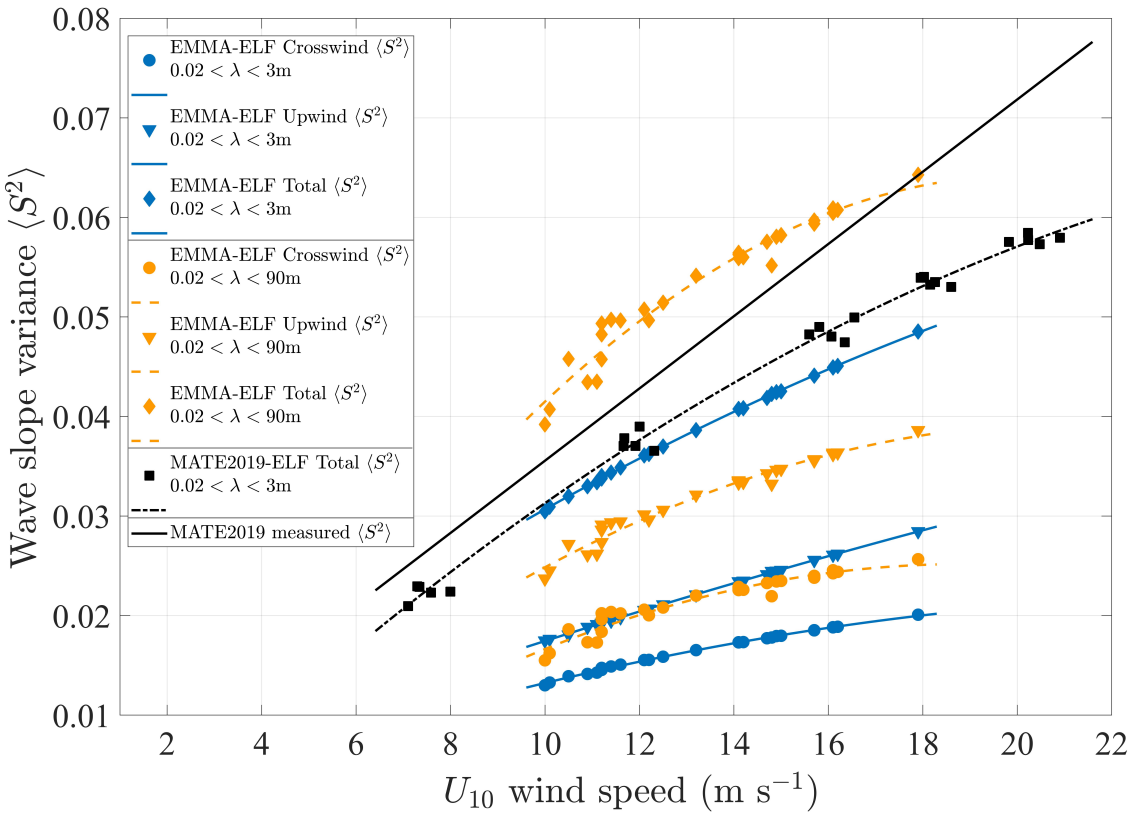

Figure 3.15: ELF model total (circles), upwind (triangles) and downwind (diamonds) $\langle S^2 \rangle$ values using EMMA field characteristics as input (wave age), as a function of wind speed U_{10}. Results are distinguished according to the 2cm $< \lambda <$ 3 m range (blue symbols and solid lines), and the 2cm $< \lambda <$ 90 m (orange symbols and dashed lines). MATE2019 total $\langle S^2 \rangle$ calculated with ELF using laboratory measurements as input (blue dashed-dotted line), and the measured laboratory $\langle S^2 \rangle$ values (cf. Fig. 3.12), are also shown. Overall, the symbols represent the different measured inputs to the ELF model.

The MATE2019-ELF model predicts that omnidirectional $\langle S^2 \rangle$ values in the laboratory are approximately 15% lower than for EMMA-ELF over the 2cm $< \lambda <$ 90m range for

the same wind speed. The longer swell-like wave components in the field contribute to 15% of $\langle S^2 \rangle$ relative to the laboratory λ range. The MATE2019-ELF configuration also shows that the laboratory spectrum-derived $\langle S^2 \rangle$ is higher than in the field over the 2cm $< \lambda <$ 3 m range, by approximately 15%. The ELF model therefore attibutes higher $\langle S^2 \rangle$ values to the laboratory wave spectrum presenting relatively lower wave ages, than in the high-frequency portion of the wave spectra obtained from higher wave age EMMA data. Another interesting result is the remarkably lower spread in the relationship between the MATE2019-ELF $\langle S^2 \rangle$ estimates and the wind speed compared to the laboratory (cf. Figs 3.12–3.13). This slight mismatch suggests that whilst ELF solely modulates $\langle S^2 \rangle$ according to the wave age, laboratory measurements indicate possible dependence on either other environmental factors, or a mismatch between model and laboratory $\langle S^2 \rangle$ sensitivity to wave age. By considering the MATE2019 measured $\langle S^2 \rangle$ rather than the ELF model predictions, we find that surprisingly, the total EMMA-ELF $\langle S^2 \rangle$ calculated over the 2cm $< \lambda <$ 90m range (dashed organge line and diamonds) is almost equivalent to the measured MATE2019 $\langle S^2 \rangle$ over the 2cm $< \lambda <$ 3 m range (black solid line). Indeed, comparison yields a maximum 15% deviation at 12 m s^{-1}, and a 1% deviation at 18 m s^{-1} as both EMMA-ELF and MATE2019 measurements converge for high wind speed. We note that for winds above 18 m s^{-1}, divergence is expected as the EMMA-ELF tends towards a constant $\langle S^2 \rangle$ value, in constrast with the constant increase indicated by the linear fit to laboratory data. Considering the estimated laboratory anisotropy when comparing with the Cox and Munk (1956) formulation (of approximately 0.66 - cf. Fig. 3.12), this would mean that the total laboratory $\langle S^2 \rangle$ would be approximately 30% higher than for the EMMA-ELF case. However, comparing with Fig. 3.12, we find that the presented ELF model values calculated from using EMMA data are approximately 30% lower than values predicted by the Cox and Munk (1956) formulation for a same wind speed (cf. Fig. 3.12). This strong deviation in total omnidirectional $\langle S^2 \rangle$ values between the Cox and Munk (1956) formulation and the Elfouhaily et al. (1997) model is not common. Present study ELF values are particularly low compared with other studies (e.g. Bringer et al. (2013)), and requires further investigation.

EMMA-ELF and MATE2019-ELF $\langle S^2 \rangle$ estimates converge towards a constant value for increasing winds (cf. Fig. 3.15). We seek to investigate the effect of wave age on the measured and modelled wave-slope variance. Figure 3.16 presents measured laboratory (black solid line and crosses), MATE2019-ELF total (purple solid line and circles), and MATE2019-ELF upwind (blue solid line and triangles) $\langle S^2 \rangle$ values as a function of the wave age. Results show that the laboratory $\langle S^2 \rangle$ values are higher than MATE2019-ELF model estimates for younger developing waves, but the difference is reduced for older and more developed waves. These results could suggest that the ELF model has difficulty to accurately reproduce wind-forced spectra at such small gravity wave scales, which is reminicent of conclusions made from Fig. 3.14. Despite the current deviations between model and laboratory measurements, and the difficult upscaling from the laboratory to the field using ELF, the higher order influence of the wave age on the wave-slope vari-

ance is evidenced by present study laboratory measurements and the theoretical model proposed by Elfouhaily et al. (1997). Further investigation is required, such further comparison between laboratory and field $\langle S^2 \rangle$ behaviour. Our current solution is to rely on a wind speed-dependent formulation for $\langle S^2 \rangle$, merging laboratory observations with the formulation proposed by Cox and Munk (1956) (cf. Fig. 3.12).

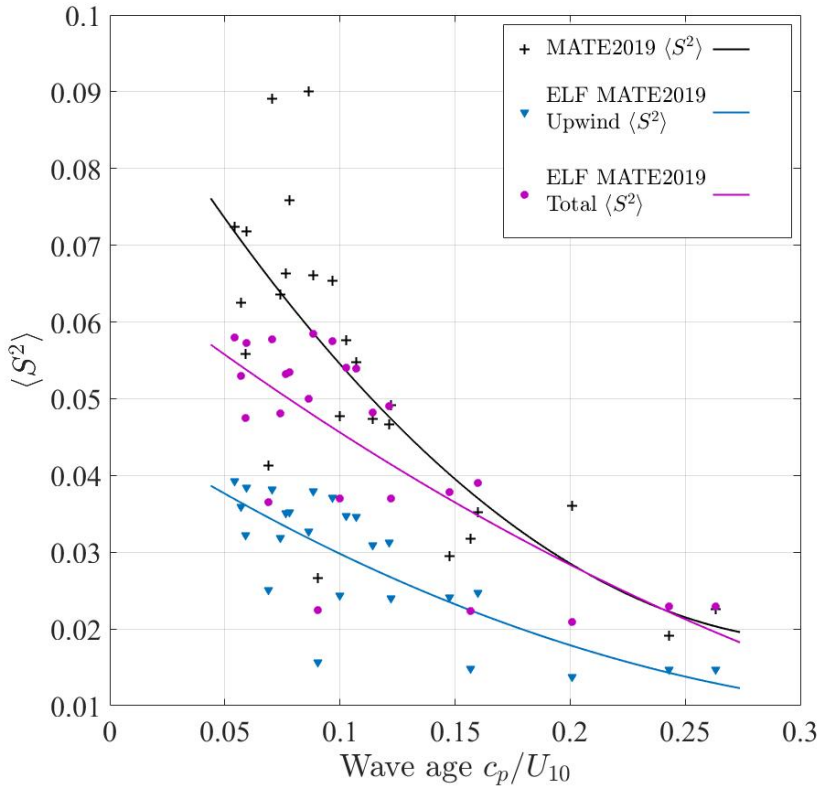

Figure 3.16: MATE2019 measurements (black solid line and crosses) and MATE2019-ELF estimates of $\langle S^2 \rangle$, represented as a function of wave age. Omnidirection (purple solid line and circles) and upwind (blue solid line and triangles) MATE2019-ELF estimates are shown. Solid lines are polynomial functions fitted to the data. MATE2019-ELF estimates are made from c_p and U_{10} values measured in the laboratory.

The corrected CM formulation predicts the laboratory $\langle S^2 \rangle$ with an ± 0.01 uncertainty, approximately equivalent to 10% of the $\langle S^2 \rangle$ value range. As a result the CM formulation, may not allow to differentiate between the wide range of sea states encountered in the field or in the laboratory for an identical wind speed.

3.4.2 Comparing Laboratory and Field Concentrations

As shown previously, the sea spray generation flux is comparable with existing parameterizations formulated from field observations (cf. Fig. 3.8). It is also interesting to compare field and laboratory concentrations. Several questions arise, such as the differences in concentrations resulting from the different proportions of accumulated aerosols advected from further upwind as a result of the drastically different fetch lengths. Another issue is

the sea spray sample height, as measurements in the field are rarely made within the first meters above the sea surface, contrary to laboratory conditions.

As a first step, the laboratory data is recalculated to the 10 m reference height using the vertical profile law proposed by Piazzola et al. (2015), valid for U_{10} = 10 m s^{-1} wind speed, and sizes greater than 0.75 µm radius

$$\frac{n(z)}{n_{10}} = (\frac{z}{10})^{-s} \tag{3.7}$$

where *n(z)* is the number concentration at the sample height z for a given radius r, n_{10} the number concentration 10 meters above the surface, and s is the vertical concentration profile slope. Based on aerosol extinction studies, Piazzola et al. (2015) suggests that s is approximately constant for particles in the 0.5–5 µm. This profile law describes heuristically correct increase in concentrations with proximity to the water surface.

We only consider the 0.5–7 µm radius size range, as the number concentration adjustment to 10 meters above the MWL (Eq. 3.7) is not necessarily valid for the larger droplets. The laboratory aerosol size distribution was measured at U_{10} = 11.5 m s^{-1}, 82 cm from the water surface with the intermediate wave condition. The resulting wave age is c_p/u_* = 3.2. Also represented are data acquired during the MIRAMER campaign (Laussac et al. 2018), at 12 km fetch, U_{10} = 10 m s^{-1}, and wave age $c_p/u_* \approx 4.9$. This allows comparable wave age values to be used in the present comparison. After height correction to 10 meters above the water surface, Fig. 3.17 compares laboratory (black crosses) and MIRAMER field concentrations (dashed black curve). Results show that aerosol concentrations measured in the field are higher than those measured in the wind tunnel by a factor 2−10 for radii 0.5 to 7 μm.

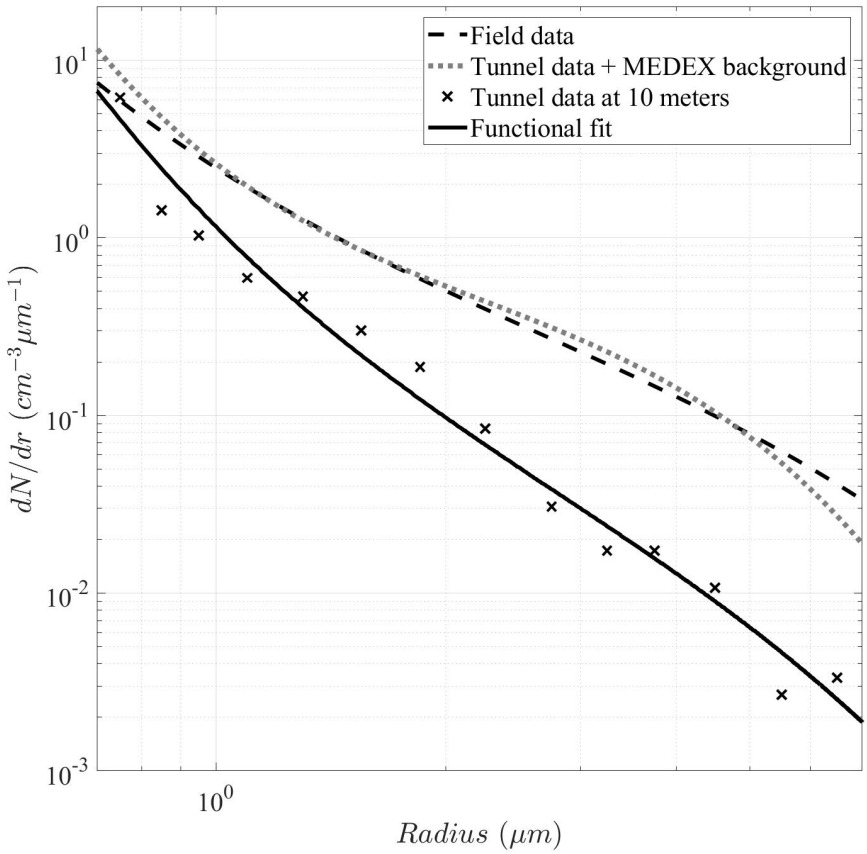

Figure 3.17: Tunnel dN/dr estimated at 10 meters above MWL for wind speed $U_{10} = 11.5\ m\ s^{-1}$ (solid back line), the dN/dr from MIRAMER at 10 $m\ s^{-1}$ and 12 km fetch with $c_p/u_* = 4.9$ (dashed black line), and the tunnel dN/dr with added MEDEX background for 10 $m\ s^{-1}$ and 12 km fetch (dotted grey line).

Aerosol concentrations in the field are a mixture of sea spray generated upwind or locally, as well as a background concentration in atmospheric aerosols. In the laboratory, aerosols are generated locally. As the smaller particles considered here have longer atmospheric residence times, the absence of this advected concentration may explain the differences observed between laboratory and field concentrations. The advected concentration is obtained using the MEDEX parametric model, providing the aerosol size distribution of a given wind speed and fetch length (Piazzola et al. 2003). As field and laboratory concentrations are compared for similar wave ages and wind speeds, the MEDEX model is parametered with the 12km fetch at which the MIRAMER data was collected. Figure 3.17 shows that summing MEDEX background estimates with laboratory concentrations corrected to 10 meters (grey doted curve) leads to an aerosol distribution comparable to that measured in the field. This lets us think that field number concentration are the sum of the advected background aerosols and the instantaneous aerosol production. Also, this suggests that for particles greater than 4µm radius, the advected aerosols at 12 km fetch represent 90% or more of the total number of aerosols. We must add here that this

exercise is purely investigative, and that the results presented above are highly subject to error as a result of questions on the validity of Eq. 3.7 for the considered droplet size range and wind speeds. Furthermore, the 10 meter height correction to laboratory concentrations may not be valid as the different laboratory and field wave heights may suggest a different emission layer height z_e (cf. Fig. 1.9, Sect. 1.3.1). Future study should include a comparison of laboratory and field concentration profiles, though data in the latter case is extremely scarce.

3.5 Discussion

3.5.1 Summary

We investigated the sea spray generation processes for different wind and wave combinations in the Pytheas Institute tunnel facility. We demonstrated that wave breaking (Sect. 3.2) and airflow characteristics (Sect. 2.4), of great importance to sea spray generation, are comparable in the laboratory and field. Sea spray concentrations over the 7–35 μm radius range are found to depend on both wind speed and sea state. The larger droplet concentrations are found in conditions with high values for whitecap coverage and wave-slope variance. The wave-slope variance is found to depend on both wind speed and sea state such as the wave age (cf Sect. 3.4.1).

Sea spray generation is calculated assuming logarithmic concentration profiles (cf. Sect. 3.2.5). For the spume droplet domain ($r > 20$ μm), the generation flux scales well with the wave-slope variance $\langle S^2 \rangle$, which is related to wave-breaking processes on a range of spatial scales, and the airflow at the air-sea interface. The wave-slope variance $\langle S^2 \rangle$ outperforms the wave age, even though this is a useful heuristic tool to estimate wind–wave equilibria, as well as the wind–sea Reynolds number R_B. Both use peak wave statistics. The good performance of $\langle S^2 \rangle$ is in agreement with an increasing number of microphysical studies that relate wave-slope to turbulent events such as airflow separation and wind shear, which are thought to drive the surface tearing of spume droplets at the wave crests (Banner and Melville 1976; Kawai 1981; Reul et al. 2008; Mueller and Veron 2014a; Buckley and Veron 2019).

In turn, $\langle S^2 \rangle$ is outperformed by a combined number $P_S = \langle S^2 \rangle u*^3/\nu_a g$, describing the wave-slope-variance-modulated wind-energy input to the waves. This is especially true for the smaller bubble-mediated jet droplets in the 7–20 μm range, and is most likely the result of combining the parameters $\langle S^2 \rangle$ and u_*^3. This latter parameter has a well-documented relationship with the wave energy dissipation (Wu 1988). The concept of combined scaling parameters has also been explored by other authors (Brumer et al. 2017; Lenain and Melville 2017a).

Our sea spray generation flux is within an order of magnitude to other fluxes established in the field or the laboratory (Sect. 3.2.6), which is in accordance with the

typical spread reported in the literature (Andreas 1989; Veron 2015). Two SSGFs deemed valid for wind speeds ranging 12–20 m s^{-1} and droplet radii 3–35 µm are proposed. One SSGF (denoted B21b) scales with the combined scaling number P_S, and the other SSGF (denoted B21a) with the wave-slope variance alone.

Efforts are made to upscale the SSGF scaling parameters from the laboratory to the field. Study results show that a number of key physical processes present similar behaviour, as shown when studying the relationship between whitecap coverage and wave-slope variance (cf. Fig. 3.1.2). This is further investigated by comparing $\langle S^2 \rangle$ measured in the laboratory with the wind-dependent Cox and Munk (1956) formulation. The Cox and Munk (1956) formulation predicts an omnidirectional $\langle S^2 \rangle$ greater than in the laboratory by a factor 1.5. The good match found after a factor 0.66 correction applied to the Cox and Munk (1956) formulation is equivalent to claiming that the laboratory $\langle S^2 \rangle$ solely represents the upwind $\langle S^2 \rangle$ component, which is compatible with the upwind alignment of the wave gauge array. The 0.66 correction factor may also partly compensate the absence of swell in the laboratory, which also contribute to a small but nevertheless important part of the omnidirectional $\langle S^2 \rangle$ in the field. Further investigation using the wave age-dependent Elfouhaily et al. (1997) wave model reveals that the omnidirectional $\langle S^2 \rangle$ in the laboratory is only 15% lower than in the field, indicating that the low wave age in the laboratory, allowing for high $\langle S^2 \rangle$ values, result in comparable $\langle S^2 \rangle$ values with the field. The 0.66 correction factor may then allow to compensate for the missing crosswind and swell components of $\langle S^2 \rangle$ in the laboratory, which seem to evolve as a linear function of wind. In this case, laboratory anisotropy may be closer to 0.8 than to 0.66. The particularly low $\langle S^2 \rangle$ values produced by ELF require further investigation, and could possibly result from the input wave age conditons provided by the EMMA campaign. Finally, using laboratory measurements as input for the ELF model, both ELF and experimental data point towards a decrease in the $\langle S^2 \rangle$ for increasing wave age. Relatively scarce measurements in the field, especially at wind speeds above 20 m s^{-1}, beg the question of how $\langle S^2 \rangle$ evolves according to wind and wave properties, and therefore air-sea fluxes such as sea spray. In the following, we use the corrected Cox and Munk (1956) formulation and therefore only consider dependence of the wave-slope variance on wind.

Finally, instead of comparing sea spray vertical fluxes (cf. Sect. 3.2.6), we compare laboratory and MIRAMER field concentrations for comparable wave ages. As a first step, laboratory concentrations for droplets smaller than 7 µm radius are corrected to 10 meters above the water surface using a profile law proposed by Piazzola et al. (2015). The resulting laboratory concentrations are found to be lower than in the field by a factor 2 (particles near 1 µm) to a factor 10 (particles near 5 µm). Using the MEDEX fetch-dependent model, the background concentrations corresponding to a 12 km fetch are added to the 10-meter laboratory concentrations. The addition of the background leads to concentrations very close to that found in the field at 10 meters. This suggests that the laboratory sea spray concentrations, as a result of the relatively short fetch, are mainly representative of the generation flux. In the jet, film and jet droplet ranges, 90% of

field number concentrations at 10 meters could result from fetch-dependent atmospheric accumulation of aerosols.

3.5.2 Wave-Slope Variance and Traditional Scaling Parameters

We scale sea spray generation with four non-dimensional parameters: wave age, wind–sea Reynolds number, wave-slope variance, and P_S (Sect. 3.3). The results indicate a relation between the scaling performance and the complexity of the non-dimensional number. Wave age and wind–sea Reynolds number are fairly easy to determine, but offer a limited scaling performance. In contrast, P_S offers the best scaling, but requires determination of both $\langle S^2 \rangle$ and u_*^3. In this respect, our wave-slope variance-dependent SSGF seems a good compromise. Nevertheless, it may be difficult to measure $\langle S^2 \rangle$ in the field. $\langle S^2 \rangle$ can be estimated from measured or modelled wave spectra (Elfouhaily et al. 1997). It is possible to infer $\langle S^2 \rangle$ from more accessible parameters such as the wind speed U_{10} (Eq. 3.1), or whitecap coverage $W(\%)$ (Eq. 3.2), as the wave-slope variance $\langle S^2 \rangle$ has often been considered proportional to both the wind speed at U_{10} and the friction velocity u_* (Cox and Munk 1956; Lenain et al. 2019). In a similar fashion, it is important to note that many authors obtain $W(\%)$ from the wind speed (e.g. Monahan and Muircheartaigh 1980). Though not explicitly presented here, $\langle S^2 \rangle u*^3/\nu_a g$ and $\langle S^2 \rangle$ (and to a lesser extent R_B) outperform the measured U_{10}, u_* and $W(\%)$ for the scaling of sea spray generation in the tested laboratory configurations, especially for larger droplets. The whitecap coverage $W(\%)$ presents R^2 values ranging between 0.2 and 0.45 over the 7–35 µm range, with best results over the jet droplet range. The scaling performances of U_{10} and u_* are lower than for $W(\%)$ overall, except for the smaller radii of the jet droplet range where U_{10} and u_* show a good correlation with the sea spray generation, with R^2 values reaching maxima of 0.49 and 0.54 (for $r = 7$ µm), respectively. These better results over the jet droplet range are consistent with the performances of the combined number P_S with the u_*^3 term. Furthermore, this shows that $\langle S^2 \rangle$ carries additional information (despite the good correlation between $\langle S^2 \rangle$ and $W(\%)$ – cf. Eq. 3.2) about the wave field relative to these three parameters, such as the presumed role of the wave-slope in the modulation of the airflow and surface-tearing mechanisms.

Unlike $\langle S^2 \rangle$, U_{10} and u_* are not found to be appropriate tools for the upscaling and extrapolation of sea spray generation and whitecap coverage from the laboratory to the field, similar to observations made by Toba et al. (2006) when comparing tunnel and field data. Although $\langle S^2 \rangle$ outperforms U_{10} and u_*, there are conditions in which the wind parameters scale the aerosol concentrations as successfully. This pertains to smaller droplets ($r < 12.5$ µm) and relatively low wind speeds of 8 and 12 m s^{-1}, and a wave field that is forced by the wind. In these circumstances, sea spray consists almost exclusively of the bubble-mediated jet droplets produced from breaking waves under conditions of strong wave–wind equilibrium. Further analysis of our laboratory data reveals that the linear relation between U_{10} and $\langle S^2 \rangle$ presented by Cox and Munk (1956) (Eq. 3.1) is best

observed for the conditions corresponding to pure wind forcing. This is consistent with the good scaling performance of U_{10} and u_* under these conditions, as mentioned above. However, notable deviations from this linear relationship are observed with other types of wave forcing, which we attribute to the sensitivity of $\langle S^2 \rangle$ to wave–wind equilibria (quantified here with wave age). It is also possible that the observed fluctuations result from the monochromatic properties of the longer wave conditions that experience relatively less wind forcing, resulting in lower wave energy in the higher frequencies of the wave spectrum. The possibility to generate a wave spectra using a programmable wave maker, such as the Joint North Sea Wave Project (JONSWAP) spectra (Hasselmann et al. 1973), is worth considering in future work. In this study, JONSWAP wave fields generated by the wavemaker seem to produce similar results to the tested monochromatic waves (cf. Fig. 3.13).

3.5.3 On Upscaling from the Laboratory to the Field

An attempt is made to upscale laboratory $\langle S^2 \rangle$, essential scaling parameter for both proposed SSGFs, to the field. Consensus is found on the reduction of $\langle S^2 \rangle$ for increasing wave age, confirming that the wind speed and the sea state both modulate $\langle S^2 \rangle$. Further research is required to qualify the different processes in the laboratory and in the field. Results indicate that a $\langle S^2 \rangle$ background corresponding to the contribution of the longer swell waves may well explain the lower upwind and omnidirection components in the laboratory when compared with the Elfouhaily et al. (1997) model. Also, it is possible that at small wave scales, ELF struggles to reproduce the frequency shift in the wave spectrum towards lower frequencies (observed in the laboratory) resulting from the wind forcing. Finally, the deviations between the laboratory and the ELF model may result from abnormally high $\langle S^2 \rangle$ laboratory values as a result of the monochromatic wind-forced, steep, and highly breaking waves. It is also possible that the direction spread in the ELF spectral model is too anisotropic in such high wind conditions were the $\langle S^2 \rangle$ is thought to become increasingly isotropic (Walsh et al. 1998). The corrected Cox and Munk (1956) is currently our best option for the scaling of the SSGFs in the field, despite essential sea state information contained in the Elfouhaily et al. (1997) model. It is possible that better upscaling from the laboratory to the field requires wave models that do not depend on the wave age alone. Research in this field is ongoing, as the contribution of different wave scales to $\langle S^2 \rangle$ remains an open question (Bringer et al. 2013).

Another approach to upscaling is the comparison between laboratory and field sea spray concentrations. Study results show that the laboratory concentrations, once corrected to 10 meters above MWL and added to the fetch-dependent advected concentrations, is almost equivalent to MIRAMER sea spray concentration measurements. These results rely on many assumptions such as the validity of the vertical concentration profile law for relatively large droplets, and the accuracy of the MEDEX fetch-dependent model for the estimation of the fetch-dependent background concentrations. The 0.5–7

µm radius range considered for this study is also subject to evaporation effects in the laboratory that may significantly impact the presented results. Reproducing the present study for larger spume droplets would require better knowledge of their vertical concentration distribution in the field. The constant profile slope assumed by Piazzola et al. (2015) regardless of the particle radius is contrary to observations made in the laboratory (cf. Fig. 3.3). Other effects such as the water composition, different between the field and the laboratory, can impact processes such as whitecapping, as well as air-droplet thermodynamic effects such as evaporation. Other approaches to upscaling are worth considering for future study, such as the consideration of different emission layer heights z_e as a results of the different significant wave heights observed in the laboratory and the field.

Chapter 4

Numerically Modelling Sea Spray Transport

Contents

4.1 Introducing Modelling Efforts

As previously described, the weather and the climate can be altered by the radiative impact of aerosols, their role as cloud condensation nuclei, as well as their effects on heat, moisture and momentum fluxes in and out the marine atmospheric boundary layer. The good understanding of these impacts require accurate knowledge of the quantity, composition and spatial distribution of these aerosols. Numerical atmospheric and ocean models allow to study and predict the weather and the climate. The good representation of air-sea interactions, often parameteric, is important for the understanding of both oceanographic and atmospheric processes (Pianezze et al. 2018; Lemarié et al. 2021). For the modelling of sea spray, Lagrangian models come at a numerical cost that make them

inoperable for routine meteorological applications (Mestayer et al. 1996; Mueller and Veron 2014a). This chapter therefore presents results obtained using Eulerian models that allow to resolve the classical aerosol transport equations (e.g. Equ. 1.8–1.9), but do not resolve dynamic and thermodynamic air-droplet processes (e.g. Equ. 1.15). As a compromise, simulations are run with the assumption of r_{80} radii at equilibrium with ambient 80% relative humidity conditions. These assumptions are considered valid for the present study droplet size range, and the atmospheric conditions met during the MIRAMER and SUMOS field campaigns as well as the MATE2019 laboratory study (cf. Chapter 2).

Two complementary numerical models are used to evaluate wave-wind-dependent sea spray generation formulations. The two-dimensional MACMod model allows for the parameterization of a large number of SSGFs as a result of the low numerical cost of simulations. This model is designed for the theoretical study of aerosol transport in controlled and adustable environmental conditions. Physical processes important for sea spray transport (e.g. aerosol source and deposition fluxes, turbulent diffusion, whitecapping, friction velocity, etc) can also be parametered. In constrast with the MesoNH model, MACMod is not as well adapted for realistic cases as a result of its two-dimensional (x and z) configuration and horizontally homogenous wind field. The more complex MesoNH model allows for the consideration of orographic effects on the airflow, and can be forced by observations, as well as model hindcasts and forecasts as provided by ECMWF, thus allowing for realistic simulations. The numerical cost of MesoNH simulations is relatively high.

Most of the source functions presented in Table 4.1 are implemented and compared with MIRAMER experimental data, and allow to select SSGFs for regional scale modelling with the three-dimensional MesoNH mesoscale model. MesoNH is used for more realistic regional-scale modelling over both the North-East Atlantic Ocean and the North-West Mediterranean. This is achieved with B21a, B21b and OVA14 (Ovadnevaite et al. 2014) SSGFs.

Table 4.1: Selection of SSGF parameterizations with the addition of the B21a and B21b source functions.

Parameterization	Size Range (μm)	Scaling Parameter	Study Range U_{10} (m s $^{-1}$)
M86	0.3–20 (r_{80})	U_{10}	6–13
S93	1–25 (r_{80})	U_{10}	0–30
A98	2–500 (r_{80})	U_{10}	0–32.5
G03	0.07–20 (r_{80})	U_{10}	6–17
OVA14	0.015–3 (r_D)	$u_* H_s/\nu_w$	3–18
L18	0.5–20 (r_{80})	c_p/u_*	8–16
B21A	3–35 (r_{80})	$\langle S^2 \rangle$	12–20
B21B	3–35 (r_{80})	$R_B \langle S^2 \rangle \frac{c_p}{u_*}^{-1}$	12–20

4.2 Fetch-dependent 2D Simulations with MACMod

4.2.1 Numerical Configuration

The MACMod Marine Aerosol Concentration Model was designed and validated at the Mediterranean Institute of Oceanography for the study of atmospheric aerosol transport (Tedeschi and Piazzola 2011; Piazzola et al. 2015; Laussac et al. 2018). This Eulerian model is two-dimensional (along the x and z axes), and uses a 302×26 regular grid for the present study, with 302 cells along the horizontal x axis at 1 km resulution, and 26 cells along the vertical z axis with increased resolution near the sea surface, making for a 302 km × 650 m grid. At the top of the model, the sea spray concentration is equal to zero. The finite volume discretization method (Patankar 1980) is used for the approximation of transport, represented by the general balance equation presented in Chapter 1 (cf. Eq. 1.10). The initial upwind background concentrations associated with mainly continental sources are obtained using the MEDEX (Mediterranean Extinction) model (Piazzola et al. 2003). Despite an implicit numerical scheme, the model's numerical and physical stability is ensured with an automatically adjusted numerical timestep to ensure that Courant-

Friedrichs-Lewy (CFL) conditions are respected. The simulation ends once the aerosol field reaches stationnary conditions, using a concentration variability threshold.

4.2.2 Physical Configuration

The model is composed of three layers, including a viscous sublayer, a surface layer, and a mixing layer. The viscous sublayer, located at the water surface, is a thin ($\approx 10^{-3}$ m) layer saturated in humidity (99% relative humidity) and dominated by molecular diffusion. Above it, the vertically contant-flux and turbulent surface layer is dominated by turbulent diffusion and gravitational deposition. At the top of the surface layer, where the mixing layer lies, the vertical aerosol flux is approximated as the sum of the turbulent diffusion and gravitational fluxes (cf. Fig. 1.9, Sect 1.3.1).

As a result of the relatively low computational costs of the MACMod model, a range of sea spray generation functions was tested for comparison. Are represented all the SSGFs shown in Table 4.1, with the exception of the Smith et al. (1993), Andreas (1998) and Gong (2003) source functions, that are very similar to the Monahan et al. (1986) SSGFs over the presented radius and wind speed range. Air density is set at 1.19 kg m^{-3}, and the particle density is set at 1172 kg m^{-3} corresponding to the density of saline droplets having reached equilibrium 80% ambient relative humidity. The vertical flux is equal in both layers and equal to the deposition flux. The deposition velocity is presented as

$$V_d = \frac{(k'_d + V_g(r_w))(k'_c + V_g(r_d))}{k'_d + k'_c + V_g(r_w)} \tag{4.1}$$

where k'_d and k'_c are diffusion coefficients in the viscous sublayer and the surface layer respectively. The Cunningham correction for rarefaction effects in the air flow around the particles, C_r, is added to the calculation of gravitational deposition velocity in the viscous sublayer

$$V_g(r_w) = \frac{2\rho_{99} g r_{99}^2}{9\nu_a} C_r(r_{99}) \tag{4.2}$$

and the surface layer

$$V_g(r_d) = \frac{2\rho_{80} g r_{80}^2}{9\nu_a} C_r(r_{80}) \tag{4.3}$$

where $\rho_{80} \approx 1.17 \times 10^3$ kg m^{-3} and $\rho_{99} \approx 1.043 \times 10^3$ kg m^{-3}, the droplet densities estimated for ambient relative humidities of 80% and 99% respectively. ν_a is the dynamic viscosity of air, and g is the gravitational acceleration. r_{80} and r_{99} can be approximated from the dry particle radius r_0:

$$r_{99} \approx 2r_{80} \approx 4r_0. \tag{4.4}$$

In MACMod, each simulation allows to model the distribution of sea spray for a single radius, and several simulations are required to reconstruct an aerosol distribtion spectrum. Aerosols interactions such as accumulation, coagulation, evaporation and bursting are not considered. Evaporation effects can be neglected considering r_{80} equilibrium, and aerosol interactions can be neglected as a result of the relative scarcity of sea spray aerosols (Veron 2015). As required in the case of the OVA14 SSGF, the significant wave height H_s is parameterized using the fetch-dependent relationship (Hasselmann et al. 1973), adapted to the North-Western Mediterranean from data acquired during the EMMA campaign (Lafon et al. 2004) (cf. Equ. 1.32). The whitecap coverage required for the calculation of the M86 and L18 sea spray generation fluxes is calculated according to the formulation proposed by Monahan and O'Muircheartaigh (1986) (cf. Eq. 1.38).

The wind field is pre-determined and independant from the aerosol composition which has no feedback effects on the flow in the presented simulations. For simplicity, neutral conditions are imposed with equal and homogenous air and water temperatures set at 18°C. The friction velocity u_* is calculated using the formulation proposed by Large and Pond (1981) (Eqs. 1.24–1.25). The friction at the water surface is represented by the friction velocity u_* used for the calculation of the turbulent diffusion, and the roughness length for momentum z_0 for the calculation of the vertical wind speed profile.

As previously described in Sect. 1.4.3, the wave-slope variance $\langle S^2 \rangle$ can be a multi-scale parameter, and depend on multiple wave characteristics such as the wave age (cf. Sect. 3.4.1). First, the modified Cox and Munk (1956) formulation is used with the 0.66 correction factor (cf. Sect 3.4.1). The formulation is integrated in the MACMod model thus calculating the $\langle S^2 \rangle$ values at each cell of the 2D domain. The wind speed is horizontally homogenous in the domain, as is the wave-slope variance. The expected higher order dependence of $\langle S^2 \rangle$ on wave age is not considered with this parameterization.

The Elfouhaily et al. (1997) model (cf. Sect. 1.4.2) can also be implemented into the MACMod model. The wave age is computed from the phase speed, as well as the non-dimensional fetch calculated from the fetch length and the U_{10} wind speed. The phase speed formulation requires the wave peak frequency f_p, calculated here using

$$f_p = \frac{\alpha g}{U_{10}} X^{\beta} \tag{4.5}$$

where α=1 and β=0.54 as determined for the North-Western Mediterranean by Lafon et al. (2004).

4.3 Realistic 3D Regional Modelling with MesoNH

4.3.1 Numerical Configuration

The MesoNH regional simulations come at a much higher numerical cost than the MACMod model, and are run using the OSU-Pytheas computer cluster for parallel computing. In the present study, we use version 5.4 of the MesoNH model (Lac et al. 2018). The model solves the conservation equations of momentum, mass, humidity, scalar variables and the thermodynamic equation derived from the conservation of entropy under the anelastic approximation. The Runge-Kutta methods are applied for the momentum transport, and the forward-in-time integration is applied for the rest of the model. For numerical stability, the model timestep is set close to 40 seconds. In this study a horizontal 300×270 grid is used for the North-West Mediterranean, and a 300×300 is used for the North-East Atlantic. The grids are horizontally regular, with a 2 km resolution. The atmosphere is vertically composed of 48 layers, ranging from the mean water level to 24 km altitude. In the present study, the model is forced at its boundaries by the ECMWF model every three hours, between which predictive modelling allows hourly outputs.

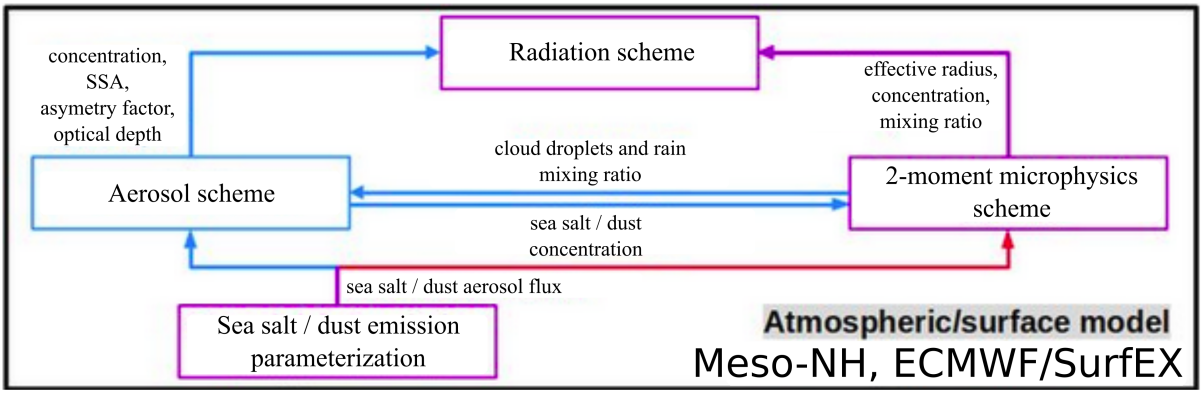

Figure 4.1: Schematic of Meso-NH and the SURFEX system with ECMWF wind forcings. Adapted from Barthe et al. (2021).

MesoNH is coupled to the SurfEX module, which allows to simulate the atmosphere-surface exchanges (Masson et al. 2013). The module contains the SEAFLUX and the ISBA schemes, which allow to resolve the aerosol, heat, moisture and momentum fluxes at the air-sea interface. In our simulations, a two-moment scheme is used, allowing the total concentration and the median radius of the different aerosol modes change. The modal standard deviation is kept constant. The role of the sea spray as cloud condensation nuclei is not activated here, but is a possibility for future research.

4.3.2 Physical Configuration

By default, the Seinfeld and Pandis (1997) expression for aerosol deposition velocity is used. Modes are transported, in contrast with individual particles in MACMod. In the

presented simulations, the modal median is able to vary. It varies with the often particle size-dependent effects of aerosol sources and sinks. The standard deviation of the modes, however, is kept constant in each model cell for each moment. Number concentrations of particles of a given size can be extracted by summing all the lognormal modes transported by the model. Though not considered here, the model also allows to transport different moments of the aerosol spectrum, thus providing mass and volume concentrations. In the MesoNH simulations, we implement the B21a, B21b and OVA14 SSGFs. The density of the particles is set to that of droplets having reached the r_{80} equilibrium radius at 80% relative humidity. As in MACMod, $\rho_{80} \approx 1172$ kg m^{-3}. In the case of dry salt particles, the particle density becomes 2200 kg m^{-3}. This is used in the case of the OVA14 SSGF, describing the generation of dry salt particles. The ocean-wave WAM model (ECMWF-IFS) based on Komen et al. (1996) provides wave information at 0.1 degree resolution necessary for the significant wave height-dependent OVA14 sea spray function (cf. Equ. 1.33). As the present study does not verify the validity of the wave model over the study areas and periods, and as the waves are not directly coupled to the MesoNH atmospheric model, $\langle S^2 \rangle$ is estimated by the model using the corrected Cox and Munk (1956) formulation (cf. Sect 3.4.1). The wave-age dependence of $\langle S^2 \rangle$ (cf. Sect. 3.4.1) is therefore not accounted for in the following MesoNH results.

Two numerical domains were defined for the study of sea spray transport in the North-West of the Mediterranean basin, and in the North-East of the Atlantic Ocean. In the Mediterranean the numerical grid is defined to allow for sufficient fetch lengths in the few cases of Westerly or Southerly winds observed during the MIRAMER field compaign. In the Atlantic, the domain was centered on the Bay of Biscay where the SUMOS campaign took place. To limit computational costs, the grid does not extend very far westward, which could theoretically result in the underestimation of sea spray concentrations if fetch length resolved by the model is significantly different from reality. Considering that most strong wind conditions were Easterly and Southerly during the SUMOS campaign, this configuration is not thought to affect model results. Compared with the MACMod detch-dependent model, the use of a regional scale model such as MesoNH allows to simulate realistic wind fields, therefore allowing to compare outputs with all MIRAMER and SUMOS stations without prior knowlegdge of the fetch length at each station.

Including Other Aerosol Sources

In Southern Europe, sources of aerosols also include dusts largely transported from the Sahara desert. These dusts are transported Northwards to Europe with Southerly winds over the Mediterranean Basin. In the case of the MIRAMER and SUMOS field campaigns periods over which the MACMod and MesoNH simulations are run, no significant dust events were noted. As a result, we neglect dusts in the simulations. Future study, however, will have to include dusts as well as other types of coarse mode aerosols, which can co-exist and interact with sea spray in the MABL.

4.4 Results

4.4.1 MACMod

The two-dimensional MACMod model is parametered with different SSGFs. The simulations are run in conditions similar to those encountered during the MIRAMER field campaign, to allow for comparison with observations. As the model is fetch-dependent, only the conditions during which the fetch could be estimated for MIRAMER sample stations were used. In Figures 4.2–4.3, concentrations are represented as a function of fetch length for each different SSGF. Concentrations are extracted from the model 13 meters above the MWL; the output height closest to the approximate height of the CSASP instruments during the MIRAMER campaign. Black curves represent the B21a (solid line) and B21b (dashed) SSGFs. M86, L18 and OVA14 SSGFs are represented by blue, red and orange solid lines, respectively. As shown in Figure 4.2, a scenario with a $U_{10} = 10$ m s^{-1} case allows to compare simulations with four stations at 12, 60, 180 and 270 km fetch lengths. In Figure 4.3, simulation results are presented for $U_{10} = 16$ m s^{-1}, with a single station available at 150 km fetch. For both wind speed cases, sea spray number concentrations are presented for radii 5µm (panels a) and 10µm (panels b).

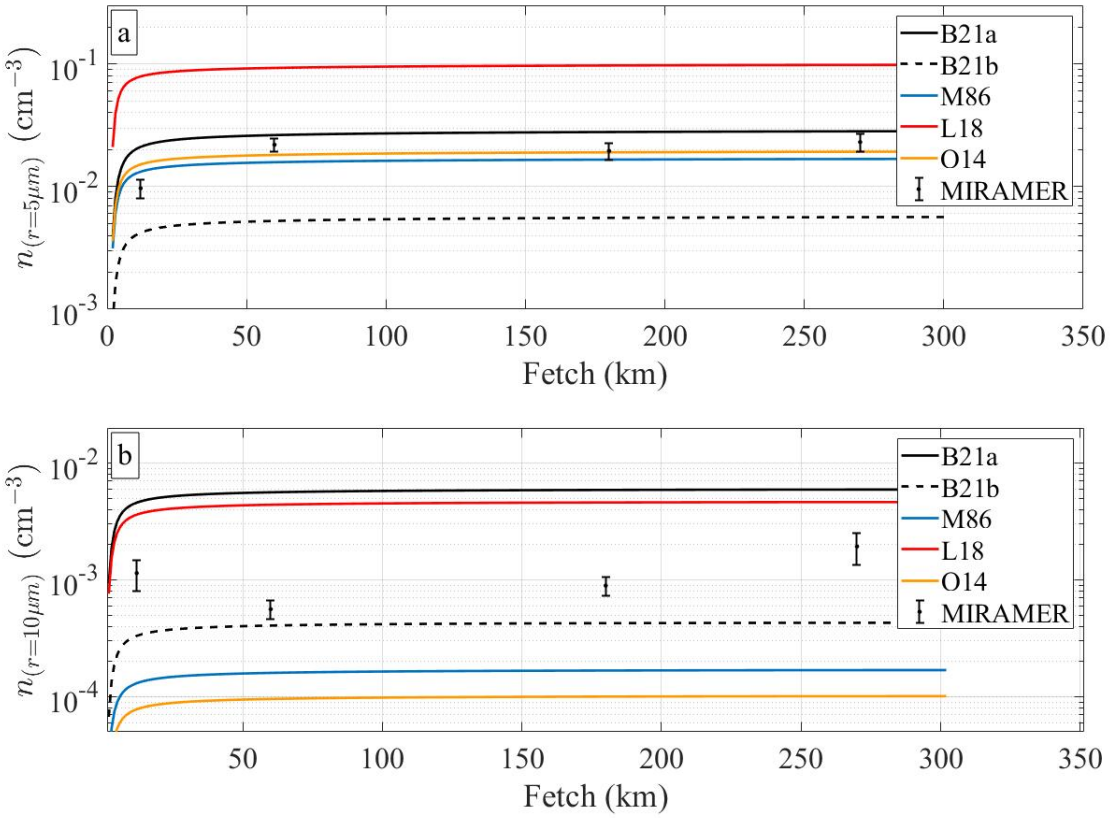

Figure 4.2: MACMod simulated concentrations of (a) 5µm and (b) 10µm radius particles represented as a function of increasing fetch length, for $U_{10} = 10$ m s^{-1}. Black curves represent the B21a (solid line) and B21b (dashed) SSGFs. M86, L18 and OVA14 SSGFs are represented by blue, red and orange solid lines, respectively.

At $U_{10} = 10$ m s^{-1} (cf. Fig. 4.2), OVA14 is found to perform best for particles of radius 5µm, despite being slightly beyond the SSGF radius validity range. M86 and B21a also perform well with less than a factor 2 deviation from the experimental data. B21b is found to underestimate by a factor 6 relative to the data, and L18 to overestimate by a factor 8. For particles of radius 10µm, L18 and B21a are found to overestimate by factors 3.5 and 4.5 relative to observations, respectively. B21b continues to underestimate by a factor 6, whilst M86 and OVA14 drop significantly to underestimate by factors 8.2 and 9 respectively. This is in agreement with the sharp decrease in the M86 generation flux (similar to Smith et al. (1993), cf. Fig. 3.8) and the OVA14 generation flux (cf. Fig. 3.10) for particles larger than 5µm. The underestimation by the B21b SSGF is rather expected, as energy dissipation at the air-sea interface may scale with u_*^2 rather than u_*^3 at winds below 15 m s^{-1} approximately (cf. Sect. 3.5.1).

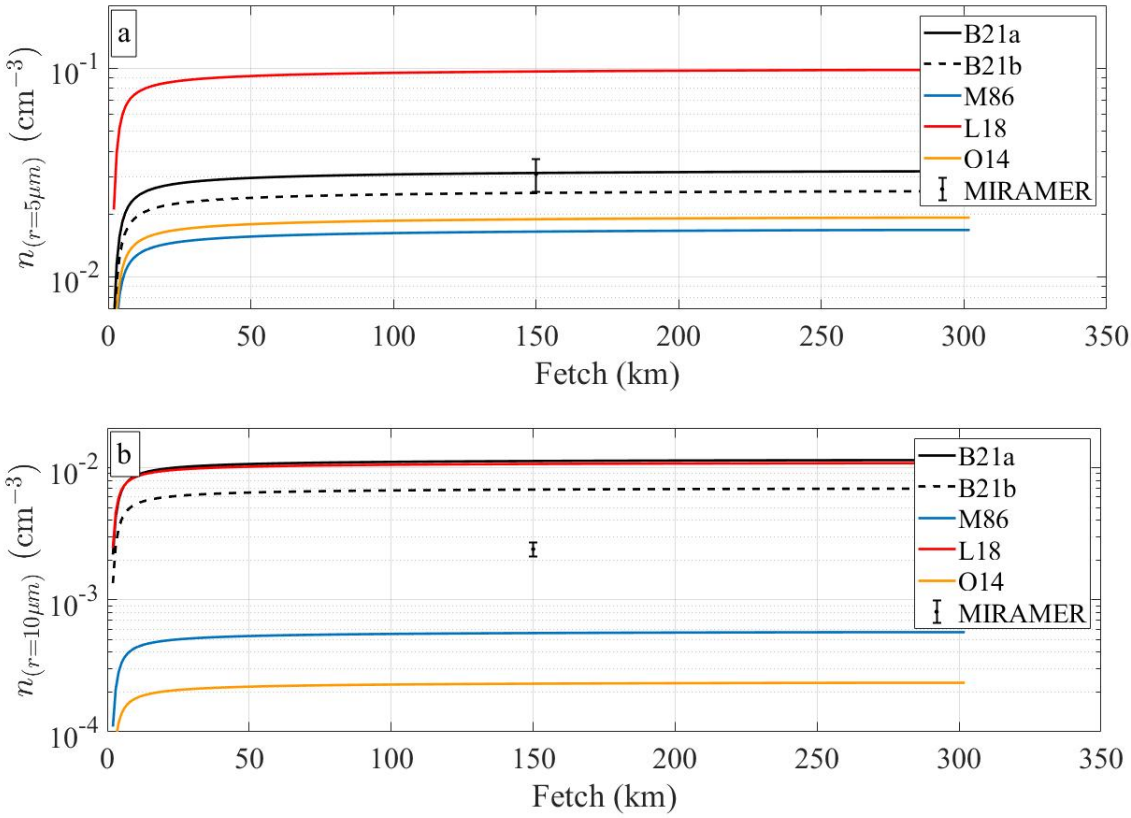

Figure 4.3: MACMod simulated concentrations of (a) 5µm and (b) 10µm radius particles represented as a function of increasing fetch length, for $U_{10} = 16$ m s^{-1}. Black curves represent the B21a (solid line) and B21b (dashed) SSGFs. M86, L18 and OVA14 SSGFs are represented by blue, red and orange solid lines, respectively.

At $U_{10} = 16$ m s^{-1} (cf. Fig. 4.3) and the smaller 5µm particles, no significant deviation is found between B21a and the data. Relative to observations, B21b, OVA14 and M86 understimate by factors 1.5, 2 and 2.2 respectively, and L18 overestimates by a factor 6.5. For the larger 10µm particles, deviations between the model and the single available station are larger. For B21b, L18 and B21a, the model overestimates by factors 4.3, 8 and 8.3, respectively. For M86 and OVA14, the model underestimates by factors 6 and 9.2, respectively.

For both wind speeds, concentration increase for increasing fetch, but converge towards a constant value for fetches greater than 100 km, approximately. As both the wind speed and $\langle S^2 \rangle$ are constant over the length of the domain, this suggests that the sea spray generation and sedimentation fluxes have reached equilibrium. Available MIRAMER data for the evaluation of MACMod parameterizations are scarce, especially at high wind speeds and with the fetch lengths required required for comparison with the model.

The MACMod model simulates sea spray generation and transport as a function of fetch. Though wave-wind coupling is not activated, it is possible to prescribe fetch-dependent wave parameterizations at the surface. In the above, the wave-slope vari-

ance $\langle S^2 \rangle$ used for B21a abd B21b SSGFs was obtained using the corrected wind speed-dependent Cox and Munk (1956) formulation (CM) (cf. Sect. 3.4), and is therefore constant and independent of the fetch. We have shown from laboratory observations and a wave spectral model that $\langle S^2 \rangle$ generally decreases for increasing wave age. We investigate the effects of wave age on the B21a SSGF by prescribing upwind $\langle S^2 \rangle$ estimates to sea surface in MACMod, obtained using the Elfouhaily et al. (1997) model (ELF). Figure 4.4 presents MACMod sea spray concentrations for the B21a with the corrected CM formulation (herein B21aCM, horizontal axis) versus B21a using the ELF model (herein B21aELF, vertical axis). The wind speed is U_{10} = 10 m s^{-1}, and the concentrations are extracted 13 meters above the MWL. The coloured dots allow to compare B21aCM and B21aELF concentrations for 0–300 km fetch lengths at a 1 km resolution.

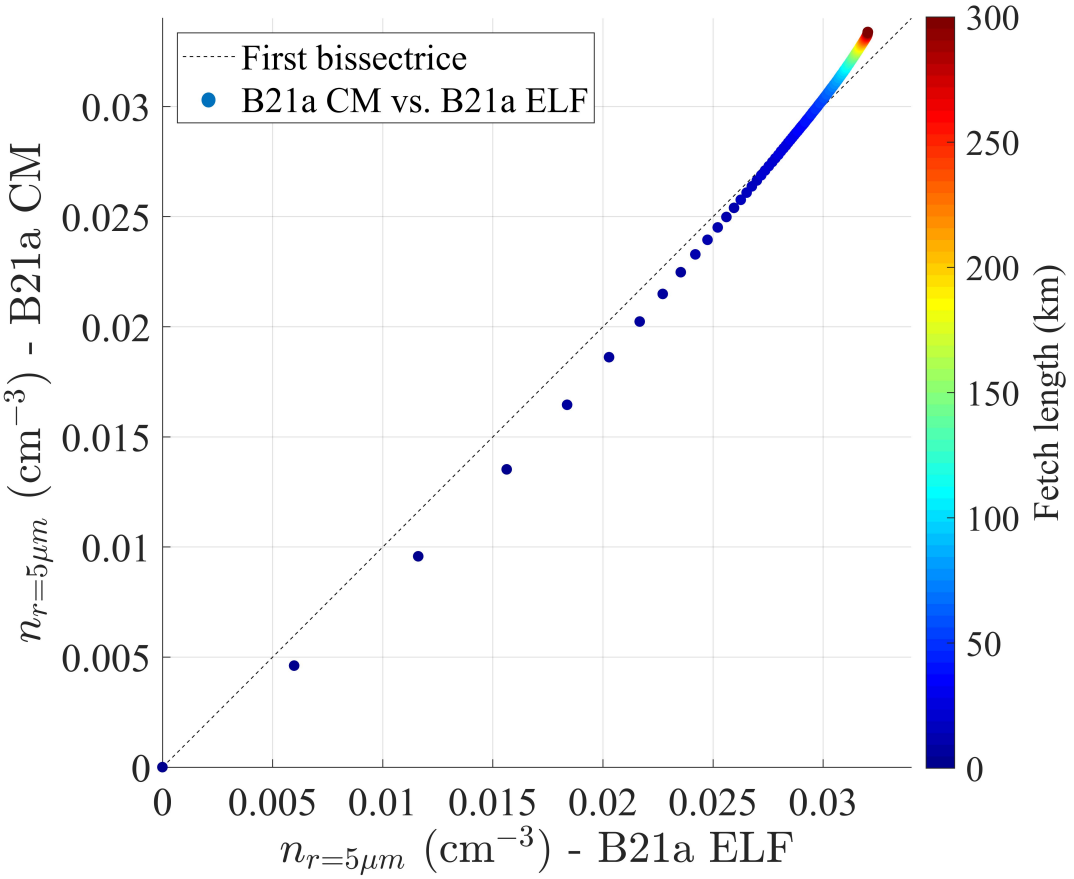

Figure 4.4: Comparison of MACMod simulated sea spray concentrations using the corrected Cox and Munk (1956) (vertical axis) and Elfouhaily et al. (1997) (horizontal axis) formulations for the calculation of the wave-slope variance, here for the B21a SSGF and U_{10} =10 m s^{-1}. The comparison between B21a-ELF and B21a-CM is represented by the colored dots, the color scheme of which indicates the fetch length of each simulated concentration. The dashed line represents the first bissectrice.

Results show that B21aCM concentrations are relatively lower than for B21aELF up to the 30 kilometer fetch mark. At its peak, the deviation between both parameterizations reaches 11 % relative to the first bissectrice. For fetch lengths greater than 30 km, B21aELF concentrations decrease to become lower than that predicted by B21aCM, by approximately 5%. The concentrations predicted by both parameterizations tend towards a constant value for fetch lengths above 250 km. The behaviour of B21aELF corroborates the decrease in $\langle S^2 \rangle$ with wave age observed in Sect. 3.4.1. According to these results, accuracy in sea spray generation can be expected to increase when considering the wave age dependence of $\langle S^2 \rangle$. Further research is required to assess the possible use of the ELF model for the forcing of B21a and B21b laboratory-based source functions in regional models such as MesoNH.

4.4.2 MesoNH

MesoNH simulations of sea spray generation and transport are interpreted and compared with field observations collected during MIRAMER and SUMOS field campaigns. To limit numerical simulation and storage costs, MesoNH simulations over the MIRAMER period were limited to the 19^{th}–26^{th} May 2008 period, with 13 of the 17 sample stations (cf. Table 2.1, Sect. 2.2.1). Similarly, simulations run over the SUMOS campaign ranged over the ten day 10^{th}–20^{th} February 2021 period. For clarity, only the results of the B21b SSGF are shown over the MIRAMER study period, whilst B21a, B21b and OVA14 SSGFs performances are shown for SUMOS.

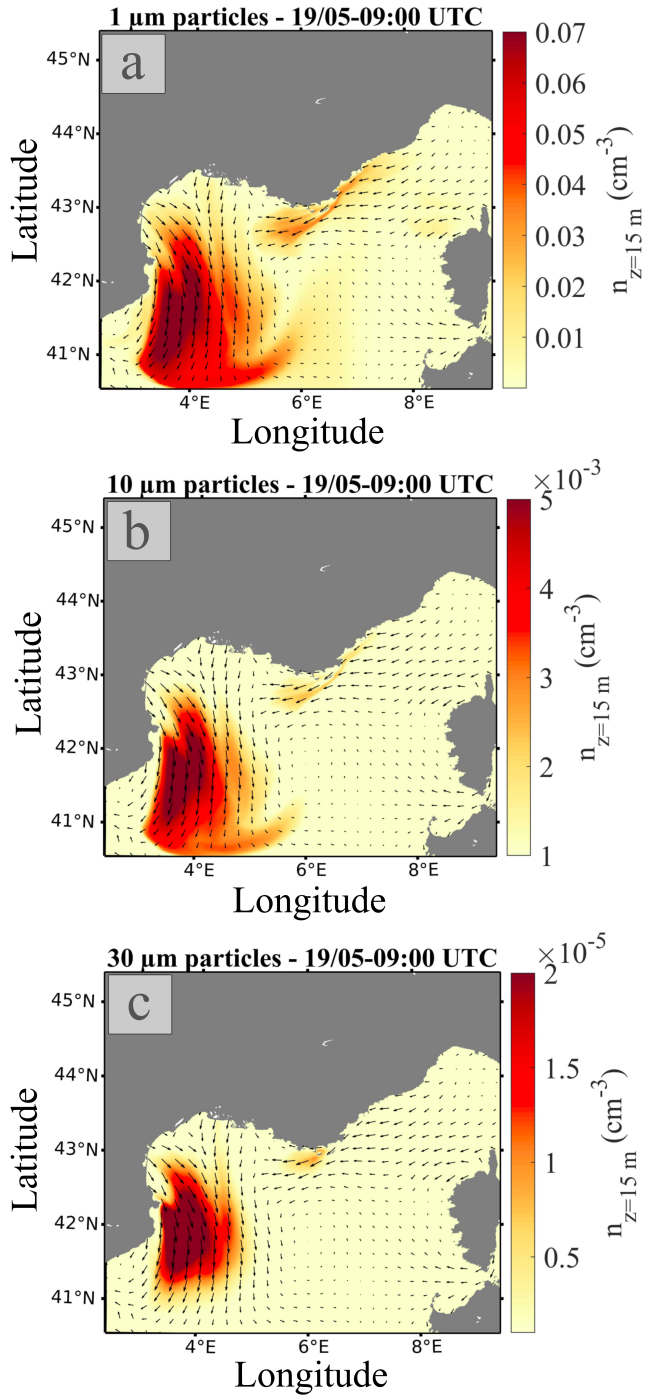

Figure 4.5: B21b MesoNH predictions of sea spray number concentrations in the North-Western Mediterranean, 15 meters above MWL of sea spray for radii (a) 1, (b) 10, and (c) 30 µm.

The MesoNH numerical simulations are run over the MIRAMER campaign period. A first observation is the apparent relationship between wind speed and sea spray concentrations. Figure 4.5 presents examples of aerosol concentrations obtained 15 meters above the MWL on the 19th May 2008 for radii 1, 10 and 30 µm and the B21b SSGF. Wind direction and intensity are represented by arrow directions and size. For all presented radii, concentrations increase with wind speed. In the South-West of the study domain, the model predicts Northerly winds reaching up to 12 m s^{-1} (U_{10}) off the Spanish coast generate a plume of sea spray. We can note that the spatial extent of the plume is greater for the smaller particles (cf. Fig. 4.5a). As we look at increasingly larger droplets in Figs 4.5 b–c, the spatial extent of the plume becomes smaller. This is in agreement with the higher residence times of smaller particles that can travel further, in contrast with the greater deposition fluxes of heavier spume droplets. To verify the accuracy of the model, we compare MesoNH wind speed and number concentrations with measurements made onboard the R/V Atalante at the same height above the MWL, using a nearest neighbour technique.

Figure 4.6 presents timeseries of wind speed (cf. Fig. 4.6a) and sea spray number concentrations (cf. Fig. 4.6b) over the duration of the MIRAMER campaign. Solid grey lines represent the model outputs, and the black open circles represent MIRAMER measurements. In cases where no field data is available, the represented scalars are taken from

the average vessel location during the campaign. Doubled black circles indicate when a station spread over two hourly model outputs. Over the study period, the wind speed is slightly underestimated by the model with a average 6.9 m s^{-1}, compared with 7.3 m s^{-1} measured onboard R/V Atalante. This 5% overall deviation is quite small, but reaches much higher values at individual stations, reaching a factor 7 underestimation by the model at 18:30 UTC on 20th May 2008. In a similar fashion, the model overestimates concentrations overall, as can be seen from Fig. 4.6b for 3.5 µm droplets. Though not graphically represented, on average the model underestimates concentrations relative to observations for radius 1.5 µm by a factors 2.5. The model overestimates concentrations for radii 3.5 and 10 µm by factors 3.2 and 1.6, respectively.

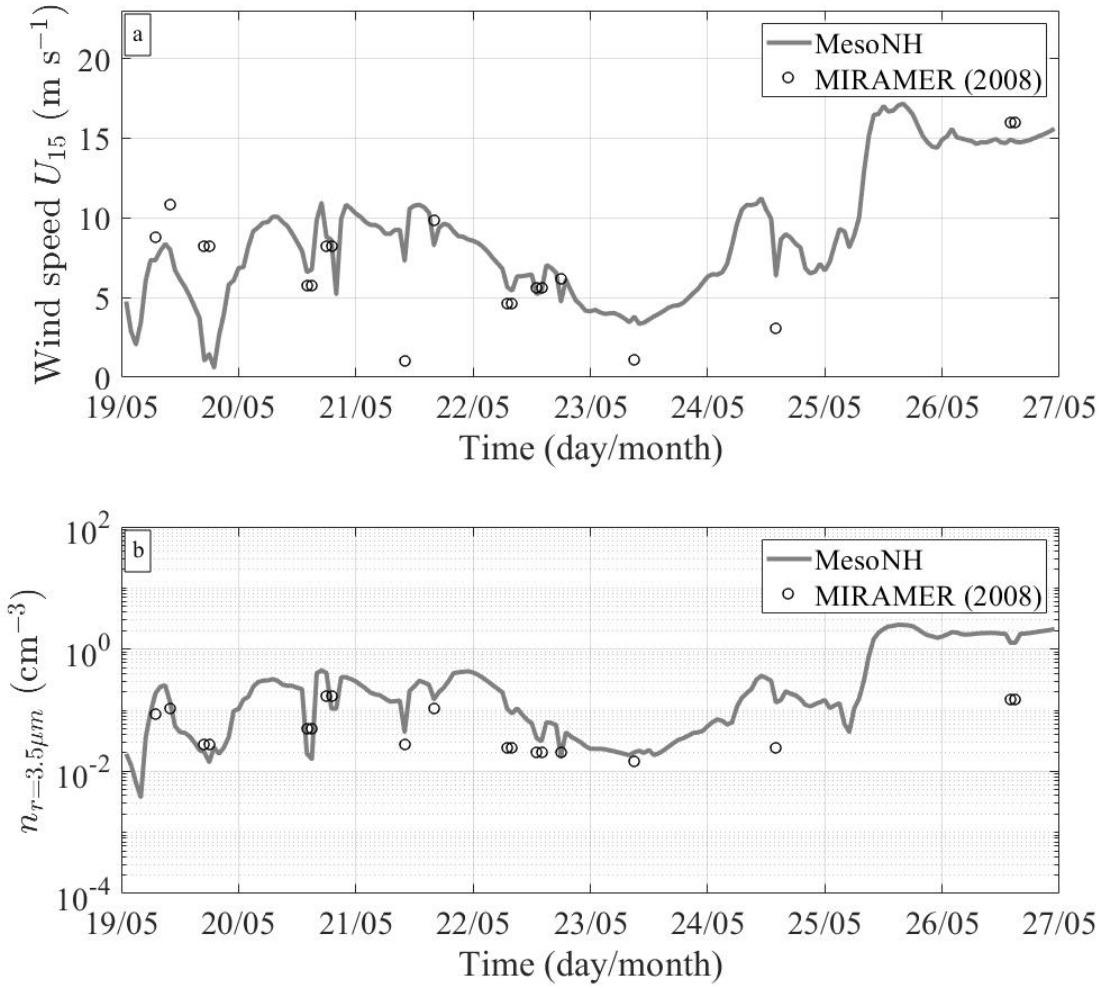

Figure 4.6: MesoNH predictions (solid grey line) and MIRAMER observations (black open circles) (a) wind speed and (b) sea spray concentration estimates 15 meters above the MWL.

As we further investigate model performance, Fig. 4.7 illustrates the regression lines opposing observation and model results for wind speed (cf. Fig. 4.7a), and sea spray concentrations for 1.5, 3.5 and 10 µm radius (cf. Fig. 4.7b–d). The strong deviations in each case are highlighted by the moderate to low R^2 values of the regression lines. In

agreement with Fig. 4.6a, Fig. 4.7a shows that the wind speed is generally overestimated by the model for speeds below 6 m s^{-1}, and underestimated for higher wind speeds. Signficant deviations limit the linear regression line R^2 values to 0.71.

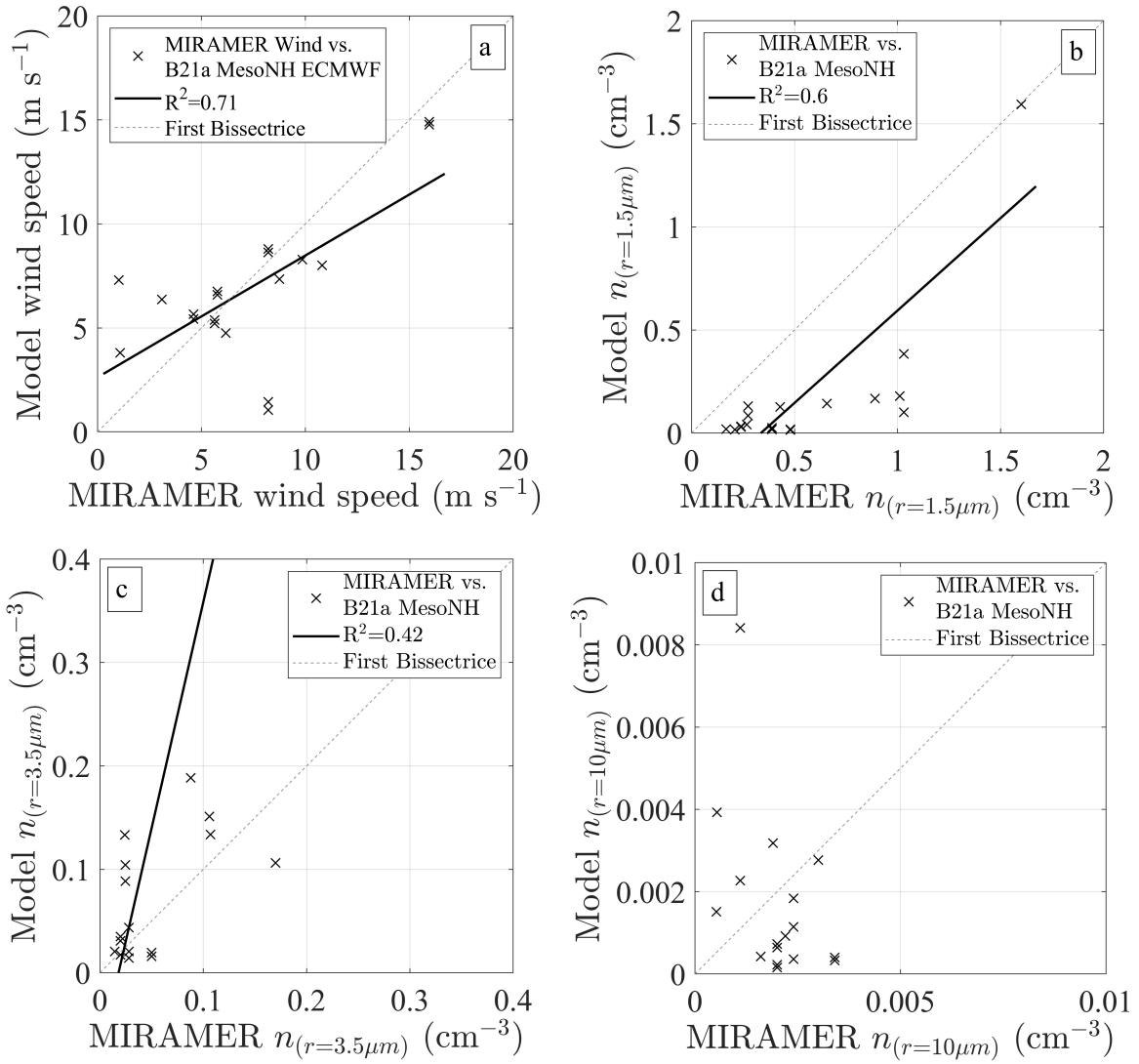

Figure 4.7: MIRAMER (horizontal axes) and MesoNH model (vertical axes) comparative plots of (a) wind and (b–d) sea spray concentrations. Presented concentrations correspond to radii (b) 1.5, (c) 3.5 and (d) 10 µm. Sea spray generation is parameterized using B21b. Regression lines (black solid lines) and corresponding R^2 values are shown.

The wind speed drives sea spray generation in OVA14, and especially B21a and B21b SSGFs as a result of the corrected Cox and Munk (1956) parameterization for $\langle S^2 \rangle$. Current MesoNH simulations (cf. Fig 4.5) allow to reproduce the general increase in sea spray concentrations for increasing winds, as observed in the field (cf. Fig. 2.4, Sect 2.2). When comparing model results with MIRAMER field observations, results show that the model fails to accurately reproduce observed wind events, and therefore sea spray concentrations (cf. Fig. 4.7). Recalling that the study area is close to the coastline, a possible explanation for the observed discrepancies could be the proximity of the study area to the coastline and resulting orographic pertubations that the model may stuggle to reproduce. Another

possible source of error may be the validity of the B21a and B21b SSGFs at such low wind speeds. Whilst the underestimation of the smallest droplet concentrations (cf. Fig. 4.7b) is expected as they stand out of the SSGFs 3–35 μm radius range, the overestimation of modelled sea spray concentrations may also result from the limited U_{10} 16–20 m s^{-1} validate range in the laboratory. Finally, the observed discrepancies may also result from the MIRAMER field data. Indeed, the short MIRAMER sample durations (cf. Table 2.1, Sect. 2.2.1), and the possible obstruction of a CSASP sensor by a nearby navigation light, may have resulted in poor count statistics, which particularly effect the accuracy of the larger droplet concentration estimates. Further study is necessary to understand the origin(s) of such discrepancies.

MesoNH during SUMOS

As presented above for the MIRAMER campaign, we compare MesoNH predictions with field data collected during the SUMOS campaign. As the model produces an aerosol concentration spectrum over a desired size range, comparison can be made with the measured spectra in the field. To this end, we fit a polynomial function to each averaged spectrum at each sample station, which allows to smooth the spectrum (cf. Fig. 4.10).

Figure 4.8 shows that in contrast with the MIRAMER campaign, good agreement is found between modelled and observed wind speed 15 meters above the MWL. As done in the Mediterranean study domain, a nearest neighbour method is used to find the model outputs closest in space and time to the SUMOS aerosol stations. Over the study period, mean observed and modelled wind speeds are 12.6 and 12.1 m s^{-1}, respectively. The model understimates the wind speed by 4% relative to observations. The model successfully reproduces the wind speed variations during the study period, as shown by Fig. 4.8a with R^2 =0.93 for all considered stations. The model seems to underestimate high wind speeds, as shown in Fig. 4.8b where the model wind speeds seem to reach a maximum in the whereabout of 16 m s^{-1}. This can also be observed in Fig. 4.8a where the model does not successully reproduce the observed peak at 21.4 m s^{-1} on 12th February 2021. However, the satisfactory model accuracy over the presented stations allows to better evaluate the sea spray transport performance with B21a and B21b wind-forced SSGFs.

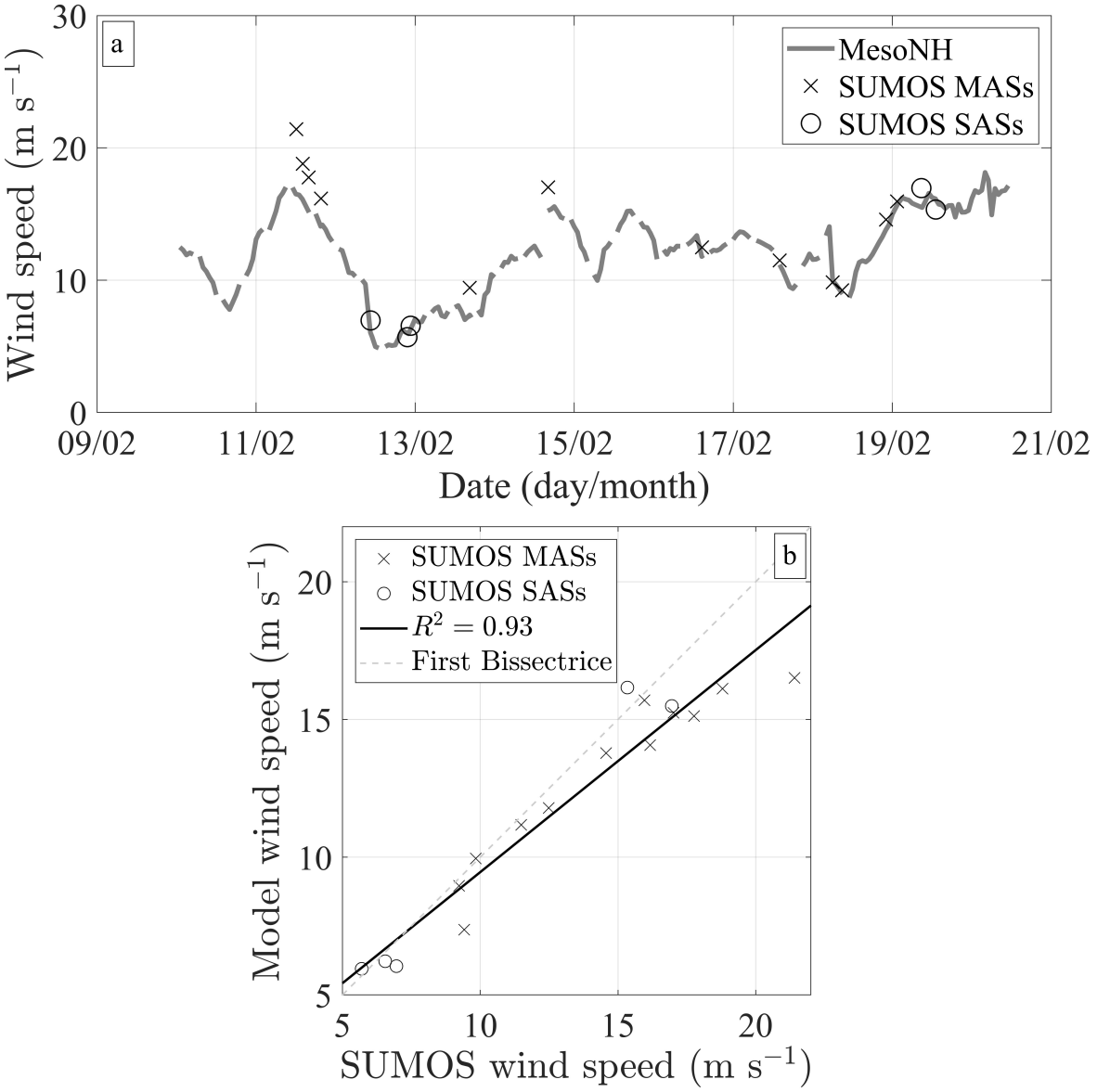

Figure 4.8: (a) timeseries of SUMOS foremast wind speed measurements at mobile (X symbols) and stationary ($\circ$ symbols) aerosol stations, and MesoNH modelled wind speeds at each R/V Atalante location. (b) Regression plot comparing measured (horizontal axis) and modelled (vertical axis) wind speeds at the vessel location, and the corresponding R^2 value.

In Figure 4.9, concentrations modelled using B21a, B21b and OVA14 SSGFs are compared with foremast sea spray measurements, with the example of 2.25 (cf. Fig 4.9a), 9.5 (cf. Fig 4.9b) and 19.75 µm (cf. Fig 4.9c) sea spray particles. The corresponding statistics are presented in Table 4.2 below. Similar to observations made from the SUMOS field data in Sect. 2.3.2 the highest winds do not necessarily correspond with the highest concentrations for droplets below 5 µm radius (cf. Fig. 2.11). Despite the highest observed winds on 12$^{\text{th}}$ February 2021, measurements and numerical simulations all point towards higher 2.25 µm particle concentration events over the 14–17 May 2021 period. The 14–17 February 2021 period was marked by southerly winds and longer fetches compared to the 12$^{\text{th}}$ where winds were south-easterly and the sample stations were closer to the coastline (cf.

Figs 2.6 & 2.8, Sect. 2.3.1). These different fetches allow smaller particles to accumulate in the MABL. For these smaller 2.25 µm particles, deviations between the three SSGFs reach up to an order of magnitude in some cases. On average, the OVA14 SSGF leads to concentrations 3.53 times lower than observed in the field, and displays similar sensitivity to weather events as the other SSGFs. For smaller particles, the OVA14 SSGF results in a strong overestimation of concentrations, reaching five orders of magnitude for r = 0.1 µm (cf. Fig. 4.10). For particles greater than 3 µm, OVA14 leads to a strong underestimation of concentrations exceeding six orders of magnitude at radius 9.5 µm. For particles greater than 5 µm, the highest concentrations are found for the highest modelled wind conditions, as shown with the examples of Figs. 4.9b–c. This is reminicent of the observation made from simulations made during the MIRAMER campaign, showing a stronger dependence of sea spray concentrations on more local winds for increasingly large droplets. Across the measured concentration spectrum, the B21b SSGF demonstrates a particularly good sensitivity to the range of wind conditions by better reproducing concentrations in high wind (e.g. 12$^{\text{th}}$ February) and lower wind conditions (e.g. 13$^{\text{th}}$ February) compared with OVA14 and B21a SSGFs. Overall, the good results obtained with B21b are corroborated by the lowest $RMSE$ and deviation factors values calculates relative to the field data (cf. Table 4.2). An exception to this rule is the statistically comparable performance of the B21a SSGF over the spume droplet range, i.e. radii in the vicinity of 20 µm and above. Over the study size range the B21a SSGF generally does not allow to correctly represent concentrations at low and moderate wind speeds, but seems to perform better when the model wind speed is greater. Such observations made for B21a may be a result of the laboratory study 16–20 wind speed range. Laboratory results also indicate that B21a is best suited for the spume droplet range, which can potentially explain these modelling results.

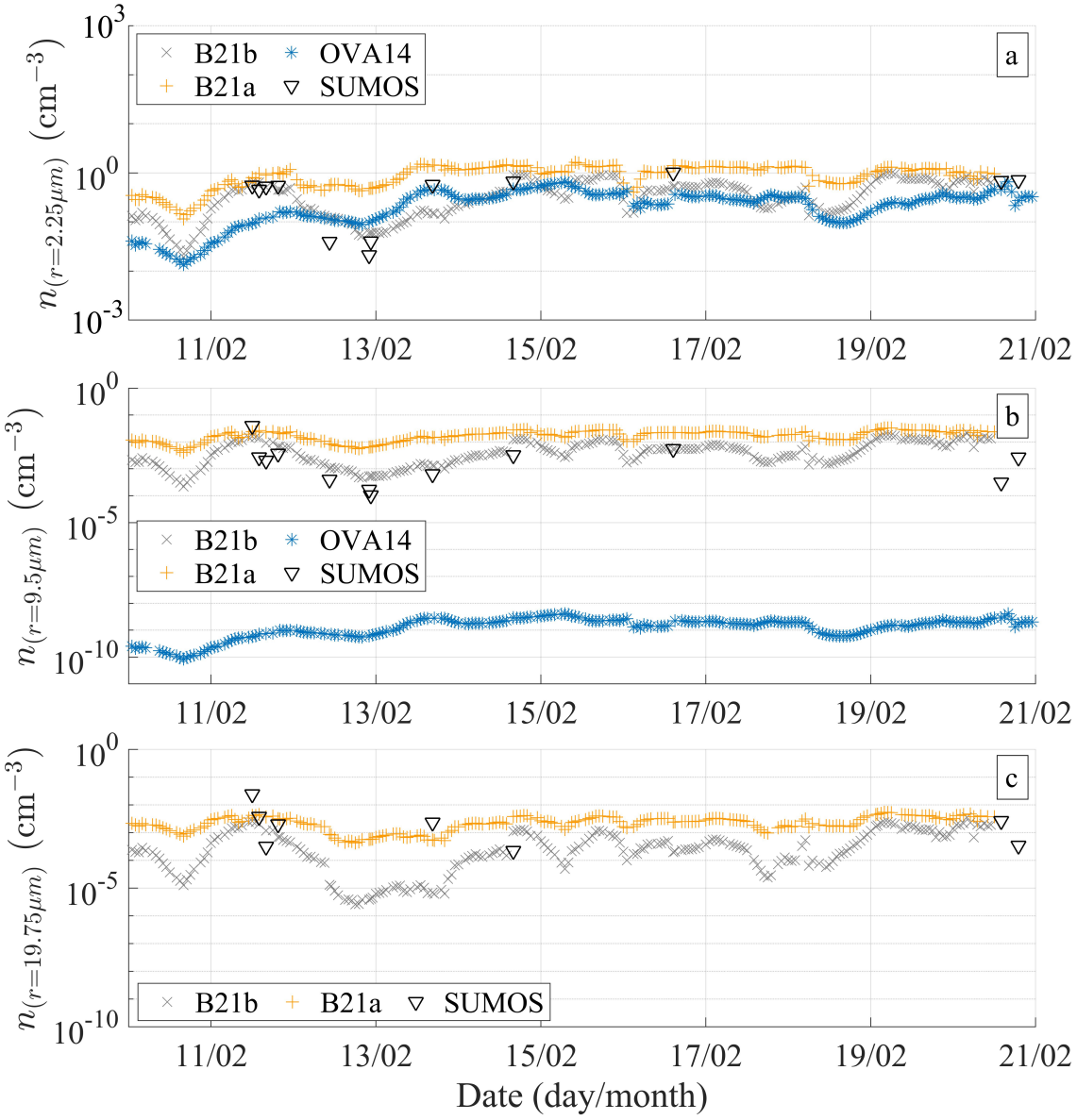

Figure 4.9: Examples of modelled and observed sea spray concentrations for particle radii (a) 2.25, (b) 9.5 and (c) 19.75 µm. Field observations (black open triangles), and modelled concentrations using B21a (orange "+" symbols), B21b (grey "×" symbols) and OVA14 (blue "∗" symbols) SSGFs are shown.

Table 4.2 presents statistics describing MesoNH model performances for the prediction of sea spray concentrations at the SUMOS sample locations. The deviation factor is calculated by dividing the mean measured concentrations by the mean modelled concentrations, and better highlights the deviations of sometimes several orders of magnitude. OVA14 performance is not shown for the 19.75 µm as a result of the ever-increasing deviations for increasing sea spray droplet size.

Table 4.2: Model concentration statistics for B21a, B21b and OVA14 SSGFs at the considered SUMOS sample stations. Statistical measures include simulation standard deviation, as well as the deviation factor, the coefficient of determination R^2 and the root mean square error ($RMSE$) obtained relative to field observations. Examples of results are presented for sea spray particles of radius 2.25, 9.5 and 19.75 µm.

	2.25 µm radius			9.5 µm radius			19.75 µm radius	
	B21a	B21b	OVA14	B21a	B21b	OVA14	B21a	B21b
Deviation factor	0.56	1.24	3.56	0.23	0.64	4.8×10^{6}	1.15	3.98
Standard deviation	0.33	0.28	0.15	0.008	0.0056	10^{-9}	0.0015	8.3×10^{-4}
Determination coefficient R^2	0.73	0.47	0.11	0.05	0.35	0.01	0.07	0.25
Root mean square error	0.46	0.23	0.47	0.02	0.008	0.01	0.006	0.006

4.4.3 Combining OVA14 with B21 SSGFs

An objective of this thesis is to propose a wind and wave dependent SSGF spanning the largest possible size range. Indeed, the ability to accurately predict sea spray concentrations over a wide range of particle sizes offers a more complete understanding of their contribution on weather-making and climate processes, such as cloud formation and radiative effects. Completing the laboratory SSGFs with the OVA14 SSGF is suggested in Sect. 3.3.1, where the generation flux intensities show reasonable agreement around 2 µm, where both parameterizations meet. This is further investigated here, as we aim to combine the modelled concentrations using the OVA14 and B21a SSGFs. To verify these results, the MesoNH model aerosol spectra are compared with the aerosol spectra measured during SUMOS.

Figure 4.10 presents model and measured aerosol spectra, with the example of the 14$^{\text{th}}$ February 2021 at 4 PM (UTC) and U_{10}=16.6 m s^{-1}. The MesoNH modelled B21b (thick grey line) and OVA14 (thick blue line) concentration spectra are shown. The concentrations of both SSGFs reach similar values over the 1–2 µm radius range, similar to the generation fluxes (cf. Sect. 3.3.1). As briefly described above, the OVA14 SSGF significantly overestimates concentrations relative to observations for smaller particles, reaching five orders of magnitude for radius r= 0.1µm. For larger particles, the OVA14 SSGF results in a equally signifcant underestimation of concentrations. The B21b SSGF makes for a reasonably good fit to observations over the SSGF validity range, but strongly underestimates concentrations beneath it. Data collected at the top of the foremast, limited to the maximum 22.75 µm radius, does not allow to evaluate the performance of the model up to the 35 µm laboratory validity range of B21b.

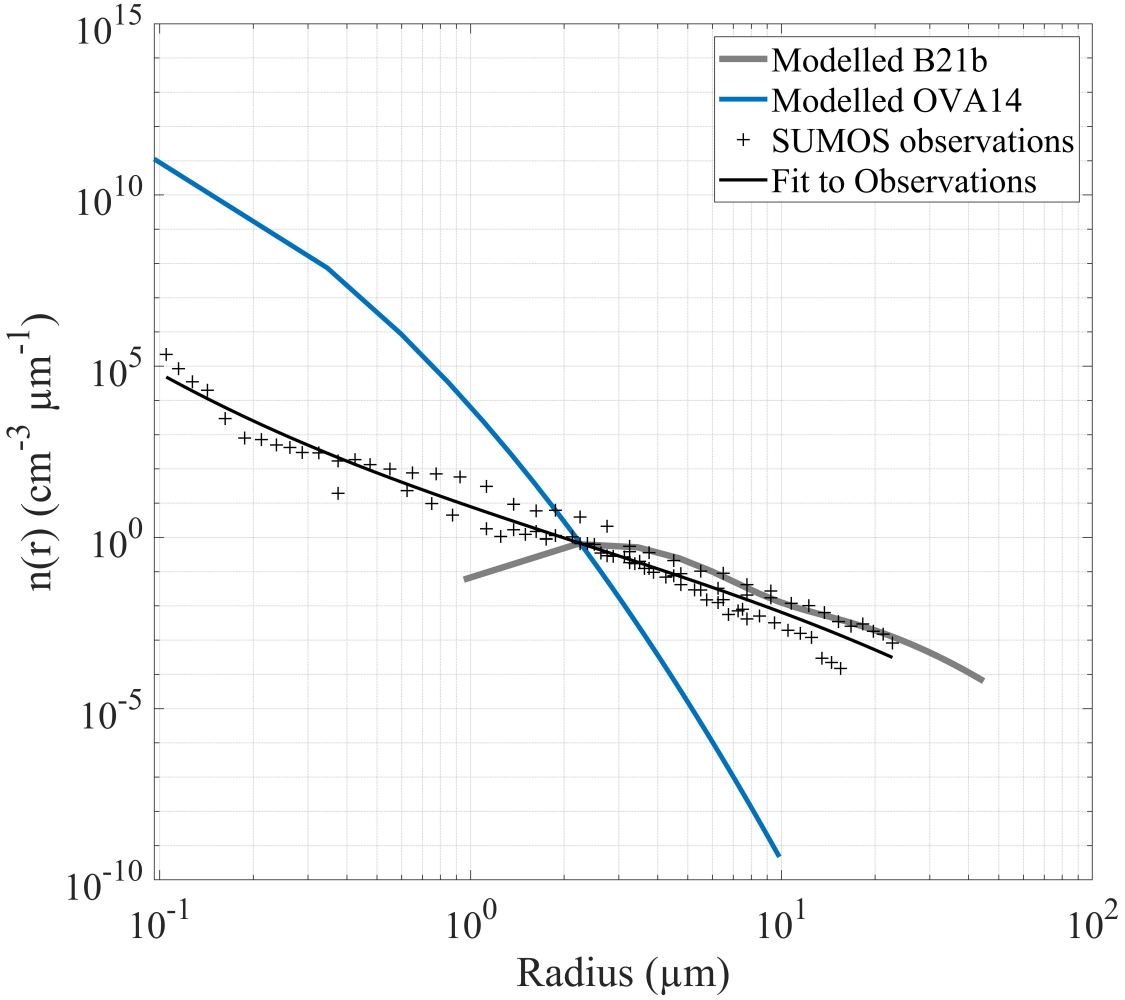

Figure 4.10: MesoNH modelling results with B21b (solid thick grey line) and OVA14 (solid thick blue line) SSGFs, and corresponding SUMOS aerosol observations (black "+" signs). A fitting curve is shown, as used for the comparison between field and model observations (thin black line).

Study results indicate numerical simulations using OVA14 do not allow to accurately reproduce the concentrations measured onboard the R/V Atalante. The OVA14 generation flux of these smaller and longer lifetime particles may be too strong, leading to the accumulation of large quanties of these smaller aerosols. The OVA14 SSGF therefore cannot be used to extend the laboratory B21a and B21b – performing reasonably well in full scale conditions – to smaller particles. Further study is required to understand these results, such as the verification of model significant wave height estimates. The model may also fail to represent some atmospheric aerosol sinks, such as wet aerosol deposition. Indeed, the 12$^{\text{th}}$ and 13$^{\text{th}}$ were met with mild rain conditions, which may have partially depleted the atmosphere of long-living and long-travelling aerosols.

Concentration Profiles and Optical Depth

The atmospheric optical depth (herein AOD) describes the opacity of the atmosphere to incident solar radiation as a result of the absorbing and scattering effects of atmospheric aerosols. In coastal regions, marine aerosols can become dominant (Katoshevski et al. 1999; Sellegri et al. 2001), and can therefore be expected to affect the AOD. The AErosol RObotic NETwork (AERONET) boasts 25 years of AOD measurements from observatories over the globe. We present a tentative approach for the study of sea spray concentrations and the contribution to the AOD using AERONET AOD measurements made at the coastal Saint Mandrier (Var region, South of France) observatory in 2008, at the same time as the MIRAMER campaign. We focus on the 21st May 2008 where the weak ($\approx$ 2 m s^{-1}) and North-Westerly winds in the morning change to become mild ($\approx$ 11 m s^{-1}) and of Westerly origin in the afternoon (cf. Fig. 4.10b).

Figure 4.10c compares the AERONET AOD (red open circles) with sea spray concentrations modelled with MesoNH using the B21b SSGF at the location of the Saint Mandrier observatory. Results show that the measured AOD oscillates around 0.16 during the day, but reaches 0.24 towards 6 PM (UTC). The modelled concentration of 7 μm sea spray particles, shown by the blue solid line, increases during the day as a result of the increasing wind speed. Whilst the increased sea spray concentration is expected to contribute to the increase in AOD, any obvious correlation cannot be observed. Exceptions even arise, such as the peak in AOD at 6 AM, occuring during light winds in the absence of sea spray, and therefore probably resulting from a number of continental aerosol sources such as dusts or pollution. The choice of the Saint Mandrier observatory data results from AOD availability during the MIRAMER simulations, but also allows to highlight the frequent issue of orographic effects for this type of approach, often reliant on coastal observatories. Indeed, as can be seen in Fig. 4.10a, the Saint Mandrier station (black dot) is sheltered from Westerly winds by land. In such cases, classical models do not sufficient physically and spatially resolve the processes at play. Furthermore, the estimation of the sea spray contribution to the AOD requires a complete spectrum, as proposed by the combination of OVA14 and B21 SSGFs. An example of coastal processes that are omitted in current numerical simulations is the effect of bathymetric wave breaking on sea spray generation (De Leeuw et al. 2000; Van Eijk et al. 2011).

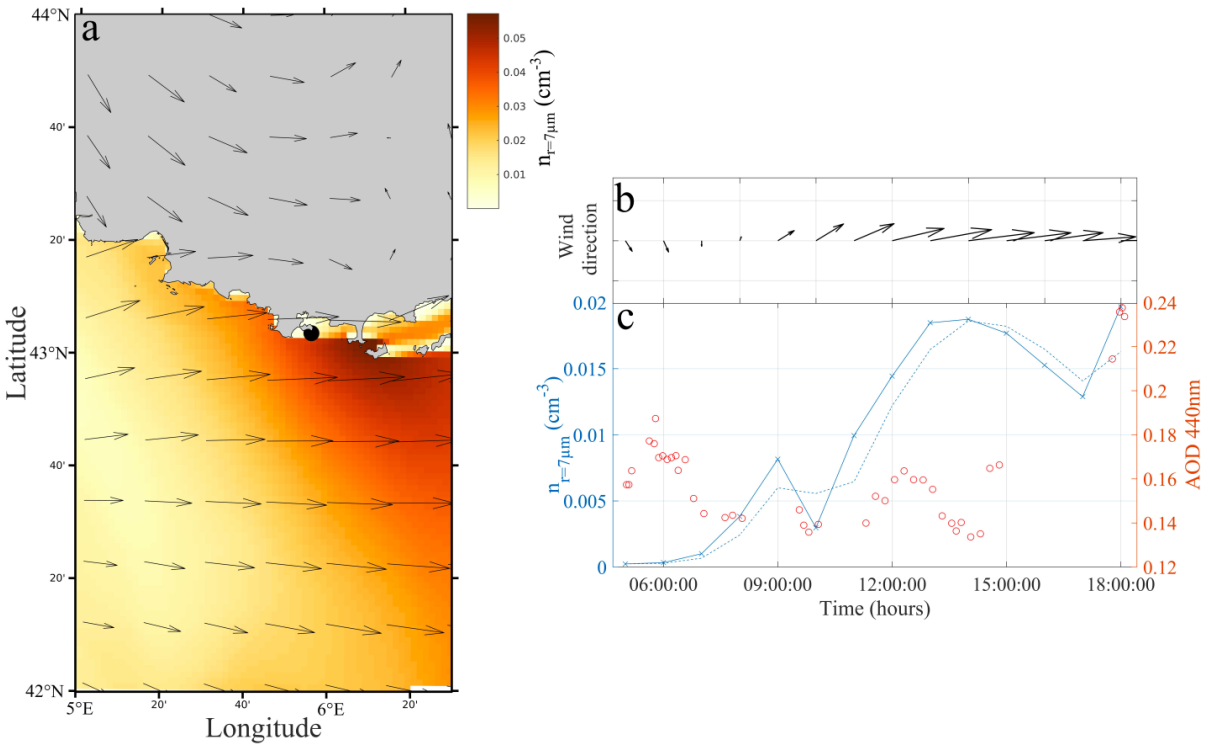

Figure 4.11: Use of (a) modelled sea spray concentrations of 7 µm particles with MesoNH using the B21b for comparison with (c) AERONET AOD measurements (red open circles) at the Saint Mandrier observatory (black dot in panel a). The modelled wind speed and direction are indicated in panel. Wind directions are also shown in panel a (arrow), as well as 15 meter altitude concentrations on 21st May 2008 at 4 PM. Panels b–c are courtesy of Alexandra Cuevas (MIO).

The role of sea spray on atmospheric optical depth, as well as the fate of sea spray in coastal and continental regions is an active field of research. The estimation of the sea spray contribution to the AOD requires accurate knowledge of sea spray aerosols over the entire size spectrum, as well as the associate wavelength-dependent aerosol extinction. The MIO laboratory has been investigating the impact of atmospheric extinction by marine aerosols as part of the ANR MATRAC project. The collection of AOD, aerosol concentration and composition measurements from observatories at Mediterranean and Atlantic-facing locations aims to further improve the fetch-dependent MEDEX extinction code (Piazzola and Kaloshin 2005).

4.5 Discussing Numerical Modeling Results

MACMod and MesoNH models are parameterized with field and laboratory-derived SS-GFs. Model results are compared with field data collected in the North-West Mediterranean and the North-East Atlantic during the MIRAMER and SUMOS reseach cruises. Atmospheric humidity as well as air and water temperature measurements during both campaigns allow to assume low air-droplet heat fluxes, and r_{80} droplet equilibrium radii

in relative humidity conditions close to 80%. In these conditions, Eulerian models allow to predict wind speed sea spray generation and tranport with acceptable error.

In the case of the MIRAMER campaign, discrepancies between modelled and measured wind speeds at the research vessel locations is a possible explanation for the strong deviations observed for sea spray concentrations. In this case, the performance of the SSGFs cannot be evaluated. Such deviations may result from the proximity of the study area to the coastline, inducing orographic effects on the flow which the numerical may not fully resolve as a result of the 2 km grid resolution. Comparison between observed and modelled concentrations is especially complicated for particles greater than 5µm radius, where no agreement is found between the model and observations (cf. Fig. 4.7d). Another possible source of error are the MIRAMER sea spray measurements which were hampered by relatively low wind speeds and short sampling durations which can be detrimental to count statistics. Further research is required to investigate the accuracy of both model and field observations.

MesoNH performance is much improved in the context of the SUMOS campaign, as shown with a $R^2 = 0.93$ value and a small bias between model predictions and field observations of wind speed. During SUMOS, the average deviation between laboratory SSGFs and observations over the study period is relatively low. This suggests that the corrected Cox and Munk (1956) formulation representative of the upwind $\langle S^2 \rangle$ in the laboratory results in a satisfactory sea spray flux amplitude across a range of wind conditions. As also shown using the MACMod model, the OVA14 performs reasonably well for particles on the 1–5 µm radius range, but increasingly underestimates concentrations for larger particles, and overestimates concentrations for smaller particles. B21b laboratory SSGF performs best over the film, jet and spume droplet ranges, but underestimates spume droplets at wind speeds, especially below 15 m s^{-1}. The B21b laboratory SSGF, initially calibrated from data collected over the U_{10} 16–20 m s^{-1} range and deemed valid over the U_{10} 12–20 m s^{-1} range, is scaled by $\langle S^2 \rangle$ and u_*^3, the latter being commonly used for the scaling of wave energy dissipation and the wave–wind momentum flux (Wu 1988; Fairall et al. 2009). Whilst more data is required to investivate this, u_*^2 may be more applicable than u_*^3 for wind speeds below 15 m s^{-1}, as also suggested by Andreas (1998). Similarly, MesoNH results show that the B21a SSGF does not allow for the accurate prediction of wind speeds below 15 m s^{-1}, suggesting that the SSGF is especially adapted to the 16–20 m s^{-1} wind speed range, and maybe higher. The good modelling results in the North-East Atlantic are encouraging. Further research in a wider range of conditions is necessary to better evaluate the potential of the laboratory SSGFs, but is hampered by rare field observations at such high wind speeds. Field data combining wind, wave and sea spray measurements, necessary for the validation of regional models remains scarce.

The B21b and OVA14 concentration spectra are tentatively compared, with the aim of combining both parameterizations and thus offering a more complete formulation for sea spray. Results show that the OVA14 SSGF leads to systematic significant deviations

in concentrations from the experimental data other than over the 1–5 μm radius range (cf. Fig. 4.10), despite earlier promising results when comparing both size-dependent generation flux strengths (cf. Fig. 3.10). As the B21b proved to best match the field data over the SSGF's radius validity range, we attempt to relate the modelled sea spray concentrations to the aerosol optical depth (AOD) in the context of the MIRAMER campaign. Whilst there is no clear outcome of this attempt, the approach suggests AOD measurements gathered over 25 years by AERONET as an additional method for the validation of aerosol concentrations, considering the otherwise scarce field aerosol observations. For this to be achieved, suggest that possible difficulties for numerical models to resolve orographic effects be avoided by selecting wind conditions and AERONET stations favourable to the exposure of marine aerosols alone. Furthermore, the contribution of bathymetric wave breaking is not yet considered in models, and could allow to better understand the very complex atmospheric composition in coastal regions.

Chapter 5

Discussions and Conclusions

Contents

5.1 Discussion

5.1.1 Laboratory Wind and Wave Dependent SSGFs

The sea spray generation flux, traditionally scaled with wind speed (Smith et al. 1993; Gong 2003), is increasingly scaled with wind and wave characteristics (Ovadnevaite et al. 2014; Troitskaya et al. 2018; Laussac et al. 2018). Indeed, sea spray generation is mainly associated with wave breaking and the ejection of large droplets from the breaking wave crests through surface tearing mechanisms. During the MATE2019 laboratory campaign conducted at the Pytheas Institute tunnel facility, the sea spray generation flux was obtained using the log-profile flux method. A range of wind and wave combinations was tested, allowing for different generation fluxes. Logarithmic wind and concentrations profiles show that all requirements are met for the use of this method, such as the positionning of aerosol probes in the constant flux layer above the emission layer, and the neutral conditions observed during the experiments.

Results show that over the spume droplet size range (r >20 μm), the wave-slope variance $\langle S^2 \rangle$ scales best with the generation flux. Over the study 7–35 μm radius range,

$\langle S^2 \rangle$ outperforms other non-dimensional number for the scaling of the generation flux, such as the wave age, and the wind–sea Reynolds number R_B. $\langle S^2 \rangle$ is in turn outperformed by the combined number $P_S = \langle S^2 \rangle u*^3/\nu_a g$, describing the wave-slope-variance-modulated wind-energy input to the waves. This is especially true over the 7–20 μm radius range where the smaller bubble-mediated jet droplets are dominant. u_*^3, used by authors to scale wave energy dissipation and the wave-wind momentum flux particularly contributes to these good performances. The concept of combined scaling parameters has also been explored by other authors (Brumer et al. 2017; Lenain and Melville 2017a). The laboratory fluxes are comparable to the range of SSGFs found in the literature for similar conditions, and two SSGFs are proposed for the scaling of the laboratory fluxes obtained over the U_{10} 16–20 m s^{-1} range (cf. Table 3.2, Sect. 3.3). Upon combination with the L18 SSGF, both SSGFs, scaled with $\langle S^2 \rangle$ (B21a) or P_S (B21b) are deemed valid over the 3–35 μm radius range, and the U_{10} 12–20 m s^{-1} range. The advantage of using $\langle S^2 \rangle$ for the scaling of sea spray generation resides in the strong connection with wave breaking (Stokes 1880; Duncan 1981; Ramberg and Griffin 1987) and surface tearing mechanisms such as airflow separation by describing sea surface geometry. In contrast with peak wave statistics represented in non-dimensional numbers such as wave age, or the wind–sea Reynolds number R_B, $\langle S^2 \rangle$ allows to consider multiscale wave statistics within the limits imposed by metrological and modelling constraints.

5.1.2 Upscaling Laboratory Results to the Field

The validity of the laboratory SSGFs in full-scale field conditions is investigated (cf. Sect. 3.4). To do so, the $\langle S^2 \rangle$ scaling parameter is compared with an existing formulation proposed from the omnidirectional field observations by Cox and Munk (1956) (denoted CM) as well as an omnidirectional wave spectral model (Elfouhaily et al. 1997) (denoted ELF). The linear relationship between the U_{10} wind speed and $\langle S^2 \rangle$ in the CM formulation is proportionate to the relationship observed in the laboratory when averaging across all wind and wave combinations. A correction factor applied to the CM formulation (cf. Fig. 3.12, Sect. 3.4.1) provides a good match to our data. This correction suggests that the laboratory $\langle S^2 \rangle$ is representative of the upwind component in a highly anisotropic wave field. Further investigation with the ELF model also suggests that this correction factor compensates the missing yet minor contribution of longer swell-type wave components in the laboratory is minor ($\approx 15\%$ of total $\langle S^2 \rangle$). The corrected CM formulation is chosen for the use of the laboratory SSGFs in numerical modelling efforts, and the relationship between $\langle S^2 \rangle$ and U_{10} is assumed linear. However, both laboratory observations and simulations with the ELF model suggest a higher order influence of wave age on $\langle S^2 \rangle$, with a observed decrease in $\langle S^2 \rangle$ for increasing wave age. As $\langle S^2 \rangle$ has been found to increase with the whitecap coverage, this corroborates the observed decrease of whitecap coverage for increasing wave age in the field (Schwendeman and Thomson 2015; Brumer et al. 2017).

An attempt is made to upscale sea spray concentrations from the laboratory to the field. The laboratory concentrations are corrected to the 10 meter reference using a vertical profile law proposed by Piazzola et al. (2015). To these corrected concentrations, and considering the wave age of the intermediate wave condition tested in the laboratory, we add the background concentrations calculated by the MEDEX fetch-dependent code (Piazzola and Kaloshin 2005). The sum of the corrected concentrations and the background concentrations results in concentrations similar to observations made during the MIRAMER campaign at a similar wave age. Though this approach is purely investigative, results seem to indicate that the laboratory concentrations are representative of the generation flux, with the absence of particles accumulated over long fetch lengths. In this case, the generation flux would seems to represent 10% of the overall concentrations measured in the field.

5.1.3 Sea Spray Transport Modelling

Both the MACMod and the MesoNH models are used in a complementary fashion for the study of sea spray transport. In both models, the sea spray flux is provided for particles having reached the r_{80} equilibrium radius for conditions of 80% relative humidity. This assumption, compatible with the used SSGFs as well as the conditions met during the MATE2019, SUMOS and MIRAMER campaigns, allows to neglect thermodynamic air-droplet effects on transport. The two-dimensional MACMod model offers the possibility to model in idealized conditions with horizontally homogenous wind fields, as well as to employ a range of sea spray generation, wind and sea surface parameterizations. MACMod results reveal that when compared with MIRAMER data, the B21a, B21b and OVA14 SSGFs are good choices for the modelling of sea spray. Furthermore, comparing corrected CM and ELF (upwind) parameterizations for $\langle S^2 \rangle$ shows that at shorter fetches below 30 km and U_{10} =10 m s^{-1}, the corrected CM predicts $\langle S^2 \rangle$ values up to 11% lower than for ELF, but 5% higher for longer fetches. The consideration of the wave age may therefore help improve predictive accuracy with B21a and B21b in future study.

The MesoNH model is not coupled to a wave model. The corrected wind-dependent CM formulation offers a solution for the estimation of $\langle S^2 \rangle$. The model is run using B21a, B21b and OVA14 SSGFs. Realistic regional-scale modelling with MesoNH reveals strong deviations between modelled and measured wind speeds during the North-Western MIRAMER (2008) field campaign (cf. Fig. 4.7). Such discrepancies are expected to impact sea spray prediction, and therefore make it difficult to evaluate the performances of the different SSGFs. We note, however, that the best results are found for small radii near 1.5µm. These results are attributed to the proximity of the study area to the coast, as well as the low wind speeds and low sample durations that hampered sea spray measurements during MIRAMER. In the case of the North-East Atlantic SUMOS (2021) campaign, correspondance between modelled and measured winds speeds at the sample stations is significantly improved, as shown with $R^2 = 0.93$ (cf. Fig. 4.8). Better results are also

found for sea spray concentrations. The OVA14 SSGF is found to strongly overestimate and underestimate concentrations for particles below and above the 1–5 μm size range, respectively. Both B21a and B21b perform reasonably well. B21b is found to perform best with seemingly greater senstivity to the variations in concentrations observed in the field, mainly driven by the u_*^3 term. B21a performs equally well for the larger particles typical of the spume droplet range (cf. Fig. 4.9, Table 4.2), reminiscent of the good scaling performances of spume droplet generation by $\langle S^2 \rangle$ observed during MATE2019. Overall, results indicate that the upscaled laboratory SSGFs perform reasonably well in field conditions.

5.1.4 Completing the Laboratory SSGFs

In the case of the MATE2019 experiment, freshwater is used, and the absence of surfactants and of gaseous precursors is assumed. In these conditions, the laboratory measurements are only considered applicable for particle radii greater than 7 μm, where jet and spume droplets dominate, and where evaporation effects over the length of the tunnel facility are limited. To complete the laboratory results, the fluxes are extended to 3 μm using the fetch-dependent L18 SSGF obtained using MIRAMER observations and modelling using the MACMod model (Laussac et al. 2018). To further extend the B21a and B21b SSGFs to lower particles, we consider combining them with the OVA14 SSGF adapted to smaller marine aerosols. B21 SSGFs prove to be a good match with OVA14 SSGF, as they meet over the 3–4 μm radius range, at the lower limit of the B21 validity range (cf. Fig. 3.10, Sect 3.3.1). Numerical results with the MesoNH model differ, as the OVA14 SSGF is found to strongly overestimate concentrations relative to SUMOS observations within the 0.015–3 μm radius validity range, reaching more than five orders of magnitude for $r = 0.1\mu$m (cf. Fig. 4.10, Sect. 4.4.3).

5.1.5 Importance of Accurate Wind and Wave Representation

In the presented MesoNH simulations, the wind is the main driver of sea spray generation. The accuracy of wind predictions is therefore of great importance for sea spray concentration accuracy. In the case of the MIRAMER campaign, analysis reveals significant deviations between the model and field observations. These deviations are possibly explained by the orographic effects of the nearby coastline on wind prediction considering the 2 km model resolution, as well as the relatively short MIRAMER sample stations. In the case of the SUMOS campaign, where the sample stations were further from the coastline and sample durations were longer, a better match was found between modelled and measured wind speed and sea spray concentrations. Despite this, model wind speeds were found to be underestimated relative to observations for $U_{10} > 15$ m s^{-1}. In the presented simulations, the model is forced by the ECMWF model. Current efforts to investigate these discrepancies include the use of the higher resolution AROME meteorological forc-

ings.

Using laboratory observations, multilinear regression indicates that sea spray generation seems to scale best with the wave-slope variance $\langle S^2 \rangle$ and the friction velocity cubed u_*^3. $\langle S^2 \rangle$ and u_*^3 are not the simplest parameters to measure or model. As we move towards the use of more complex parameterizations for sea spray generation in numerical models, sea spray concentration accuracy strongly rely on the accuracy of wind and wave models. Current efforts to improve model accuracy include the coupling of atmosphere, ocean and wave models. Such developments allow to consider additional physical processes at play, with the examples of the modulation of wave characteristics by ocean currents (Romero et al. 2017) and internal waves (Lenain and Pizzo 2021). Furthermore, the effects of bathymetry on gravity wave breaking are relatively well documented. The consideration of wave-bottom interactions and wave breaking on sea spray generation (De Leeuw et al. 2000; Van Eijk et al. 2011) is important to understand the contribution of aerosols to atmospheric processes. The scaling of sea spray generation by $\langle S^2 \rangle$ may mean that the laboratory SSGFs are applicable in coastal regions, as well as in the field. Further research is required to explore this.

5.1.6 Sea Spray Numerical Modelling

In previous sections, experimental campaigns and modelling efforts have allowed to study sea spray generation and transport, with promising results obtained with the laboratory-derived SSGFs. Sea spray modelling is subject to fair number of degrees of freedom, such as the accuracy of the SSGFs, of forcing environmental parameters, of aerosol transport terms and parameterizations. In this context, with the aim of improved accuracy wide variety of conditions, further research is required to constrain these problems. During MesoNH simulations, the modal medians adapt to atmospheric aerosol processes, whilst the standard deviations are constant. Further study, with the help of additional field and laboratory measurements, are required to evaluate environmental effects on modal behaviour. Another important assumption made during the thesis, is the negligible dynamic and thermodynamic air-droplet effects on sea spray transport, as well as MABL characteristics. In both field campaigns, and the laboratory experiments, the relative humidity was assumed equal to 80%, and atmospheric conditions were assume stable as a result of the small observed air-sea temperature gradients. In other regions and seasons, air-sea heat fluxes are significant and contribute to extreme weather events. In such cases, authors speculate that dynamic and thermodynamic air-droplet processes can dominate the flux problem (Fairall et al. 2009; Soloviev and Lukas 2010; Richter and Sullivan 2014). To this day, feedbacks of sea spray remain an open question (Mueller and Veron 2014a).

Studies have compared Lagrangian and Eulerian model performances using the data collected in the large air-sea interaction facility, and found comparable results between both methods for sea spray transport and evaporation for freshwater droplets (Pruppacher and Klett 1978) in the spume droplet dominated size range (Mestayer et al. 1996). Eu-

lerian models are shown to perform rather well for the transport of sea spray. However, accuracy on sea spray characteristics and the resulting heat and momentum feedbacks on the MABL can be improved. The SeaCluse code developed in the late 90s approaches this problem simulating droplet transport and droplet dynamic and thermodynamic air-droplet interactions seperately (Mestayer et al. 1996).

As we seek to converge towards "full-scale" mesoscale modelling of sea spray, we use the simulated carrier fluids in Eulerian MesoNH and MACMod models for the sea spray transport. However, transport can also be affected by the change in sea spray characteristics transiting in the MABL, namely as a result of evaporation effects and the resulting release of pure water from the saline droplet. Furthermore, the heat, moisture and momentum feedbacks of droplets on the properties of the airflow need to be integrated to better understand the role of sea spray on weather, and ultimately the climate. To do this, research efforts have aimed to compare and reconciliate Eulerian and Lagrangian approaches proposed by Edson and Fairall (1994), Edson et al. (1996) and Richter et al. (2019) among others. With the considerable numerical costs and stability constraints of these methods, new methods are proposed. A kinetic approach, resolving the exchanges of internal and kinetic energy between droplets and ambient air, has been suggested to reconcile both Eulerian and Lagrangian approaches with the help of fluid models, thus producing a Eulerian atmosphere-droplet coupled model for the study of transient droplet and MABL characteristics (Veron and Mieussens 2020).

5.1.7 Feedbacks of Sea Spray on the Marine Atmospheric Boundary Layer

Recent studies have focused on the effects of sea spray mediated enthalpy (Andreas 1992; Rastigejev and Suslov 2019) and momentum fluxes (Rastigejev et al. 2011) on the characteristics of the MABL and of extreme weather events such as tropical cyclones (Andreas and Emanuel 2001; Bao et al. 2011; Sroka and Emanuel 2021).

Heat and Moisture Feedbacks

The study of feedbacks of sea spray on MABL characteristics is an active field of research, but is complicated by the difficulty to measure sea spray, heat and moisture fluxes in the field. Andreas (1992) proposed a method for the estimation of the sea spray-mediated latent and sensible heat fluxes, and concluded that the latent heat flux is substantial. The sea spray feedbacks are size-dependent, as (Bianco et al. 2011) showed that small drops evaporate at moderate wind speeds, whilst large drops at high winds enhance the sensible heat flux (Andreas and Emanuel 2001). Unlike the more classical surface fluxes at the air-sea interface (Stull 1988), the spray heat flux is a volume flux through its association with the sea spray volume generation flux. The spray mediated fluxes are therefore highly dependent on SSGF accuracy.

The MATE2019 laboratory SSGFs have proven to be accurate in a wide range of wind

and wave conditions, B21b especially. We use the B21b SSGF to evaluate the consequences of sea spray on the enthalpy flux. The SSGF is extended to $r_{80} \approx 100\mu$m for the purpose of this short study. Figure 5.1a shows the sea spray generation function values for winds of 15 (solid line) and 25 m s^{-1} (dashed line). The corresponding volume fluxes are shown in Fig. 5.1b. The 25 m s^{-1} wind speed is typical of very high wind speed events such as Medicanes.

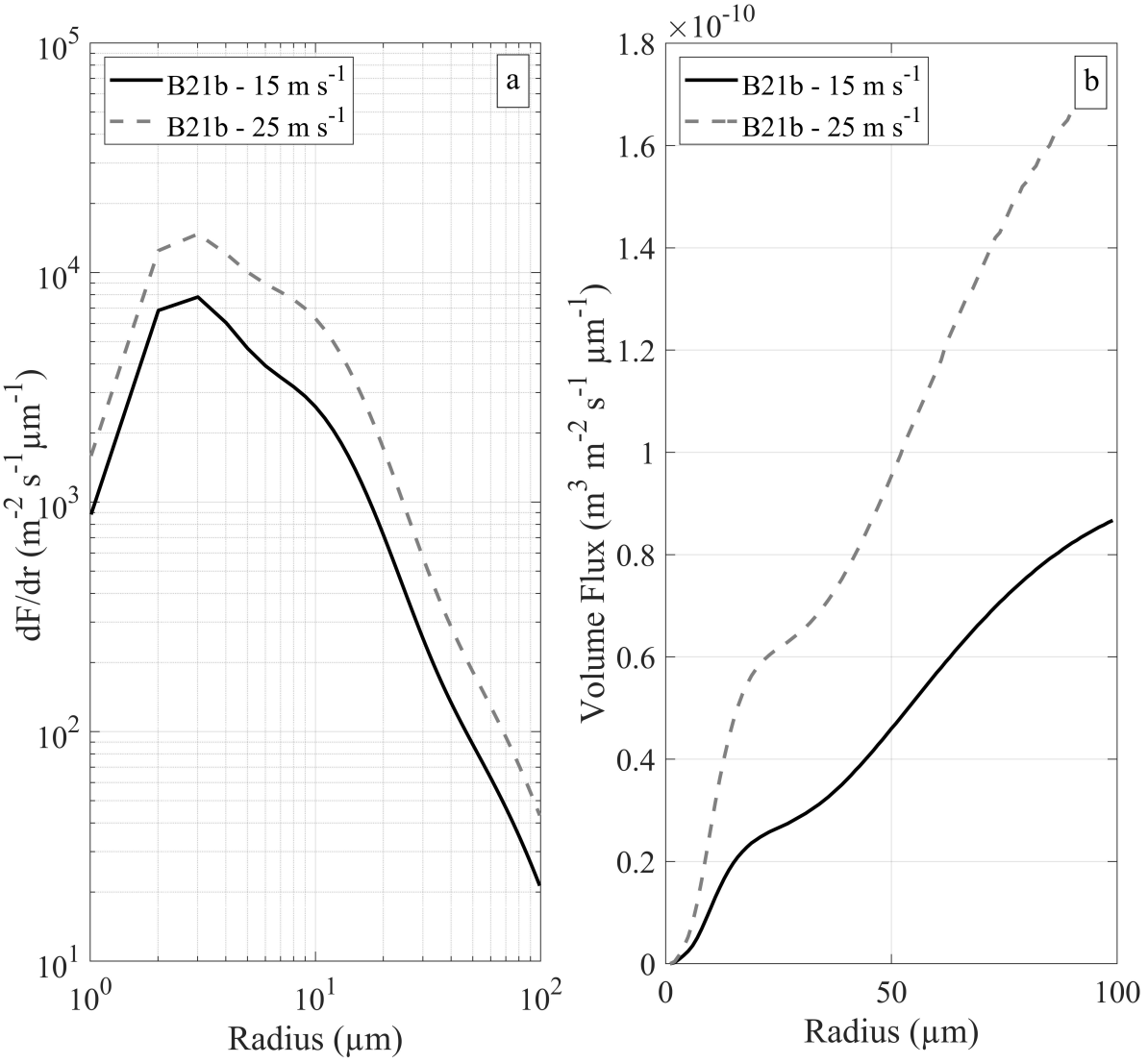

Figure 5.1: The (a) B21b sea spray generation fluxes and corresponding (b) volume fluxes for 15 (solid line) and 25 m s^{-1} (dashed line) condition.

According to (Andreas 2002, 2005), the rate at which all droplets with initial radius r_0 exchange sensible heat with the air can be expressed as

$$H_{sp}(r_0) = \rho_w C_{ps}(T_s - T_{eq})[1 - exp(-\tau_f/\tau_T)]\Big(\frac{4\pi r_0^3}{3}\frac{dF}{dr_0}\Big), \tag{5.1}$$

where H_{sp} is the droplet-mediated sensible heat. In turn, the rate at which all droplets

with initial radius r_0 exchange latent heat with the air is

$$E_{sp}(r_0) = \rho_w L_v \Big[1 - \Big(\frac{r(\tau_f)}{r_0}\Big)^3\Big] \Big(\frac{4\pi r_0^3}{3}\frac{dF}{dr_0}\Big), \tag{5.2}$$

where E_{sp} is the droplet-mediated latent heat. C_{ps} is the specific heat of seawater at constant pressure, and ρ_s is the seawater density. T_s is the sea surface temperature, and the initial droplet temperature. T_{eq} is the equilibrium droplet temperature. τ_f and τ_T are the time scales over which the droplet re-enters the sea, and reaches the equilibrium temperature, respectively. According to (Andreas 1989), the initial radius flux can be calculated from the equilibrium radius flux using

$$\frac{dF}{dr_0} = \frac{dF}{dr_{80}}\frac{dr_{80}}{dr_0}, \tag{5.3}$$

where dr_{80}/dr_0=$0.506r_0^{-0.024}$. Figure 5.2 shows the corresponding E_{sp} and H_{sp} absolute values as functions of r_0 in case of the same conditions of the previous cases outlined above. The air and sea water temperature were set to 13°C and 10°C, respectively. Unsurprisingly, the latent heat contribution is the largest. By integrating under each curve for 15 m s^{-1} wind speeds, we find the spray-mediated H_{sp} and E_{sp} heat fluxes, of 0.1 and 4.9 W m^{-2} respectively. For very high wind speeds, the H_{sp} and E_{sp} values amount to 0.2 and 50 W m^{-2}, respectively. These values are lower than those predicted by Andreas (1992) in similar conditions, by a factor 3.

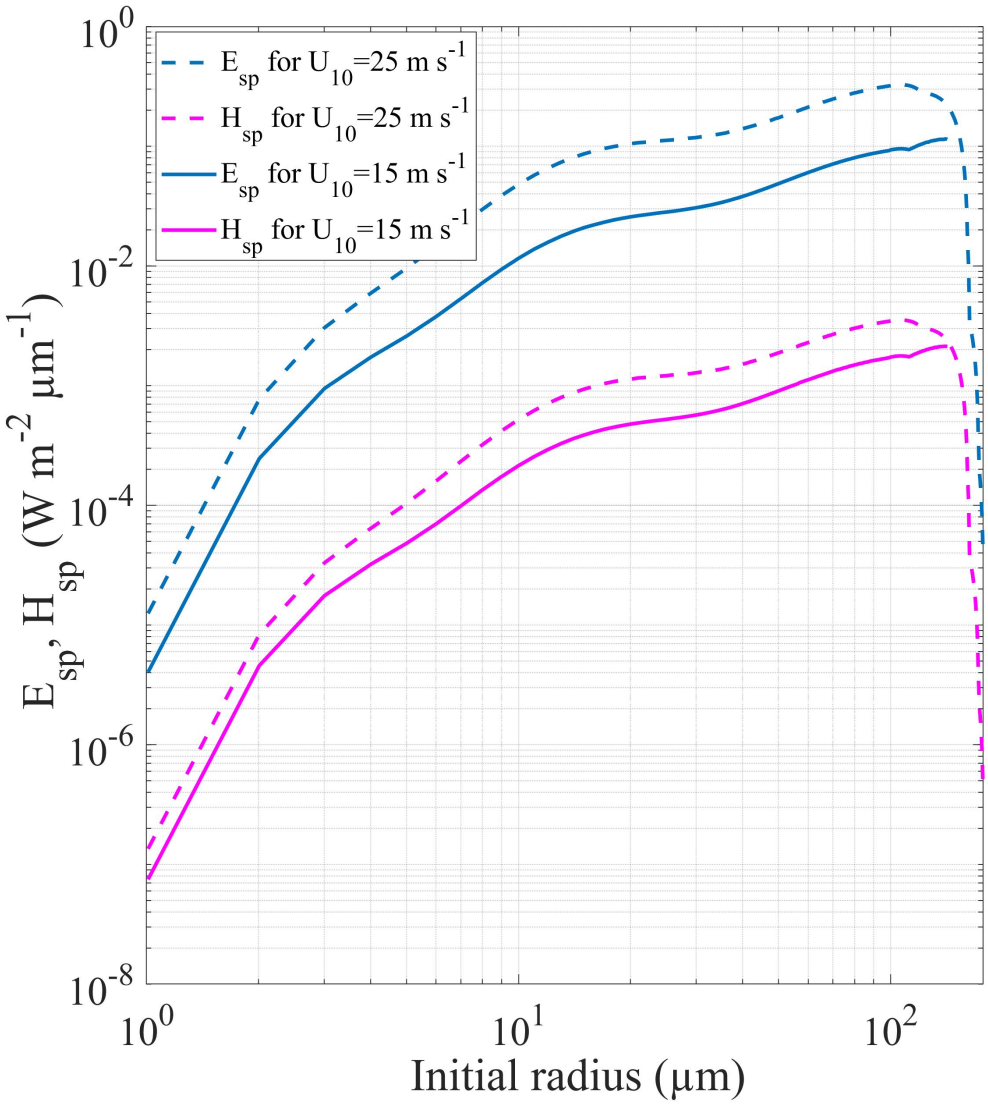

Figure 5.2: Spray-mediated heat fluxes for U_{10} = 15 (solid lines) and 25 m s^{-1} (dashed lines). Following the color-coding in Fig. 1.9 (Sect. 1.3.1), the latent and sensible heat flux components E_{sp} and H_{sp} are represented in blue and magenta.

For the 15 m s^{-1} wind speed case, and similar water and air temperatures (during the SUMOS campaign), the MesoNH numerical model predicts H_{tot} and E_{tot} values near 100 W m^{-2}. According to these results, the contribution of sea spray seems rather small in these conditions. These low values relative to Andreas (2002) can partly be explained by the understimation of the total volume flux in this study, as the B21b does not extend far in the spume droplet range. This is problematic, as the peak in the volume flux is beyond the study range, at approximately 200 µm radius. Another possible reason for these lower values is the lower generation flux predicted by B21b relative to the Andreas (1998) SSGF in the spume droplet range. These results further stress the importance of accurate sea spray SSGFs. Further research is required to evaluate spume droplets in the spume droplet range, which is hampered by generally low count statistics, and difficult deployment in

high to extreme wind speed conditions. This is especially important considering the importance and strong uncertainties of heat flux estimates in extreme wind conditions where sea spray contributions are thought to be important (Fairall et al. 1994; Richter and Sullivan 2014; Rastigejev and Suslov 2019).

Momentum Feedbacks, a Two-Phased Layer

Turbulent kinetic energy and buoyant production change when the droplets evaporate and alter the stability of the boundary layer (cf. Appendix 7), modifications of the Monin-Obukhov similarity theory in the presence of sea spray have been considered (Bao et al. 2011; Bianco et al. 2011; Kudryavtsev and Makin 2011). Furthermore, sea spray droplets located in both the emission layer and the evaporation layer (cf. Fig. 1.9, Sect. 1.3.1) can influence the transfer of momentum from the wind to the waves by constituting a two-phased layer (Soloviev and Lukas 2010). According to the sandwich model by Lighthill (1999), spray forms a layer than can be conceptualized as a third fluid, "sandwiched" between the sea and air, acting as a lubrication layer that dampens the turbulent mixing and its corresponding energy dissipation, and ultimately decreases the surface drag of the air flow (Kudryavtsev and Makin 2011). We note however than concerning this hypothesis that sea spray can affect the moment flux between the wind and the underlying waves, Fairall et al. (2009) find by comparing the weights of air and spray droplets in a given volume, the effect of the spray on the momentum flux would be less than 0.3%. Though very difficult to quantify, the effects of sea spray on the momentum flux are thought to be much greater in strong and extreme wind speed conditions (Fairall et al. 2009; Soloviev and Lukas 2010; Kudryavtsev and Makin 2011). Different formulations exist for the calculation of the viscosity of two phased media (Adams et al. 1941; Cicchitti et al. 1959; Awad and Muzychka 2008), often developped for industrial applications. Such formulations allow to estimate the viscosity of a two-phased fluid from the volumetric ratio between air and water. Such laboratory experiments reveal that the friction loss is caused by the effects of viscosity or pressure, thus corroborating the speculations on sea spray-mediated viscosity modulation. Though not investigated in the present thesis, further research is required to understand such effects on the momentum flux. A possible particle-size-dependence could be interesting to investigate, as larger sea spray particles have relatively significant inertia (Veron 2015), thus increasing the viscosity in the "sandwich" layer.

5.2 Conclusion and Perspectives

Recent improvements in the integration of higher-order wave-field properties in numerical wave models (Cathelain 2017) and the coupling of wave, atmospheric, and circulation models (Pianezze et al. 2018) provide an impetus for the study of sea spray generation processes. This study is dedicated to the better understanding of sea spray generation dependence on wind and wave characteristics in the open ocean, sea spray transport, as

well as the role of sea spray on MABL characteristics. Our results have shown that the integration of the wave field is essential for the better scaling of the sea spray generation. In this respect, the wave–wind tunnel is an ideal environment for the study of sea spray production in a wide variety of wave fields and in high wind speeds representative of extreme events. The tunnel facilitates the complex experiments required to understand the generation processes at the microphysical scale, such as airflow separation, and the effects of spray on heat, moisture, and momentum fluxes at the air–sea interface. Ideally, such experiments should be performed with salt water, for easier comparison with field experiments, because salt water and fresh water lead to differences in aerosol concentrations and distributions (Fairall et al. 2009; Mehta et al. 2019). Other authors have also recently highlighted the need to further investigate scaling of sea spray generation and dynamics between laboratory and field conditions, as well as its complexity (Nilsson et al. 2021).

Like a learning loop, we have developed, upscaled and field-trialled wind and wave-dependent sea spray generation functions from measurements made in the laboratory. Validated with the help of field measurements acquired during the MIRAMER and SUMOS campaigns, regional models using laboratory generation functions allow for accurate sea spray concentration predictions over the jet and spume droplet range, and over a wide range of environmental conditions. We strongly highlight the importance of continuing to develop increasingly accurate and complete SSGFs, with the inclusion of atmospheric aerosols from a variety of sources, such as biogenic aerosols, dusts, and pollution. As air-droplet dynamic and thermodynamic processes in the MABL are associated with the sea spray generation flux, more accurate SSGFs as proposed in the present thesis are encouraging for the more better understanding of sea spray on atmospheric phenomena, extreme weather events especially. Also, aerosols have been shown to play an essential role in cloud formation and precipitation (Ramanathan et al. 2001), changing the weather and challenging forecasts of extreme weather events such as tropical cyclones (Wang et al. 2014; Sroka and Emanuel 2021). The effects of sea spray in a future climate are very uncertain. Whilst some models predict a reduction in the global sea salt burden from the present-day to year 2100 (Liao et al. 2006), other authors predict little change (Mahowald et al. 2006), or a sizeable increase (Bellouin et al. 2011).

As we work towards universal SSGFs valid for a wide range of (complex) environmental conditions, further understanding of the effect of multiscale (i.e., millimeter to meter scale) boundary processes on sea spray fluxes is necessary. This includes the possible effects induced by a range of physical phenomena including overlapping wave fields, directional spreading of wave spectra (Peureux et al. 2018), and wave–current interactions affecting surface wave properties such as wave height (Ardhuin et al. 2017; Marechal and Ardhuin 2021) and wave breaking (Romero et al. 2017). As the present study has highlighted the importance of the wave-slope variance in modelling droplet fluxes, we signal the urgent need for a better understanding of small-scale sea surface characteristics (Jähne and Riemer 1990). Unfortunately, field measurements of these small-scale characteristics have been relatively sparse (Munk 2009), not in the least because the presence of whitecaps

complicates the retrieval of slope-variance estimates (Cox and Munk 1956; Lenain et al. 2019). Authors suggest that breaking crest length measurements allow to extend the study of wave components down to microscale breakers at the gravity-capillary transition (Sutherland and Melville 2013). As the breaking crest length allows to separate active and passive whitecaps, it is a powerful tool for the scaling of sea spray concentrations (Lenain and Melville 2017a) and generation fluxes (Mueller and Veron 2009; Veron 2015).

Appendix

1. Laboratory Waves

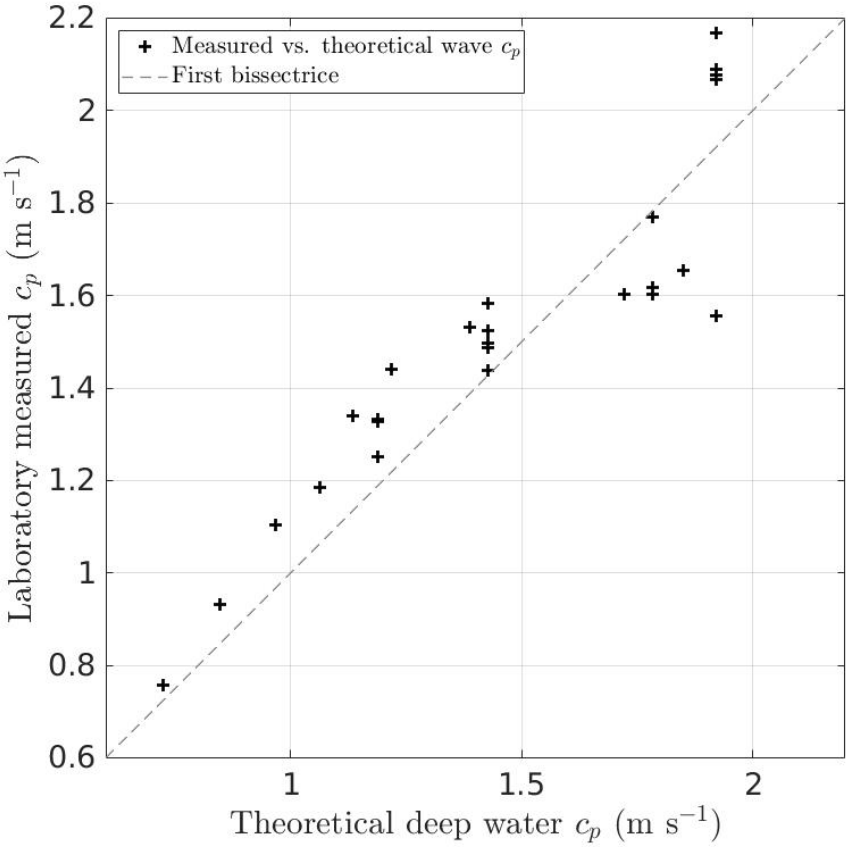

Figure A.1: Regression of MATE2019 measured (vertical axis) and theoretical phase speed (horizontonal axis) for all 25 wind and wave combinations (including the JONSWAP wavemaker forcing).

The wave phase speed is especially important in this thesis for the estimation of the wave age, as well as the configuration of a wave age-dependent wave spectral model (Elfouhaily et al. 1997). With MATE2019 data, Fig. A.1 presents the phase speed obtained from the observed wave phase shift as a function of the theoretical deep water phase speed using wave gauge measurements as input. Overall good correspondance is found between both approaches. The slight deviation from the first bissectrice near 1.7 m s^{-1} marks a decrease in measured c_p values. This may result from the proximity of the

long wave case to the intermediate water case, especially under conditions of strong wind forcing.

2. Laboratory Wave Spectra

In most cases, MATE2019 conditions were generated by a programmable wavemaker. Figure A.2 presents measured elevation spectra for the long wave case and five different wind forcings over the U_{10} 8–20 m s^{-1} range. f^{-4} and f^{-5} shapes are shown, typically representative of the equilibrium and saturation range. As the wind forcing increases, so does the elevation, especially in the higher frequency range as we tend towards conditions of wind and wave equilibrium. In parallel, the harmonics detected by Fourier analysis are progressively reduced.

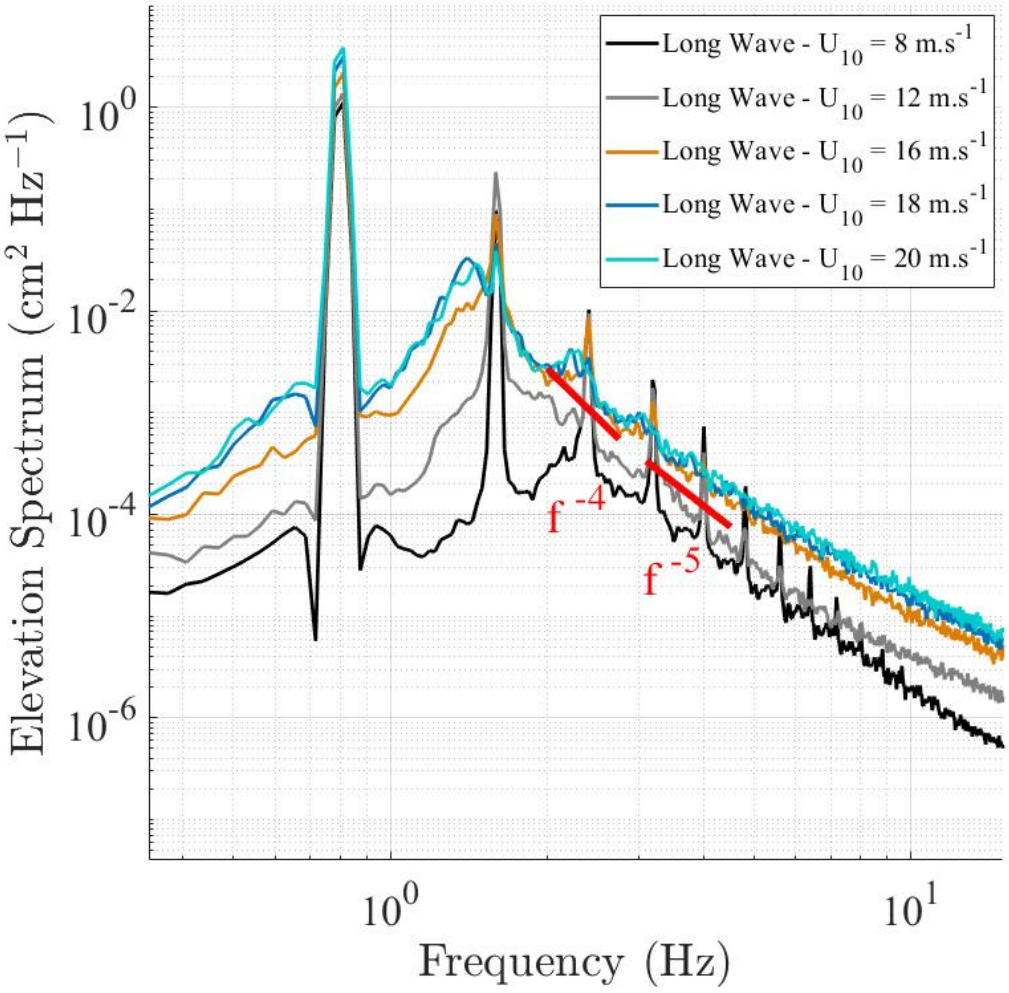

Figure A.2: Elevation spectra measured during MATE2019 for the long wave condition.

3. MOS Theory

Figure A.3 represents all vertical wind profiles measured for all 25 wind and wave combinations tested during MATE2019 as a function of $ln(z/z_0)$ and $\frac{U(z)k}{u_*}$ terms. The collapse of observations along the first bissectrice demonstrate that Monin and Obukhov (1954) theory is valid in the laboratory, with logarithmic wind profiles.

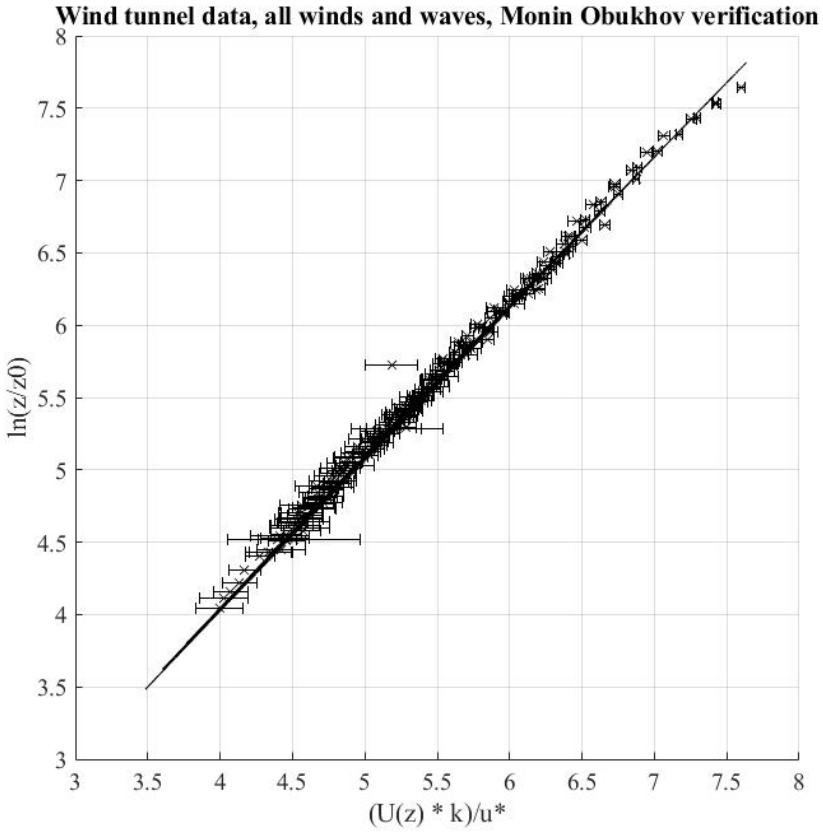

Figure A.3: $ln(z/z_0)$ as a function of $\frac{U(z)k}{u_*}$ for MATE2019 laboratory wind speed profiles, for all wind and wave combinations.

4. Aerosol Measurements

Aerosols concentration measurements are necessary for the estimation of a generation flux. Traditionally, sea spray aerosols have been quantified according to their mass and radius through the analysis of try aerosols deposited onto filters, or direct concentration measurements using optical systems.

Usually difficult to deploy due to their limited mobility, sensors have typically been located on land, planes, or on ships. It has been shown that deployment in this way can also pertub the concentration measurements. It is also possible to carry out measurements of aerosols using remote sensing (Fairall et al. 2014; Ma et al. 2020). Recent developments have also lead to the modification and miniaturisation of intrumentation for deployment using unmanned airborne vessels or unmanned surface vessels.

Intercomparison and intercalibration of the increasing range of platform and instrumentation methods is necessary for the reduction of the high concentration and generation flux deviations observed between authors.

5. On CSASP Sensor Sampling

CSASP systems have been used in a variety of conditions and have been shown to be reliable (Frick and Hoppel 2000; Savelyev et al. 2014; Petelski et al. 2014). These sensors have isokinetic inlets that are designed to permit a constant flow rate, and therefore a constant sample volume per unit time in which aerosols are counted. Tests during the MATE2019 deployment at the Luminy facility aimed to verify this, in 15 different incident wind speeds ranging from 0 to 15 m s^{-1}. A hot film wind sensor (E+E Elektronik, Langwiesen, Austria) was inserted through the side of a tube placed around the CSASP sensor outlets out of which the air flows through an integrated fan system designed to regulate the sensor flow. The tubes were printed to match the exact size of the outlets of both CSASP-100-HV-ER and CSASP-200 probes. The output flow rate of the probes was calculated from the probe outlet wind speeds (cf Fig. A.3) and, assuming incompressible flow, the Bernouilly equation. Knowledge of the flow rate allowed to recalculate the sample volume per unit time of the probes, and to compare with the information provided by the manufacturer.

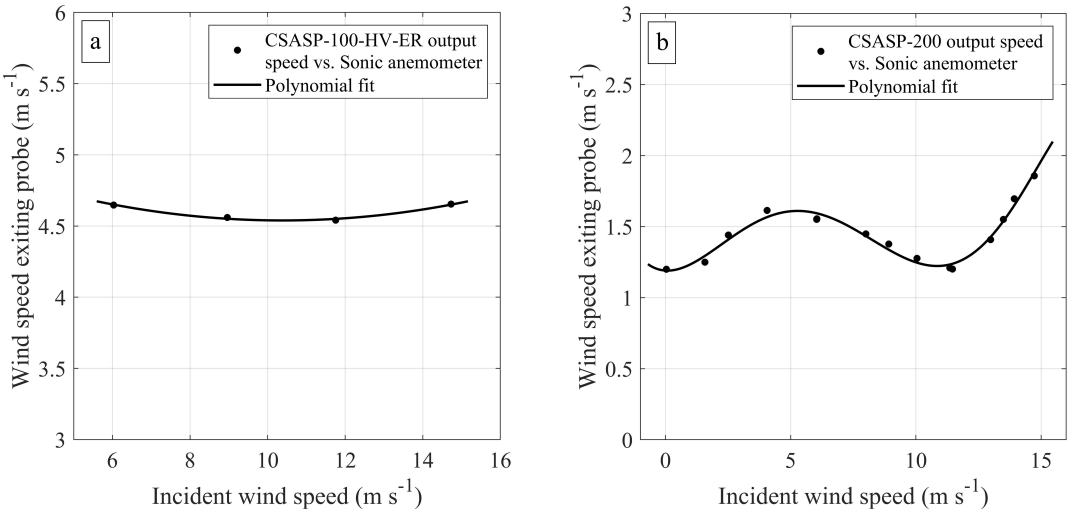

Figure A.4: Measurements of wind velocities exiting probes (vertical axis) as a function of the incident wind speed.

As shown in Fig. A.3a, the wind had little influence on the CSASP-100-HV-ER, and values were found to match factory settings. The CSASP-200 showed a non-linear response to the incident wind. The CSASP-200 sample volumes were therefore corrected according to the incident wind speeds using a 6-degree polynomial function fitted to the

experimental data over the 0–15 m s^{-1} wind speed range. We think this may be due to the larger wind surface area of the CSASP-200 inlet, with mixed impacts of the inlet isokinetic properties and the regulation of the flow in the intrument by the fan. These inlets are an essential component for the rerouting of the samples particles with limited pertubation by the probes. This study highlights the complexity of aerosol particle sampling.

6. Whitecap Estimation

Illustration of the different steps undertaken for the estimation of the whitecap coverage $W(\%)$ in the laboratory.

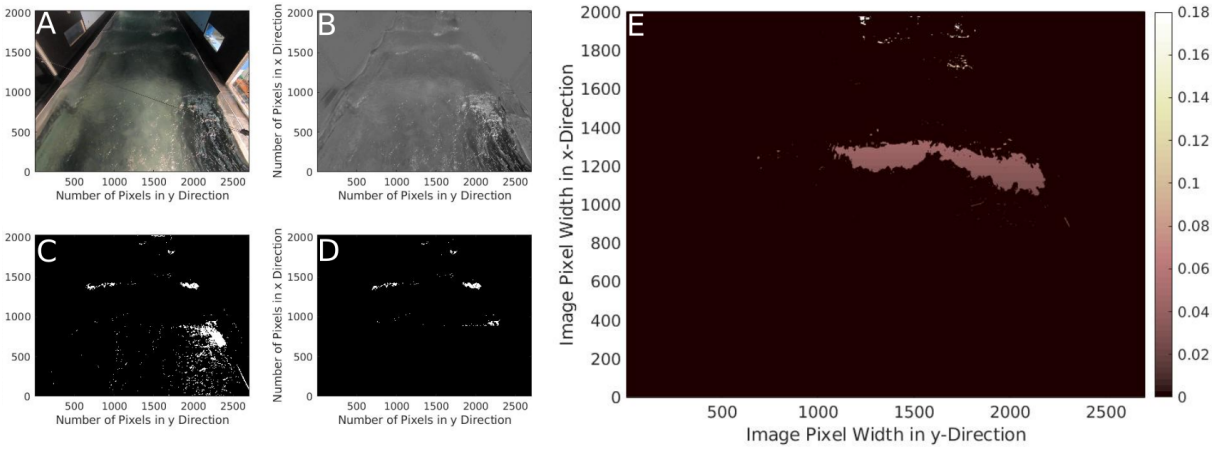

Figure A.5: (A) Example snapshot of the water surface during MATE2019 (B) Substraction of the image mean (C) Application of colour cut-off threshold (D) Removal of area subject to sunglitter (E) Calculation of the surface area of individual pixels indicated by the colorbar (in cm^2).

7. Laboratory Relative Humidity and Temperature Profiles

During the MATE2019 experiments, vertical relative humidity (%) and temperatures were measured. The average water temperature T_w and air temperature T_a was of 18 and 25°C, respectively. Figure A.6 presents the measured profiles for the wind–wave condition for a range of four wind speeds. Figure A.5a shows that the relative humidity profile tends towards 100% as we approach the mean water level (z=0), whilst Fig. A5b shows that the air temperature decreases with proximity to the surface. Interestingly, the highest humidity gradients, and the highest vertical temperature gradients are found for the lowest wind speeds, but are reduced at higher wind speeds. This can be attributed to the increased turbulent mixing that occurs are higher winds, therefore increasing vertical homogeneity. The effects of the presence of sea spray is difficult to elucidate. However, the evaporation of droplets leads to the heating of ambient air (cf. Sect. 1.2.5). For U_{10} wind speeds equal or greater than 16 m s^{-1}, the heating effect of droplet evaporation may result in the slowed rate of decrease in T_a within 20 cm from the water surface, and

even an increase in T_a in some cases. The lines are logarithmic fitting functions, and corresponding R^2 values are provided.

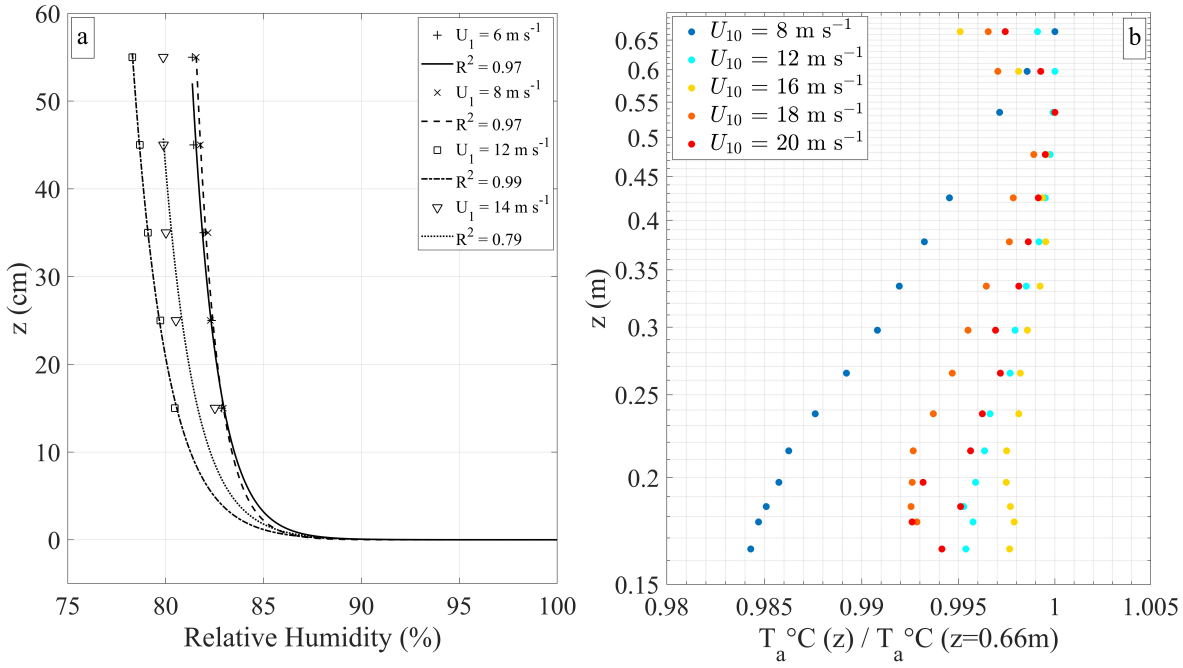

Figure A.6: (a) Vertical relative humidity and (b) air temperature profiles measured during the wind–wave laboratory condition, and a range of wind speeds. The temperature profiles are represented as the ratio between the temperature $T_a(z)$ at height z, and the temperature $T_a(z = 0.66m)$ 0.66 meters above the mean water level.

Bibliography

Adams M, WH WW, Bryan R (1941) Vaporization inside horizontal tubes. Trans ASME 63:545–552

Amante C, Eakins BW (2009) Etopo1 arc-minute global relief model: procedures, data sources and analysis

Andreas EL (1989) Thermal and size evolution of sea spray droplets. U.S. Army Cold Reg Res Eng Lab Hanover, Tech Rep 89-11

Andreas EL (1992) Sea spray and the turbulent air-sea heat fluxes. J Geophys Res: Oceans 97(C7):11,429–11,441, DOI 10.1029/92JC00876

Andreas EL (1998) A new sea spray generation function for wind speeds up to 32 m/s. J Phys Ocean 28(11):2175–2184, DOI 10.1175/1520-0485(1998)028<2175:ANSSGF>2.0.CO;2

Andreas EL (2002) A review of the sea spray generation function for the open ocean. Adv Fluid Mech 33:1–46

Andreas EL (2005) Approximation formulas for the microphysical properties of saline droplets. Atmospheric Research 75(4):323–345

Andreas EL, Emanuel KA (2001) Effects of sea spray on tropical cyclone intensity. Journal of the atmospheric sciences 58(24):3741–3751

Andreas EL, Persson POG, Hare JE (2008) A bulk turbulent air–sea flux algorithm for high-wind, spray conditions. Journal of Physical Oceanography 38(7):1581–1596

Andreas EL, Jones KF, Fairall CW (2010) Production velocity of sea spray droplets. J of Geophys Res: Oceans 115(C12)

Angle KJ, Crocker DR, Simpson RM, Mayer KJ, Garofalo LA, Moore AN, Garcia SLM, Or VW, Srinivasan S, Farhan M, et al. (2021) Acidity across the interface from the ocean surface to sea spray aerosol. Proceedings of the National Academy of Sciences 118(2)

Anguelova M, Barber RP, Wu J (1999) Spume drops produced by the wind tearing of wave crests. J Phys Ocean 29(6):1156–1165, DOI 10.1175/1520-0485(1999)029<1156:SDPBTW>2.0.CO;2

Apel JR (1994) An improved model of the ocean surface wave vector spectrum and its effects on radar backscatter. Journal of Geophysical Research: Oceans 99(C8):16,269–16,291

Ardhuin F, Gille ST, Menemenlis D, Rocha CB, Rascle N, Chapron B, Gula J, Molemaker J (2017) Small-scale open ocean currents have large effects on wind wave heights. J Geophys Res: Oceans 122(6):4500–4517

Awad M, Muzychka Y (2008) Effective property models for homogeneous two-phase flows. Experimental Thermal and Fluid Science 33(1):106–113

Babanin AV, Soloviev YP (1998) Field investigation of transformation of the wind wave frequency spectrum with fetch and the stage of development. Journal of Physical Oceanography 28(4):563–576

Banner ML, Melville WK (1976) On the separation of air flow over water waves. J Fluid Mech 77(4):825–842

Banner ML, Gemmrich JR, Farmer DM (2002) Multiscale measurements of ocean wave breaking probability. J Phys Ocean 32(12):3364–3375

Bao JW, Fairall CW, Michelson S, Bianco L (2011) Parameterizations of sea-spray impact on the air–sea momentum and heat fluxes. Monthly Weather Review 139(12):3781–3797

Barthe C, Bousquet O, Bielli S, Tulet P, Pianezze J, Claeys M, Tsai CL, Thompson C, Bonnardot F, Chauvin F, et al. (2021) Impact of tropical cyclones on inhabited areas of the swio basin at present and future horizons. part 2: Modeling component of the research program renovrisk-cyclone. Atmosphere 12(6):689

Bellouin N, Rae J, Jones A, Johnson C, Haywood J, Boucher O (2011) Aerosol forcing in the climate model intercomparison project (cmip5) simulations by hadgem2-es and the role of ammonium nitrate. Journal of Geophysical Research: Atmospheres 116(D20)

Berny A, Popinet S, Séon T, Deike L (2021) Statistics of jet drop production. Geophysical Research Letters 48(10):e2021GL092,919

Bianco L, Bao JW, Fairall C, Michelson S (2011) Impact of sea-spray on the atmospheric surface layer. Boundary-layer meteorology 140(3):361–381

Birmili W, Hoffmann T (2006) Environmental pollutants | particulate and dust pollution, inorganic and organic compounds. In: Laurent GJ, Shapiro SD (eds) Encyclopedia of Respiratory Medicine, Academic Press, Oxford, pp 110–120, DOI https://doi.org/10.1016/B0-12-370879-6/00133-2

Blanchard DC (1963) The electrification of the atmosphere by particles from bubbles in the sea. Prog Ocean 1:73–202

Bock EJ, Hara T, Frew NM, McGillis WR (1999) Relationship between air-sea gas transfer and short wind waves. J Geophys Res: Oceans 104(C11):25,821–25,831

Boisot O, Nouguier F, Chapron B, Guérin CA (2015) The go4 model in near-nadir microwave scattering from the sea surface. IEEE Transactions on Geoscience and Remote Sensing 53(11):5889–5900

Boucher O, Randall D, Artaxo P, Bretherton C, Feingold G, Forster P, Kerminen VM, Kondo Y, Liao H, Lohmann U, et al. (2013) Clouds and aerosols. In: Climate change 2013: the physical science basis. Contribution of Working Group I to the Fifth Assessment Report of the Intergovernmental Panel on Climate Change, Cambridge University Press, pp 571–657

Bouin MN, Lebeaupin Brossier C (2020) Surface processes in the 7 november 2014 medicane from air–sea coupled high-resolution numerical modelling. Atmospheric Chemistry and Physics 20(11):6861–6881

Boulon J, Sellegri K, Hervo M, Laj P (2011) Observations of nucleation of new particles in a volcanic plume. Proceedings of the National Academy of sciences 108(30):12,223–12,226

Bourras D, Reverdin G, Giordani H, Caniaux G (2004) Response of the atmospheric boundary layer to a mesoscale oceanic eddy in the northeast atlantic. Journal of Geophysical Research: Atmospheres 109(D18)

Bourras D, Weill A, Caniaux G, Eymard L, Bourlès B, Letourneur S, Legain D, Key E, Baudin F, Piguet B, et al. (2009) Turbulent air-sea fluxes in the gulf of guinea during the amma experiment. Journal of Geophysical Research: Oceans 114(C4)

Bourras D, Cambra R, Marié L, Bouin MN, Baggio L, Branger H, Beghoura H, Reverdin G, Dewitte B, Paulmier A, et al. (2019) Air-sea turbulent fluxes from a wave-following platform during six experiments at sea. Journal of Geophysical Research: Oceans 124(6):4290–4321

Bréon F, Henriot N (2006) Spaceborne observations of ocean glint reflectance and modeling of wave slope distributions. Journal of Geophysical Research: Oceans 111(C6)

Bringer A, Chapron B, Mouche A, Guérin CA (2013) Revisiting the short-wave spectrum of the sea surface in the light of the weighted curvature approximation. IEEE Trans Geosci Remote 52(1):679–689

Brooks SD, Thornton DC (2018) Marine aerosols and clouds. Annual review of marine science 10:289–313

Brumer SE, Zappa CJ, Brooks IM, Tamura H, Brown SM, Blomquist BW, Fairall CW, Cifuentes-Lorenzen A (2017) Whitecap coverage dependence on wind and wave statistics as observed during SO GasEx and HiWinGS. J Phys Ocean 47(9):2211–2235

Buckles J, Hanratty TJ, Adrian RJ (1984) Turbulent flow over large-amplitude wavy surfaces. Journal of Fluid Mechanics 140:27–44

Buckley M, Veron F, Yousefi K (2020) Surface viscous stress over wind-driven waves with intermittent airflow separation. Journal of Fluid Mechanics 905

Buckley MP, Veron F (2017) Airflow measurements at a wavy air–water interface using piv and lif. Experiments in Fluids 58(11):1–20

Buckley MP, Veron F (2019) The turbulent airflow over wind generated surface waves. Euro J Mech-B/Fluids 73:132–143

Callaghan AH, Deane GB, Stokes MD, Ward B (2012) Observed variation in the decay time of oceanic whitecap foam. J Geophys Res: Oceans 117(C9)

Canepa E, Builtjes PJ (2017) Thoughts on earth system modeling: From global to regional scale. Earth Sci Rev 171:456–462

Carruthers D, Choularton T (1986) The microstructure of hill cap clouds. Quarterly Journal of the Royal Meteorological Society 112(471):113–129

Cathelain M (2017) Development of a deterministic numerical model for the study of the coupling between an atmospheric flow and a sea state. PhD thesis, Ecole Centrale de Nantes (ECN)

Chalikov D, Rainchik S (2011) Coupled numerical modelling of wind and waves and the theory of the wave boundary layer. Boundary-layer meteorology 138(1):1–41

Chen Y, Cheng Y, Ma N, Wolke R, Nordmann S, Schüttauf S, Ran L, Wehner B, Birmili W, Gon HA, et al. (2016) Sea salt emission, transport and influence on size-segregated nitrate simulation: a case study in northwestern europe by WRF-Chem. Atmos Chem and Phys 16(18):12,081–12,097

Cicchitti A, Lombardi C, Silvestri M, Soldaini G, Zavattarelli R (1959) Two-phase cooling experiments: pressure drop, heat transfer and burnout measurements. Centro Informazioni Studi Esperienze, Milan, Tech rep

Cipriano RJ, Blanchard DC (1981) Bubble and aerosol spectra produced by a laboratory 'breaking wave'. J Geophys Res: Oceans 86(C9):8085–8092

Coantic M, Ramamonjiarisoa A, Mestayer P, Resch F, Favre A (1981) Wind-water tunnel simulation of small-scale ocean-atmosphere interactions. J Geophys Res: Oceans 86(C7):6607–6626

Conticini E, Frediani B, Caro D (2020) Can atmospheric pollution be considered a co-factor in extremely high level of sars-cov-2 lethality in northern italy? Environmental pollution 261:114,465

Cox C, Munk W (1956) Slopes of the sea surface deduced from photographs of sun glitter. Bull Scripps Inst Ocean

Daisey J, Cheney J, Lioy P (1986) Profiles of organic particulate emissions from air pollution sources: status and needs for receptor source apportionment modeling. Journal of the Air Pollution Control Association 36(1):17–33

De Leeuw G, Neele FP, Hill M, Smith MH, Vignati E (2000) Production of sea spray aerosol in the surf zone. Journal of Geophysical Research: Atmospheres 105(D24):29,397–29,409

Demoisson A, Tedeschi G, Piazzola J (2013) A model for the atmospheric transport of sea-salt particles in coastal areas. Atmos Res 132:144–153

Donelan MA, Pierson Jr WJ (1987) Radar scattering and equilibrium ranges in wind-generated waves with application to scatterometry. Journal of Geophysical Research: Oceans 92(C5):4971–5029

Donelan MA, Hamilton J, Hui W (1985) Directional spectra of wind-generated ocean waves. Philos Trans R Soc Lon Ser A, Math Phys Sci 315(1534):509–562

Drennan WM, Zhang JA, French JR, McCormick C, Black PG (2007) Turbulent fluxes in the hurricane boundary layer. part ii: Latent heat flux. Journal of the atmospheric sciences 64(4):1103–1115

Duncan J (1981) An experimental investigation of breaking waves produced by a towed hydrofoil. Proc Roy Soc Lon Math Phys Sci 377(1770):331–348

Dupuis H, Guerin C, Hauser D, Weill A, Nacass P, Drennan W, Cloché S, Graber H (2003) Impact of flow distortion corrections on turbulent fluxes estimated by the inertial dissipation method during the fetch experiment on r/v l'atalante. Journal of Geophysical Research: Oceans 108(C3)

Edson J, Fairall C (1994) Spray droplet modeling: 1. lagrangian model simulation of the turbulent transport of evaporating droplets. J Geophys Res: Oceans 99(C12):25,295–25,311

Edson J, Anquetin S, Mestayer P, Sini J (1996) Spray droplet modeling: 2. an interactive eulerian-lagrangian model of evaporating spray droplets. Journal of Geophysical Research: Oceans 101(C1):1279–1293

Edson JB, Jampana V, Weller RA, Bigorre SP, Plueddemann AJ, Fairall CW, Miller SD, Mahrt L, Vickers D, Hersbach H (2013) On the exchange of momentum over the open ocean. Journal of Physical Oceanography 43(8):1589–1610

van Eijk AM, Tranchant BS, Mestayer PG (2001) Seacluse: Numerical simulation of evaporating sea spray droplets. J Geophys Res: Oceans 106(C2):2573–2588

Elfouhaily T, Chapron B, Katsaros K, Vandemark D (1997) A unified directional spectrum for long and short wind-driven waves. J Geophys Res: Oceans 102(C7):15,781–15,796

Ervens B, Turpin B, Weber R (2011) Secondary organic aerosol formation in cloud droplets and aqueous particles (aqsoa): a review of laboratory, field and model studies. Atmospheric Chemistry and Physics 11(21):11,069–11,102

Fairall C, Davidson K (1986) Dynamics and modeling of aerosols in the marine atmospheric boundary layer. In: Ocean White, Springer, pp 195–208

Fairall C, Kepert J, Holland G (1994) The effect of sea spray on surface energy transports over the ocean. Global Atmos Ocean Syst 2(2-3):121–142

Fairall C, Banner M, Peirson W, Asher W, Morison R (2009) Investigation of the physical scaling of sea spray spume droplet production. J Geophys Res: Oceans 114(C10)

Fairall C, Pezoa S, Moran K, Wolfe D (2014) An observation of sea-spray microphysics by airborne doppler radar. Geophysical Research Letters 41(10):3658–3665

Fairall CW, Bradley EF, Hare J, Grachev AA, Edson JB (2003) Bulk parameterization of air–sea fluxes: Updates and verification for the coare algorithm. Journal of climate 16(4):571–591

Fitzgerald JW (1991) Marine aerosols: A review. Atmospheric Environment Part A General Topics 25(3):533–545, DOI https://doi.org/10.1016/0960-1686(91)90050-H

Frick G, Hoppel W (2000) Airship measurements of ship's exhaust plumes and their effect on marine boundary layer clouds. J Atmos Sci 57(16):2625–2648

Friedlander SK (1977) Smoke, dust and haze: Fundamentals of aerosol behavior. New York

Garratt JR (1994) The atmospheric boundary layer. Earth-Science Reviews 37(1-2):89–134

Gibson ER, Hudson PK, Grassian VH (2006) Physicochemical properties of nitrate aerosols: Implications for the atmosphere. The Journal of Physical Chemistry A 110(42):11,785–11,799

Giorgi F, Lionello P (2008) Climate change projections for the mediterranean region. Glob Plan Change 63(2-3):90–104

Gong S (2003) A parameterization of sea-salt aerosol source function for sub-and supermicron particles. Glob Biogeoc Cycl 17(4)

Grare L, Lenain L, Melville WK (2013) Wave-coherent airflow and critical layers over ocean waves. Journal of Physical Oceanography 43(10):2156–2172

Hara T, Sullivan PP (2015) Wave boundary layer turbulence over surface waves in a strongly forced condition. Journal of Physical Oceanography 45(3):868–883

Hasselmann K, Barnett T, Bouws E, Carlson H, Cartwright D, Enke K, Ewing J, Gienapp H, Hasselmann D, Kruseman P, et al. (1973) Measurements of wind-wave growth and swell decay during the joint north sea wave project (JONSWAP). Ergänzungsheft 8-12

Hauser D, Caudal G, Guimbard S, Mouche A (2008) A study of the slope probability density function of the ocean waves from radar observations. Journal of Geophysical Research: Oceans 113(C2)

Heintzenberg J, Covert D, Dingenen RV (2000) Size distribution and chemical composition of marine aerosols: a compilation and review. Tellus B: Chemical and Physical Meteorology 52(4):1104–1122

Hoarau T, Barthe C, Tulet P, Claeys M, Pinty JP, Bousquet O, Delanoë J, Vié B (2018) Impact of the generation and activation of sea salt aerosols on the evolution of tropical cyclone dumile. Journal of Geophysical Research: Atmospheres 123(16):8813–8831

Holling CS, et al. (1995) What barriers? what bridges. Barriers and Bridges to the Renewal of Ecosystems and Institutions 3(4)

Holmes P, Lumley JL, Berkooz G (1996) Turbulence, Coherent Structures, Dynamical Systems and Symmetry. Cambridge Monographs on Mechanics, Cambridge University Press, DOI 10.1017/CBO9780511622700

Holthuijsen L, Herbers T (1986) Statistics of breaking waves observed as whitecaps in the open sea. J Phys Ocean 16(2):290–297

Hoppel W, Frick G, Fitzgerald J (2002) Surface source function for sea-salt aerosol and aerosol dry deposition to the ocean surface. Journal of Geophysical Research: Atmospheres 107(D19):AAC–7

Huang J, Jaeglé L, Shah V (2018) Using caliop to constrain blowing snow emissions of sea salt aerosols over arctic and antarctic sea ice. Atmospheric Chemistry and Physics 18(22):16,253–16,269

Husain NT, Hara T, Buckley MP, Yousefi K, Veron F, Sullivan PP (2019) Boundary layer turbulence over surface waves in a strongly forced condition: LES and observation. J Phys Ocean 49(8):1997–2015

Iida N, Toba Y, Chaen M (1992) A new expression for the production rate of sea water droplets on the sea surface. J Ocean 48(4):439–460

Jaeglé L, Quinn P, Bates T, Alexander B, Lin JT (2011) Global distribution of sea salt aerosols: new constraints from in situ and remote sensing observations. Atmospheric Chemistry and Physics 11(7):3137–3157

Jaenicke R (1984) Physical aspects of atmospheric aerosol. In: Georgii, H. Jaeschke, W (eds) Chemistry of the unpolluted and polluted troposphere (pp. 341-373).

Jähne B, Riemer KS (1990) Two-dimensional wave number spectra of small-scale water surface waves. J Geophys Res: Oceans 95(C7):11,531–11,546

Janssen P, Janssen PA (2004) The interaction of ocean waves and wind. Cambridge University Press

Johansson JH, Salter ME, Navarro JA, Leck C, Nilsson ED, Cousins IT (2019) Global transport of perfluoroalkyl acids via sea spray aerosol. Environ Sci: Proc & Impacts 21(4):635–649

Katoshevski D, Nenes A, Seinfeld JH (1999) A study of processes that govern the maintenance of aerosols in the marine boundary layer. Journal of Aerosol Science 30(4):503–532

Kawai S (1981) Visualization of airflow separation over wind-wave crests under moderate wind. Boundary-Layer Meteorol 21(1):93–104

Kleiss JM, Melville WK (2011) The analysis of sea surface imagery for whitecap kinematics. Journal of Atmospheric and Oceanic Technology 28(2):219–243

Knipping EM, Dabdub D (2003) Impact of chlorine emissions from sea-salt aerosol on coastal urban ozone. Environmental science & technology 37(2):275–284

Komen GJ, Cavaleri L, Donelan M, Hasselmann K, Hasselmann S, Janssen P (1996) Dynamics and modelling of ocean waves

Korhonen H, Carslaw KS, Spracklen DV, Mann GW, Woodhouse MT (2008) Influence of oceanic dimethyl sulfide emissions on cloud condensation nuclei concentrations and seasonality over the remote southern hemisphere oceans: A global model study. Journal of Geophysical Research: Atmospheres 113(D15)

Korhonen P, Kulmala M, Laaksonen A, Viisanen Y, McGraw R, Seinfeld J (1999) Ternary nucleation of h2so4, nh3, and h2o in the atmosphere. Journal of Geophysical Research: Atmospheres 104(D21):26,349–26,353

Kudryavtsev V, Chapron B, Makin V (2014) Impact of wind waves on the air-sea fluxes: A coupled model. Journal of Geophysical Research: Oceans 119(2):1217–1236

Kudryavtsev VN, Makin VK (2011) Impact of ocean spray on the dynamics of the marine atmospheric boundary layer. Boundary-layer meteorology 140(3):383–410

Lac C, Chaboureau JP, Masson V, Pinty JP, Tulet P, Escobar J, Leriche M, Barthe C, Aouizerats B, Augros C, et al. (2018) Overview of the meso-nh model version 5.4 and its applications. Geoscientific Model Development 11(5):1929–1969

Lafon C, Piazzola J, Forget P, Le Calve O, Despiau S (2004) Analysis of the variations of the whitecap fraction as measured in a coastal zone. Boundary-Layer Meteorol 111(2):339–360

Lafon C, Piazzola J, Forget P, Despiau S (2007) Whitecap coverage in coastal environment for steady and unsteady wave field conditions. J Mar Sys 66(1-4):38–46

Large W, Pond S (1981) Open ocean momentum flux measurements in moderate to strong winds. Journal of physical oceanography 11(3):324–336

Latham J, Smith M (1990) Effect on global warming of wind-dependent aerosol generation at the ocean surface. Nature 347(6291):372–373

Laussac S, Piazzola J, Tedeschi G, Yohia C, Canepa E, Rizza U, Van Eijk A (2018) Development of a fetch dependent sea-spray source function using aerosol concentration measurements in the north-western mediterranean. Atmos Environ 193:177–189

Leck C, Keith Bigg E (2008) Comparison of sources and nature of the tropical aerosol with the summer high arctic aerosol. Tellus B: Chemical and Physical Meteorology 60(1):118–126

de Leeuw G (1986) Vertical profiles of giant particles close above the sea surface. Tellus B 38(1):51–61

de Leeuw G, Andreas EL, Anguelova MD, Fairall C, Lewis ER, O'Dowd C, Schulz M, Schwartz SE (2011) Production flux of sea spray aerosol. Rev of Geophys 49(2)

Lemarié F, Samson G, Redelsperger JL, Giordani H, Brivoal T, Madec G (2021) A simplified atmospheric boundary layer model for an improved representation of air–sea interactions in eddying oceanic models: implementation and first evaluation in nemo (4.0). Geoscientific Model Development 14(1):543–572

Lenain L, Melville WK (2017a) Evidence of sea-state dependence of aerosol concentration in the marine atmospheric boundary layer. J Phys Ocean 47(1):69–84

Lenain L, Melville WK (2017b) Measurements of the directional spectrum across the equilibrium saturation ranges of wind-generated surface waves. Journal of Physical Oceanography 47(8):2123–2138

Lenain L, Pizzo N (2021) Modulation of surface gravity waves by internal waves. J Phys Ocean

Lenain L, Statom NM, Melville WK (2019) Airborne measurements of surface wind and slope statistics over the ocean. J Phys Ocean 49(11):2799–2814

Lewis ER, Lewis R, Karlstrom KE, Lewis ER, Schwartz SE (2004) Sea salt aerosol production: mechanisms, methods, measurements, and models, vol 152. American Geophysical Union

Liao H, Chen WT, Seinfeld JH (2006) Role of climate change in global predictions of future tropospheric ozone and aerosols. Journal of Geophysical Research: Atmospheres 111(D12)

Lighthill J (1999) Ocean spray and the thermodynamics of tropical cyclones. Journal of engineering mathematics 35(1):11–42

Liu Y, Su MY, Yan XH, Liu WT (2000) The mean-square slope of ocean surface waves and its effects on radar backscatter. Journal of atmospheric and oceanic technology 17(8):1092–1105

Ma H, Babanin AV, Qiao F (2020) Field observations of sea spray under tropical cyclone olwyn. Ocean Dynamics 70(11):1439–1448

Mahowald NM, Yoshioka M, Collins WD, Conley AJ, Fillmore DW, Coleman DB (2006) Climate response and radiative forcing from mineral aerosols during the last glacial maximum, pre-industrial, current and doubled-carbon dioxide climates. Geophysical Research Letters 33(20)

Mallet M, Roger J, Despiau S, Dubovik O, Putaud J (2003) Microphysical and optical properties of aerosol particles in urban zone during ESCOMPTE. Atmos Res 69(1-2):73–97

Mallet M, Dulac F, Formenti P, Nabat P, Sciare J, Roberts G, Pelon e (2016) Overview of the chemistry-aerosol mediterranean experiment/aerosol direct radiative forcing on the mediterranean climate (charmex/adrimed) summer 2013 campaign. Atmospheric Chemistry and Physics 16(2):455–504, DOI 10.5194/acp-16-455-2016

Marechal G, Ardhuin F (2021) Surface currents and significant wave height gradients: Matching numerical models and high-resolution altimeter wave heights in the agulhas current region. J Geophys Res: Oceans 126(2):e2020JC016,564

Marmottant P, Villermaux E (2004) Fragmentation of stretched liquid ligaments. Physics of fluids 16(8):2732–2741

Mårtensson E, Nilsson E, de Leeuw G, Cohen L, Hansson HC (2003) Laboratory simulations and parameterization of the primary marine aerosol production. J Geophys Res: Atmos 108(D9)

Masson V, Le Moigne P, Martin E, Faroux S, Alias A, Alkama R, Belamari S, Barbu A, Boone A, Bouyssel F, et al. (2013) The surfexv7. 2 land and ocean surface platform for coupled or offline simulation of earth surface variables and fluxes. Geoscientific Model Development 6(4):929–960

Meagher J, Stockburger L, Bailey E, Huff O (1967) The oxidation of sulfur dioxide to sulfate aerosols in the plume of a coal-fired power plant. Atmospheric Environment 12(11):2197–2203

Mehta S, Ortiz-Suslow DG, Smith A, Haus B (2019) A laboratory investigation of spume generation in high winds for fresh and seawater. J Geophys Res: Atmos 124(21):11,297–11,312

Mestayer P, Van Eijk A, De Leeuw G, Tranchant B (1996) Numerical simulation of the dynamics of sea spray over the waves. Journal of Geophysical Research: Oceans 101(C9):20,771–20,797

Miglietta MM, Rotunno R (2019) Development mechanisms for mediterranean tropical-like cyclones (medicanes). Quarterly Journal of the Royal Meteorological Society 145(721):1444–1460

Monahan E, Davidson K, Spiel D (1982) Whitecap aerosol productivity deduced from simulation tank measurements. Journal of Geophysical Research: Oceans 87(C11):8898–8904

Monahan E, Spiel D, Davidson K (1986) A model of marine aerosol generation via whitecaps and wave disruption. In: Oceanic whitecaps, Springer, pp 167–174

Monahan EC, Muircheartaigh I (1980) Optimal power-law description of oceanic whitecap coverage dependence on wind speed. J Phys Ocean 10(12):2094–2099

Monahan EC, O'Muircheartaigh IG (1986) Whitecaps and the passive remote sensing of the ocean surface. Inter J Remote 7(5):627–642

Monin AS, Obukhov AM (1954) Basic laws of turbulent mixing in the surface layer of the atmosphere. Contrib Geophys Inst Acad Sci USSR 151(163):e187

Mueller JA, Veron F (2009) A sea state–dependent spume generation function. J Phys Ocean 39(9):2363–2372

Mueller JA, Veron F (2014a) Impact of sea spray on air–sea fluxes. Part I: Results from stochastic simulations of sea spray drops over the ocean. J Phys Ocean 44(11):2817–2834

Mueller JA, Veron F (2014b) Impact of sea spray on air–sea fluxes. part ii: Feedback effects. Journal of Physical Oceanography 44(11):2835–2853

Mulcahy J, O'Dowd C, Jennings S, Ceburnis D (2008) Significant enhancement of aerosol optical depth in marine air under high wind conditions. Geophys Res Lett 35(16)

Munk W (2009) An inconvenient sea truth: Spread, steepness, and skewness of surface slopes. Ann Rev Mar Sci 1:377–415

Myhre G, Myhre C, Samset B, Storelvmo T (2013) Aerosols and their relation to global climate and climate sensitivity. Nature Education Knowledge 4(5):7

Neumann D, Matthias V, Bieser J, Aulinger A, Quante M (2016) A comparison of sea salt emission parameterizations in northwestern europe using a chemistry transport model setup. Atmos Chem and Phys 16:9905–9933

Newell AC, Zakharov VE (1992) Rough sea foam. Phys Rev Lett 69(8):1149

Newitt D (1954) Liquid entrainment 1. the mechanism of drop formation from gas vapour bubbles. Trans Inst Chem Eng 32:244–261

Nilsson E, Rannik Ü, Swietlicki E, Leck C, Aalto PP, Zhou J, Norman M (2001) Turbulent aerosol fluxes over the arctic ocean: 2. wind-driven sources from the sea. Journal of Geophysical Research: Atmospheres 106(D23):32,139–32,154

Nilsson ED, Hultin KA, Mårtensson EM, Markuszewski P, Rosman K, Krejci R (2021) Baltic sea spray emissions: In situ eddy covariance fluxes vs. simulated tank sea spray. Atmosphere 12(2):274

Norris S, Brooks I, Moat B, Yelland M, De Leeuw G, Pascal R, Brooks B (2013a) Near-surface measurements of sea spray aerosol production over whitecaps in the open ocean. Ocean science 9(1):133–145

Norris SJ, Brooks IM, Salisbury DJ (2013b) A wave roughness reynolds number parameterization of the sea spray source flux. Geophysical Research Letters 40(16):4415–4419

O'Riordan T (2014) Environmental science for environmental management. Routledge

Ortiz-Suslow DG, Haus BK, Mehta S, Laxague NJ (2016) Sea spray generation in very high winds. J Atmos Sci 73(10):3975–3995

Ovadnevaite J, de Leeuw G, Ceburnis D, Monahan C, Partanen AI, Korhonen H, O'Dowd C, et al. (2014) A sea spray aerosol flux parameterization encapsulating wave state. Atmos Chem and Phys 14(4):1837

Pandis SN, Wexler AS, Seinfeld JH (1993) Secondary organic aerosol formation and transport — ii. predicting the ambient secondary organic aerosol size distribution. Atmospheric Environment Part A General Topics 27(15):2403–2416, DOI https://doi.org/10.1016/0960-1686(93)90408-Q

Patankar S (1980) Numerical heat transfer and fluid flow hemisphere publishing corporation. Hemis Publig Corp

Perrie W, Zhang W, Andreas EL, Li W, Gyakum J, McTaggart-Cowan R (2005) Sea spray impacts on intensifying midlatitude cyclones. Journal of Atmospheric Sciences 62(6):1867–1883

Petelski T, Markuszewski P, Makuch P, Jankowski A, Rozwadowska A (2014) Studies of vertical coarse aerosol fluxes in the boundary layer over the baltic sea. Oceanogr 56(4):697–710

Peureux C, Benetazzo A, Ardhuin F (2018) Note on the directional properties of meter-scale gravity waves. Ocean Sci 14(1):41–52

Phillips O (1969) The dynamics of the upper ocean

Phillips O (1985) Spectral and statistical properties of the equilibrium range in wind-generated gravity waves. Journal of Fluid Mechanics 156:505–531

Pianezze J, Barthe C, Bielli S, Tulet P, Jullien S, Cambon G, Bousquet O, Claeys M, Cordier E (2018) A new coupled ocean-waves-atmosphere model designed for tropical storm studies: example of tropical cyclone Bejisa (2013–2014) in the South-West Indian Ocean. J Adv Mod Earth Sys 10(3):801–825

Piazzola J, Kaloshin G (2005) Performance evaluation of the coastal aerosol extinction code "medex" with data from the black sea. Journal of aerosol science 36(3):341–359

Piazzola J, Bouchara F, de Leeuw G, Van Eijk AM (2003) Development of the mediterranean extinction code (medex). Optic Engin 42(4):912–924

Piazzola J, Forget P, Lafon C, Despiau S (2009) Spatial variation of sea-spray fluxes over a mediterranean coastal zone using a sea-state model. Boundary-Layer Meteorol 132(1):167–183

Piazzola J, Sellegri K, Bourcier L, Mallet M, Tedeschi G, Missamou T (2012) Physico-chemical characteristics of aerosols measured in the spring time in the mediterranean coastal zone. Atmos Environ 54:545–556

Piazzola J, Demoisson A, Tedeschi G (2013) Transport of aerosols in the mediterranean coastal zone. Air Pollution XXI 174:125

Piazzola J, Tedeschi G, Demoisson A (2015) A model for the transport of sea-spray aerosols in the coastal zone. Boundary-Layer Meteorol 155(2):329–350

Piazzola J, Mihalopoulos N, Canepa E, Tedeschi G, Prati P, Zarmpas P, Bastianini M, Missamou T, Cavaleri L (2016) Characterization of aerosols above the northern adriatic sea: Case studies of offshore and onshore wind conditions. Atmos Environ 132:153–162

Piazzola J, Bruch W, Desnues C, Parent P, Yohia C, Canepa E (2021) Influence of meteorological conditions and aerosol properties on the covid-19 contamination of the population in coastal and continental areas in france: Study of offshore and onshore winds. Atmos 12(4):523

Plant WJ (1982) A relationship between wind stress and wave slope. J Geophys Res: Oceans 87(C3):1961–1967

Planton S, Driouech F, Rhaz K, LIONELLO P (2016) The climate of the mediterranean regions in the future climate projections. The Mediterranean region under climate change p 83

Pollard RT (1978) The joint air-sea interaction experiment—jasin 1978. Bulletin of the American Meteorological Society 59(10):1310–1318

Pope SB (2000) Turbulent Flows. Cambridge University Press, DOI 10.1017/CBO9780511840531

Pruppacher HR, Klett J (1978) Microphysics of clouds and precipitation. Dordrecht, The Netherlands

Ramanathan V, Crutzen PJ, Lelieveld J, Mitra A, Althausen D, Anderson J, Andreae M, Cantrell W, Cass G, Chung C, et al. (2001) Indian ocean experiment: An integrated analysis of the climate forcing and effects of the great indo-asian haze. Journal of Geophysical Research: Atmospheres 106(D22):28,371–28,398

Ramberg SE, Griffin OM (1987) Laboratory study of steep and breaking deep water waves. J Water Port Coast Ocean Eng 113(5):493–506

Rastigejev Y, Suslov SA (2019) Effect of evaporating sea spray on heat fluxes in a marine atmospheric boundary layer. Journal of Physical Oceanography 49(7):1927–1948

Rastigejev Y, Suslov SA, Lin YL (2011) Effect of ocean spray on vertical momentum transport under high-wind conditions. Boundary-layer meteorology 141(1):1–20

Reul N, Branger H, Giovanangeli JP (2008) Air flow structure over short-gravity breaking water waves. Boundary-Layer Meteorol 126(3):477–505

Richter DH, Sullivan PP (2013) Sea surface drag and the role of spray. Geophysical Research Letters 40(3):656–660

Richter DH, Sullivan PP (2014) The sea spray contribution to sensible heat flux. Journal of the Atmospheric Sciences 71(2):640–654

Richter DH, Dempsey AE, Sullivan PP (2019) Turbulent transport of spray droplets in the vicinity of moving surface waves. J Phys Ocean 49(7):1789–1807

Romero L (2019) Distribution of surface wave breaking fronts. Geophysical Research Letters 46(17-18):10,463–10,474

Romero L, Lenain L, Melville WK (2017) Observations of surface wave–current interaction. J Phys Ocean 47(3):615–632

Russell P, Bergstrom R, Shinozuka Y, Clarke A, DeCarlo P, Jimenez J, Livingston J, Redemann J, Dubovik O, Strawa A (2010) Absorption angstrom exponent in aeronet and related data as an indicator of aerosol composition. Atmospheric Chemistry and Physics 10(3):1155–1169

Saliba G, Chen CL, Lewis S, Russell LM, Rivellini LH, Lee AK, Quinn PK, Bates TS, Haëntjens N, Boss ES, et al. (2019) Factors driving the seasonal and hourly variability of sea-spray aerosol number in the north atlantic. Proceedings of the National Academy of Sciences 116(41):20,309–20,314

Saruwatari A, Abe N (2014) Relationship between latent heat of sea spray and uncertainty of a meteorological field. Applied Ocean Research 44:102–111

Sauvage C, Lebeaupin Brossier C, Bouin MN (2021) Towards kilometer-scale ocean-atmosphere-wave coupled forecast: a case study on a mediterranean heavy precipitation event. Atmospheric Chemistry and Physics Discussions pp 1–45

Savelyev I, Anguelova M, Frick G, Dowgiallo D, Hwang P, Caffrey P, Bobak J (2014) On direct passive microwave remote sensing of sea spray aerosol production. Atmos Chem Phys 14(21):11,611

Saxena P, Hildemann LM (1996) Water-soluble organics in atmospheric particles: A critical review of the literature and application of thermodynamics to identify candidate compounds. Journal of atmospheric chemistry 24(1):57–109

Schulz M, de Leeuw G, Balkanski Y (2004) Sea-salt aerosol source functions and emissions. In: Emissions of Atmospheric Trace Compounds, Springer, pp 333–359

Schwendeman M, Thomson J (2015) Observations of whitecap coverage and the relation to wind stress, wave slope, and turbulent dissipation. J Geophys Res: Oceans 120(12):8346–8363

Seinfeld JH, Pandis SN (1997) Atmospheric chemistry and physics. S45 1356

Sellegri K, Gourdeau J, Putaud JP, Despiau S (2001) Chemical composition of marine aerosol in a mediterranean coastal zone during the fetch experiment. Journal of Geophysical Research: Atmospheres 106(D11):12,023–12,037

Sellegri K, O'Dowd C, Yoon Y, Jennings S, de Leeuw G (2006) Surfactants and submicron sea spray generation. J Geophys Res: Atmos 111(D22)

Slingo A (1990) Sensitivity of the earth's radiation budget to changes in low clouds. Nature 343(6253):49–51

Slinn S, Slinn W (1980) Predictions for particle deposition on natural waters. Atmospheric Environment (1967) 14(9):1013–1016

Slinn W, Hasse L, Hicks B, Hogan A, Lal D, Liss P, Munnich K, Sehmel G, Vittori O (1978) Some aspects of the transfer of atmospheric trace constituents past the air-sea interface. Atmospheric Environment (1967) 12(11):2055–2087

Smith M, Park P, Consterdine I (1993) Marine aerosol concentrations and estimated fluxes over the sea. Q J R Meteorol Soc 119(512):809–824

Smith SD (1988) Coefficients for sea surface wind stress, heat flux, and wind profiles as a function of wind speed and temperature. J Geophys Res: Oceans 93(C12):15,467–15,472

Soloviev A, Lukas R (2010) Effects of bubbles and sea spray on air–sea exchange in hurricane conditions. Boundary-layer meteorology 136(3):365–376

Soloviev AV, Lukas R, Donelan MA, Haus BK, Ginis I (2014) The air-sea interface and surface stress under tropical cyclones. Scientific reports 4(1):1–6

Spiel DE (1994) The sizes of the jet drops produced by air bubbles bursting on sea-and fresh-water surfaces. Tellus B: Chem Phys Meteorol 46(4):325–338

Spracklen DV, Arnold SR, Sciare J, Carslaw KS, Pio C (2008) Globally significant oceanic source of organic carbon aerosol. Geophysical Research Letters 35(12)

Sroka S, Emanuel K (2021) A review of parameterizations for enthalpy and momentum fluxes from sea spray in tropical cyclones. Journal of Physical Oceanography

Stokes GG (1880) Supplement to a paper on the theory of oscillatory waves. Math Phys Pap 1(314-326):14

Stull RB (1988) An introduction to boundary layer meteorology, vol 13. Springer Science & Business Media

Sullivan PP, Banner ML, Morison RP, Peirson WL (2018) Turbulent flow over steep steady and unsteady waves under strong wind forcing. Journal of Physical Oceanography 48(1):3–27

Sutherland P, Melville WK (2013) Field measurements and scaling of ocean surface wave-breaking statistics. Geophysical Research Letters 40(12):3074–3079

Tedeschi G, Piazzola J (2011) Development of a 2d marine aerosol transport model: Application to the influence of thermal stability in the marine atmospheric boundary layer. Atmos Res 101(469–479):10

Tennekes H, Lumley J (1992) A first course in turbulence mit press cambridge

Thomson J, D'Asaro E, Cronin M, Rogers W, Harcourt R, Shcherbina A (2013) Waves and the equilibrium range at ocean weather station p. Journal of Geophysical Research: Oceans 118(11):5951–5962

Toba Y, Koga M (1986) A parameter describing overall conditions of wave breaking, whitecapping, sea-spray production and wind stress. In: Oceanic whitecaps, Springer, pp 37–47

Toba Y, Komori S, Suzuki Y, Zhao D (2006) Similarity and dissimilarity in air-sea momentum and CO2 transfers: the nondimensional transfer coefficients in light of windsea reynolds number. Atmos-Ocean Inter 2:53–82

Townsend AA (1972) Flow in a deep turbulent boundary layer over a surface distorted by water waves. vol 55(4)

Troitskaya Y, Kandaurov A, Ermakova O, Kozlov D, Sergeev D, Zilitinkevich S (2017) Bag-breakup fragmentation as the dominant mechanism of sea-spray production in high winds. Scientific reports 7(1):1–4

Troitskaya Y, Kandaurov A, Ermakova O, Kozlov D, Sergeev D, Zilitinkevich S (2018) The “bag breakup” spume droplet generation mechanism at high winds. Part I: Spray generation function. J Phys Ocean 48(9):2167–2188

Tsyro S, Aas W, Soares J, Sofiev M, Berge H, Spindler G (2011) Modelling of sea salt concentrations over Europe: key uncertainties and comparison with observations. Atmos Chem and Phys 11(20):10,367–10,388

Tuel A, Eltahir EA (2020) Why is the mediterranean a climate change hot spot? Journal of Climate 33(14):5829–5843

Van Eijk A, Kusmierczyk-Michulec J, Francius M, Tedeschi G, Piazzola J, Merritt D, Fontana J (2011) Sea-spray aerosol particles generated in the surf zone. Journal of Geophysical Research: Atmospheres 116(D19)

Vandemark D, Chapron B, Sun J, Crescenti GH, Graber HC (2004) Ocean wave slope observations using radar backscatter and laser altimeters. J Phys Ocean 34(12):2825–2842

Vanderplow B, Soloviev AV, Dean CW, Haus BK, Lukas R, Sami M, Ginis I (2020) Potential effect of bio-surfactants on sea spray generation in tropical cyclone conditions. Scientific reports 10(1):1–10

Veron F (2015) Ocean spray. Ann Rev Fluid Mech 47:507–538

Veron F, Mieussens L (2020) An eulerian model for sea spray transport and evaporation. Journal of Fluid Mechanics 897

Veron F, Hopkins C, Harrison E, Mueller J (2012) Sea spray spume droplet production in high wind speeds. Geophys Res Lett 39(16)

Vivaldo G, Masi E, Taiti C, Caldarelli G, Mancuso S (2017) The network of plants volatile organic compounds. Scientific reports 7(1):1–18

Vogt M, Vallina S, Buitenhuis E, Bopp L, Le Quéré C (2010) Simulating dimethylsulphide seasonality with the dynamic green ocean model planktom5. Journal of Geophysical Research: Oceans 115(C6)

Vollestad P, Jensen A (2021) Modification of airflow structure due to wave breaking on a submerged topography. Boundary-Layer Meteorology pp 1–20

Walsh EJ, Vandemark DC, Friehe CA, Burns SP, Khelif D, Swift RN, Scott JF (1998) Measuring sea surface mean square slope with a 36-ghz scanning radar altimeter. Journal of Geophysical Research: Oceans 103(C6):12,587–12,601

Wang LP, Maxey MR (1993) Settling velocity and concentration distribution of heavy particles in homogeneous isotropic turbulence. Journal of fluid mechanics 256:27–68

Wang Y, Lee KH, Lin Y, Levy M, Zhang R (2014) Distinct effects of anthropogenic aerosols on tropical cyclones. Nature Climate Change 4(5):368–373

Woolf DK (1997) Bubbles and their role in gas exchange. Sea Surf Glob Change

Wu J (1988) Variations of whitecap coverage with wind stress and water temperature. Journal of physical oceanography 18(10):1448–1453

Wu J (1993) Production of spume drops by the wind tearing of wave crests: The search for quantification. J Geophys Res: Oceans 98(C10):18,221–18,227

Wu L, Cheng X, Zeng Q, Jin J, Huang J, Feng Y (2017) On the upward flux of sea-spray spume droplets in high-wind conditions. Journal of Geophysical Research: Atmospheres 122(11):5976–5987

Yang M, Norris SJ, Bell TG, Brooks IM (2019) Sea spray fluxes from the southwest coast of the united kingdom–dependence on wind speed and wave height. Atmospheric Chemistry and Physics 19(24):15,271–15,284

Yoon Y, Ceburnis D, Cavalli F, Jourdan O, Putaud J, Facchini M, Decesari S, Fuzzi S, Sellegri K, Jennings S, et al. (2007) Seasonal characteristics of the physicochemical properties of north atlantic marine atmospheric aerosols. J Geophys Res: Atmos 112(D4)

Yousefi K, Veron F, Buckley MP (2021) Turbulent and wave kinetic energy budgets in the airflow over wind-generated surface waves. Journal of Fluid Mechanics 920

Zhang Q, Jimenez JL, Canagaratna M, Allan JD, Coe H, Ulbrich I, Alfarra M, Takami A, Middlebrook A, Sun Y, et al. (2007) Ubiquity and dominance of oxygenated species in organic aerosols in anthropogenically-influenced northern hemisphere midlatitudes. Geophysical research letters 34(13)

Zhang S, Wang M, Ghan SJ, Ding A, Wang H, Zhang K, Neubauer D, Lohmann U, Ferrachat S, Takeamura T, Gettelman A, Morrison H, Lee Y, Shindell DT, Partridge DG, Stier P, Kipling Z, Fu C (2016) On the characteristics of aerosol indirect effect based on dynamic regimes in global climate models. Atmospheric Chemistry and Physics 16(5):2765–2783, DOI 10.5194/acp-16-2765-2016

Zhao D, Toba Y (2001) Dependence of whitecap coverage on wind and wind-wave properties. J Ocean 57(5):603–616

Zhao D, Toba Y, Sugioka Ki, Komori S (2006) New sea spray generation function for spume droplets. Journal of Geophysical Research: Oceans 111(C2)

WILLIAM BRUCH

Institut Méditerranéen d'Océanologie, Université de Toulon

Étude expérimentale et numérique de la génération et du transport des aérosols marins à l'interface air-mer pour des vents forts, et des conséquences sur les propriétés de la couche limite atmosphérique marine

Résumé en Français

Les embruns sont des aérosols en phase aqueuse générés à la surface de l'eau. Au large, ils sont générés par des mécanismes tel que le déferlement et l'écrêtage. Aujourd'hui, la connaissance portant sur les embruns excédant 20 µm de rayon reste limitée. Cette thèse vise à améliorer la compréhension des processus de génération, de transport, et les impacts sur les propriétés de la couche limite atmosphérique marine (CLAM). La campagne MATE2019 est ainsi menée à l'installation air-mer de Luminy (Marseille, France) afin d'étudier le rôle des interactions vague-vent sur la génération. Une analyse d'échelle révèle que la génération d'embruns corrèle le mieux avec la variance de pente de vagues pour les plus grosses gouttelettes 'spume' générées par écrêtage. Pour les plus petites gouttelettes 'jet' générées par éclatement de bulles, la meilleure corrélation est obtenue avec un nombre adimensionnel combinant la variance de pentes de vagues, l'age de vague, et un nombre de Reynolds adapté aux mers de vent. Il en résulte la formulation de deux fonctions de génération d'embruns dépendantes sur l'état de mer, valides pour des vents de 12–20 m s^{-1} et des rayons de 3–35 µm. Extrapolées aux conditions *in situ*, les fonctions de génération issues du laboratoire sont paramétrées dans les modèles numériques MACMod et MESO-NH, à leur tour validés à l'aide de mesures terrain, dont une nouvelle campagne de mesure effectuée pendant la thèse dans le Golfe de Gascogne. Les meilleures performances de modélisation sont obtenues avec les fonctions de génération issues du laboratoire. Ces résultats permettent de mieux appréhender l'impact des embruns sur la CLAM.

Mots clés: Interactions air-mer – Génération d'embruns – Mesures expérimentales – Modélisation

---

Experimental and numerical study of sea spray generation and transport at the air-sea interface in strong wind conditions, and of their consequences on the properties of the marine atmospheric boundary layer

English Summary

Sea spray droplets are aqueous phase aerosols generated from the water surface. In the open ocean, they are generated as a result of wind-forced wave breaking and surface-tearing mechanisms. To this day, knowledge of sea spray particles larger than 20 µm radius is sparse. The present thesis aims to improve knowledge of the sea spray generation flux, as well as transport and impacts on the properties of the marine atmospheric boundary layer (MABL). To this end, the effects of wind–wave interactions on the surface sea spray generation flux are investigated during the MATE2019 experiment, conducted at the large wave–wind facility in Luminy (Marseille, France). Scaling analysis shows that sea spray generation is best correlated with the wave-slope variance for the larger spume droplets generated by surface tearing. For smaller jet droplets generated by bubble bursting, the highest correlation is found with a non-dimensional number combining the wave-slope variance, the wave age, and a windsea Reynolds number. This resulted in the formulation of two wave-state-dependent sea spray generation functions, each valid for wind speeds 12–20 m s^{-1} and radii 3–35 µm. Upscaled to the field, the laboratory-derived generation functions are parameterized in the MACMod and MESO-NH numerical models, and validated using field data collected during the thesis in the Bay of Biscay for this purpose. Best model performances are found using the laboratory generation functions. Such results are encouraging for the study of sea spray impacts on the properties of the MABL.

Keywords: Air-sea interaction – Sea spray generation – Experimental measurements – Numerical modeling